Remote sensing applied to the Bajoca lithiniferous area

Joana Maria Cardoso Fernandes

Mestrado em Geologia
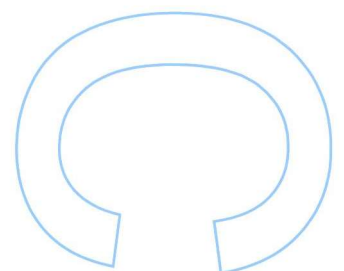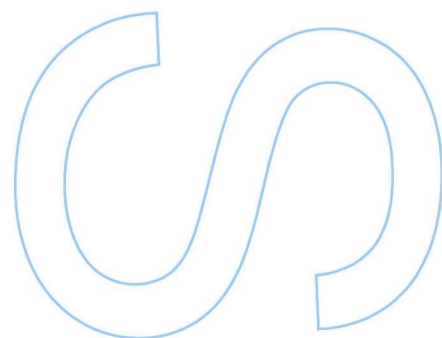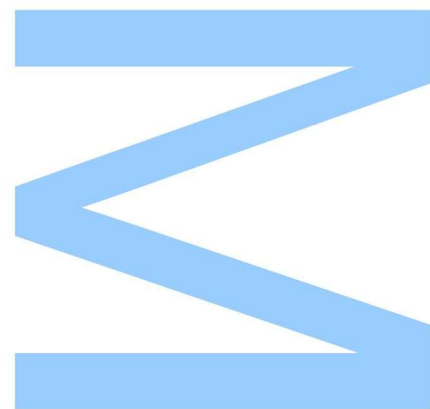Departamento de Geociências, Ambiente e Ordenamento do Território
2018

Orientador
Alexandre Martins Campos de Lima, Professor auxiliar Faculdade de Ciências da Universidade do Porto

Coorientador
Ana Cláudia Moreira Teodoro, Professor auxiliar Faculdade de Ciências da Universidade do Porto

U. PORTO

FACULDADE DE CIÊNCIAS
UNIVERSIDADE DO PORTO
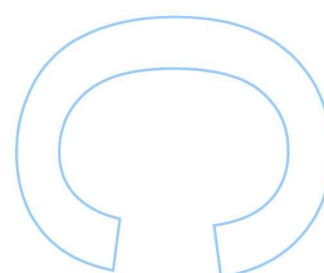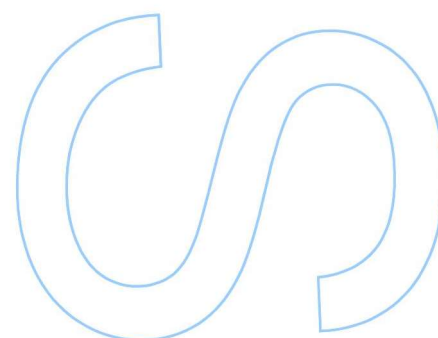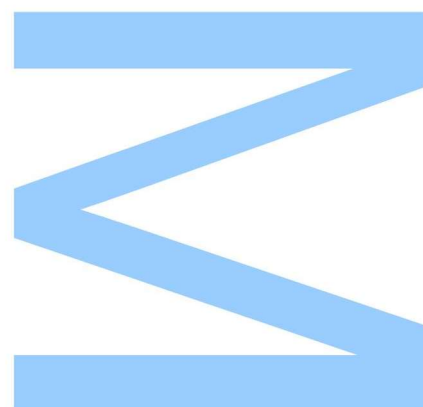
"No fundo, todos temos necessidade de dizer quem somos e o que é que estamos a fazer e a necessidade de deixar algo feito, porque esta vida não é eterna e deixar coisas feitas pode ser uma forma de eternidade."

José Saramago

Agradecimentos

Em primeiro lugar, quero agradecer à National Aeronautics and Space Administration (NASA), à United States Geological Survey (USGS) e à European Space Agency (ESA) por disponibilizarem gratuitamente as imagens de satélite sem as quais este trabalho não seria possível.

Quero também agradecer ao Laboratório Nacional de Energia e Geologia (LNEG) pelos dados atenciosamente cedidos.

À Prof. Dr. Lia Duarte, por toda a atenção e tempo dispensados, os meus sinceros agradecimentos.

Ao doutorando Ubaldo Gemusse que me tem acompanhado nesta jornada, obrigada por todas as trocas de conhecimento e de opiniões.

Quero deixar um agradecimento muito especial aos meus orientadores, o Prof. Dr. Alexandre Lima e a Prof. Dr. Ana Cláudia Teodoro, por me terem proporcionado esta oportunidade, pela confiança depositada em mim e, por toda a atenção, orientação e conselhos dados ao longo desta dissertação. Em particular, quero agradecer ao Prof. Dr. Alexandre por estar sempre preocupado em contribuir para o desenvolvimento do meu conhecimento geológico. À Prof. Dr. Ana Cláudia muito obrigada por me incentivar a divulgar publicamente os resultados do meu trabalho, enriquecendo assim o meu currículo científico e a minha experiência.

Aos meus amigos, por todos os bons momentos e histórias que partilhámos ao longo destes cinco anos. Obrigada por me aceitarem tal como sou e por se orgulharem das minhas conquistas como se fossem as vossas próprias.

À minha família que desde cedo valorizou a importância da minha educação, obrigada por terem cultivado em mim o gosto pela leitura, pelo conhecimento, por aprender. Obrigada por todos os sacrifícios que fizeram por mim e por toda a ajuda que me deram ao longo de todo o percurso.

Ao António Ascensão, obrigada por teres estado sempre a meu lado ao longo destes anos. Obrigada por todos os conselhos. Obrigada por estares sempre disposto a ouvir-me falar entusiasmada com o meu trabalho ou então a ouvir-me desabafar quando as coisas não correram tão bem. Muito obrigada por todas as correções no inglês e pela ajuda no grafismo das imagens que definitivamente melhoraram esta dissertação.

E por fim, gostava de agradecer a todos aqueles que contribuíram para a minha formação académica, desde colegas, professores até aos geólogos que tive o prazer de conhecer ao longo desta caminhada. A todos, obrigada!

Resumo

A deteção remota tem provado ser uma ferramenta muito útil na área da geologia, sendo capaz de identificar áreas alvo de prospeção para vários tipos de depósito. Só mais recentemente, essas mesmas metodologias foram usadas para a deteção de pegmatitos com lítio (Li). Este recente interesse, deveu-se à crescente importância e demanda de Li para construção de baterias para carros elétricos com vista à utilização de meios de transporte mais ecológicos. A aplicação da deteção remota na prospeção mineira baseia-se principalmente no reconhecimento de rochas hidrotermalmente alteradas que podem estar associadas aos depósitos minerais. Isto é possível porque cada mineral ou rocha tem uma assinatura espectral única que pode ser usada para a sua classificação e mapeamento geológico.

A área de estudo deste trabalho é a região de Fregeneda (Salamanca, Espanha) - Almendra (Vila Nova de Foz Côa, Portugal), onde diferentes tipos conhecidos de pegmatitos com Li foram identificados. O objetivo deste estudo foi desenvolver metodologias, considerando dados de deteção remota e algoritmos de processamento de imagem, capazes de identificar pegmatitos com Li. Esse reconhecimento foi efetuado com base em duas abordagens: a identificação de zonas de alteração hidrotermal associadas aos pegmatitos (através da discriminação de óxidos de ferro e minerais de argila) e a identificação direta de minerais de Li. Para complementar a análise espetral, também foi elaborado um mapa estrutural utilizando técnicas de deteção remota. Para tal, utilizaram-se imagens Landsat 5, Landsat 8, Sentinel-2 e ASTER com baixa cobertura de vegetação e de nuvens. O processamento de imagem foi dividido em duas etapas principais: a etapa de pré-processamento e a etapa de aplicação dos métodos de processamento de imagem. O pré-processamento envolveu a correção atmosférica e conversão para refletância de superfície, o *sub-setting* geográfico e espetral, a criação de uma máscara de vegetação e de corpos de água e *pan-sharpening* das imagens Landsat 8. Os métodos de processamento de imagem incluíram: combinações RGB (vermelho, verde, azul), rácios de bandas, análise de componentes principais (PCA) e a aplicação de filtros direcionais para extração de lineações.

Estas metodologias permitiram prever a ocorrência de óxidos de ferro e minerais de argila e discriminar entre zonas de alteração hidrotermal e zonas não alteradas. As combinações RGB autopropostas para as imagens ASTER, Landsat 5 e 8 foram capazes de discriminar os pegmatitos com Li das rochas encaixantes. Os rácios de bandas autopropostos e PCA seletiva nas mesmas bandas foram também capazes de discriminar minerais portadores de Li. Os filtros aplicados permitiram a construção de

um mapa estrutural com aproximadamente 150 lineações digitalizadas manualmente que podem ser usadas para melhorar as cartas geológicas existentes. Para concluir, a deteção remota provou ser uma ferramenta profícua na identificação de padrões estruturais (que podem ajudar a explicar a instalação dos pegmatitos) e provou ter um grande potencial na discriminação de pegmatitos com Li. Isto pode ser de grande interesse para as empresas mineiras, visto que a aplicação destes métodos pode levar a uma diminuição dos impactos dos estágios iniciais da prospeção mineira, aumentando a sua eficiência e sustentabilidade.

Palavras-chave: Lítio, Deteção remota, Combinações RGB, Rácio de bandas, PCA, Halos de alteração, Pegmatitos, ASTER, Landsat 5, Landsat 8, Sentinel-2

Abstract

Remote sensing has proved to be a powerful resource in geology capable of delineating target exploration areas for several deposit types. Only recently, these methodologies have been used for the detection of lithium (Li)-bearing pegmatites. This happened because of the growing importance and demand of Li for the construction of Li-ion batteries for electric cars in the pursuit for more environment-friendly means of transportation. The application of remote sensing to mineral exploration is mainly based on the recognition of hydrothermally altered rocks that can be associated with ore deposits. This is possible because each mineral or rock has a unique spectral signature that can be used for geological classification and mapping.

The study area of this work is the Fregeneda (Salamanca, Spain)-Almendra (Vila Nova de Foz Côa, Portugal) region, where different known types of Li-pegmatites have been mapped. The objective of this study was to develop remote sensing methodologies capable of identifying Li-pegmatites. This recognition was made based on two approaches: the identification of hydrothermally altered zones associated with the pegmatites (through the discrimination of iron oxides and clay minerals) and the direct identification of Li-bearing minerals. To complement the spectral analysis, a structural map was also elaborated using remote sensing techniques. For that, cloud free Landsat 5, Landsat 8, Sentinel-2 and ASTER images with low vegetation coverage were used. The image processing was divided in two main stages: the pre-processing stage and the image processing methods stage. The pre-processing involved the atmospheric correction and surface reflectance conversion, the geographic and spectral sub-setting, the creation of a vegetation and main water bodies mask and the pan-sharpening of Landsat 8 images. The image processing methods included: RGB (red, green, blue) combinations, band ratios, principal component analysis (PCA) and directional filtering for lineament extraction.

These methodologies allowed to predict the occurrence of iron oxides and clay minerals, and to discriminate between hydrothermally altered zones and non-altered zones. Self-proposed RGB combinations for ASTER, Landsat 5 and 8 were capable of discriminating the Li-bearing pegmatites from the host rocks. Self-proposed band ratios and selective PCA on the same bands were also able to highlight the Li-bearing minerals. The applied filters enabled the construction of a structural map with approximately 150 manually digitized lineaments which can be used to improve the existent geological maps. To conclude, remote sensing proved to be a powerful tool to identify fracture patterns (that

may help explain the pegmatite emplacement) and to have great potential for the discrimination of Li-bearing pegmatites. This can be of great interest to mining companies since they could lead to a decrease of the impacts of the early stages of exploration and an increased efficiency and sustainability of mineral exploration.

Keywords: Lithium, Remote Sensing, RGB combinations, Band ratio, PCA, Alteration halos, Pegmatites, ASTER, Landsat 5, Landsat 8, Sentinel-2

Table of contents

Table of Figures

Table of Tables

Abbreviations

ASTER – Advanced Spaceborne Thermal Emission and Reflection Radiometer

BAI – Burned Area Index

CIZ – Central Iberian Zone

CXG – "Complexo Xisto-Grauváquico"

CZ – Cantabric zone

DN – Digital Number

DOS1 – Dark Object Subtraction 1

ENE – East-northeast

EOS – Earth Observing System

E – East

ESE – East-southeast

Fe – Iron

GIS – Geographic Information Systems

GTMZ – Galiza Trás-os-Montes Zone

LCT – Lithium, Cesium, Tantalum

Li – Lithium

METI – Japanese Ministry of International Trade and Industry

Mn – Manganese

MSS – Multispectral Scanner System

N – North

NASA – National Aeronautics and Space Administration

NBR – Normalized Burn Ratio

NDVI – Normalized Difference Vegetation Index

NE – Northeast

NIR – Near Infrared

NNE – North-northeast

NNW – North-northwest

NW – Northwest

NYF – Niobium, Yttrium and rare earth elements, Fluor

OLI – Operational Land Imager

OMZ – Ossa Morena Zone

P – Pressure

PAN – Panchromatic

PCA – Principal Component Analysis

RGB – Red, Green and Blue

S – South

SCP – Semi-Automatic Classification Plugin

SE – Southeast

Sn – Tin

SNAP – Sentinel Application Platform

SPZ – South Portuguese Zone

SSE – South-southeast

SSW – South-southwest

SW – Southwest

SWIR – Shortwave Infrared

T - Temperature

TIR – Thermal Infrared

TIRS – Thermal Infrared Sensor

TM – Thematic Mapper

TOA – Top of the Atmosphere

USGS – United Sates Geological Survey

VMS – Volcanogenic Massive Sulfide Ore

VNIR – Visible and Near Infrared

W – Tungsten

W – West

WALZ – West Asturico-Leonesa zone

WNW – West-northwest

WSW – West-southwest

1 Introduction

It is impossible to ignore the current growing importance and demand of lithium (Li) for several industrial applications among which the production of rechargeable Li-ion batteries stands outs, mainly for the construction of electric vehicles in the pursuit for more environment-friendly means of transportation.

To address that demand, the identification of new Li deposits is crucial and less expensive, cleaner and faster exploration methods (when compared with classic techniques) are in order. Remote sensing could be the answer to this problem since it has already proved itself as a powerful resource to delineate target exploration areas for several deposit types. Only recently, the first steps to detect Li-bearing pegmatites using these methodologies have been made.

The existence of different known types of Li mineralization, the large number of mapped aplite-pegmatites veins and the fact that these veins often difficult the growth of vegetation, make the Bajoca region an ideal target area for remote sensing exploration.

So, the subject of the dissertation "Remote sensing applied to the Bajoca lithiniferous area" is relevant not only due to the rising economic importance of Li, but also because there are several developments to be made in the field of remote sensing applied to Li-bearing pegmatites. This work is then a first approach to this issue where a set of well-known processing methods were applied with the aim of detecting Li signatures and associated hydrothermal alteration. At the same time, other image processing methods were applied to extract structural lineaments that can also help pin-point Li-bearing pegmatites. If the proposed methodology and technology were capable of successfully identifying possible mineralized areas, the duration and costs of an exploration campaign could be drastically reduced, favouring the quick discover of new Li pegmatites and consequently mining companies.

1.1 Geographic setting

The Bajoca Mine is located 4 km W of Almendra, in the Vila Nova de Foz Côa town, Guarda district, north of Portugal (Figure 1). The homonymous mining concession (Table 1), in which most of the studies took place, is registered with the number MNC000064 at Direção Geral de Energia e Geologia.

Figure 1 – Location of the Bajoca mining concession and extended studied area.

The concession belongs to the Fregeneda-Almendra aplite-pegmatite field, spreading from the Almendra-Barca D'Alva region (Vila Nova de Foz Côa and Figueira de Castelo Rodrigo towns) to La Fregeneda and Hinojosa del Duero towns (Salamanca, Spain). Situated in the transition between Beira Alta and Alto-Douro regions, the aplite-pegmatite field is delimitated at north by the Douro river, at east by the Vilariça's fault valley and is divided in two by the Águeda river (materializing the border between Portugal and Spain).

Since the Bajoca concession represents a relatively small area (1.16909 km^2), it is necessary to extend the studied in order to incorporate more information.

Table 1 – Vertex coordinates of the Bajoca mining concession. Coordinate System: UTM29N WGS84.

Vertex	X (m)	Y (m)	Vertex	X (m)	Y (m)
1	666430.33	4541169.03	11	666438.17	4540903.64
2	666965.21	4541174.35	12	666434.16	4540924.10
3	668058.00	4541885.14	13	666433.50	4540950.69
4	668067.95	4540885.36	14	666415.78	4540973.31
5	667068.17	4540875.41	15	666417.35	4540985.93
6	666875.17	4540173.58	16	666469.85	4541035.54
7	666675.22	4540171.59	17	666528.86	4541074.32
8	666422.95	4540784.51	18	666537.74	4541096.31
9	666478.71	4540828.06	19	666520.55	4541125.74
10	666484.26	4540864.01	20	666451.66	4541125.75
			21	666439.58	4541143.73

1.2 State of the art

The study area is covered in the Portuguese side by sheets 15-A Vila Nova de Foz Côa (Silva *et al*., 1990a) and 15-B Freixo de Espada à Cinta (Silva *et al*., 1990b), of the geological map at the scale of 1:50,000, as well as the respective explanatory notes (Silva & Ribeiro, 1991; Silva & Ribeiro). The area is also covered by the simplied geological map of the Vale do Côa's Archeological Park at the scale 1:80,000 (Ribeiro, 2001).

Most of the existent studies in this region are not recent. Nevertheless, they comprehend subjects such as Geology (*e.g.* Medeiros & Faria, 1953; Pinto, 1984a, b), Economic Geology, Geochemistry (*e.g.* Oliveira & Cramez, 1982; Oliveira *et al.,* 1982), Geomorphology (*e.g.* Patrício, 1944; Ferreira, 1971, 1978), Hydrogeology (*e.g.* Silva & Ribeiro, 1991), Archaeology, amongst others.

Several publications cover the different types of mineralization of this region, namely W, Sn and Li mineralizations. Goinhas & Viegas (1982) *in* Silva & Ribeiro, (1991) referred to the occurrences and potential of the tin and tungsten in this region and their exploration methods. Ramos *et al*. (1978) *in* Silva & Ribeiro, (1991) performed a geological and mining exploration in the Almendra – Castelo Maior region. Gaspar (1997) approached W, Sn and Li mineralizations in the Barca D'Alva region, with an emphasis in the tungsten mineralizations in calcossilicated rocks of the Riba D'Alva mine. Mateus (1995a, b *in* Vieira, 2010) studied the metallogenic potencial of the late Variscan phases, especially concerning the sulphide and gold mineralizations associated with the Vilariça's fault. Charoy & Noronha (1999) studied the geochemistry and the paragenesis of the

Almendra pegmatite and associated plutons, concluding that the lepidolite has a secondary, metassomatic origin. Gaspar & Inverno (2000) referred the mineralogy and metassomatic evolution of scheelite skarns in the Riba D'alva mine.

Almeida (2003) adressed the petalite aplitpegmatite vein from the Bajoca Mine in an exploitational, petrographic and geochemical point of view. Other related publications worth mentioning are the geochemical study of the Li-bearing veins performed by Lima *et al*. (2003a), the mineralogical zoning of the petalite vein of the Bajoca Mine presented by Lima *et al*. (2003b) and the scientific and tecnologhical caracterization of rare elements aplite-pegmatites in the Almendra region (Lima *et al*., 2003c).

Vieira (2010) developed a work about the rare elements aplite-pegmatites from the Almendra-Barca D'Alva region. The mencioned work comprehended the characterization and classification of the veins as well as petrographic, geochemical and mineralogical studies. From his work and investigation, other publications followed: Vieira & Lima (2005a, b; 2007); Vieira *et al*. (2007a; 2007b; 2007c; 2008) Roda *et al*. (2007; 2010); Lima *et al*. (2010).

In what concerns the application of remote sensing data and image processing techniques in mineral exploration in this region or, in fact, in any field of geology, there are no published works. Nonetheless, during the last decades, some advancements have been made in remote sensing, in other locations of Portugal.

However, the amount of studies which deal with the application of remote sensing in mineral exploration is not vast. Most of them used interpretation of aerial photos or satellite images for lineament extraction (*e.g.* Pereira *et al.,* 2012; Manuel *et al.,* 2015). Other studies deal with spectral analysis of satellite images and some coupled it with lineament extraction.

In a preliminary study, Lima *et al.* (2014) used ASTER images to determine the remote sensing data potential in the geological exploration of Freixeda area (Mirandela). Sinergeo & UM (2013), in the scope of the project PROSPEG, used Landsat and Spot images in an attempt to determine the localization of granitic pegmatites in several areas of Portugal (Ponte da Barca-Terras de Bouro, Chaves, Viseu-Satão and Guarda). Frutuoso (2015) mapped hydrothermal alteration associated with gold mineralization in the Chaves License, using Landsat 8 data. The target exploration map obtained resulted from combination of image spectral analysis, lineament extraction and other geological data. Manuel *et al*. (2017) used Landsat 8 image spectral analysis and lineament

extraction to target potential locations of W, Sn and Au mineralizations in the Góis-Castanheira de Pêra area.

Other remote sensing applications in Portugal are, for example: the evaluation of gas shale potential (Barberes, 2015) and the detection of hydrocarbon emanations (Barberes *et al*., 2015) in the South Portuguese Zone; as a basis for geologic mapping in central Portugal (Rabaça *et al.,* 2004) and in the Moura-Ficalho area (Sides *et al.,* 2000) or as a tool for lithological characterization and discrimination in Rocha da Pena (Paixão *et al*., 2013).

Worldwide, remote sensing has been used in mineral exploration since the 70's. Most of studies concern in the application of remote sensing in hydrothermal gold exploration (*e.g.* Moradi *et al*., 2015). Other publications detail the use of remote sensing in other deposit types, such as: epithermal gold deposits (*e.g.* Crósta *et al*., 2003), porphyry copper deposits (*e.g.* Pour & Hashim, 2015), brine deposits (*e.g.* Sabins & Miller, 1994 *in* Sabins,1999). Carlin-type gold deposits (*e.g.* Rockwell & Hofstra, 2008), skarn deposits (*e.g.* Rowan & Mars, 2003) and volcanogenic massive sulfide ore (VMS) deposits (*e.g.* Berger *et al*., 2003 *in* Van der Meer, 2012).

Only recently, the first steps on the application of remote sensing to Li mineralizations were made: Perrotta *et al.* (2005) used ASTER images for a trial mapping of Li-bearing pegmatites in Vale do Jequitinhonha region, Brazil; and Mendes *et al.* (2017) applied a similar methodology in the identification of Li minerals' spectral signatures in view of future identification of unknown ore deposits.

2 Remote sensing principles

In order to fully understand the approach used in this work, it is necessary to provide some basic principles about remote sensing.

Sabins (1997) described remote sensing as "the science of acquiring, processing, and interpreting images and related data, acquired from aircraft and satellites that record the interaction between matter and electromagnetic energy".

In other words, remote sensing consists in the measurement of the electromagnetic energy emanated or reflected from the Earth's surface. Depending on how the energy is used and detected, two forms of remote sensing could be defined (Figure 2): (i) if the source of energy is the sun, then it is called passive remote sensing; (Richards & Jia, 2006; JARS, 1993); (ii) if the energy is emitted by the sensor, then it is called active remote sensing (Richards & Jia, 2006; JARS, 1993).
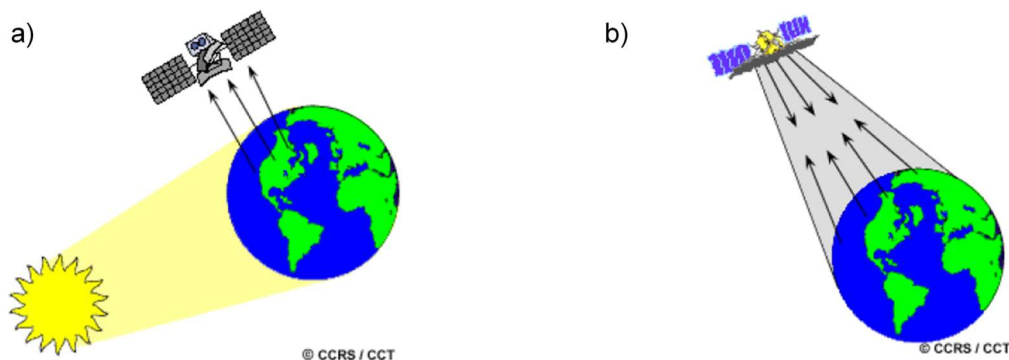
Figure 2 – (a) passive and (b) active sensors. Adapted from: JARS, 1993.

The electromagnetic spectrum is "the system that classifies, according to wavelength, all energy (from short cosmic to long radio) that moves, harmonically, at the constant velocity of light" (Figure 3; NASA, 2013). Passive sensors use the energy from the visible and infrared (near, shortwave and thermal) regions of the electromagnetic spectrum. Minerals have important absorption features in these regions, that is why passive sensors are the most used in the field of geology. Active sensors measure the energy from the microwave region (Figure 3).
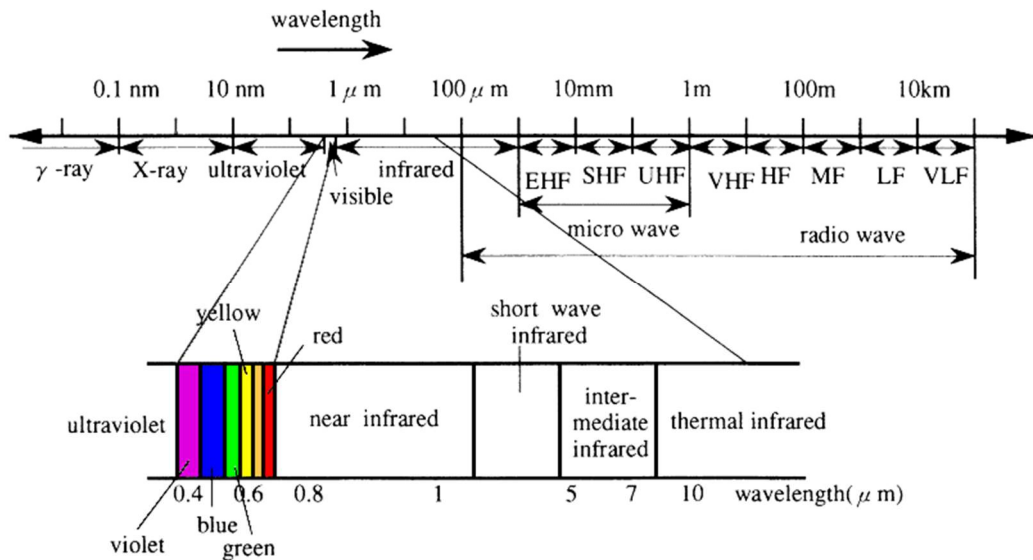
Figure 3 – The electromagnetic spectrum. Adapted from: JARS, 1993.

The solar energy interacts with the atmosphere and depending on the wavelength different phenomena occur (absorption, scattering and refraction). This means that the sensors can't acquire all the solar radiance that reaches the top of the atmosphere, and atmospheric corrections are mandatory. The regions of the electromagnetic spectrum in which the atmospheric absorption is low are called atmospheric windows (Figure 4). The remote sensing uses these regions (windows).
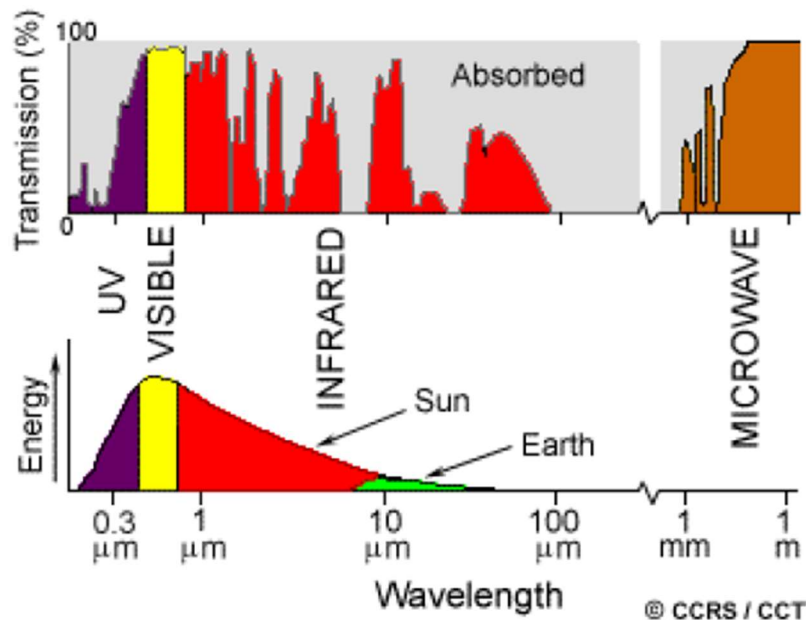
Figure 4 – Comparison between the characteristics of the sun and the Earth, two common energy sources, and the atmospheric windows available (JARS, 1993).

These sensors can be on board of aircrafts, satellites and, more recently, drones, measuring the electromagnetic radiation at specific wavelength ranges (frequently called bands; Figure 5). More specifically, the sensors measure a physical parameter named radiance, which corresponds to the brightness in a given direction toward the sensor.

Another important physical parameter is the reflectance, i.e. the ratio of reflected versus total power energy.
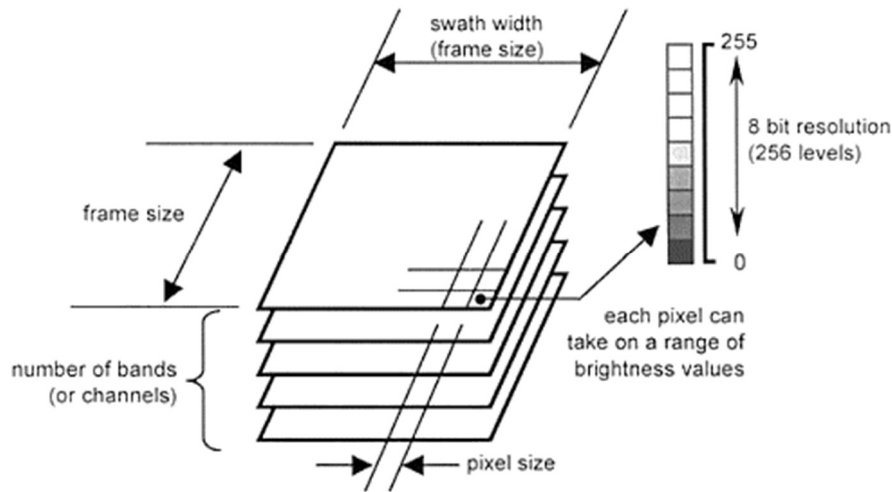
Figure 5 - Technical characteristics of digital image data (Richards & Jia, 2006).

The measurements made by the sensor are quantized and converted into a digital image (raster) composed by a bi-dimensional matrix of picture elements (pixels). The intensity of each pixel corresponds to a discrete numerical value – a Digital Number (DN) (Figure 5; (NASA, 2013; Richards & Jia, 2006). These raster images present different characteristics (or resolutions) depending on the sensor, namely:

- The spatial resolution refers to the size of the smallest possible feature that can be detected (CCRS, 2015a). In other words, it is related to the dimension in the terrain corresponding to the area represented by a pixel. The smaller the dimension, the greater the spatial resolution.

- The spectral resolution is related to the ability of a sensor to define fine wavelength intervals and, consequently the number of spectral bands that the sensor can cover (CCRS, 2015b). The narrower the wavelength range for a given channel or band, the better the spectral resolution.

- The radiometric resolution describes the sensors' ability to discriminate very slight differences in electromagnetic energy (CCRS, 2016). It is usually measured in bits (binary digits) and corresponds to the maximum number of brightness levels available (maximum range of DNs) (Figure 5; Richards & Jia, 2006).

- For satellites sensors, the temporal resolution is also considered, and corresponds to the time required for revisiting the same area of the Earth (NASA, 2013).

As referred before, remote sensing can play an important role in mineral exploration, and may even lead to the discovery of several ore deposits.

According to Sabins (1999) there are two main different approaches of remote sensing to mineral exploration: (i) the first uses geological and fault mapping to localize mineral deposits; (ii) the second, is based on the recognition of hydrothermally altered rocks that can be associated with ore deposits. This is possible because each mineral or rock has a unique spectral signature (i.e. the reflectance as a function of wavelength), and therefore these signatures can be used for geological classification and mapping. In particular, the identification of the mineral assemblage resulting from hydrothermal alteration, can allow the recognition of mineralized areas (*e.g.* Sabins, 1999; Rajesh, 2004; Moradi *et al.*, 2015).

In a first instance, the spectral signatures of rocks and minerals are acquired in laboratory and spectral libraries are created. This spectral information is essential for the interpretation of remotely sensed data and the identification of the different lithologies and mineral assemblages. The most complete spectral library (Kokaly *et al.*, 2017) is provided by the United States Geological Survey (USGS) and can be accessed for free at USGS (2017a).

Figure 6 summarizes how the application of remote sensing in geology works and the role of these spectral signatures.

The spectral signatures acquired by remote sensing are different from those acquired in laboratory. This can happen for several reasons: the sensors usually don't measure the reflectance in all wavelengths continuously, unlike the laboratory spectroradiometers; and/or several minerals (or even rocks, depending on the spatial resolution) can be present in one pixel and the result is a spectral mixing (which represents one of the main obstacles in remote sensing).
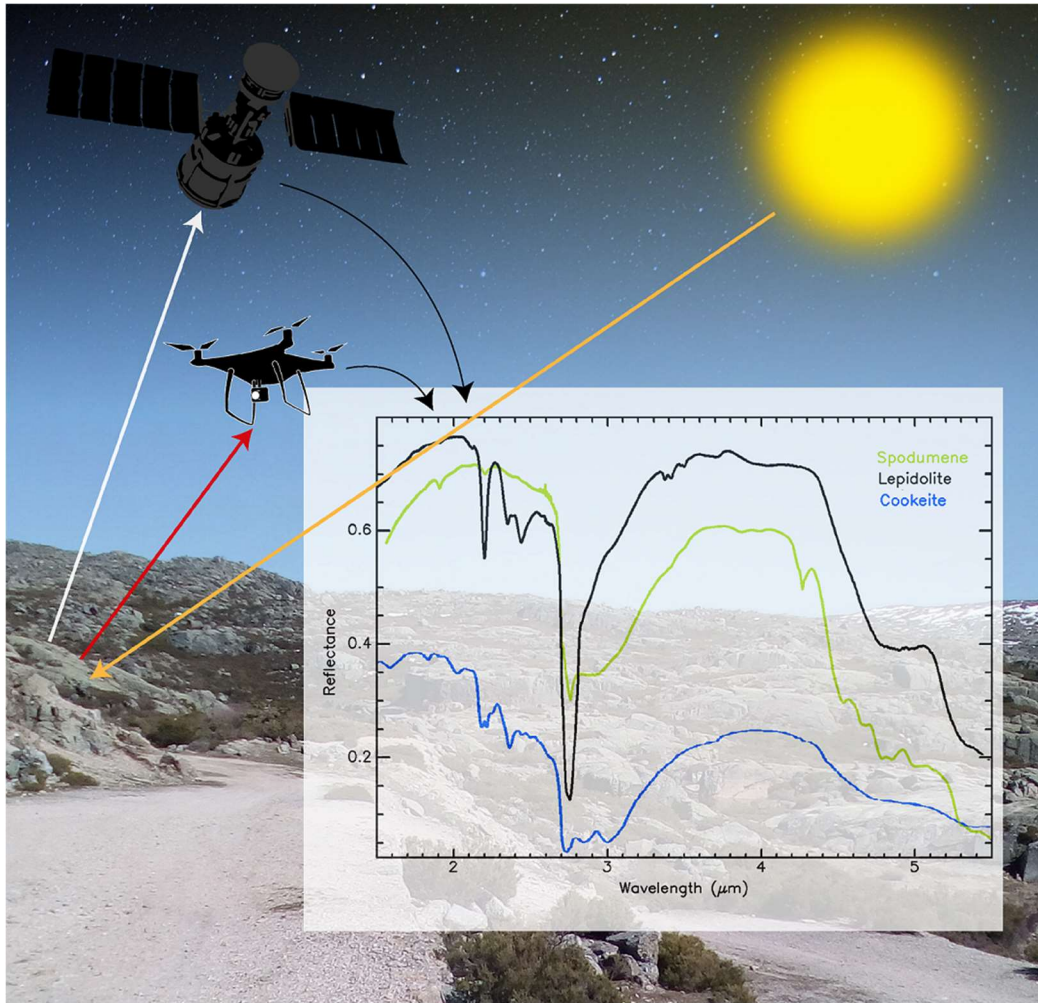
Figure 6 – Illustrative scheme of the remote sensing principles: the sensors, on board of satellite or drones, measure the Sun's electromagnetic energy reflected in the surface of the Earth. Each mineral or rock has a unique spectral signature that is acquired by the sensor and can be used for geological classification and mapping. Mineral spectra: Kokaly *et al.*, 2017.

It is also important to refer the history and characteristics of the different remote sensing satellite missions used in this work.

The Landsat program represents the world's longest continuously acquired collection of space-based moderate-resolution multispectral land remote sensing data (USGS, 2017b). It is the result of a joint effort of the United States Geological Survey (USGS) and the National Aeronautics and Space Administration (NASA). Since the early 1970's, Landsat as provided fundamental resources for research areas such as geology, forestry, regional planning, education, mapping, and global change (USGS, 2017b).

Until now, Landsat counts with seven successful and one failed missions (Figure 7; USGS, 2017c). In each mission a new satellite was launched. The last mission corresponds to Landsat 8, which was launched in 2013. Landsat 9 is planned to be launched in late 2020 (USGS, 2017c).

Figure 7 – Landsat missions' timeline (USGS, 2017c).

Landsat 1-3 carried two sensors: the Return Beam Vidicon (RBV) and the Multispectral Scanner System (MSS) (NASA, 2018a, b, c). The temporal resolution was 18 days. Landsat 4 also carried the MSS sensor and a new one called Thematic Mapper (TM) (NASA, 2018d). Landsat 4 temporal resolution was 16 days.

Landsat 5 was launched in 1984 and carried the same payload as Landsat 4: the MSS and the TM instruments (NASA, 2018e). The MSS sensors acquired data in four spectral bands in the visible and near infrared (NIR) with a spatial resolution of 68 m X 83 m (Table 2; NASA, 2018f). The TM is a multispectral scanning sensor more advanced than the MSS (NASA, 2018g).TM data are sensed in seven spectral bands simultaneously: three bands in the visible, one in the NIR and two in the shortwave infrared (SWIR), all with a 30 m resolution; and one band in the thermal infrared (TIR) with a 120 m resolution (Table 2; NASA, 2018g). The approximate scene size is 185 km X 185 km in the MSS and 185 km X 172 km in the TM (NASA, 2018f, g). The temporal resolution of Landsat 5 was 16 days.

Table 2 – Landsat 5 MSS and TM bands' characteristics (Adapted from: NASA, 2018f, g).

Landsat 5					
Multispectral Scanner System (MSS)			**Thematic Mapper (TM)**		
Bands	**Wavelength (μm)**	**Resolution***	**Bands**	**Wavelength (μm)**	**Resolution**
1 - Green	0.5-0.6	68 m X 83 m	**1 - Blue**	0.45-0.52	30 m
2 - Red	0.6-0.7	68 m X 83 m	**2 - Green**	0.52-0.60	30 m
3 - NIR	0.7-0.8	68 m X 83 m	**3 - Red**	0.63-0.69	30 m
4 -NIR	0.8-1.1	68 m X 83 m	**4 - NIR**	0.76-0.90	30 m
*Spatial Resolution: 68 m X 83 m (commonly resampled to 57 m, or 60 m)			**5 - SWIR**	1.55-1.75	30 m
			6 - TIR	10.41-12.5	120 m
			7 -SWIR	2.08-2.35	30 m

Landsat 7 carries the Enhanced Thematic Mapper Plus (ETM+) sensor, an improved version of the Thematic Mapper instruments that were onboard Landsat 4 and 5 (USGS, 2017d). ETM+ acquires seven spectral bands: bands 1-5 and 7, similar to those of TM.

with a spatial resolution of 30 m; and new band 8, a panchromatic band with 15 m of resolution (USGS, 2017e). The thermal band 6 has an improved spatial resolution of 60 m. The approximate scene size is 170 km north-south by 183 km east-west (USGS, 2017e). The temporal resolution is 16 days.

Landsat 8 has two different instruments: the Operational Land Imager (OLI) and the Thermal Infrared Sensor (TIRS). The resultant product consists of nine spectral bands with a spatial resolution of 30 meters for bands 1 to 7 and 9, and 15 m for band 8 (panchromatic); and two thermal bands (10 and 11) collected at 100 meters (Table 3; USGS, 2017e). Each band consists of a 16-bit grayscale image. The approximate scene size is similar to Landsat 7 (USGS, 2017e). The temporal resolution is 16 days.

New bands 1 (ultra-blue) and 9 (cirrus) are useful for coastal and aerosol studies, and for cirrus cloud detection, respectively. Bands 2 to 4 correspond to the visible, band 5 corresponds to NIR, and band 6 and 7 correspond to the SWIR. The thermal bands provide more accurate surface temperatures.

Table 3 – Landsat 8 OLI and TIRS bands' characteristics (USGS, 2017e).

Landsat 8 Operational Land Imager (OLI) and Thermal Infrared Sensor (TIRS)		
Bands	**Wavelength (µm)**	**Spatial Resolution (m)**
Band 1 - Ultra Blue (coastal/aerosol)	0.435 - 0.451	30
Band 2 – Blue	0.452 - 0.512	30
Band 3 – Green	0.533 - 0.590	30
Band 4 – Red	0.636 - 0.673	30
Band 5 - Near Infrared (NIR)	0.851 - 0.879	30
Band 6 - Shortwave Infrared (SWIR) 1	1.566 - 1.651	30
Band 7 - Shortwave Infrared (SWIR) 2	2.107 - 2.294	30
Band 8 – Panchromatic	0.503 - 0.676	15
Band 9 – Cirrus	1.363 - 1.384	30
Band 10 - Thermal Infrared (TIRS) 1	10.60 - 11.19	100 * (30)
Band 11 - Thermal Infrared (TIRS) 2	11.50 - 12.51	100 * (30)

* TIRS bands are acquired at 100 meter resolution, but are resampled to 30 meter in delivered data product.

The ASTER (Advanced Spaceborne Thermal Emission and Reflection Radiometer) is an imaging instrument onboard of Terra satellite, the flagship satellite of NASA's Earth Observing System (EOS), launched in December 1999 (JPL, 2004a). It resulted from a collaboration between NASA and Japan's Ministry of Economy Trade and Industry – METI (JPL, 2004b). ASTER captures high spatial resolution data in 14 bands whose spatial resolution varies with wavelength (Table 4): 15 m in the visible and near infrared (VNIR), 30 m in the SWIR, and 90 m in the thermal infrared (TIR) (JPL, 2004b, c). ASTER

also provides stereo viewing capability for digital elevation model creation (JPL, 2004b). The temporal resolution is 16 days. Due to a sensor failure SWIR data acquired since April of 2008 is not available.

Table 4 – ASTER bands' characteristics (Adapted from: JPL, 2004c).

	VNIR	**SWIR**	**TIR**
Spectral Range	Band 1 0.52 - 0.60 μm	Band 4 1.600 - 1.700 μm	Band 10 8.125 - 8.475 μm
	Band 2 0.63 - 0.69 μm	Band 5 2.145 - 2.185 μm	Band 11 8.475 - 8.825 μm
	Band 3 0.76 - 0.86 μm	Band 6 2.185 - 2.225 μm	Band 12 8.925 - 9.275 μm
		Band 7 2.235 - 2.285 μm	Band 13 10.25 - 10.95 μm
		Band 8 2.295 - 2.365 μm	
		Band 9 2.360 - 2.430 μm	
Ground Resolution	15 m	30 m	90 m
Quantization	8 bits	8 bits	12 bits

Sentinel-2 is a high-resolution, multi-spectral imaging mission developed by the European Space Agency (ESA) in the frame of Copernicus land monitoring services (ESA, 2018a, b). The full Sentinel 2 mission comprises twin polar-orbiting satellites (A and B) in the same orbit, phased at 180° to each other, to make possible a high revisit period of 5 days at the Equator (ESA, 2018b). Sentinel-2 acquires 13 spectral bands (Table 5): four bands at 10 m, six bands at 20 m and three bands at 60 m spatial resolution (ESA, 2018a, b). The orbital swath width (or scene size) is 290 km.

Figure 8 establishes a comparison between Landsat 8, Sentinel-2 and ASTER bands.
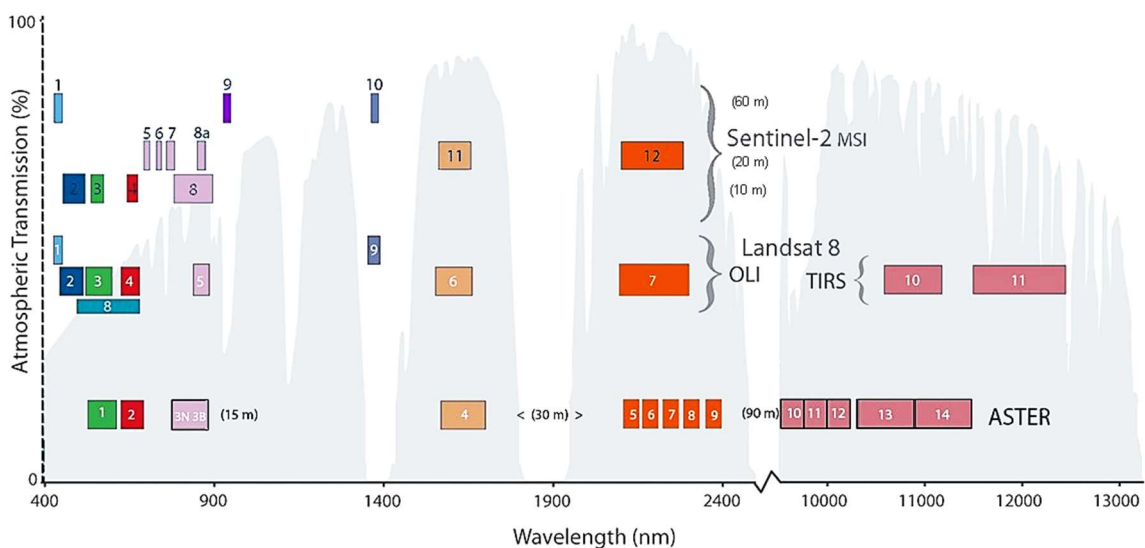
Figure 8 – Comparison between Landsat 8, Sentinel-2 and ASTER bands (Adapted from: USGS Landsat Program, 2017).

Table 5 – Sentinel 2A and 2B bands' characteristics (ESA, 2018c).

Band Number	Sentinel 2A Central wavelength (nm)	Bandwidth (nm)	Sentinel 2B Central wavelength (nm)	Bandwidth (nm)	Spatial resolution (m)
1	443.9	27	442.3	45	60
2	496.6	98	492.1	98	10
3	560.0	45	559	46	10
4	664.5	38	665	39	10
5	703.9	19	703.8	20	20
6	740.2	18	739.1	18	20
7	782.5	28	779.7	28	20
8	835.1	145	833	133	10
8[a]	864.8	33	864	32	20
9	945.0	26	943.2	27	60
10	1373.5	75	1376.9	76	60
11	1613.7	143	1610.4	141	20
12	2202.4	242	2185.7	238	20

In the digital image processing, Landsat 5 and 8, ASTER and Sentinel-2 multispectral products were chosen because their spectral range is more adequate for geology purposes than other missions' products. This is due to important absorption mineral features in the NIR and SWIR that must be covered by the specific band's spectral ranges.

Sentinel bands have better spatial resolution (10 and 20 m) which is very important to better detect pegmatites of smaller dimensions, but because it is a recent mission, long term comparative studies are impossible to make. In opposite, the continuity of Landsat missions allows a comparison between Landsat 8 and Landsat 5 images and consequently, a spectral evolutionary study of the mineralized pegmatites before and during their exploitation. On the other hand, ASTER products have a higher number of bands in the SWIR region, making it the most used satellite for geological studies, as the vast bibliography proves (e.g. Rowan & Mars, 2003; Crósta *et al.*, 2003; Moradi *et al*., 2015).

3 Pegmatites: definition, classification and zoning

This chapter presents some introductory facts about the pegmatitic systems and their classification.

3.1 Definition

According to Brongniart (1813), the term "pegmatite" was originally proposed by the French mineralogist R. J. Haüy to characterize a "graphic granite". Therefore, this concept was mostly a textural designation used to describe coarse-grained rocks with an intergrowth of graphic quartz and pertitic microcline.

Other definitions (*e.g.* Jackson, 1997; Clark & Steigeler, 2000) describe pegmatite as a very coarse-grained igneous rock, usually of granitic composition, that tend to be enriched in rare elements such as lithium, beryllium, tantalum. The term is then often associated with rocks of granitic composition and coarse grain size. Nonetheless, there are also pegmatites of mafic, ultramafic or carbonatitic nature, and they frequently present large variations in grain size. Another term – "aplite" – is used to characterize the finer granulometry facies.

In order to fill the gaps of the previous definitions, London (2008) proposed a unified definition for pegmatite: "an essentially igneous rock, commonly of granitic composition, that is distinguished from other igneous rocks by its extremely coarse but variable grain-size, or by an abundance of crystals with skeletal, graphic, or other strongly directional growth-habits. Pegmatites occur as sharply bounded homogeneous to zoned bodies within igneous or metamorphic host-rocks".

3.2 Classification

Several authors proposed different classification systems, but the majority focus on granitic pegmatites (*e.g.* Buddington, 1959; Ginsburg *et al.*, 1979 *in* Černý & Ercit, 2005).

The currently most used classification is the proposed by Černý (1991a) and later revised by Černý & Ercit (2005). The authors improved the classification system elaborated by Ginsburg *et al.*, (1979) *in* Černý & Ercit (2005). which is based in the pegmatite emplacement depth and its relationship with the metamorphism and granites.

The classification of Černý & Ercit (2005) distinguishes five main classes considering the host rocks' pressure (P) and temperature (T) conditions: (i) abyssal, (ii) muscovite, (iii)

muscovite – rare-element, (iv) rare-element, and (v) miarolitic pegmatite class (Figure 9).

Each class is subdivided, based on geochemical criteria, mineral assemblages and/or textural attributes, in subclasses. These subclasses are then subdivided in types and subtypes (Figure 9) according to mineralogical and/or geochemical characteristics.

Černý (1991a) and Černý & Ercit (2005) also refer to the concept of petrogenetic families, recognizing three families: LCT (Lithium, Cesium, Tantalum), NYF (Niobium, Yttrium and rare earth elements, Fluor), and mixed NYF + LCT. This family system classification is only valid for pegmatites of plutonic derivation: Rare Element and Miarolitic classes (Figure 9).

3.3 Pegmatite zoning

Pegmatites present zoning at different scales: from internal zoning to a regional scale zoning (or spatial distribution).

3.3.1 Regional zoning

Trueman & Černý (1982) and Černý (1991b) defined a regional zoning pattern for LCT family pegmatites where the veins are distributed around a said parental granitic pluton with sequentially more fractionated veins at higher distances of to the parental pluton (Figure 10).

Figure 9 – The pegmatite classification scheme adopted by Černý & Ercit (2005). (From London, 2008).

Černý (1991b) model proposes a sequence of eight categories of different pegmatite types and sub-types with increasing fractionation degree, from the source to periphery: (i) barren, (ii) rare-earth type, (iii) beryl type, beryl-columbite sub-type, (iv) beryl type, beryl-columbite-phosphate subtype, (v) complex type, including spodumene, petalite and amblygonite subtypes, (vi) complex type, lepidolite subtype, (vii) albite-spodumene type, and (viii) albite type.

However, a well expressed concentric zoning around the parental pluton is rarely observed (as pointed by this model's author, Černý (1991b)), mainly because of the influence of potential pre-intrusive host structures and by the level of erosion exposure.
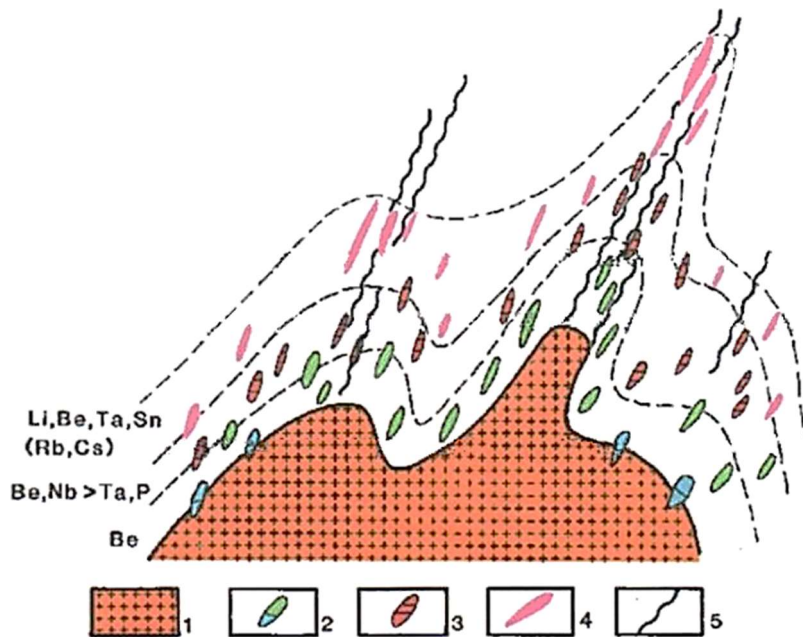
Figure 10 – Schematic representation of regional zoning of pegmatites related to parental pluton: 1 – parental granite; 2 – sterile or beryl-bearing pegmatites; 3 – beryl type pegmatites with phosphates; 4 – complex type pegmatites; 5 – fracture zone. Adapted from Simmons *et al*. (2003).

Simmons & Webber (2008) suggested an alternative genetic model for veins emplaced farther away from the granitic pluton: instead of being the result of differentiation of a parent granitic melt, the veins originated from direct anatexis of a specialized protolith.

For the eastern side of the Fregeneda-Almendra aplite-pegmatite field, Roda (1993) and Roda *et al.* (1999), proposed that the veins resulted from direct anatexis of the quartz- and feldspar-bearing metasediments with posterior fractionated crystallization (mixed model).

3.3.2   Internal zoning

The development of internal zoning in pegmatites is very frequent and it manifests itself in textural and compositional changes. Pegmatites may even present a very complex and heterogenous internal structure (Černý, 1991a).

The same author (Černý, 1991a) distinguished three main types of internal structure: (i) homogenous, (ii) zoned, and (iii) layered structures. Zoned pegmatites are the most common and diverse, while homogenous and layered pegmatites are less abudant

Zoned pegmatites are constituted by up to nine different untis with variable textural characteristics and mineral modes (Černý, 1991a). The more evolved patterns are related to highly fractionated intrusions with complex mineralizations.

According to Heinrich (1948) and Cameron *et al*. (1949)., in a zoned pegmatite is possible to discriminate three main units (Figure 11): (i) zones of primary crystallization, named from the margins inward as the border, wall, intermediate (outer-, middle, inner-, core-margin), zones, and the core; (ii) replacement bodies, formed under lithologic or structural control at the expense of the pre-existing units; and (iii) fracture fillings in dilated dislocations.
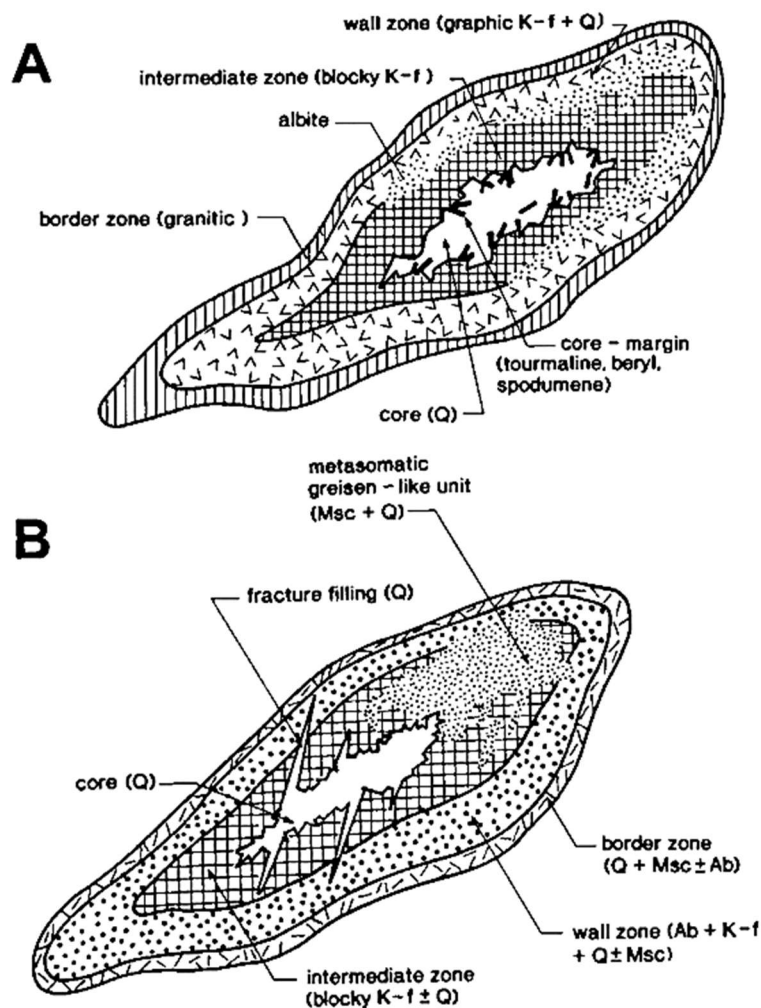
Figure 11 – Horizontal section scheme of internal structure of zoned pegmatites (Černý, 1991a). It is possible to identify the border, wall and intermediate zones, as well as the core of the primary zones. The concentric pattern of the primary zones is cross-cut by fracture fillings and replacement bodies (metasomatic unit).

4 Geological setting

In this chapter, it will be done a geological description of the area in study, focusing on the characterization of local granitoids, metasediments and outcropping aplite-pegmatite veins.

4.1 Regional geology

The Bajoca mine belongs to the Iberian Massif, the biggest and most complete fragment of the European Variscan Belt, outcropping in the western part of the Iberian Peninsula. This Variscan belt corresponds to a long mountain range spreading from the south of the Iberian Peninsula to the northeast of Bohemia, reaching 3000 km in length and between 700 and 900 km in width (Pérez-Estaún *et al*., 2004). It resulted from the closure of the Rheic ocean and consequent collision between Laurussia at north and Gondwana to the south, after the closing of some oceanic sequences that included few continental masses of inferior dimension like Avalonia and Armorica (Matte & Ribeiro, 1975; and Brun & Burg, 1982 *in* Pérez-Estaún *et al*., 2004; Matte, 1986, 2001). This collision corresponds to the Variscan orogeny which marks the beginning of the Variscan cycle (560-245 Ma). This orogeny was responsible for the deformation of the majority of pre-Mesozoic formations in Europe between Devonian (390 Ma) and Carbonic (290/280 Ma) ages (*e.g.* Dias & Ribeiro, 1995; Matte, 1986, 2001; Noronha *et al*., 1979; Ribeiro *et al*., 1990).

The different paleogeographic, structural, magmatic and metamorphic characteristics of the Iberian Massif took Lotze (1945) *in* Pérez-Estaún *et al*. (2004) to subdivide it in zones parallel to the Variscan structures. Later on, these zones were modified by Julivert *et al*. (1972;1974) and Farias *et al*. (1987) (Figure 12). Nowadays, the Iberian Massif is divided in the following geotectonic zones: Cantabric zone (CZ), West Asturico-Leonesa zone (WALZ), Central Iberian Zone (CIZ), Ossa Morena Zone (OMZ), South Portuguese Zone (SPZ) and Galiza Trás-os-Montes Zone (GTMZ) (Lotze, 1945 *in* Pérez-Estaún *et al*., 2004; Julivert *et al*., 1972; 1974; Farias *et al*., 1987).

4.1.1 Central Iberian zone

The studied area lies within the Central Iberian Zone (CIZ), which occupies the central portion of the Iberian Massif (Figure 12) and mainly consists of autochthonous pre-Mesozoic metasediments, intruded by rare pre-Variscan granites and various Variscan granitoids (*e.g.* Martínez Catalán *et al*., 2004; Dias *et al*., 2000; Noronha, 2007).
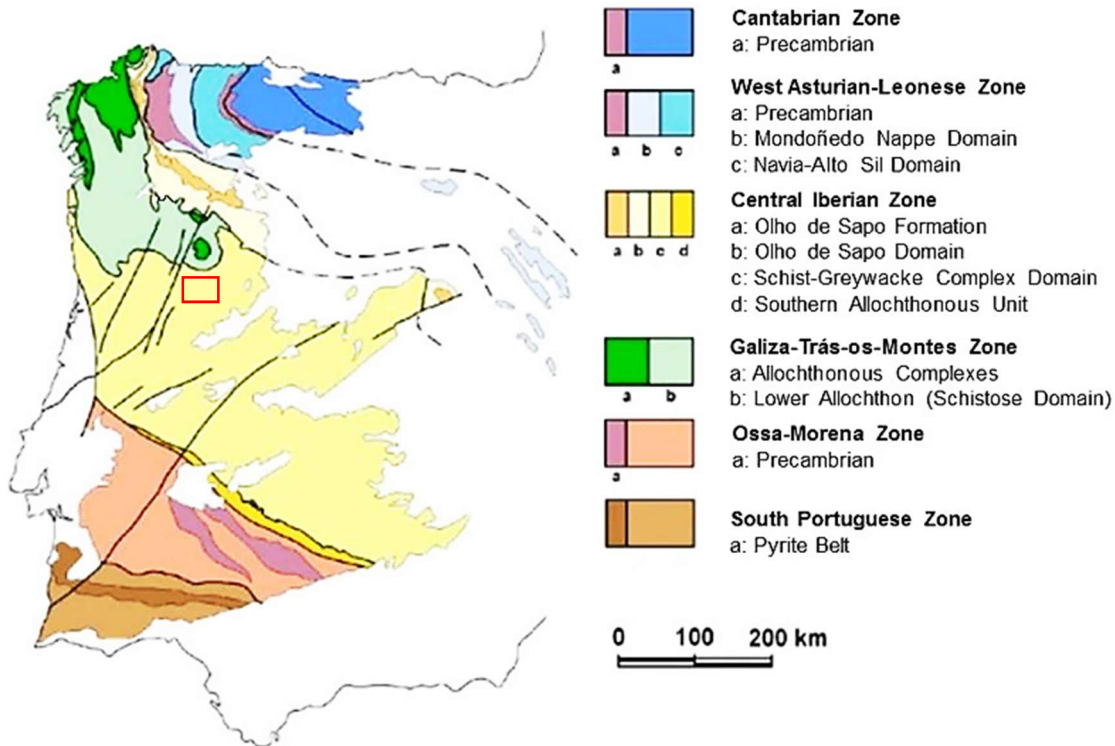
Figure 12 – Subdivision of the Iberian Massif in geotectonic zones, according to Lotze (1945 *in* Pérez-Estaún *et al*., 2004), Julivert *et al*. (1972;1974) and Farias *et al*. (1987) (Pérez-Estaún *et al*., 2004). Location of the studied area (red rectangle).

4.1.1.1 *Lithostratigraphy*

From the lithostratigraphic point of view, the CIZ's autochthonous is composed by two sets of geological units (Ribeiro *et al*., 1979; Dias *et al*., 2013): the units from the first set range from the Proterozoic to the Lower Devonian and were affected by the Variscan orogeny; the second set corresponds to late- to post-orogenic non-metamorphic continental materials from the Upper Carbonic.

The oldest Proterozoic units outcrop in the Miranda do Douro region and many authors considered it to represent Cadomian terrains upon which the metasediments from the "Complexo Xisto-Grauváquico" lie (Ribeiro, 1974; Ribeiro *et al*., 1990).

"Complexo Xisto-Grauváquico" (CXG) was the designation attributed by Carrington da Costa (1950) and reused by Teixeira (1955). Later, these terrains were renamed as Dúrico-Beirão Super Group (Sousa *et al*., 1987; Sousa & Sequeira, 1989; Silva *et al*., 1988a; 1989).

The CXG varies in age from the Upper Proterozoic to the Lower Cambrian (*e.g*. Sousa, 1984, Díez Balda *et al.,* 1990; Rodríguez Alonso *et al.,* 2004; Romão & Ribeiro, 1992) and corresponds to a monotonous pre-Ordovician pelitic-sandy flysch series. This complex resulted from the accumulation of a thick sediment column (8000 m to 11000 m), under a regime of tectonic instability, in a foreland type basin created by the CIZ's

compartmentation in fault-delimited blocks, during the Cadomian orogeny (San José *et al.,* 1990*;* Quesada, 1990 *in* Oliveira *et al.,* 1992*;* Rodríguez Alonso *et al.,* 2004).

The Dúrico-Beirão Super Group outcrops in ample antiforms located in the Douro valley and in the Beiras region, in Portugal, that extend to Spain in the Salamanca, Extremadura, Montes de Toledo and Alcudia regions (Rodríguez Alonso *et al.,* 2004). It is divided in two main units with distinct characteristics: the Douro Group (Sousa, 1982, 1983a, b;1984) and the Beiras Group (Silva *et al*., 1988b *in* Romão & Ribeiro, 1992).

Sousa (1982; 1983a, b) defined, for the Douro Group, a stratigraphic succession with six different formations that are, from the base to the top: Bateiras, Ervedosa, Rio Pinhão, Pinhão, Desejosa, and S. Domingos (Figure 13). All six formations correspond to alternations between pelitic rocks (phyllites) and metagreywackes with turbiditic characteristics (Sousa, 1982). Romão *et al*. (2005) *in* Dias *et al*. (2013) suggest that the São Domingos formation can be a sedimentary deposit related to thrust faults. The presence of calciturbidites in the Bateiras formation is exclusive to this unit and the Douro Group (Sousa, *op. cit.).* According to Sousa (1982;1983a), based on facies analysis, the basal formations present a distal turbiditic character, whilst the top formations present a proximal turbiditic character.
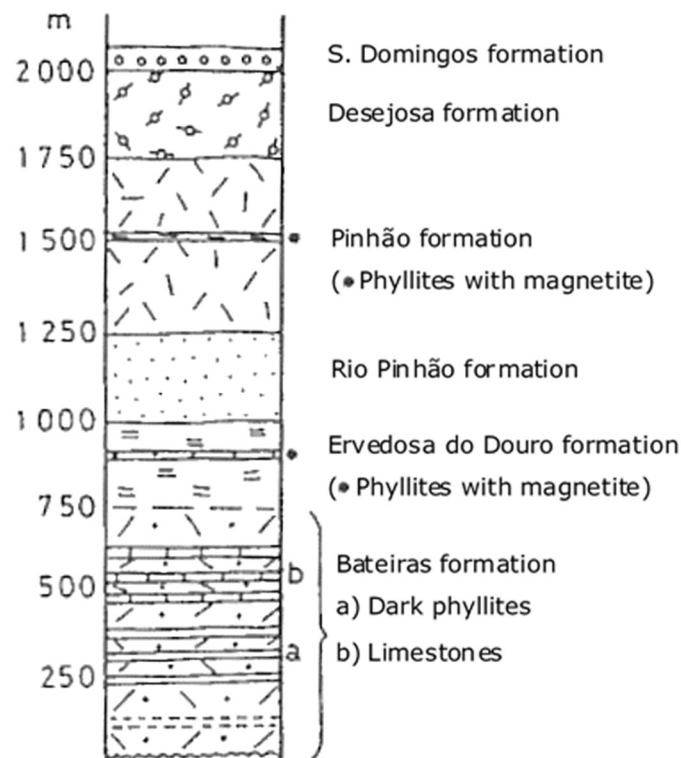
Figure 13 – Douro's group lithostratigraphic sequence, according to Sousa (1982).

Later on, Silva & Ribeiro (1985) observed that syn-sedimentary thrust faults in the Viso region (Vila Nova de Foz Côa) duplicated, in the Sardic phase, the basal formations of

the Douro Group (Figure 14). Therefore, the same authors considered the Rio Pinhão and the Pinhão formations are laterally equivalent, and consequently allochthonous, to the Bateiras and Ervedosa formations, respectively. These lateral equivalence is also recognized by (Sousa, 1981, 1982, 1983a, b).
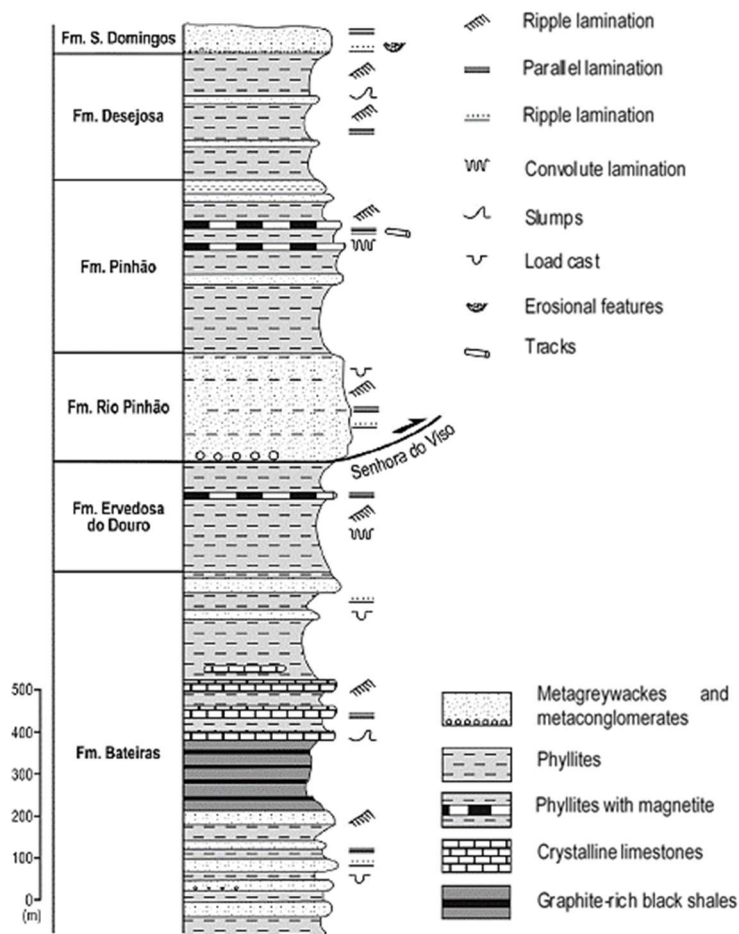
Figure 14 – Douro's Group lithostratigraphic sequence considering the existence of syn-sedimentary thrust faults duplicating the basal formations (Dias *et al.*, 2013).

The Beiras Group has some similarities with the Douro Group: it equally consists in a monotonous and thick flysch sequence, with the alternation between phyllites and metagreywackes (*e.g.* Romão & Ribeiro, 1992).

When compared with the Douro Group, the Beiras Group is characterized by a bigger facies monotony (with a dominance of pelitic rocks) and the absence of carbonated rocks (Oen, 1958; Sousa, 1982; 1983a, b).

Upon the CXG lies, locally in angular unconformity, the post-Cambrian sequence of the Lower Paleozoic (Sousa, 1984). In general, the sequence initiates with the pure Armorican quartzites unit. In some places, between the quartzites and the CXG, exist

units of volcano-sedimentary and conglomeratic nature (*e.g.* Coke *et al.*, 2001; Couto, 1993; Ribeiro, 1993).

The studied aplite-pegmatite veins intruded the above-mentioned "Complexo Xisto-Grauváquico" (CXG), more precisely the Douro Group (Sousa, 1982; 1983a, b). The CXG, in the studied region, is limited at north by the quartzitic formations from the Poiares' synclinal (Lower Ordovician), at south by the granitic complex of Mêda–Penedono–Lumbrales, at east by the Saucelle granite and at west by the Vilariça's fault. At north of the studied area, in the Moncorvo region, the Douro Group passes to the Ordovician metasediments without any notorious unconformity (Rebelo & Romano, 1986).

Locally, only tree formations from the Douro Group outcrop: the base formations, Rio Pinhão and Pinhão, with fewer cartographic expression, and the Desejosa formation with bigger representation (Silva & Ribeiro, 1991; 1994; Silva *et al.,* 1990a, b). The Bateiras and the Ervedosa formations were not detected in the region, neither were identified the syn-sedimentary thrust faults (Silva *et al.,* 1990a, b).

Here follows a brief description of the stratigraphic units with major representation in the studied area:

Rio Pinhão formation

Sousa (1982; 1983a, b) defined this unit as predominantly composed by metagraywacke-like lithologies alternating with dark stripped phyllites, generally in smaller proportions. In the area, the same features were identified by Silva & Ribeiro (1991). According to the mentioned authors, the dark-grey metagraywackes and metaquartz-graywackes dominate and the phyllites frequently have a calc-silicate nature or even pass to calc-silicate rocks. The formation also contains intercalated metaconglomerates that gradually pass to the metagraywackes, metalimestones (calc-schists) and graphite-rich phyllites, characteristic from the Bateiras formation which corroborates the possibility of stratigraphic duplication (Silva & Ribeiro, *op. cit.*).

The stated lithologies occur in spots, within the Granitic Complex of Mêda–Penedono–Lumbrales (Silva *et al.*, 1990a, b; Silva & Ribeiro, 1991; 1994).) These spots are related to the host granitoids as proven by the many intercalations of aplitic veins and granitic apophysis in the mestasediments reffered by Viegas (1983) and Gaspar (1997). Migmatization phenomena are also observed (Gaspar, 1997).

The transition to the overlaying Pinhão formation is visible by the accentuated disappearance of metagraywackes and the appearance of chloritic phyllites (Silva & Ribeiro, *op. cit*.).

<u>Pinhão formation</u>

Equally defined by Sousa (1982; 1983a, b) the Pinhão formation corresponds to a finely stratified green sequence composed by alternations between phyllites and metaquartz-graywackes, with magnetite in the middle of the formation. This unit is lithological and sedimentological similar to the Ervedosa do Douro formation (Sousa 1982; 1983a, b).

In the area, Silva & Ribeiro (1991, 1994) described the phyllites as chloritic phyllites sometimes bearing magnetite and pyrite. Silva & Ribeiro (1994) observed the occurrence of unusual lithologies in the Pinhão formation, namely dark- and light-grey metasiltstones more or less clayey. These facies present a strong affinity with some Desejosa formation's lithologies (Silva & Ribeiro, 1994).

The passage from the underlaying formation (Rio Pinhão) is marked by the disappearance of the metagreywacke benches, while the passage to the overlaying formation (Desejosa) is gradual and patent by the appearance of a greyish striped sequence (Silva & Ribeiro, 1991).

The Pinhão formation occurs in a E-W elongated strip rejected by two NNE-SSW trending strike-slip faults, one in the Bajoca mine zone (Silva *et al*., 1990a, b). This strip, in the studied area, contacts with the Granitic Complex of Mêda–Penedono–Lumbrales. In some places, the mentioned lithologies were affected by metamorphism, which obliterated the original green colour and induced the recrystallization of andalusite porphyroblasts (Silva & Ribeiro, 1994).

<u>Desejosa formation</u>

As aforementioned, this formation occupies the majority of the studied area.

Sousa (1982; 1983a, b) described the Desejosa formation as fundamentally characterized by the striped phyllites with rare metagraywacke benches intercalated. To the top, metric benches of intraformational metaconglomerates start to appear (Sousa, 1982; 1983 a, b; 1984).

Silva & Ribeiro (1991) defined the formation as a monotonous sequence and attributed the striped look to the fine alternations between dark phyllites and whitish sandstones.

In some locations (Castelo Melhor, Almendra, Ribeira de Aguiar and Quinta da Foz do Mosteiro), frequent intercalations with calc-silicate rocks occur, especially calc-silicate

metagreywackes (Sousa, 1981; 1983b; Oliveira, 1982; Silva & Ribeiro, 1991, 1994; Gaspar, 1997).

The contact between the Desejosa formation and the underlaying formation (Pinhão) is gradual, as stated before. On the other hand, the contact with the overlaying Ordovician formations can be gradual or abrupt (Silva & Ribeiro, 1991; 1994).

4.1.1.2 *Tectonic and structure*

The general structure of the CIZ is the result of the Variscan orogeny, mainly of its first and main phase that is penetrative throughout the zone (*e.g.* Dias & Ribeiro, 1994; Diez Balda *et al*., 1990; Noronha *et al*., 1979; Ribeiro *et al*., 1979; Ribeiro *et al*., 1990). However, evidences of pre-Variscan deformation exist which are materialized in two main angular unconformities (Díez Balda *et al*., 1990).

The first and oldest one separates two stratigraphic unities from the Upper Proterozoic (lower Alcudian and superior Alcudian). The deformation of Vendian age (Ediacaran) produced an incipient folding without foliation and/or metamorphism (Ortega & González-Lodeiro, 1986).

The second and most important deformation resulted from the Caledonic orogeny, specially from the Sardic phase (Lotze, 1956 *in* Díez Balda *et al*.,1990; Ribeiro, 1974; Ribeiro *et al*., 1979; Díez Balda *et al*., 1990; Teixeira, 1955). This phase generated folded structures without foliation or associated metamorphism, and created an important angular unconformity in the base of Tremadocian between the Lower Ordovician quartzites and the underlaying metasediments (Díez Balda *et al.,* 1990).

From the stated above it is perceptible that the pre-Variscan orogenies did not cause any notable deformation or metamorphism. Therefore, the main origin of the CIZ's deformation and metamorphism was the Variscan orogeny.

The Variscan orogeny was responsible for three deformation phases – D1, D2 and D3 (or F1, F2, F3) (Noronha *et al*., 1979) that, together with the late-Variscan deformation in a fragile regimen, structured the CIZ (Figure 15; Ribeiro *et al*., 1979; Noronha *et al*., 1979; 1981; Díez Balda *et al*., 1990; Dias & Ribeiro, 1995).

The D1 phase created folds with a large wavelength, mainly NW-SE trending and with a sub-vertical axial plane in the CIZ's central part, from which two sectors with vergent folds diverge: one sector with folds vergent to SW and other to NE (Ribeiro *et al*., 1979; Ribeiro, 1990; Ribeiro *et al*., 1990. This pattern is interpreted as flower structure (*e.g.* Moreira *et al*., 2010; Pereira *et al*., 1993; Ribeiro *et al*., 1979; Ribeiro *et al*., 1990; Ribeiro

et al., 2007). The folding is associated with a regional cleavage S1, parallel to the folds' axis, not always penetrative (Ribeiro *et al*., 1979; Diez Balda *et al*., 1990).

The second phase (D2) in the CIZ's autochthonous is considered a non-coaxial deformation, associated with tangential shear zones responsible for the transport and emplacement of the tectonic nappes from the allochthonous complex in the NW of Iberia (*e.g.* Ribeiro *et al*., 2006; Rodrigues, *et al*., 2013). The main D2 structures in the CIZ are normal faults NNE-SSW trending and dipping between 60º and 20º to W, and are therefore sub-perpendicular to the D1 folds (Pereira 1987; and Coke, 2000 *in* Dias *et al.,* 2013; Ribeiro *et al*., 1990).

The third deformation phase (D3) developed large open sub-vertical folds, coaxial with the D1 folds, WNW-ESE trending associated with a sub-vertical cleavage of crenulation (Pereira *et al*., 1993; Ribeiro *et al*., 1979; Diez Balda *et al*., 1990). Simultaneously, this phase was responsible for the conjugation of ductile sub-vertical sinistral and dextral shearing zones with a distensive component, respectively, WNW-ESE to NW-SE trending, and NNW-SSE trending (Iglésias & Ribeiro, 1981a; Iglésias & Ribeiro, 1981b; Ribeiro, 1974, Ribeiro *et al*., 1979). The age of the D3 phase was determined considering the installation date of syn- to post-D3 granitoids, in the time interval of 300 ± 10 Ma (Ribeiro *et al*., 1990; Pereira *et al*., 1993).
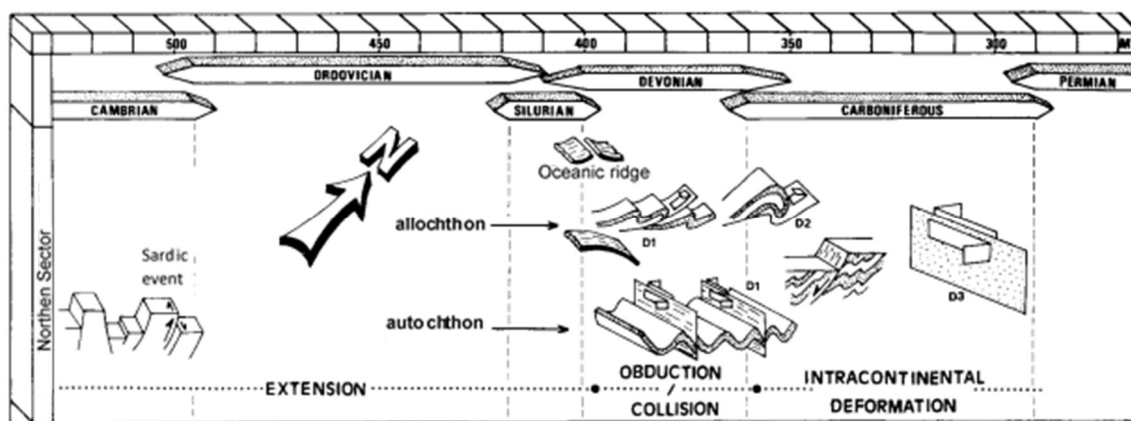
Figure 15 – Structural evolution of Central Iberian Zone (CIZ) during the Variscan cycle (Adapted from: Dias & Ribeiro, 1995).

In the post-D3 late phases the deformation occurred in a ductile-brittle and brittle regime responsible for sinistral NNE-SSW trending and dextral NNW-SSE trending strike-slip faults (Noronha *et al*., 2013; Silva & Ribeiro,1985). The Manteigas–Vilariça–Bragança fault is an example of a sinistral accident (Cabral *et al*., 1983-85; Silva & Ribeiro, 1985; Silva & Ribeiro, 1991; 1994). The installation of post-D3 Variscan granitoids was controlled by these faults since the granitoids are aligned along these fragile fractures (Ferreira *et al*., 1987; Noronha *et al*., 2013).

In what concerns the structure of the studied region, it is affected by the pre-Variscan thrust nappes (for example the Senhora do Viso thrust), which duplicated the oldest stratigraphic series from the CXG (Silva & Ribeiro, 1985), and mainly by the actuation of the D1 and D3 phases, as well as some later movements.

The folding simultaneous to the pre-Variscan thrust faults, as stated before, does not present associated cleavage. Silva & Ribeiro (1985) concluded that the thrust faults are syn-sedimentary and were emplaced by gravity sliding in an extensional regime. According to the same authors, the thrust plane behaved as a normal bedding plane and is not marked by tectonic fabrics (Silva & Ribeiro, 1985)

The main structures of the region are divided in two types: a succession of WNW-ESE trending anticline and syncline folds, resultant from the D1 phase; and fault structures (Silva & Ribeiro, 1991; 1994).

The succession of D1 folds (with vertical axial planes and sub-horizontal axes) creats a poliharmonic efect that extends from from the Poiares synclinal to the north flank of the Lamego-Penedono-Escalhão antiform (Silva & Ribeiro, 1991; 1994).

The second phase (D2) is not very intense and only manifests itself in the domains of greater metamorphic intensity, on the sector between Vila Nova de Foz Côa and La Fregeneda, Spain (Pereira, 2014; Dias *et al*., 2013). It is characterized by folds vergent to NE, with an associate sub-horizontal crenulation cleavage (Silva & Ribeiro, 1991; Dias *et al*., 2013). In the La Fregeneda mine, D2 shear zones are visible afecting the granites (Dias *et al*., 2013).

The third phase (D3) is less penetrative than the first one, but coaxial with it, minesfesting through a crenulation cleavage that affects the previous cleavage and the oldest granites (Silva & Ribeiro, 1991).

The Lamego-Penedono-Escalhão antiform was intruded by a granitic complex, described afterward. The contact between the metasediments and the granitoids from the complex is rectilinear, suggesting the existence of a tectonic contact through a previous fault that might have functioned as a conduct for the magmatic ascension and installation (Silva & Ribeiro, 1994). In the contact, the metasediments are verticalized and the veins, as well as the more competent lithologies, are boudinated (Silva & Ribeiro, 1991; 1994).

According to Silva & Ribeiro (1991; 1994), the faults in the Almendra-Barca D'Alva region are divided in two types: NNE-SSW sinistral strike-slip faults, and WSW-ENE sinistral

shearings. The strike-slip faults are related with the last Variscan movements and cut the structures previously mentioned (Silva & Ribeiro, 1991). The sinistral shearings are mainly related to the D3 phase, but some are associated with the first phase (Silva & Ribeiro, 1991).

One example of a D3 related ductile shearing is the WSW-ENE trending Quinta dos Boais shearing, that mostly afected the existant granitoids (Silva & Ribeiro, 1991; 1994). It corresponds to a former structure (that affected the Precambrian rocks) reativated by the Variscan orogeny (Silva & Ribeiro, 1994).

4.1.1.3   *Metamorphism*

The CIZ was affected by different, overlaid metamorphic events associated to the main Variscan deformation phases.

The first event, related to crustal thickening between the deformations phases D1 and D2 is characterized by a Barrovian-type metamorphism, generally low in the greenschist facies (Martínez *et al*., 1990). The higher-grade zones were observed around the antiforms and metamorphic domes (Vieira, 2010; Silva, 2012).

The isogrades generated by the first metamorphic event are cut by younger ones, related to a syn- to post-D3 metamorphic retrogradation (Silva, 2012). This low-pressure event was more effective along the late-D3 brittle-ductile shear zones. The coetaneous installation of several granitic bodies produced contact metamorphism that favoured the late and post-D3 (over)growth of biotite, andalusite, cordierite and chloritoid (Silva, 2012).

Silva (2012) also considers another metamorphic event, of the Buchan-type, during the pre-D3 migmatization of the crust that produced the granitic melts during the episode of crustal extension.

In the Bajoca region and in the entire Fregeneda-Almendra aplite-pegmatite field, this overprint of different metamorphic events it is also patent (Figure 16): the sedimentary units were affected by a continuous prograde regional metamorphism, overlaid by a contact metamorphism in the vicinities of the granitic bodies (Silva & Ribeiro, 1991; 1994; Martín-Izard *et al*., 1992; López-Plaza *et al*., 1982). A later retrogradational metamorphic event is superimposed over the contact metamorphism (Martín-Izard *et al*., 1992).

The regional metamorphism in the greenschist facies did not overcome the chlorite zone in the Almendra region, and the biotite zone in the Fregeneda region (Silva & Ribeiro, 1994; Martín-Izard *et al.*, 1992; López-Plaza *et al.*, 1982).

The metamorphic grade increases progressively to south, in the direction of the granites installed in the Lamego-Penedono-Escalhão antiform. The isogrades mapped in the Portuguese side of the aplite-pegmatite field have a W-E general trend, parallel to the contact between the granites and the metasediments from the CXG, and were affected by late-Variscan tectonic accidents (Silva *et al.*, 1990a, b; Silva & Ribeiro, 1991, 1994). In the Spanish side, the isogrades tend to follow the contacts of the Lumbrales granite (Carnicero, 1982). Martín-Izard *et al.* (1992) and López-Plaza *et al.* (1982) highlight the role of the non-outcropping Feli granite in the development of the contact metamorphism.
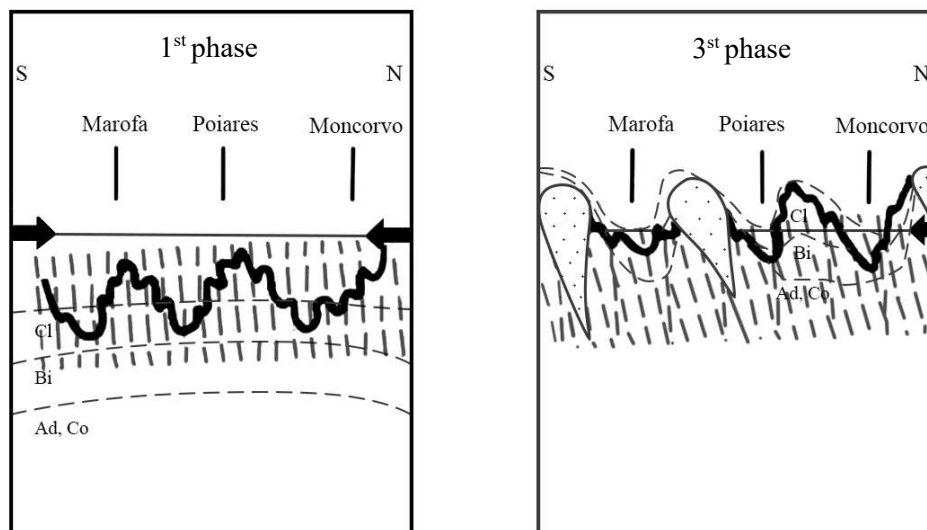
Figure 16 – Scheme representing the isotherm evolution during the Variscan deformation in the Almendra-Barca D'Alva region (adapted from: Silva & Ribeiro, 1994). During the first metamorphic pahse (D1), the regional metamorphism in the greenschist facies did not overcome the chlorite zone. After the third phase (D3), the isotherms rose along the axes of the antiforms, remaining approximately stationary in the intermediate syncline zones. Legend: cl – chlorite; bi – biotite; and – andalusite; co – cordierite.

4.1.1.4 *Variscan granitoids*

One of CIZ's distinctive characteristics is the abundance of Variscan granitoids, the majority emplaced during and after D3 deformational phase.

Three main periods of genesis are recognized for these granitoids (*e.g.* Dias *et al.*, 2000; Noronha, 2007): the first, contemporary with the crustal thickening, occurred in the phase D1; the second period, posterior to phase D1 in the autochthonous terrains (and to D2 in the allochthonous), was responsible for the largest volumes of granitoids as a result to decompression, thermal relaxation and wrench faulting (Noronha *et al.*, 1979, 1981; Dias *et al.*, 2000); and the last period, late-orogenic, corresponds to the adiabatic

decompression in an extensional regime (Ferreira *et al*., 1987; Lagarde *et al*., 1992; Stussi, 1989 *in* Dias *et al., 2000*).

The Variscan granitoids of CIZ are then very distinct, not only presenting genetical and chronological differences, but also typological. For this reason, several attempts were made to classify and group the granitoids according to geological, petrographic, structural, geochemical and geochronological criteria (*e.g*. Schermerhorn, 1956; Oen, 1958, 1970; Capdevila & Floor, 1970; Capdevila *et al*., 1973; Ferreira *et al*., 1987).

Ferreira *et al.* (1987), taking into account the relation between the installation period (referred above) and the third phase of deformation (D3), divided the Variscan granitoids in: syn-orogenic, pre-D3; syn-orogenic, syn-D3; and late- to post-orogenic (late- to post-D3). This classification also admits a group of pre-orogenic granitoids, with little expression in the CIZ.

Dias *et al.* (2010) compiled a synthesis of geochronological and petrogenetic results, establishing the emplacement intervals for four groups referred in Ferreira *et al.* (1987), Dias (2001) *in* Dias *et al*. (2010) and Noronha *et al.* (2006): 312-321 Ma for syn-D3 granitoids; 305-312 Ma for late-D3; 300 Ma for late- to post-D3 granitoids; and 290-299 Ma for post-D3 granitoids (Figure 17).

Based on petrographic and geochemical criteria, Capdevila & Floor (1970) divided the Variscan granitoids in two groups: alkaline two-micas granitoids; and biotitic calc-alkaline granodiorites and granites. The first group is intimately related with migmatites and high-grade metamorphic zones (Capdevila & Floor, 1970), and result from the crystallization of hydrous peraluminous magmas, generated by partial melting of aluminous metapelitic rocks in medium to inferior crustal levels (Capdevila *et al*., 1973; Noronha, 2007). The second is frequently related with mafic and intermediate igneous rocks, resultant from dry partial melting of deep materials (Capdevila *et al*., 1973). The two-micas granitoids are, in general, syn- to late-D3 (Dias *et al*., 2010) while biotitic granitoids can be pre- to syn-D3, late-D3, late- to post-D3 and post-D3 (Dias *et al*., 1998, 2010) and outcrop in the cores of D3 structural domes (Noronha *et al.* 1979*;*1981; Martinez *et al*., 1988).
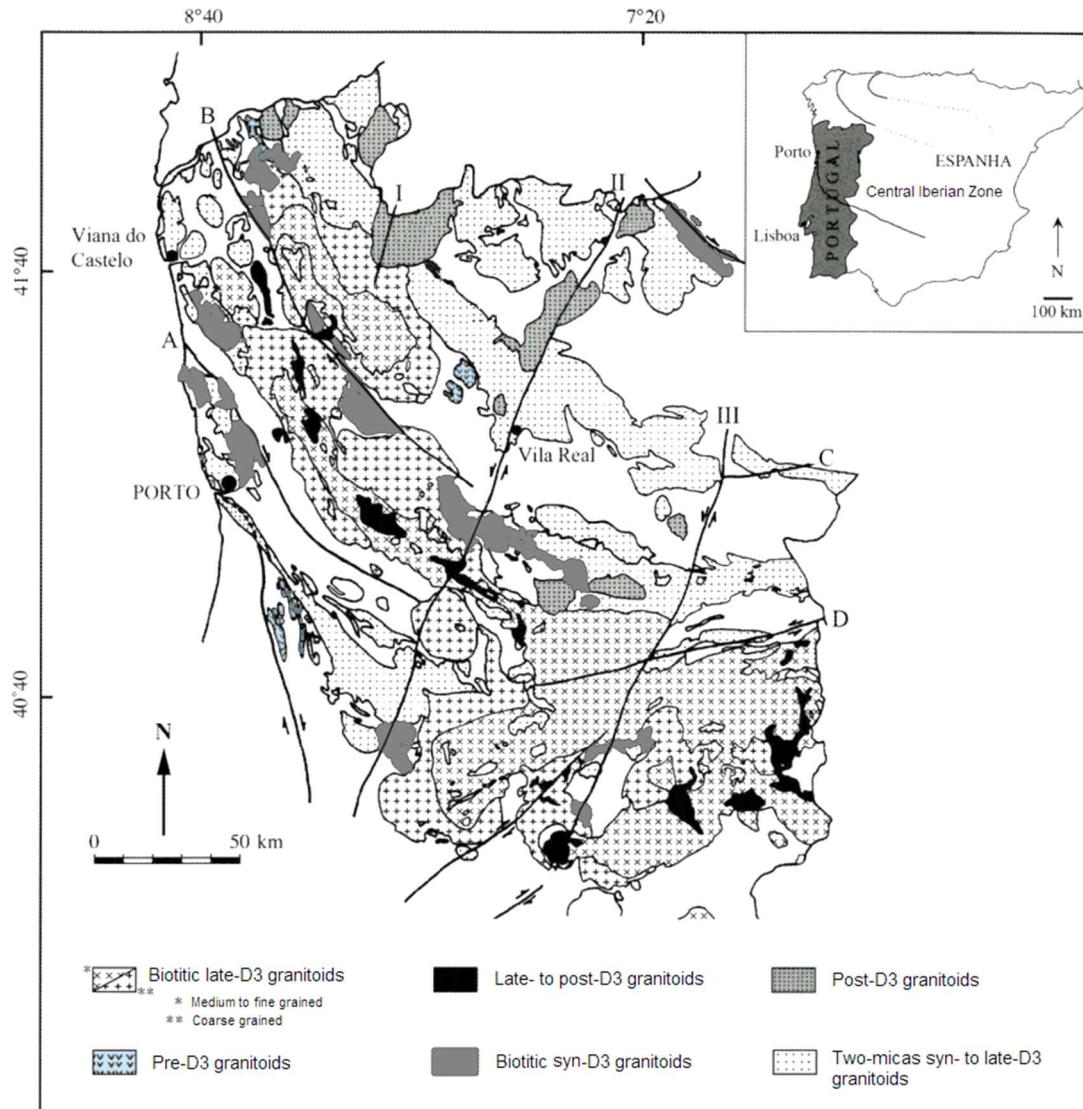
Figure 17 –Distribution of Variscan granitoids in the CIZ: A – "Sulco Carbonífero Dúrico-Beirão" shear zone; B – Viseu-Régua shear zone; Moncorvo-Bemposta shear zone; D – Traguntia-Penalva do Castelo shear zone; I – Gerês-Lovios fault; Penacova-Régua-Verin fault; III – Vilariça fault. Adapted from: Ferreira *et al*. (1987) *in* Dias *et al.* (2010).

In the surrounding region of the Bajoca mine, two-micas granites dominate (Figure 18): the granitic complex of Mêda–Penedono–Lumbrales at south; the Saucelle granite at northeast; and the non-outcropping granite of Feli, detected by drilling holes between the Riba D'Alva mine and Feli mine (Spain).

Following, some of the major characteristics of the local granitoids are compiled.

4.1.1.4.1   Granitic Complex of Mêda–Penedono–Lumbrales

Named by Bea *et al*. (1987) *in* Vieira (2010), this granitic complex represents the biggest volume of the region. The complex is composed by different facies, with transitional contacts, where the younger facies intrude the older ones (Ribeiro, 2001). The majority is syn-D3, except some lithofacies of small dimension that are later relatively to D3 (Silva & Ribeiro, 1991; 1994; Ribeiro, 2001).

The syn-D3 facies are installed in the Lamego-Penedono-Escalhão antiform and their emplacement, related to the D3 ductile shearing of Escalhão-Quinta dos Boais, should have occurred between 320 and 305 Ma (Silva & Ribeiro, 1991; 1994; Ribeiro, 2001; Dias *et al.,* 2010).

Near the Bajoca mine, the outcropping lithofacies are six: five syn-D3 and one (Quinta de Vale Flor granite) late-D3. A short description of each one is listed below, according to Silva & Ribeiro (1991; 1994) and Ribeiro (2001).

Chãs–Amargo granodiorite

Fine-to-medium grained, essentially biotitic, granodiorite with dark tones, sometimes melanocratic. It occurs in six main spots between Chãs e Vilar de Amargo, in the vicinities of the Vilariça's valley (Silva *et al.*, 1990a). South of Chãs, the bodies are E-W elongated whereas the bodies from the Vilar de Amargo region are roughly rounded.

These bodies are hosted in the Tomadias, Mêda–Escalhão, Santa Comba–Algodres and Ribeira de Massueime–Galegos granites. The Chãs–Amargo granodiorite occurs frequently as enclaves in host rocks, and gradually pass to the lithofacies that intrude it.

Tomadias granite

Fine-grained, two-micas granite, with local dark tones. It occurs in spots of several dimensions, frequently oriented, which correspond to the peripherical regions or domes of other granites. Therefore, the Tomadias granite presents a border facies character.

Mêda–Escalhão granite

This medium-grained, two-micas, leucocratic granite corresponds to the largest lithofacies of the complex, surrounding the other granitic facies like a matrix. In some places, a predominance of biotite is visible; in others, for example in the contact the metasedimentary formations, it presents a finer grain.

The Mêda-Escalhão granite is relatively homogenous except in the transition to other facies, in the border zones (in contact with the host rocks) and in the Vilar do Amargo area where enclaves of the Chãs granodiorite are frequent.

It is also locally deformed by the WSW-ENE trending ductile shearing of Quinta dos Boais.

According to Gaspar (1997), Ribeiro (2001) and Vieira & Lima (2005a, b), the Mêda-Escalhão granite more geochemically differentiated than the other facies.

Santa Comba–Algodres granite

Two-micas (muscovite > biotite), coarse-grained, leucocratic granite. It occurs in spots aligned in a NE-SW trend, which suggests that the opening of the space for its emplacement is due to movement of the regional shearings. This event would have facilitated the development of the grain size and the biotite leaching as a result of fluid circulation.

The granite passes gradually to the Chãs, Tomadias, Mêda-Escalhão and Galegos-Ribeira de Massueime granitoids, with which it contacts. In the proximity with the Chãs granodiorite, frequent granodiorite enclaves are observed.

Galegos–Ribeira de Massueime granite

Medium-to-coarse-grained, porphyritic and leucocratic granite which presents lithological and textural features similar to the Mêda-Escalhão granite. The two granites are distinguishable because the Galegos-Ribeira de Massueime granite presents feldspar megacrysts (oriented sometimes) and a larger quantity of biotite in the matrix.

This facies occurs in disseminated spots and passes gradually to the other granites.

Quinta de Vale Flor granite

Two-micas (muscovite >> biotite), leucocratic, medium- or rarely fine-grained granite with tourmaline. Locally, the facies can be strongly sheared.

As aforementioned, this granite represents a later facies relatively to the third deformation phase (late-D3), thus occurring in small spots in the middle of the earlier facies. These spots are distributed by shearing zones and the vicinities of quartz veins, allowing fluid circulation to possibly cause the biotite leaching and the appearing of tourmaline.

4.1.1.4.2   Saucelle granite

Late-to-post-D3, two-micas (muscovite >> biotite), medium-to-coarse-grained granite with sulphides (Silva & Ribeiro, 1994). Denominated as Chão de Calvo granite in the sheet 15-B of the geological map at the scale of 1:50.000 (Silva *et al*., 1990b; Silva & Ribeiro, 1994).

The granite outcrops SSE of Freixo de Espada à Cinta, near the Saucelle dam, and extends to the oriental part of the aplite-pegmatite field, in Spain. It is installed in the Vila Real-Carviçais antiform and intruded the Desejosa formation (Silva & Ribeiro, 1994).

4.1.1.4.3   Feli non-outcroping granite

The existance of a non-outcroping granitic dome near the Feli mine (La Fregeneda, Spain) is referred in several publications: Viegas *et al*. (1983-85); Mangas (1987) *in* Martín-Izard *et al*. (1992); Gaspar (1997).

Vieira (2010) described the Feli granite as leucocratic, fine-to-medium-grained with muscovite >> biotite. The same author dated the granite as 305,0 ± 3,3 Ma old, and concluded (taking also into account the petrographic analisys) that the Feli granite can be classified as a late-D3 granite.

4.2 The veins from the Fregeneda-Almendra aplite-pegmatite field

This section is dedicated to the description of the outcropping aplite-pegmatite veins, with an especial emphasis on the mineralized ones.

Taking into account the criteria established by Roda (1993) and Roda *et al.* (1999) based on the mineralogy, morphology, internal structure, relation with the host rocks and the spatial distribution of the veins, Vieira (2010) distinguished 11 types of veins (Figure 18): T1 – Intra-granitic aplite-pegmatite veins; T2 – Quartz veins with andaluzite; T3 – Aplite-pegmatite veins and apophysis; T4 – Simple, concordant aplite-pegmatite veins; T5 – Potassium feldspar-bearing aplite-pegmatite veins; T6 – Simple, discordant aplite-pegmatite veins; T7 – Petalite-bearing aplite-pegmatite veins; T8 – Spodumene-bearing aplite-pegmatite veins; T9 – Spodumene- and lepidolite-bearing aplite-pegmatite veins; T10 – Lepidolite-bearing aplite-pegmatite veins; T11 – Quartz veins with cassiterite.

Following and according to Vieira (2010), a description of the aplite-pegmatites T7 to T10 is presented, since the focus of this work is the Li-bearing pegmatites:

T7 – Petalite-bearing aplite-pegmatite veins

These veins are clearly discordant, with a N-S to N30ºE trend and sub-vertical dip, and over a meter thick. Mineralogically, they are mainly composed by petalite, quartz, albite and potassium feldspar. Minor phases include muscovite and cassiterite. Montebrasite, columbite-tantalite minerals and eucryptite occur as accessory phases. Although some zones with a higher content of petalite exist, no internal zoning was described.

They outcrop in the Pinhão and Desejosa formations, further away from the existing granites when compared with T1-T6 veins. In the contact with the host rocks occurs tourmalinization.

The best example is the vein from the Bajoca mine (Almendra). The referred vein outcrops as a two-meter thick dike and its thickness increases with the depth, exceeding the 30 m.

T8 – Spodumene-bearing aplite-pegmatite veins

The spodumene-bearing veins are very similar to the petalite ones in terms of mineralogy, dimension and attitude. The main difference is the dominant phase – spodumene – and its association with primary petalite in some veins (in the Alberto mine, La Fregeneda, Spain).
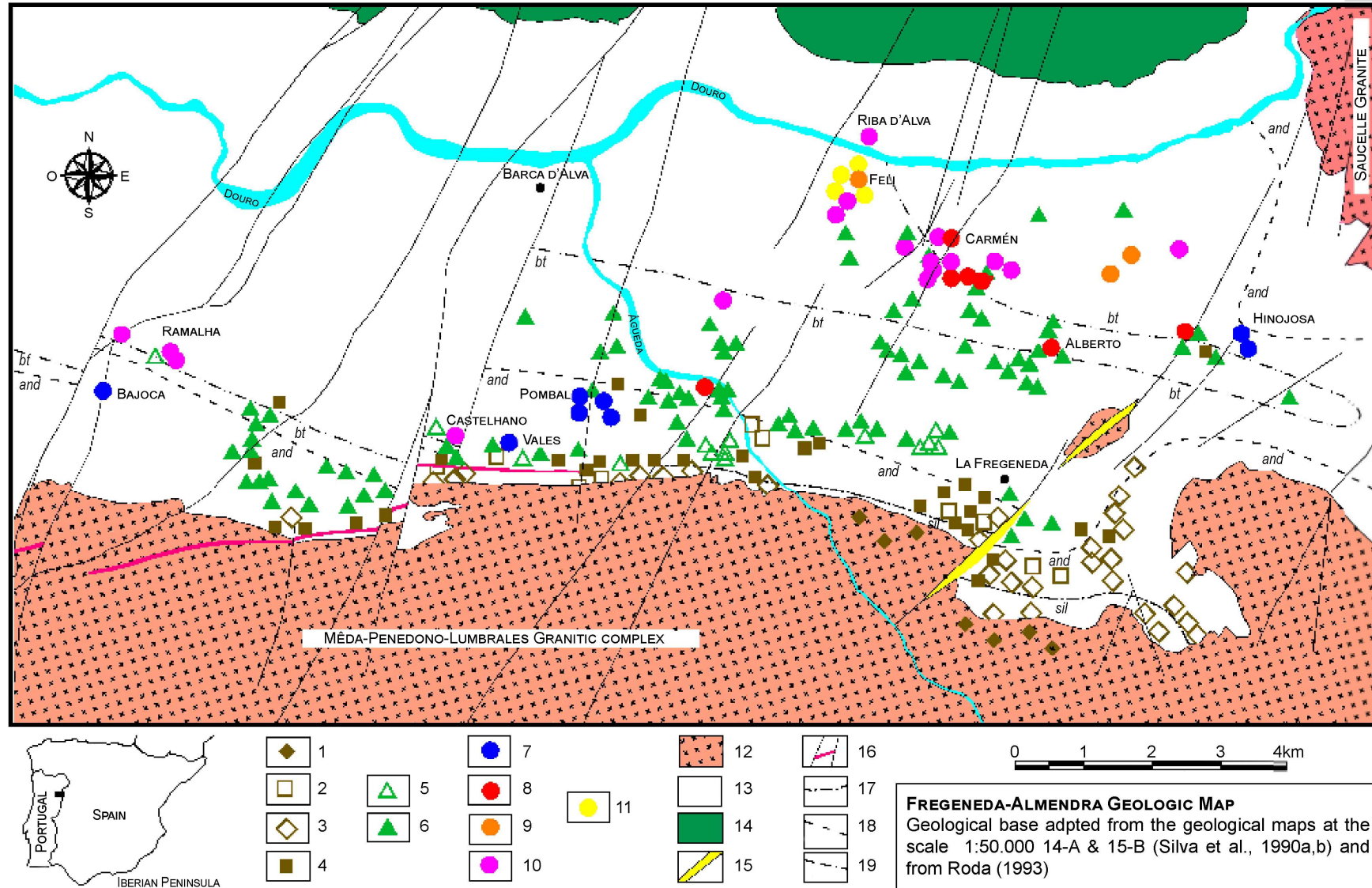
Figure 18 – Simplified geological map of the Fregeneda-Almendra aplite-pegmatite field (adapted from Vieira, 2010). Type veins: (1) intra-granitic - T1; (2) quartz with andaluzite - T2; (3) apophysis - T3; (4) simple discordant -T4; (5) with potassium feldspar - T5; (6) simple discordant- T6; (7) with petalite - T7; (8) with spodumene - T8; (9) with lepidolite and spodumene - T9; (10) with lepidolite - T10; (11) quartz with cassiterite - T11. (12) Syn- to late-D3 granites; (13) metasediments (CXG); (14) Ordovician formations; (15) quartz veins; (16) granitic/rhyolitic porphyry and faults. Isograds: (17) sillimanite; (18) andaluzite; (19) biotite.

Other than spodumene and petalite, the vein mineralogy includes potassium feldspar, albite and quartz as major phases. Muscovite can occur as a minor phase, and montebrasite, Fe-Mn phosphates and cassiterite as accessory minerals. In the contact with the host rocks it also occurs tourmalinization.

T8 veins are more abundant in eastern side of the Fregeneda-Almendra pegmatite field (between La Fregeneda and Hijinosa del Duero) and the main body outcrops in the Alberto mine. In the western side, only one vein has been discovered in the location of Vau (near Águeda river).

T9 – Spodumene- and lepidolite-bearing aplite-pegmatite veins

These veins present quartz, feldspars, Li-bearing muscovite (lepidolite) and spodumene as the main phases. Muscovite, cassiterite and montebrasite occur in a smaller percentage. Accessory phases include apatite, Nb-Ta oxides, Fe-Mn phosphates and eucryptite.

T9 veins often present an internal banded structure with quartz- and lepidolite-rich zones alternating with zones richer in potassium feldspar and albite. The spodumene occurs as prismatic crystals associated with lepidolite and potassium feldspar, defining a comb-like structure normal to the contacts with the host rocks.

They outcrop even further away from the granites when compared with the previous described veins and show tourmalinization in the contact. They are also sub-vertical and discordant with the host rocks – N-S to N30ºE trend.

The best exempla of T9 veins is the vein from the Feli mine (La Fregeneda, Spain).

T10 – Lepidolite-bearing aplite-pegmatite veins

These veins outcrop in the Desejosa formation, in the areas farthest from the granites. They are sub-vertical and aligned according to a N10º to N40ºE direction, discordant from the host rocks which show tourmalinization in the contact zone. Their thickness is lesser than 3 meters.

Mineralogically, the dominant phases are quartz, feldspar and lepidolite. Muscovite, cassiterite, montebrasite and Nb-Ta oxides can occur in smaller percentages. Although it is not common, T10 veins can present a banded structure.

All these vein types (7, 8, 9 and 10) belong to the LCT family, REE-Li subclass and Complex type of the Černý & Ercit (2005) classification (Vieira, 2010).

According to internal structure, chemical composition and mineralogy, Vieira (*op. cit*.) grouped the eleven types of veins in three categories: (i) sterile, intra-granitic, concordant bodies (types 1, 2, 3 and 4); (ii) intermediate, discordant bodies (types 5 and 6); (iii) evolved, discordant and Li-, F- and/or Sn-rich veins (types 7, 8, 9, 10 and 11).

The distribution of the aplite-pegmatites veins in the Fregeneda-Almendra field, in general, and of these three groups, in particular, is spatially zoned relatively to geological and metamorphic factors:

(i)   The sterile veins outcrop closest to the granites, while the more evolved and enriched veins outcrop in the farthest areas (Vieira, 2010; Roda, 1993);

(ii)   The different types of mineralization are distributed by specific metamorphic isogrades. The lower the metamorphic grade is, the more differentiated the veins (Vieira, 2010). Sterile veins are then emplaced in the higher-grade metamorphic zones; petalite-bearing aplite-pegmatites (T7) only occur in the andaluzite-sillimanite; and spodumene-bearing veins are emplaced in the biotite and/or chlorite zones (Vieira, 2010).

Vein distribution is also influenced by the regional structures. Sterile veins are emplaced in the tectonic foliation of third deformation phase (S3) which presents a N100º-N120ºE (WNW-ESE) general trend (Vieira, 2010; López-Plaza *et al*., 1982). Locally, some veins can slightly cut or fold the metasediments' foliation (López-Plaza *et al*., 1982). López-Plaza *et al*. (1982) consider that the emplacement of these veins was conditioned by a D3 shear zone.

In what concerns the mineralized aplite-pegmatite veins, Vieira (2010) considers that they were emplaced in late-tectonic NNE-SSW and NE-SW sinistral strike-slip faults; Martín-Izard *et al*. (1992) proposed that the veins near Feli were controlled by a shear zone related to the uplift of a non-outcropping granitic dome; Viegas (1983) and López-Plaza *et al*. (1982) consider that the veins were emplaced in N10º-N25ºE tension fractures. For Viegas (*op. cit*.) these tension fractures are related with the tension relief that caused the late-Variscan strike-slip faults. López-Plaza *et al*. (1982) describes the fractures as cross joints aligned perpendicularly to the axis of the folds. The same authors also refer that some of the NNE-SSW veins present a curvature that may indicate that the shear zone which controlled the emplacement of the sterile veins was still active.

The structural relationship between different vein types allows to comprehend the temporal evolution of the aplite-pegmatite emplacement stages: for example, type 11 veins (with cassiterite) are folded and cross-cut by younger type 9 veins (Vieira, 2010).

Based on structural data like this and on other geochemical, isotopic and modeling data, the same author concluded the Fregeneda-Almendra aplite-pegmatite veins are the result of different magmatic process syn-, late- and post-D3.

Finally, structural and geochemical similarities between type 6 veins (simple discordant) and types 7 (petalite) and 8 (spodumene) took Vieira (*op. cit.*) to suspect that some of the type 6 veins could hold complex non-outcropping mineralizations.

5 Methodology

The materials and data used, and the methodology followed in this work are described in this chapter.

5.1 Data

For the digital image processing and interpretation, Landsat 5 TM, and Landsat 8 OLI, ASTER and Sentinel-2 MSI multispectral products were used.

For the spectral analysis, Level 1 cloud free raster images (cloud cover less than 10%) were downloaded. To obtain better results, only the images with fewer vegetation coverage were considered. A quantitative measurement of the amount of vegetation was made using a vegetation index (Normalized Difference Vegetation Index – NDVI).

Landsat 5 TM images were acquired on 02/09/1990 (path 203, row 32), Landsat 8 OLI images on 04/09/2014 (path 203, row 32), ASTER images on 28/06/2004 (path 203, row 31) and Sentinel-2 on 27/10/2017 (tile number T29TPF). All the images cover the study area.

The satellite products can be downloaded for free in several platforms, but the USGS's "Earth Explorer" (USGS, 2018) is most used, and in it all products used in this work can be found.

Each Level 1 product normally consists of compressed file that contains the respective band images in a GeoTIFF or JPEG2000 format, accompanied with a metadata file. The number and characteristics of the bands were described in detail in Chapter 2.

5.2 Image processing

The image processing main goal is to extract qualitative and/or quantitative information relevant for the chosen application (Lillesand *et al.*, 2015). It can be divided in different stages: (i) pre-processing; (ii) processing stage *sensu stricto* which involves image transformation and extraction; and (iii) post-processing.

After the image download, the processing and classification tasks were performed in a Geographic Information Systems (GIS) environment, mainly in QGIS. The geographic information systems allow the use of geographic information, its integration with a large amount of other data (for example, geological or remote sensing data) and its analysis. QGIS is a free and open source GIS software that allows the installation of several user-created plugins some of which are dedicated to remote sensing applications. The plugin used in this work was the Semi-Automatic Classification Plugin – SCP (Congedo, 2016).

Taking into account that more powerful remote sensing software are also very expensive, it's our belief that free open source tools are capable of serving the objectives of the present work.

Esri ArcMap and the Sentinel Application Platform (SNAP) were also used as complementary tools of SCP.

By trial and error, it was attempted to establish a spectral analysis methodology capable of detecting lithium mineralizations. To achieve this goal, on the Fregeneda-Almendra pegmatite field, RGB combinations, band ratios and principal component analysis (PCA) were performed. A structural map was also produced based on manual lineament extraction. Afterwards, the results obtained were integrated with the data provided by other sources (structural and lithological data obtained from the Geological Map of Portugal).

The methodology followed throughout this work is schematically represented in Figure 19.

5.2.1 Pre-processing

Before the image analysis, the satellite images need a pre-processing stage that will be described below. The objective of this stage is to eliminate different distortions in the images and to prepare them to the processing methods.

All level 1 products were already geometrically corrected.

5.2.1.1 *Sub-setting*

5.2.1.1.1 Geographic sub-setting

As referred before, the multispectral images acquired have a high spatial coverage (of several square kilometres – 185 km X 172 km in the TM sensor, 170 km X 183 km for OLI and TIRS, 60 km^2 for ASTER, and 290 km^2 for Sentinel-2). Therefore, is was necessary to clip the images to the study area. It was decided to consider the surroundings of the Bajoca mining concession and extend the zone of interest to Spain in order to incorporate two more open pit explorations in the Fregeneda-Almendra aplite-pegmatite field. These open pits (Feli and Alberto mines, both exploiting Li) are important because they provide more spectral information for the images' analysis.
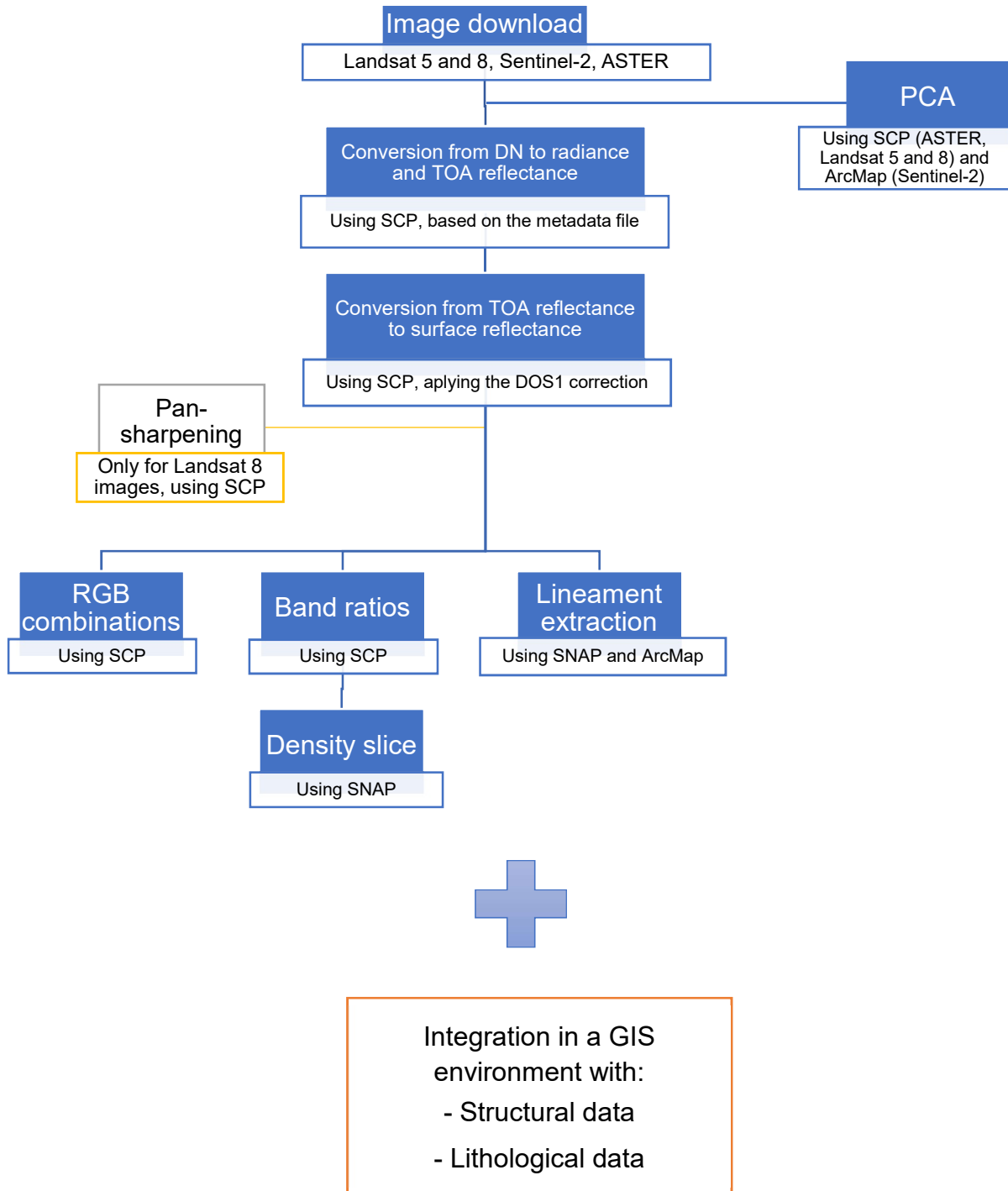
Figure 19 – Flow chart of the methodologies to be followed.

5.2.1.1.2 Spectral sub-setting

Not all bands of the different satellite products are adequate for geological applications. So, in order to facilitate the application of the image processing algorithms these bands should be excluded from the band set.

In this study, Landsat 8 deep blue (1), panchromatic (8) and cirrus (9) bands were excluded from the further analysis. However, the panchromatic band was used as a sharpening band (see below in section 5.2.1.4). In the case of Sentinel-2, coastal aerosol (1), red edge (5, 6 and 7), water vapour (9) and cirrus (10) bands were also excluded.

5.2.1.2 *Atmospheric correction and surface reflectance conversion*

To minimize scattering and atmospheric absorption effects, both the Landsat and ASTER digital numbers (DNs) were converted to top of the atmosphere (TOA) reflectance. In the case of ASTER images, the original DNs already corresponded to radiance. The conversion used the information contained in the metadata files downloaded with the images. Sentinel-2 images are already provided in TOA reflectance.

In SCP, the conversion to TOA reflectance is made according to the equation 1:

$$\rho_p = \frac{\pi \times L_\lambda \times d^2}{ESUN_\lambda \times cos\theta_s} \qquad (1)$$

where:

L_λ = Spectral radiance at the sensor's aperture (at-satellite radiance)

d = Earth-Sun distance in astronomical units (provided in the metadata files)

$ESUN_\lambda$ = Mean solar exo-atmospheric irradiances

θ_s = Solar zenith angle in degrees, which is equal to $\theta_s = 90° - \theta_e$ (where θ_e is the Sun elevation)

A DOS1 (Dark Object Subtraction 1) atmospheric correction (Chavez, 1996) was applied, to convert TOA reflectance to surface reflectance. This conversion is not performed on the thermal bands. The DOS1 correction is one of the simplest type of atmospheric correction, because it is an image-based correction. The algorithm identifies the dark regions in the image. Theoretically, the DNs of these dark regions should be close to zero, but in fact the DNs are higher due to the interaction with the atmosphere (scattering phenomena). The difference between the expected value (zero) and the measured one is calculated by the algorithm. Subsequently, the difference is subtracted to all image pixels. Therefore, the DOS1 atmospheric correction is only applicable when the images contain dark zones such as water bodies in the NIR band.

In the case of the Sentinel-2, the conversion of TOA reflectance to surface reflectance in SCP does an automatic rescale of the images: pixels of 20 m bands are split in 4 pixels of 10 m whose values are the same as the original 20 m pixel.

5.2.1.3 *Masking*

In order to reduce spectral variability and noise contamination, vegetated areas and main water bodies were masked out from the image analysis. The mask was created using the information resulting from Normalized Difference Vegetation Index (NDVI) computation. For ASTER and Sentinel-2 images, the mask assigns the value 0 for water and typically for regions where NDVI is higher than 0.2 (value that indicates the presence of vegetation according to Weier & Herring, 2000). In the case of Landsat images, the NDVI threshold considered was higher – 0.25 for Landsat 5 and 0.3 for Landsat 8 – because the previous value masked a big part of the image.

The NDVI is calculated using the red and near infrared (NIR) bands, according to equation 2 (Tucker, 1979):

$$NDVI = \frac{NIR - RED}{NIR + RED} \tag{2}$$

5.2.1.4 *Pan-sharpening*

Since some pegmatites present relatively small dimensions, a higher spatial resolution, is better to identify them in the satellite images.

To overcome this problem, in Landsat 8 images, an image processing method called pan-sharpening was employed. In this specific case, it was applied the Brovey Transform according to the method proposed by Johnson *et al.* (2012). It consists in a combination between the spectral information contained in the multispectral bands (which spatial resolution is 30 m), with the spatial resolution of the panchromatic band (15 m). The final product is composed by multispectral bands 2 through 7 with a 15 m resolution.

The Brovey Transform is showed in the equation 3:

$$MSpan = \frac{MS \times PAN}{I} \tag{3}$$

where MS represents the multispectral band, PAN the panchromatic band and I is the Intensity (which is a function of multispectral bands).

For Landsat 8, in SCP, the Intensity is calculated according to equation 4:

$$I = \frac{0.42\ \times Blue + 0.98\ \times Green + 0.6\ \times Red}{2}$$

<div align="right">(4)</div>

5.2.2 Image processing methods

This section describes the image processing methods used. The goal of their application is to transform the images highlighting the features with interest to extract (Lillesand *et al.*, 2015). The processing methods often use the decision-making capability of the computer to recognize and classify pixels based on their signatures (Sabins, 1997).

The majority of the image processing methods allows to discriminate between hydrothermally altered and unaltered rocks which is essential in mineral exploration (Pour & Hashim, 2015). The interaction with hydrothermal fluids frequently generates a halo around the mineralization, providing an exploration target considerably larger than the deposit itself (Rajesh, 2004). The style and extent of the halo of alteration depends the type of mineral deposit (Rajesh, 2004).

5.2.2.1 *RGB combinations*

RGB (red, green, blue) combinations are an image enhancement technique where three different multispectral or thermal bands are inserted, one at a time, in the red, green or blue channels. The result is a colour composite that should enhance hydrothermally altered rocks and lithological units at regional scale (Pour & Hashim, 2015). The bands were chosen based on laboratory spectra of the Li-bearing minerals and of minerals related to hydrothermal alteration (Figure 20 and Figure 21).

For example, clay and carbonate minerals have absorption features from 2.1 to 2.4 µm and reflectance from 1.55 to 1.75 µm (Ali & Pour 2014); silicate minerals present high emissivity in the region between 10.30 and 11.70 µm (Ali & Pour 2014); iron oxides and sulphate minerals commonly have a strong reflectance near red and low blue reflectance (Han & Nelson, 2015). On its turn, Li-bearing minerals have important absorption features around 2.2 µm; lepidolite has another absorption feature between 0.5 and 0.6 µm. If the bands that contain these specific mineral absorption and reflectance features are included in the RGB combinations, the latter should be capable of discriminating the minerals in question.
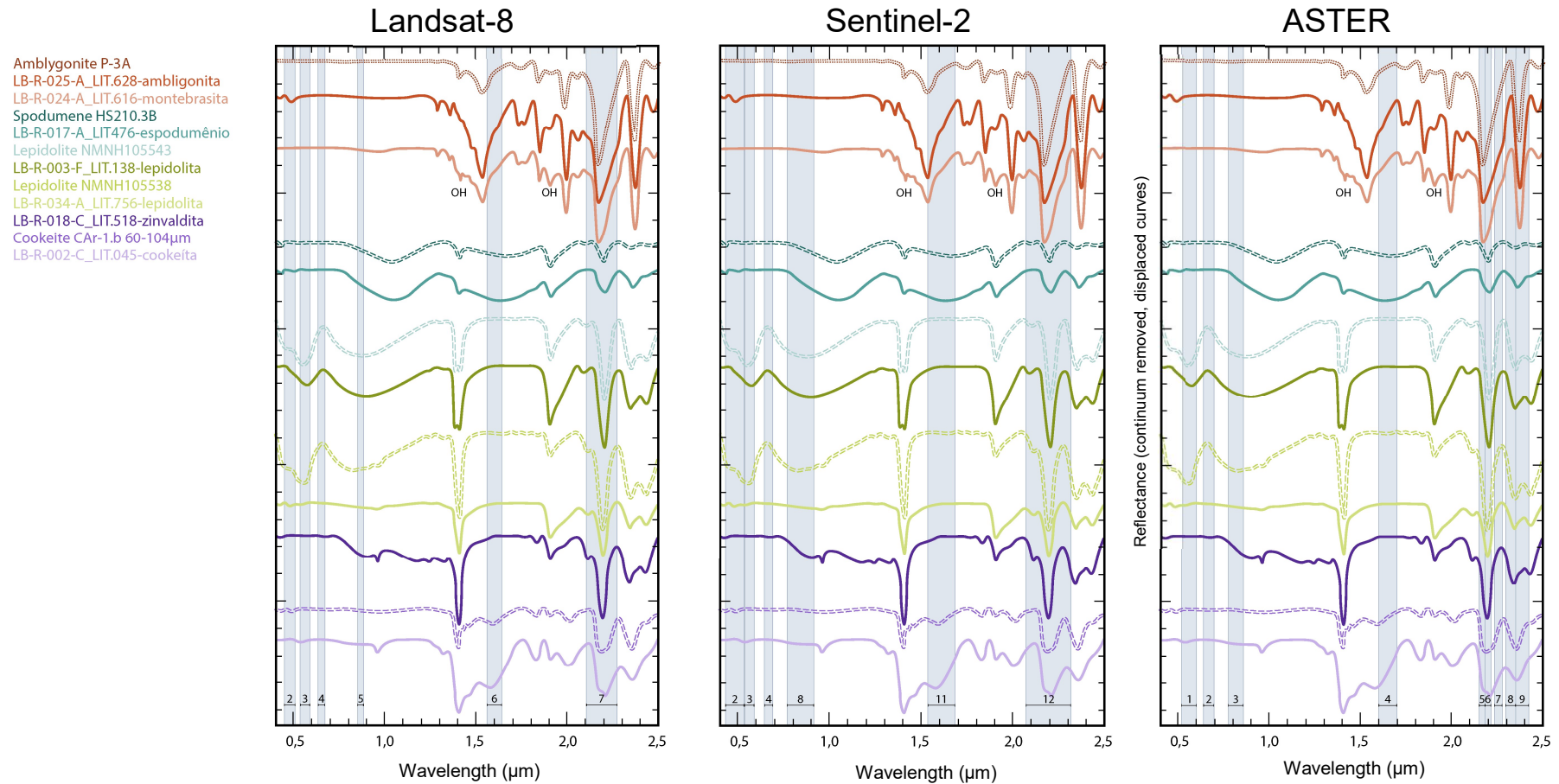
Figure 20 – Overlap of Landsat 8, Sentinel-2 and ASTER bands to the spectral curves of Li-bearing minerals (adapted from: Costa *et al*., 2016). Reflectance curves with continuum removed. Doted curves belong to the ECOSTRESS Spectral Library and dashed curves to USGS spectral library. OH⁻ marks hydroxyl absorption features.

Self-proposed as well as known combinations from the literature were then tested (Tables 6 and 7).

For the ASTER image, RGB combination 6-2-1 was tested to discriminate between gossan areas, alteration zones and host rocks (Kalinowski & Oliver, 2004); combination 6-3-1 was applied to enhance hydrothermal gossans (Kalinowski & Oliver, 2004) and 7-4-2 combination was tested in order to identify and enhance geological structures (Kalinowski & Oliver, 2004). To evaluate the content and distribution of silicate minerals, RGB combination 13-14-9 was proposed based on the combination used for Landsat 8 by Ali & Pour (2014) and Pour & Hashim (2015). Based on mineral spectra of Figures 20 and 21 and by trial and error, the RGB combinations 1-6-13, 2-1-13, 4-9-2 and 5-1-14 were proposed to identify Li-mineralizations.

Table 6 – RGB combinations tested for the ASTER product.

RGB	Feature	Reference
6-2-1	Gossan, alteration, host rock	Kalinowski & Oliver, 2004
6-3-1	Hydrothermal gossans	Kalinowski & Oliver, 2004
7-4-2	Enhancing structures	Kalinowski & Oliver, 2004
1-6-13		**Self-proposed**
2-1-13		**Self-proposed**
4-9-2		**Self-proposed**
5-1-14		**Self-proposed**
13-14-9	Silicate minerals	**Self-proposed based on Ali & Pour, 2014; Pour & Hashim, 2015**

In the case of Landsat 8, some of the known RGB combinations tested were: (i) to identify hydrothermally altered rocks, 5-6-7 (Pour & Hashim, 2015), 5-7-3 and 5-7-10 (Mia & Fujimitsu, 2012); (ii) to identify iron oxides and clay minerals, 2-5-7 and 6-5-7 (Ali & Pour, 2014); (iii) to identify silicate minerals, 10-11-7 (Ali & Pour, 2014; Pour & Hashim, 2015); (iv) to identify lithological contrasts, 6-7-4 (Mwaniki *et al.,* 2015). Self-proposed RGB combinations capable of differentiating Li-mineralizations included: 3-2-7, 3-2-11 and 7-3-11.

Based on some of overlap/equivalence between Landsat 8, Landsat 5 and Sentinel-2 bands (Figure 7), it was made a correspondence between the bands used in Landsat 8 RGB combinations and Landsat 5/Sentinel-2 bands to create similar combinations. In the case of Sentinel-2, the correspondence between bands was only made for visible, NIR and SWIR because this sensor has no bands in the TIR region.

Table 7 – RGB combinations tested for Landsat 8, Landsat 5 and Sentinel-2.

RGB combination			Feature	Reference
Landsat 8	Landsat 5	Sentinel-2		
2-5-7	1-4-7	2-8-12	Iron oxides and clay minerals	Ali & Pour, 2014
5-6-7	4-5-7	8-11-12	Hydrothermally altered rocks	Pour & Hashim, 2015
5-7-3	4-7-2	8-12-3	Hydrothermally altered rocks	Mia & Fujimitsu, 2012
5-7-10	4-7-6	–	Hydrothermally altered rocks	Mia & Fujimitsu, 2012
6-5-7	5-4-7	11-8-12	Iron oxides and clay minerals	Ali & Pour, 2014
6-7-4	5-7-3	11-4-12	Lithogical contrasts	Mwaniki *et al.,* 2015
10-11-7	–	–	Silcate minerals	Ali & Pour, 2014; Pour & Hashim, 2015
3-2-7	2-1-7	3-2-12		**Self-proposed**
3-2-11	2-1-6	–		**Self-proposed**
7-3-11	7-2-6	–		**Self-proposed**

5.2.2.2 *Band ratios*

The band rationing is a technique in which the DNs (brightness values) of one band are divided for the digital numbers of another band. The ratios are based on the peaks and troughs of a reflectance curve: usually, the band with higher reflectance is divided by a band with low reflectance.

This method is useful for highlighting certain features or materials that cannot be seen in raw bands (Inzana *et al.*, 2003; Sabins, 1997; Ali & Pour, 2014). It also eliminates shadowing and topographic effects making it appropriate for complex terrain (Mwaniki *et al.,* 2015). Band ratios are also useful when combined with other bands in RGB combinations.

Overall, the band ratio technique works reasonably well for visualization, but it is inadequate for mapping, or other quantitative applications (Han & Nelson, 2015).

According to Sabins (1999), there are two groups of minerals associated with hydrothermally altered rocks: (i) alunite and clay minerals like illite, kaolinite, and montmorillonite, and (ii) iron oxides and sulfates. Taking this into account, band ratios that discriminate these minerals should highlight hydrothermally altered zones as bright pixels.
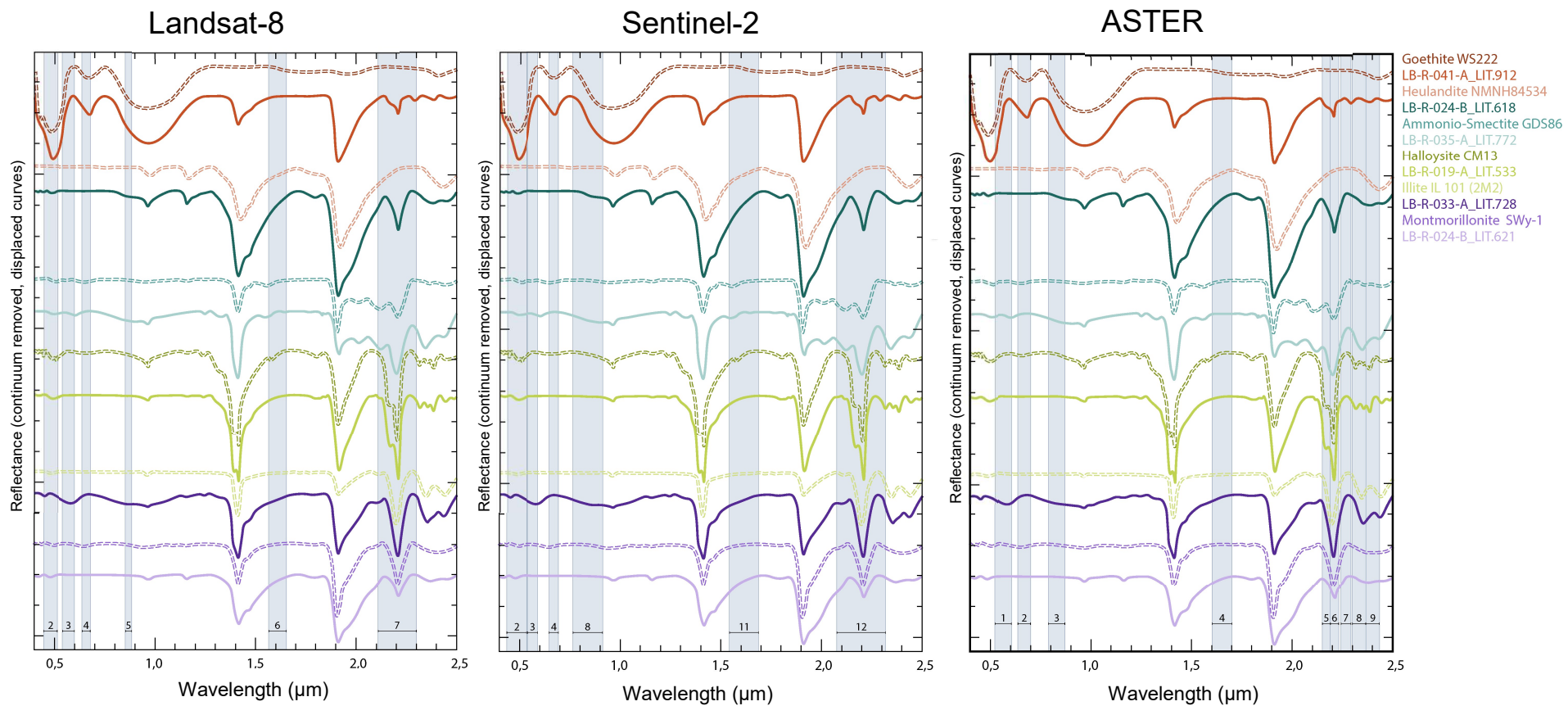
Figure 21 – Overlap of Landsat 8, Sentinel-2 and ASTER bands to the spectral curves of petalite alteration minerals and other associated minerals (adapted from: Costa *et al*., 2016). Reflectance curves with continuum removed. Dashed curves belong to USGS spectral library.

Taking this into account, some known ratios from the literature were tested during this work in order to identify and enhance hydrothermally altered rocks (Tables 8 and 9). To identify Li-bearing pegmatites and based on the mineral reflectance curves' peaks and troughs of Figures 20 and 21, and on the USGS spectral library (Kokaly *et al.*, 2017), several band ratios were also proposed (Tables 8 and 9).

Table 8 – Tested band ratios for the ASTER product.

Band ratio	Feature	Reference
1/3	Spodumene	**Self-proposed**
2/1	Ferric iron	Kalinowski & Oliver, 2004
4/3	Ferric oxides	Kalinowski & Oliver, 2004
4/5	Silicate alteration	Kalinowski & Oliver, 2004
4/6	Montebrasite	**Self-proposed**
4/8	Cookeite	**Self-proposed**
4/10	Halloysite; montebrasite	**Self-proposed**
5/3	Goethite	**Self-proposed**
5/10	Heulandite; illite	**Self-proposed**
5/13	Goethite	**Self-proposed**
6/2	Lepidolite; cookeite	**Self-proposed**
7/5	Kaolinite	Kalinowski & Oliver, 2004
7/6	Muscovite; lepidolite; (spodumene)	Kalinowski & Oliver, 2004 **Self-proposed** for Li-minerals
8/5	Amblygonite; montebrasite	**Self-proposed**
11/10	Silica	Kalinowski & Oliver, 2004
11/12	Silica	Kalinowski & Oliver, 2004
12/6	Lepidolite	**Self-proposed**
12/9	Lepidolite	**Self-proposed**
12/10	Lepidolite; cookeite	**Self-proposed**
13/10	Silica	Kalinowski & Oliver, 2004
14/12	Quartz rich rocks	Kalinowski & Oliver, 2004

Table 9 – Tested band ratios for Landsat 8, Landsat 5 and Sentinel-2.

Band ratio			Feature	Reference
Landsat 8	Landsat 5	Sentinel-2		
3/2	2/1	3/2	Goethite, halloysite	**Self-proposed**
3/5	2/4	3/8	Spodumene	**Self-proposed**
4/2	3/1	4/2	Iron oxides	Ali & Pour 2014; Sabins, 1999
4/3	3/2	4/3	Ferric iron	**Self-proposed based on Kalinowski & Oliver, 2004**
4/7	3/7	4/12	Lepidolite (cookeite, amblygonite; montebrasite)	**Self-proposed**
6/5	5/4	11/8	Ferrous minerals	Ali & Pour 2014; Mia & Fujimitsu, 2012
6/7	5/7	11/12	Alunite and clay minerals	Ali & Pour 2014; Pour & Hashim 2015; Sabins, 1999
10/7	6/7	−	Heulandite	**Self-proposed**

In order to enhance the band ratio results, a primary method of classification named Density Slice was applied in SNAP. This method consists in the analysis of the ratio image histogram and in the attribution of a color to each histogram segment. A color ramp was applied in which cold colors represent the lower values and hot colors the higher values (see section 6.2). The resultant images emphasize subtle grey-scale differences that may be imperceptible to the viewer (Sabins, 1997).

5.2.2.3 *Principal Component analysis (PCA)*

Principal Component analysis (PCA) is a multivariate statistical technique used to enhance and separate certain types of spectral signatures from the background (Gabr *et al.,* 2010; Moradi *et al.*, 2015). This technique reduces the redundancy of correlated data by applying a linear transformation (Ali & Pour 2014; Mia & Fujimitsu, 2012). The PCA selects uncorrelated linear combinations (eigenvector loadings) of variables in such a way that each successively extracted linear combination, or principal component (PC), has a smaller variance (Singh & Harrison 1985 *in* Mia & Fujimitsu, 2012). The eigenvalues provide information based on the magnitude and sign of about which spectral properties of vegetation, rocks and soils are responsible for the statistical variance mapped into each PC (Mia & Fujimitsu, 2012; Loughlin, 1991). The result is a set of uncorrelated bands.

In this work two main approaches were applied: the first consisted in the application of PCA to all visible, NIR and SWIR bands of each satellite sensor; the second approach consisted in a selective PCA, in which PCA was applied to selected subsets of the satellites' bands.

In what concerns the selective PCA, two techniques were then applied: (i) the application or adaptation of the "Crosta technique" (Loughlin, 1991) in which the PCA is applied to a subset of four bands; (ii) the application or adaption of the technique proposed by Chavez & Kwarteng (1989) where PCA is applied to a subset of two bands.

The subsets chosen to the application of the selective PCA and the target information to extract are presented in Table 10.

Table 10 – Chosen subsets to the application of selective PCA and respective target mineral information.

Target mineral information	Subset				Reference
	ASTER	Landsat 8	Landsat 5	Sentinel-2	
Alunite	1,3,5,7	–	–	–	Crosta *et al*. (2003)
Illite and muscovite	1,3,5,6	–	–	–	
Kaolinite and smectite	1,4,6,9	–	–	–	
Kaolinite	1,4,6,7	–	–	–	
Ferric iron	–	2, 4	1, 3	2, 4	Chavez & Kwarteng (1989)
	–	2, 4, 5, 6	1,3, 4, 5	2, 4, 8, 11	Loughlin (1991)
Hydroxyl minerals	–	6, 7	5, 7	11, 12	Chavez & Kwarteng (1989)
	–	2, 5, 6, 7	1, 4, 5, 7	2, 8, 11, 12	Loughlin (1991)
Li-bearing minerals	1, 3	3, 5	2, 4	3, 8	**Self-proposed**
	1,3,11,14	2,3,5,11	1,2,4,6	2,3,8,11	**Self-proposed**

Similar to the aforementioned for RGB combinations, a correspondence between the bands used in the Landsat subsets and Sentinel-2 were made.

5.2.2.4 *Lineament extraction*

Since the emplacement of aplite-pegmatite veins in the Fregeneda-Almendra field was influenced by the regional structures, a structural map was elaborated based on the manual extraction of linear features from satellite images.

Structural discontinuities and other tectonic related features often result in morphological lineaments such as fault scarps, joints and fold axis (Ramsay & Huber, 1987). According to Hung *et al.* (2005), the structural phenomena (can result in different types of lineaments: (i) straight stream and valley, (ii) aligned surface depressions, (iii) soil tonal changes, (iv) alignments in vegetation, (v) vegetation type and height changes, or (vi) abrupt topographic changes.

The lineaments are formed by edges, which can be marked by pronounced differences in brightness or, like in most cases, they are marked by subtle brightness differences in the image and may be difficult to recognize (Sabins, 1997). Edge enhancement techniques are then applied to overcome this problem.

In this case, only Sentine-2 images were used because the accuracy of lineament extraction is strongly dependent on the spatial resolution of the image (Prasad *et al*., 2013): a higher resolution imagery results in a higher quality of lineament map. Band 11 was selected due to the importance of SWIR in geological applications.

Directional filtering was the image processing technique employed to make edge enhancements. More specifically, four different Prewitt filters were applied, each for a particular direction: N-S, E-W, NE-SW and NW-SE (Figure 22). The filters were created and applied in SNAP in area bigger than the studied area to try to include regional structures in the final structural map (see Appendix E).

Afterwards, the lineaments were manually digitized over the filtered images in a GIS environment (ArcMap). Only the lineaments that did not correspond to the faults mapped in the geological maps at the scale of 1:50,000 (Silva *et al*., 1990a, b) were extracted. ArcMap's "World Imagery" basemap was utilized as an assistent tool to evaulate if the lineaments presented in filtered images corresponded to geological structural features or man-made features like roads (see Appendix E).

Finally, the digitized lineaments were compared to a detailed geologic map at the scale of 1:10,000 (Viegas, 1983; Appendix A) to assess the accuracy of the employed method (Appendix E).

N-S

-1	-1	-1
0	0	0
1	1	1

E-W

-1	0	1
-1	0	1
-1	0	1

NE-SW

0	-1	-1
1	0	-1
1	1	0

NW-SE

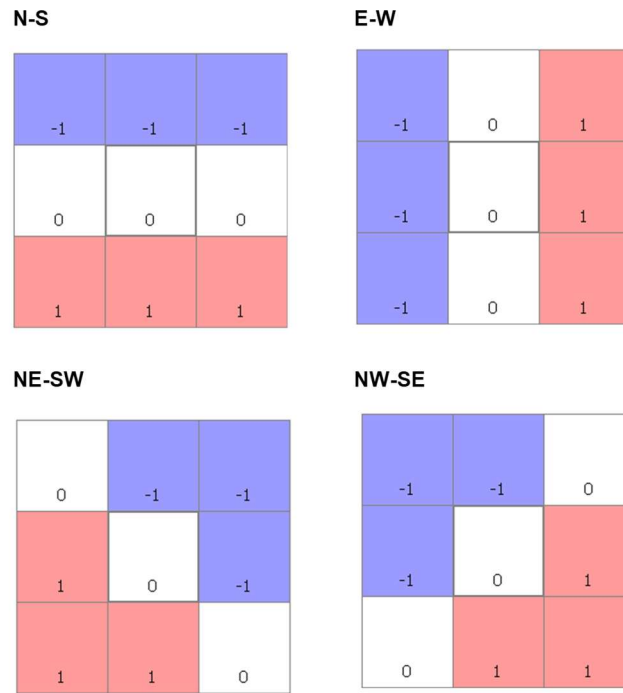| -1	-1	0
-1	0	1
0	1	1

Figure 22 – Prewitt filters applied in SNAP for directional edge enhancement.

6 Results

In this chapter, the results obtained from the application of the image processing techniques are presented.

6.1 RGB Combinations

In this section are presented the RGB combinations able to highlight compositional differences, hydrothermally altered zones and Li-mineralizations.

To map and distinguish iron oxides and clay minerals, the best RGB combinations were founded 2-5-7 for Landsat 8 and 2-8-12 for Sentinel-2 (Figure 23), both containing a band in the visible, another in the NIR and other in the SWIR.

In both sensors, urbanized areas and ploughed fields present a bright white color, water bodies are represented in black and vegetated areas appear in green color in Figure 23-a) and -c) and are fully masked in Figure 23-b) and -d). The metasediments from the CXG are clearly distinguished from the granites: the former presents a pink, salmon-like color in the Landsat 8 images (Figure 23-a, -c) and a brownish-yellow color in Sentinel-2 images (Figure 23-b, -d); the granites appear in purple in Figure 23-a) and -c), and in blue color in Figure 23-b) and -d). Intense blue and intense purple areas correspond to iron-rich zones and present a different composition that will be more described later on (section 6.2). In order to identify the possible cause of the compositional differences, specific spectral indices (Appendix B) that discriminate between burned and unburned areas were applied. The burned areas were mapped (Appendix B), and a correspondence between these areas and the intense blue and intense purple zones is clear (Figure 23).

Bajoca, Feli and Alberto mines mainly appear in bright pink in Landsat 8 images (Figure 23-a, -c) and light pink in Sentinel-2 images (Figure 23-b, -d). White spots in these zones could also indicate the presence of iron minerals as well as clay minerals since the white color is due to high reflectance in the three bands.
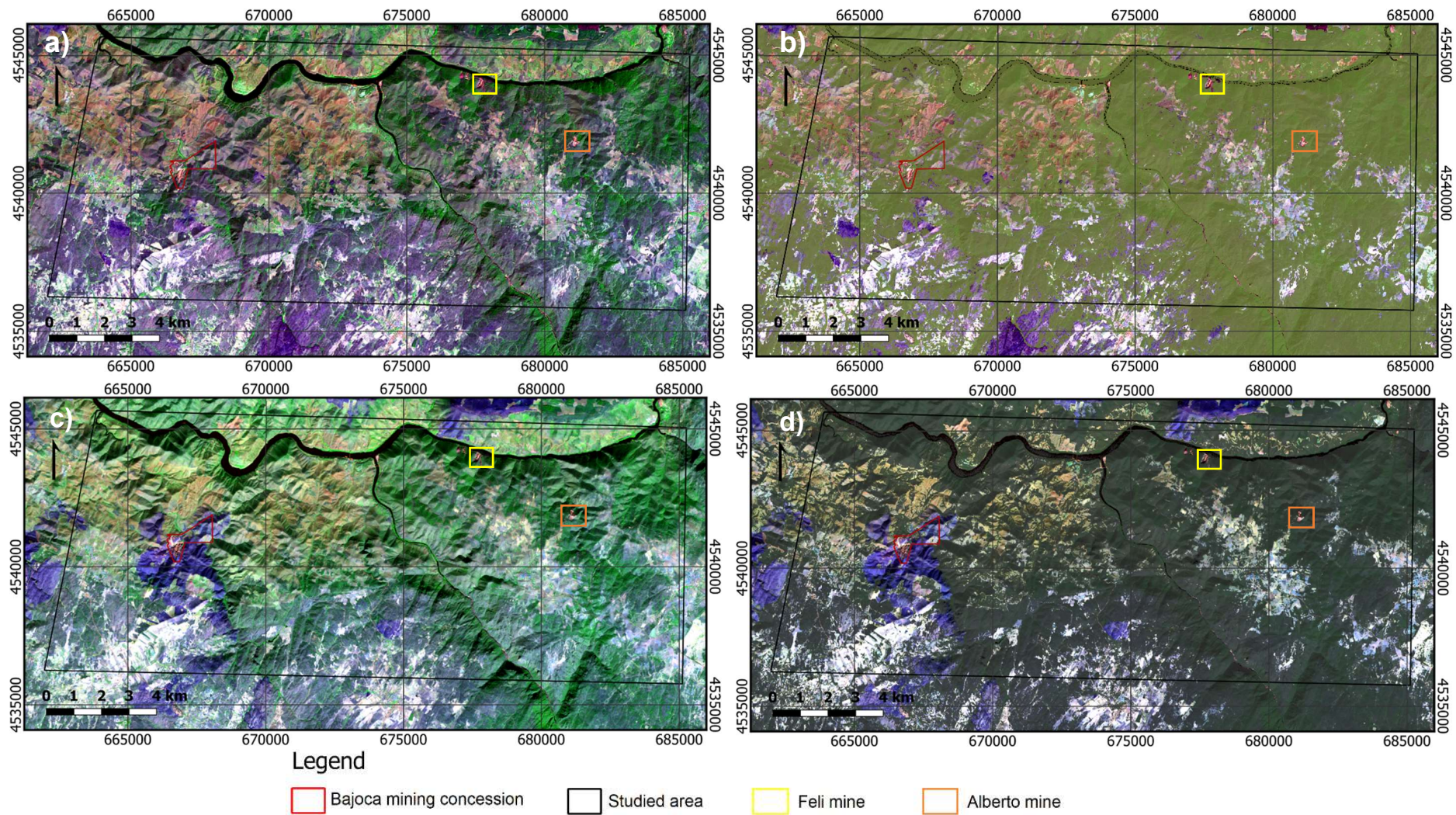
Figure 23 – RGB combinations that discriminate between iron oxides and clay minerals: a) RGB 2-5-7 for Landsat 8; b) RGB 2-5-7 with a water and vegetation mask; c) RGB 2-8-12 for Sentinel-2; d) RGB 2-8-12 with a water and vegetation mask. Intense purple areas (a and b) and intense blue areas (c and d) show the highest iron oxide content. Some white spots in the Bajoca and Alberto mines could indicate a simultaneous presence of iron oxides and clay minerals. Coordinate System: UTM29N WGS84.

The RGB combinations that better identify hydrothermally altered rocks are 5-7-3 for Landsat 8 (Figures 24-a and 25-a), 4-7-2 for Landsat 5 (Figures 24-b and 25-b) and 8-12-3 for Sentinel-2 (Figures 24-c and 25-c). All these combinations contain a NIR band in the red channel, a SWIR band in the green and a visible band in the blue channel.

In the three sensors, urbanized areas and ploughed fields present a bright white color; water bodies are represented in black; vegetated areas appear in red color in Figure 24 and are fully masked in Figure 25; the metasediments from the CXG present purple color; and the granites are represented in light- to medium-green color. Intense green areas in all images correspond to burned forest areas.

In the Fregeneda-Almendra aplite-pegmatite field, open pit mines appear with a bluish tint probably indicating some hydrothermal alteration. In Landsat 5 images (Figures 24-b and 25-b), the pegmatites from Bajoca and Alberto were not being exploited, and no sign of hydrothermal alteration is visible. A deep analysis of Figures 24 and 25 allows to identify other areas in the metasediments that present a bluish color. The burned areas present a color that also indicates hydrothermal alteration, but different from the one identified in Li-bearing zones. More detailed studies are needed to understand why these burned areas appear in intense green color: can the chemical and geological changes due to heat exposure cause similar signatures to the ones resultant of hydrothermal alteration processes?

These RGB combinations are also very good at enhancing geological structures like geological faults.
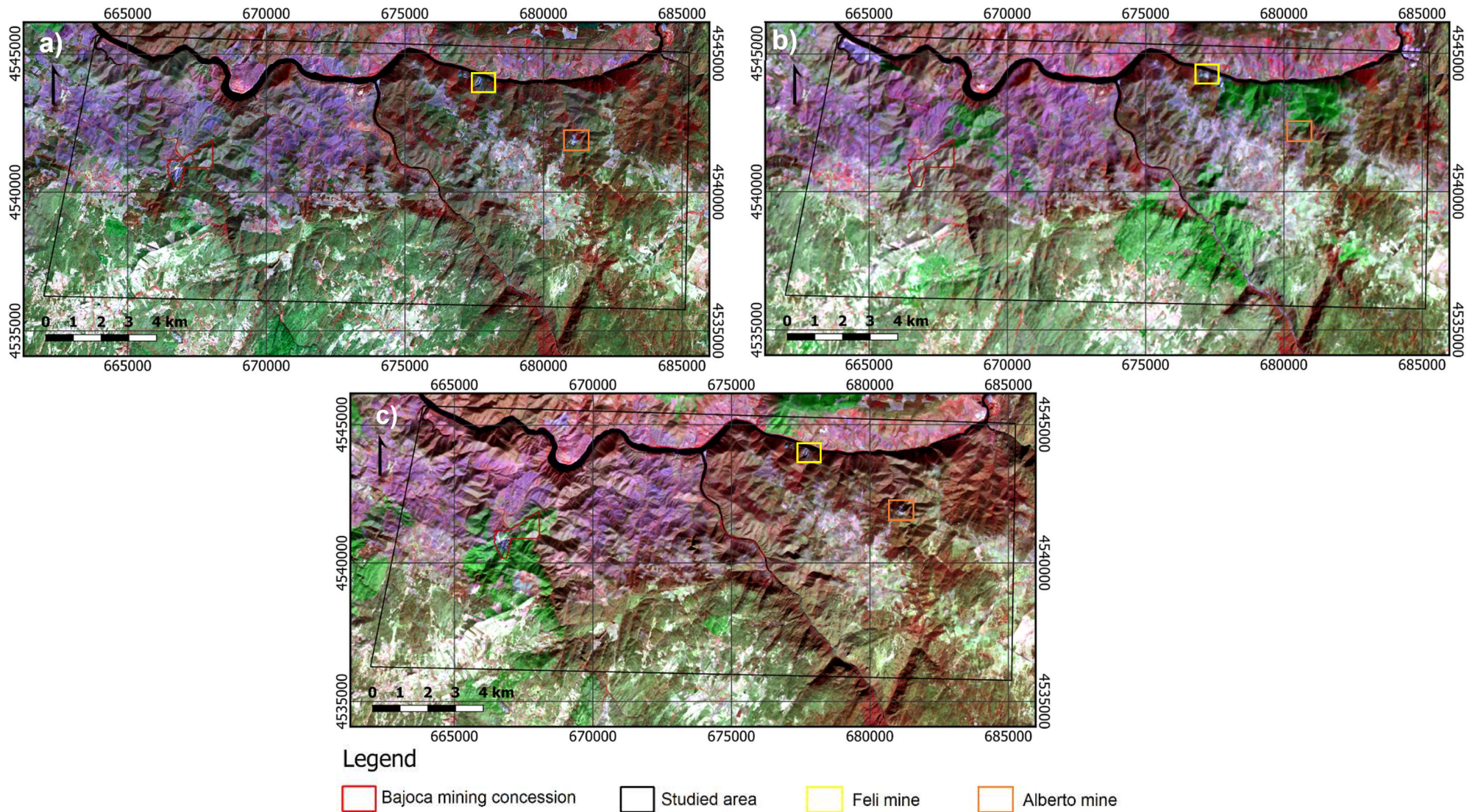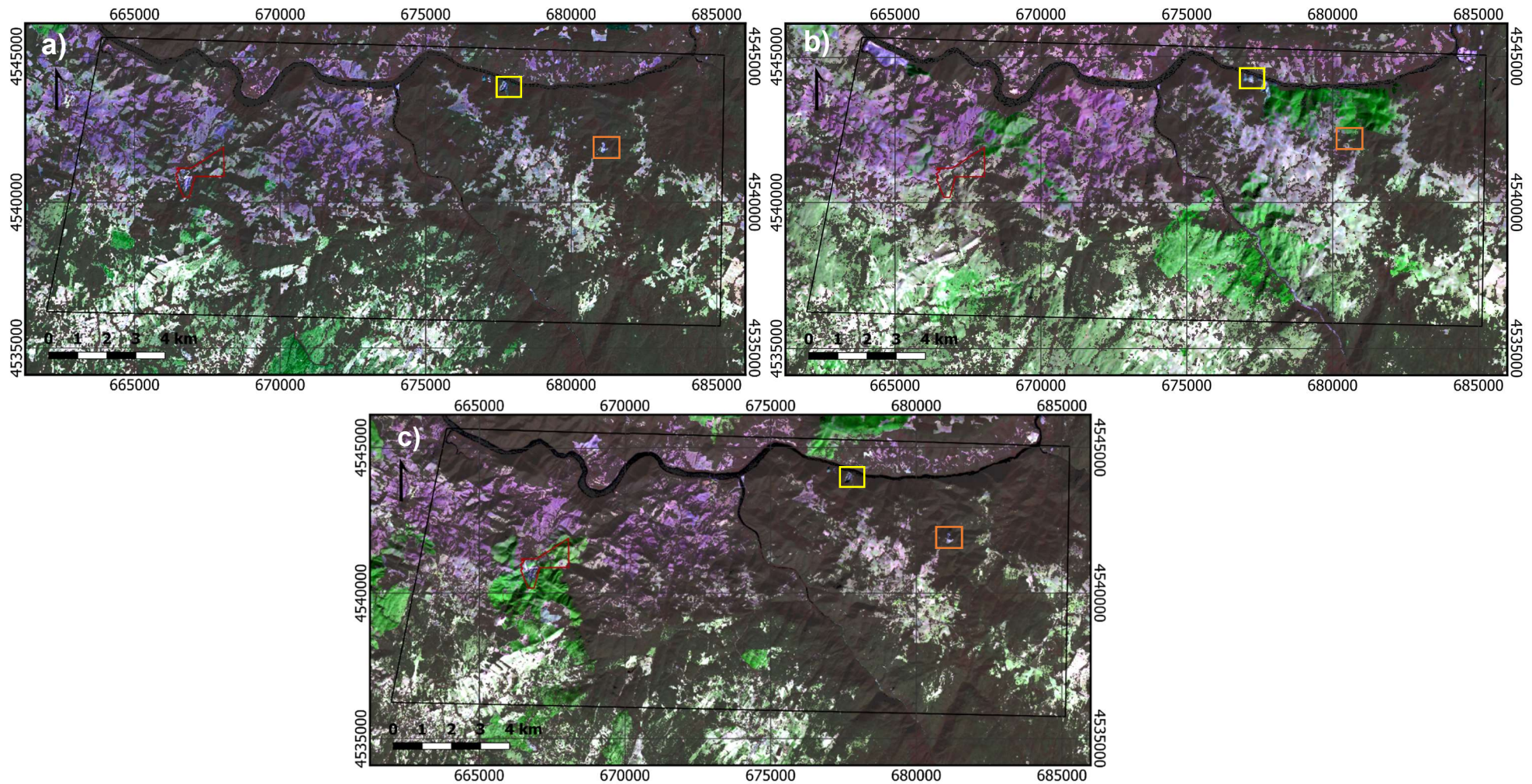
Figure 24 – RGB combinations to highlight hydrothermally altered areas: a) RGB 5-7-3 for Landsat 8; b) RGB 4-7-2 for Landsat 5; c) RGB 8-12-3 for Sentinel-2. Red areas correspond to vegetated areas. Light green represents the granites while purple color represents the metasediments. Hydrothermally altered rocks show be discriminated in deep green and deep blue clorors, but deep green colors appear to correlate to burned areas. Known Li-bearing areas present a blue color indicating hydrothermal alteration, apart from Bajoca and Alberto mines in the Landsat 5 image.

Figure 25 – Same RGB combinations of Figure 24 that highlight hydrothermally altered areas but with a water and vegetation mask: a) RGB 5-7-3 for Landsat 8; b) RGB 4-7-2 for Landsat 5; c) RGB 8-12-3 for Sentinel-2. Light green represents the granites while purple color represents the metasediments. Hydrothermally altered rocks show be discriminated in deep green and deep blue colors, but deep green colors appear to correlate to burned areas. Known Li-bearing areas present a blue color indicating hydrothermal alteration, apart from Bajoca and Alberto mines in the Landsat 5 image.

The self-proposed RGB combinations that best highlight Li-mineralizations are divided in two sets. The first is composed by a SWIR band in the red channel, a visible band in the green one and a thermal band in the blue one: 5-1-14 for ASTER (Figure 26), 7-3-11 for Landsat 8 (Figure 27-a, b) and 7-2-6 Landsat 5 (Figure 27-c, d).

In the three sensors, urbanized areas and ploughed fields present a bright white or yellow color, water bodies are represented in black, the metasediments from the CXG present in general a blue or bluish color; and the granites are represented in purple. Burned areas show an intense purple color, especially in Landsat 5 images (Figure 27-c, d). Mineralized zones appear in a yellowish green or green color but only where Li-bearing pegmatites outcrop: in Landsat 5 images (Figure 27-c, d) there is no distinct signal in the Bajoca or Alberto mines. Vegetated areas are not differentiated by these combinations but appear fully masked in Figures 26-b), Figure 27-b) and Figure 27-d), hence the importance of a vegetation mask.
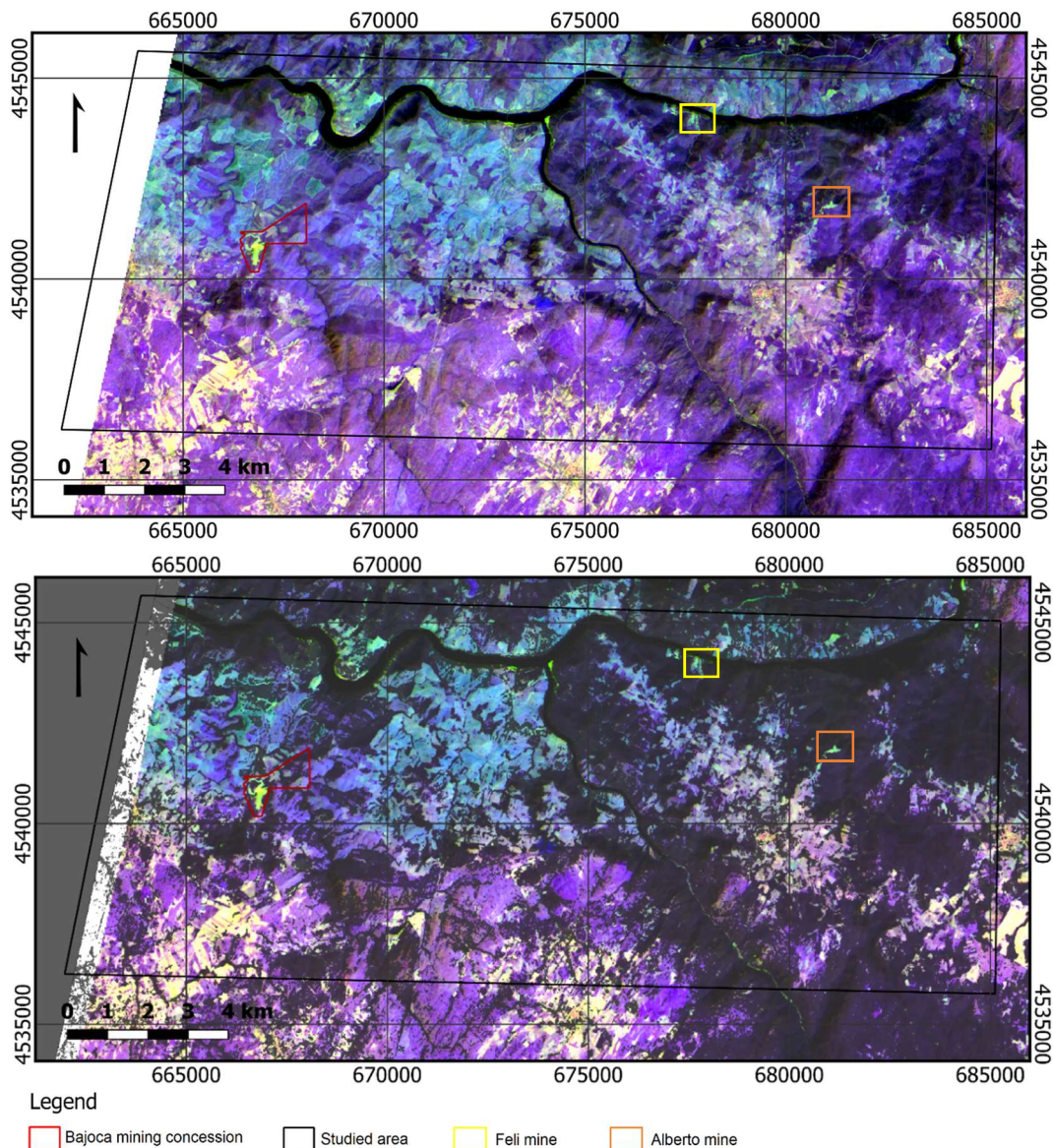

Figure 26 – RGB combination 5-1-14 for ASTER to discriminate Li-bearing minerals: a) with no mask; b) with a water and vegetation mask. Granites appear in purple, while the metasediments appear in blue. Known Li-mineralized areas appear in a greenish color.
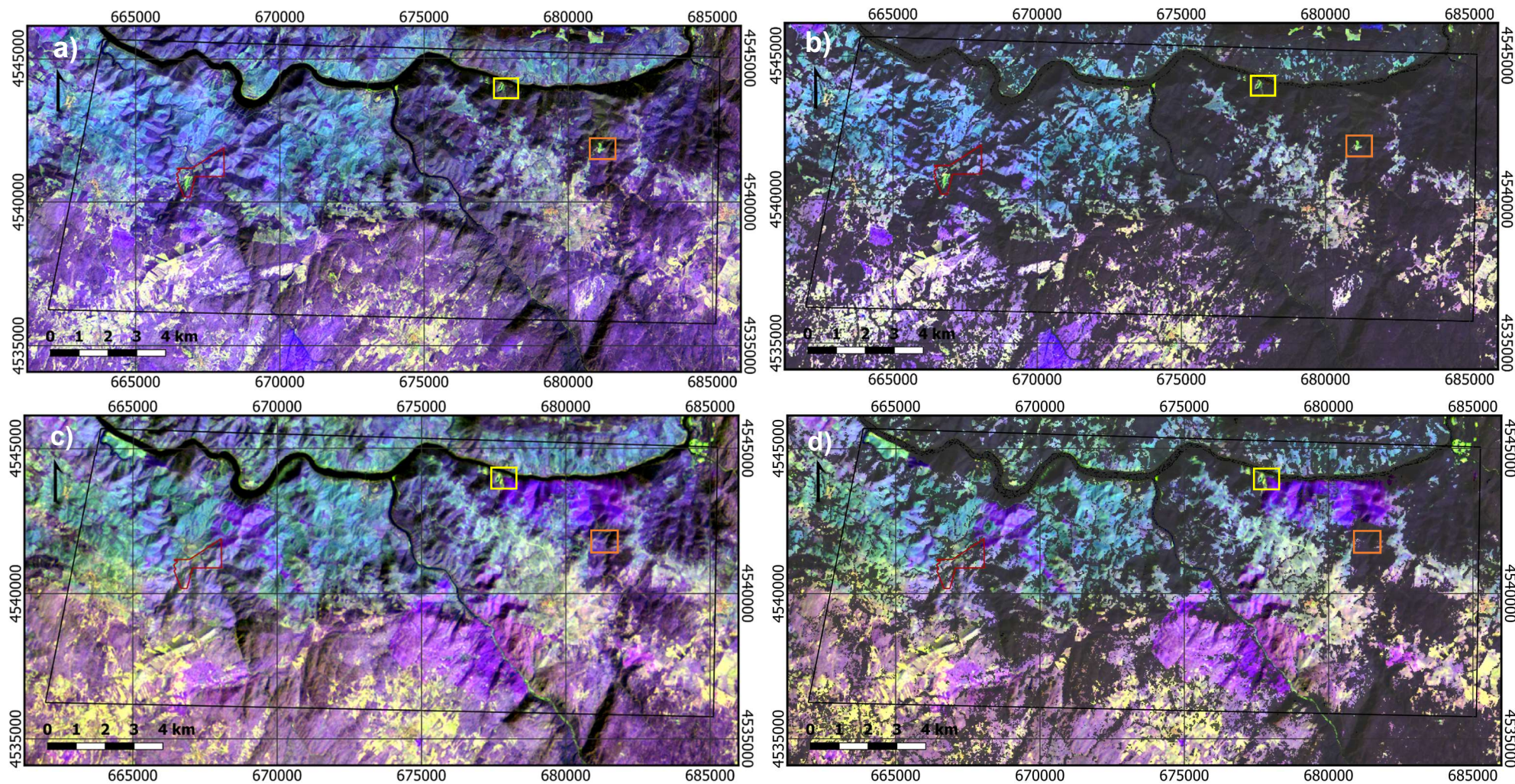
Figure 27 – RGB combinations to discriminate Li-bearing minerals: a) RGB 7-3-11 for Landsat 8; b) RGB 7-3-11 with a water and vegetation mask; c) RGB 7-2-6 for Landsat 5; d) RGB 7-2-6 with a water and vegetation mask. Granites appear in purple, while the metasediments appear in blue. Known Li-mineralized areas appear in a greenish color, except for Bajoca and Alberto mines in Landsat 5 images (when the veins did not outcrop).

The second set that better highlights Li-mineralizations is composed by two visible bands and a thermal band: 2-1-13 for ASTER (Figures 28-a and 29-a), 3-2-11 for Landsat 8 (Figures 28-b and 29-b) and 2-1-6 for Landsat 5 (Figures 28-c and 29-c). Since Sentinel-2 does not have available a band in TIR region, the thermal band was swapped by a SWIR band – RGB combination 3-2-12 (Figures 28-d and 29-d).

In the first three sensors, urbanized areas and ploughed fields present a bright yellow or yellowish white color, while water bodies are represented in black. Known mineralized areas also present a bright yellow, except for the Bajoca and Alberto mines in Landsat 5 images (Figures 28-c and 29-c). There is no clear distinction between the metasedimentes, the granites or between the vegetated areas. The latter appears masked in Figure 29.

In the case of Sentinel-2 images (Figures 28-d and 29-d), urbanized areas and ploughed fields present a bright white color; the difference between vegetated areas and granitic rocks is not clear but these zones appear in blue or blueish grey color while the metasediments from the CXG appear in yellow. Known mineralized areas also appear in yellow, making it impossible to distinguish between potential and non-potential zones with lithium.

Burned areas tend show a more intense blue color in all images. It is also worth mentioning that when these burned areas are differentiated, independently of the RGB combination, they present a signature similar but stronger than the one produced by the granitoids, whether the burned areas are located in the metasedimentary terrains or in the granitic terrains.
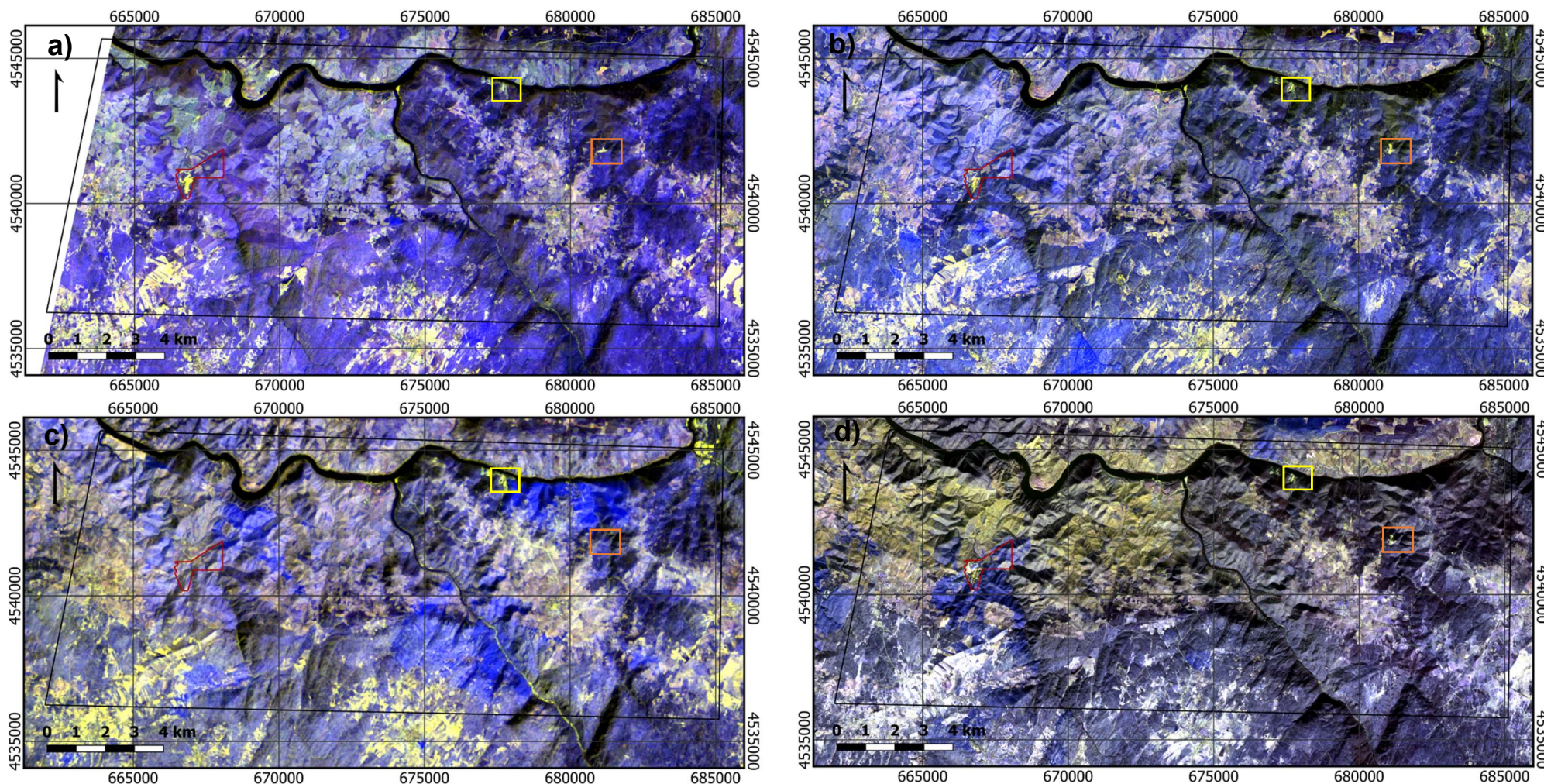
Figure 28 – RGB combinations to highlight Li-mineralized areas: a) RGB 2-1-13 for ASTER; b) RGB 3-2-11 for Landsat 8; c) RGB 2-1-6 for Landsat 5; d) RGB 3-2-12 (with a SWIR band instead of a thermal band) for comparison. Known Li-bearing areas appear in yellow. In a) to c), some urbanized areas and ploughed field also appear in yellow. In d), due to the lack of a thermal band, there is no distinction between Li-mineralized areas and the metasediments. Burned areas present intense blue color.
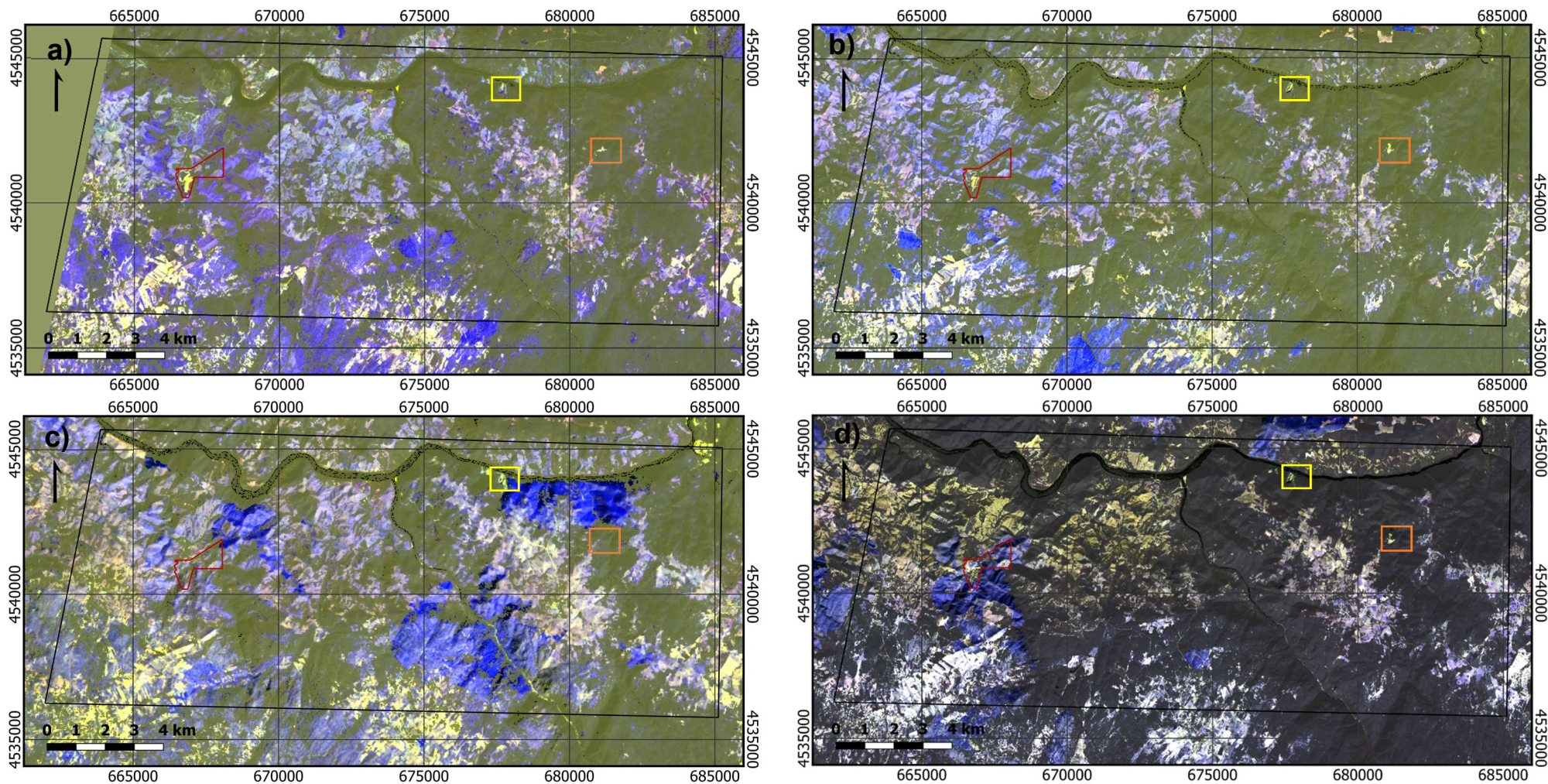
Figure 29 – Same RGB combinations of Figure 28 that highlight Li-mineralized areas but with a water and vegetation mask: a) RGB 2-1-13 for ASTER; b) RGB 3-2-11 for Landsat 8; c) RGB 2-1-6 for Landsat 5; d) RGB 3-2-12 (with a SWIR band instead of a thermal band) for comparison. Known Li-bearing areas appear in yellow. In a) to c), some urbanized areas and ploughed field also appear in yellow. In d), due to the lack of a thermal band, there is no distinction between Li-mineralized areas and the metasediments. Burned areas present intense blue color.

6.2 Band ratios

To map hydrothermally altered rocks several band ratios were applied in order to highlight minerals associated with hydrothermal alteration. The best results are presented in this section as well as the band ratios that better differentiate Li-bearing rocks. The resulting images present different surface reflectance values which limits a direct comparison between images. Nonetheless, there are no significant differences between them, with exception of the burned areas (Appendix B). For that reason, and since the information presented by the equivalent band ratios of the different sensors is in part redundant, some of the band ratios are presented in Appendix C.

Iron oxides, such as hematite and magnetite, are frequently associated with these alteration zones. Band ratio 4/2 for Landsat 8 (Appendix C) and Sentinel-2 (Figure 30-d, -e, -f), and band ratio 3/1 for Landsat 5 (Appendix C) discriminate iron oxides as bright pixels because iron minerals have low reflectance in blue and high reflectance in red. Band ratio 2/1 for ASTER (Figure 30-a, -b, -c) highlights minerals bearing ferric iron also in bright pixels.

Figure 30-a is a color density slice version of ASTER's 3/1 band ratio (Figure 30-c), whose color intervals were attributed based on the histogram presented in Figure 30-b. Yellow and red areas correspond to the highest surface reflectance values (yellow ≈ 1.24; red ≥ 1.35) and therefore should correlate with altered rocks.

Figure 30-d is a color density slice version of Sentinel-2's 4/2 band ratio (Figure 30-f), whose color assignments are shown in the histogram presented in Figure 30-e. Yellow and red areas correspond to the highest surface reflectance values (yellow ≈ 2.06; red ≥ 2.31) and therefore should also correlate with altered rocks.

However, in all the cases, the highest contents of iron oxides/minerals with ferric iron appear to correlate with urbanized areas and agricultural fields, as well as Douro's fluvial terraces from the Quaternary composed mainly by sandstones and clays. No discernible difference between the metasediments and the granites is visible. Known mineralized areas present low- to -medium contents of iron oxides/minerals with ferric iron. The lowest values correspond mainly to vegetated and burned areas.
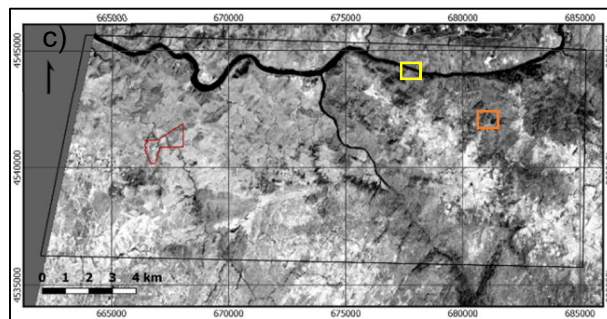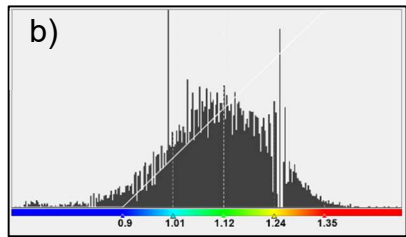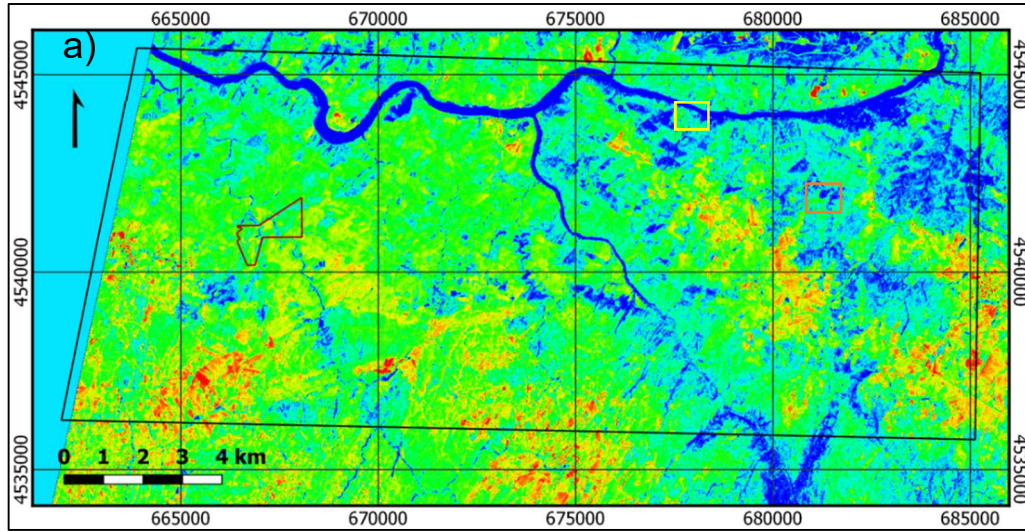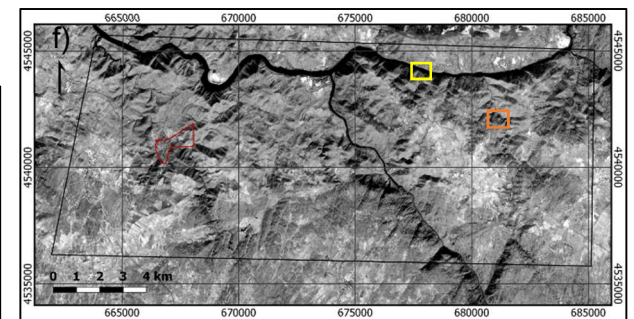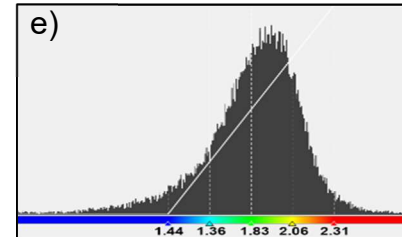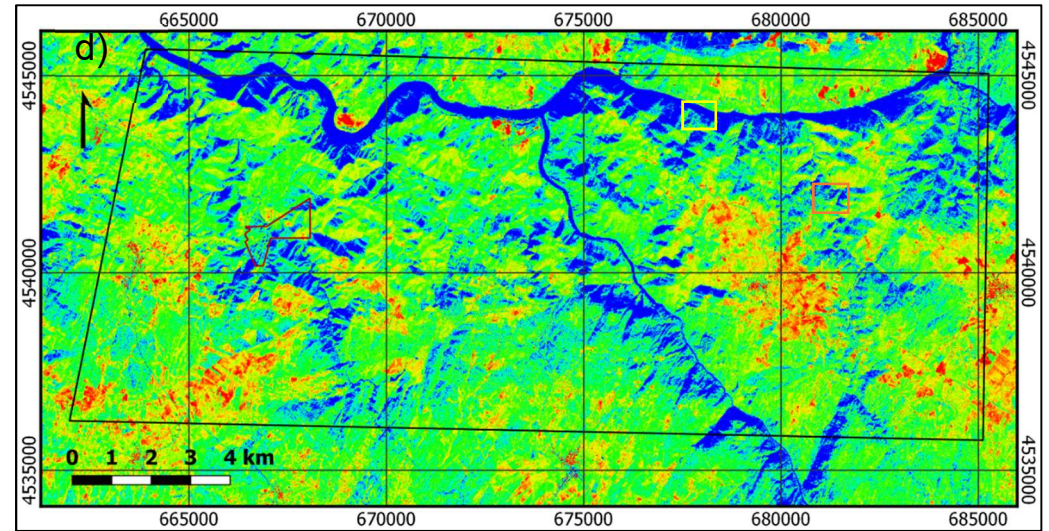
Figure 30 – Ferric iron (ASTER) and iron oxide (Sentinel-2) mapping through band rationing: a) ASTER's ratio 2/1 image with density slice (high ratio values shown in red); b) histogram for ASTER's 2/1 image; c) ASTER's ratio 2/1 image; d) Sentinel-2's ratio 4/2 image with density slice (high ratio values shown in red); e) histogram for Sentinel-2's 4/2 image; f) Sentinel-2's ratio 4/2 image.

To map ferrous minerals band ratio 6/5 was applied to Landsat 8 images (Figure 31-a, -b, -c), ratio 5/4 to Landsat 5 (Figure 31-d, -e, -f) and 11/8 ratio to Sentinel-2 (Appendix C). The resulting images are very similar to the result of band ratio 4/3 in ASTER images to discriminate ferric oxides (Appendix C). It would be expected that the results of ratio 4/3 (mapped ferric oxides) were similar to the mapped ferric iron minerals, but that does not happen.

A color density slice version of band ratio 6/5 for Landsat 8 (Figure 31-c) is shown in Figure 31-a, with color assignments shown in the histogram presented in Figure 31-b. Yellow and red areas correspond to the highest surface reflectance values (yellow ≈ 1.61; red ≥ 1.82) and therefore should indicate altered rocks.

Figure 31-d is a color density slice version of Landsat 5's 5/4 band ratio (Figure 31-f), whose color intervals were attributed based on the histogram showed in Figure 31-e. Yellow and red areas correspond to the highest surface reflectance values (yellow ≈ 1.51; red ≥ 1.8) and therefore should also indicate altered rocks.

In all cases, there is a clear difference in the iron content of granites and metasediments from the CXG: granitoid rocks present a higher content of ferrous minerals/ferric oxides. Burned areas present the highest contents even when compared with the granites.

The Quaternary fluvial terraces present dark blue color, which indicates low content of ferrous minerals/ferric oxides. Known mineralized areas present low- to -medium contents. Red colors near Feli mine in Landsat 5 images (Figure 31-d) are due to fire exposure (the open-pit area presents light blue color).
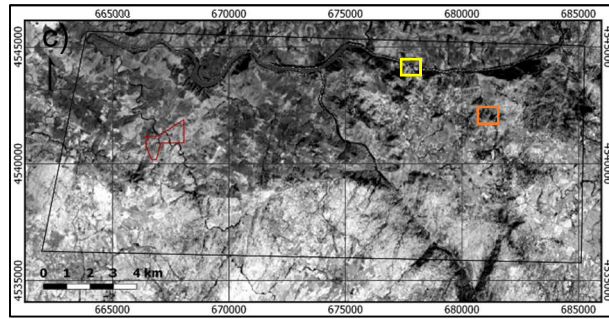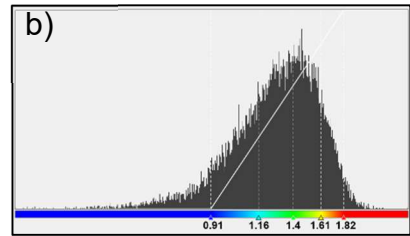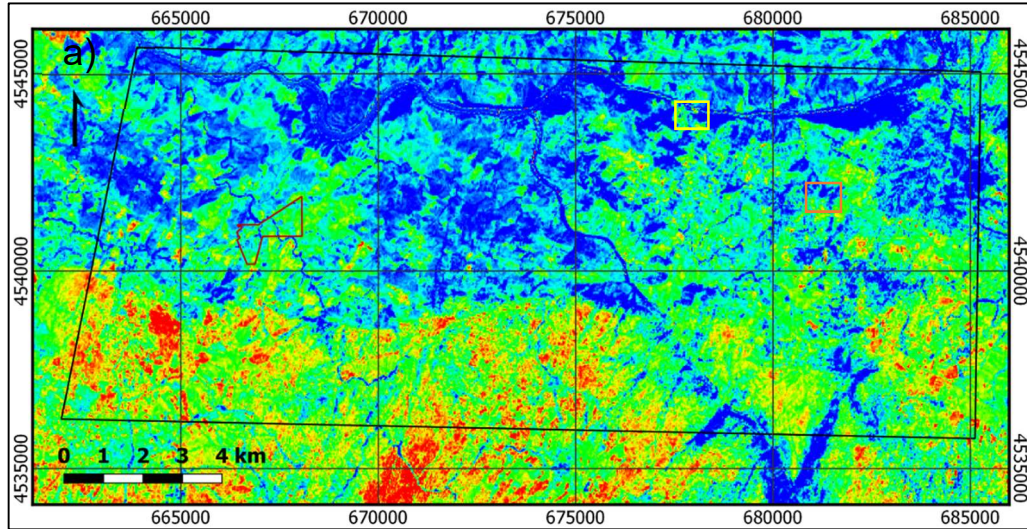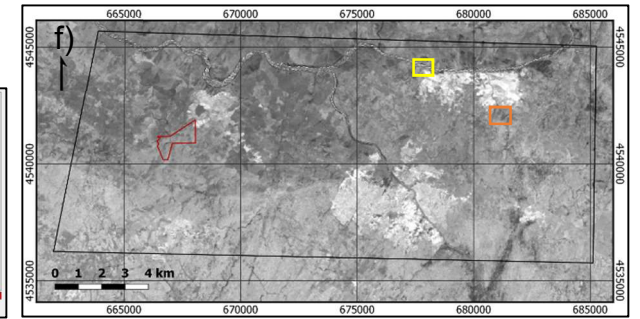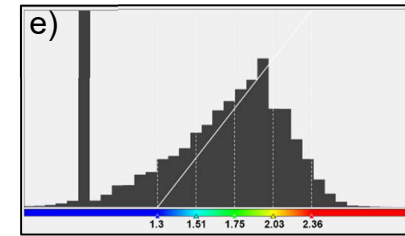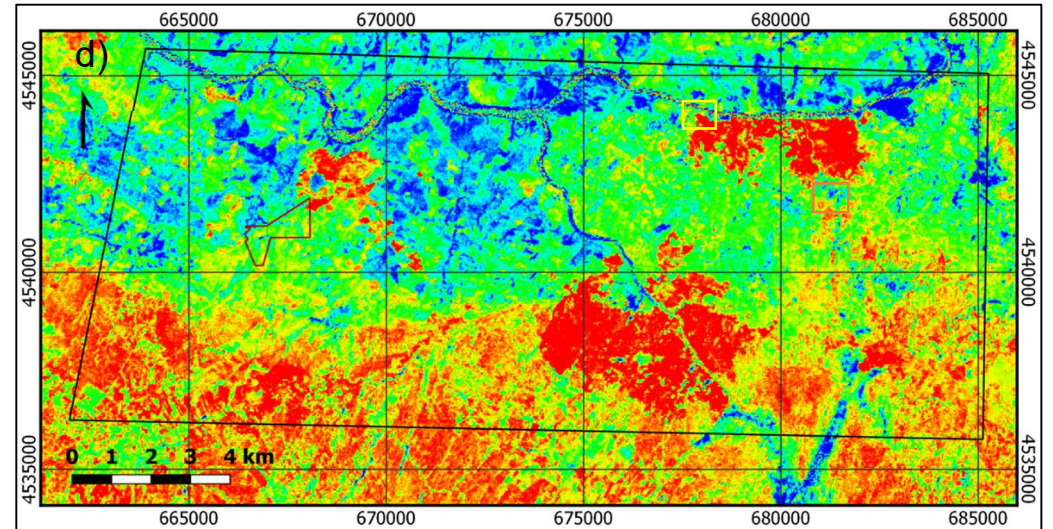
Figure 31 – Ferrous mineral mapping through band rationing: a) Landsat 8's ratio 6/5 image with density slice (high ratio values shown in red); b) histogram for Landsat 8's 6/5 image; c) Landsat 8's ratio 6/5 image; d) Landsat 5's ratio 5/4 image with density slice (high ratio values shown in red); e) histogram for Landsat 5's 5/4 image; f) Landsat 5's ratio 5/4 image.

Other minerals frequently associated with hydrothermal alteration are alunite and/or clays such as kaolinite, montmorillonite and others. To map these minerals band ratio 6/7 was applied to Landsat 8 images (Figure 32-a, -b, -c), ratio 5/7 to Landsat 5 (Figure 32-d, -e, -f) and 11/12 ratio to Sentinel-2 (Appendix C). In the ASTER's case, band ratio 7/5 was applied to map kaolinite (Figure 33).

A color density slice version of band ratio 6/7 for Landsat 8 (Figure 32-c) is shown in Figure 32-a, with the respective color assignments shown in the histogram presented in Figure 32-b. Yellow and red areas correspond to the highest surface reflectance values (yellow ≈ 1.66; red ≥ 1.83) and therefore should indicate altered rocks.

Figure 32-d is a color density slice version of Landsat 5's 5/7 band ratio (Figure 32-f). The color intervals of the density slice image were attributed based on the histogram showed in Figure 32-e. Yellow and red areas correspond to the highest surface reflectance values (yellow ≈ 1.55; red ≥ 1.7).

In the case if Landsat (5 and 8) and Sentinel-2, there is no marked difference in the alunite and/or clay content of granites when compared with the metasediments from the CXG; burned areas present the lowest contents in alunite and/or clay minerals as evidence by the dark blue color; the fluvial terraces from the Quaternary present yellow to red color, which indicates high- to very-high content in alunite or clays. Known mineralized areas present very low- to -medium contents.
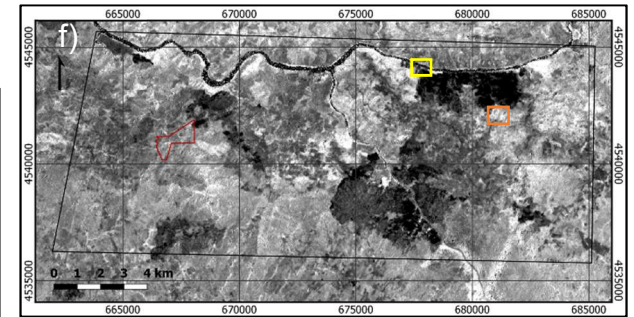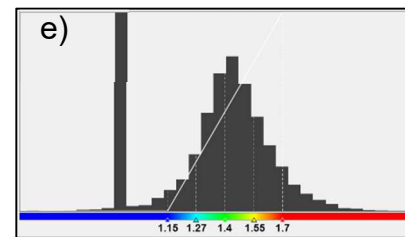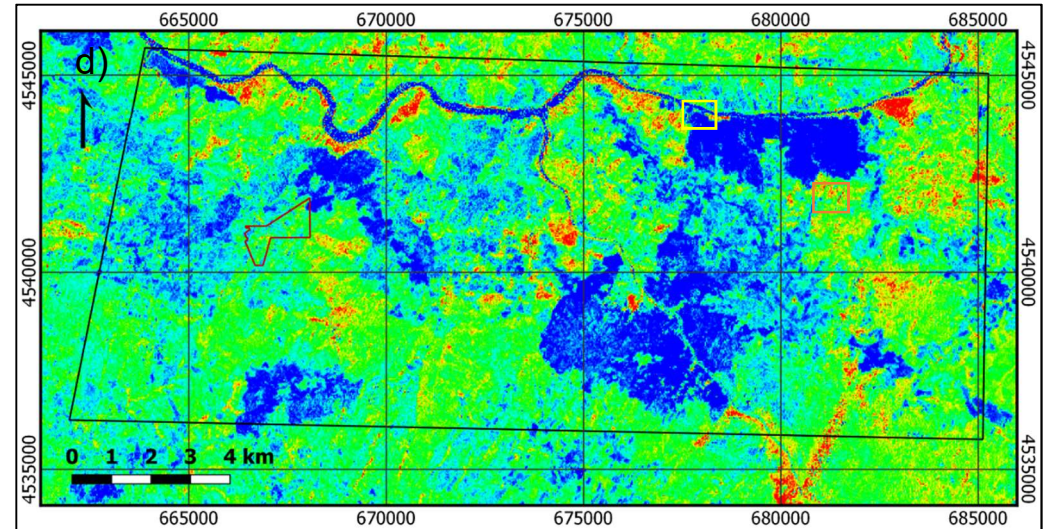
Figure 32 – Alunite and clay mapping through band rationing: a) Landsat 8's ratio 6/7 image with density slice (high ratio values shown in red); b) histogram for Landsat 8's 6/7 image; c) Landsat 8's ratio 6/7 image; d) Landsat 5's ratio 5/7 image with density slice (high ratio values shown in red); e) histogram for Landsat 5's 5/7 image; f) Landsat 5's ratio 5/7 image.
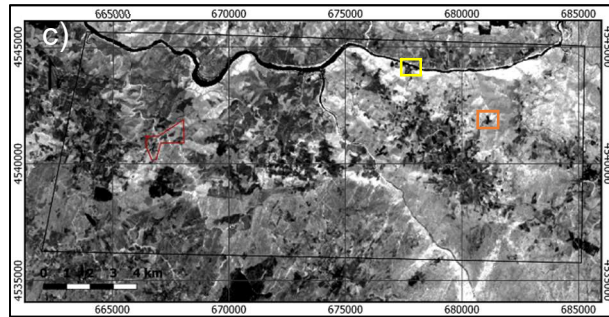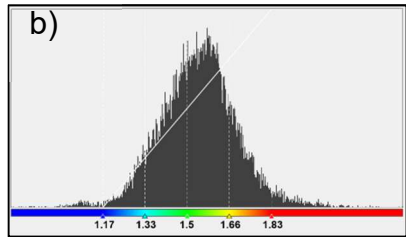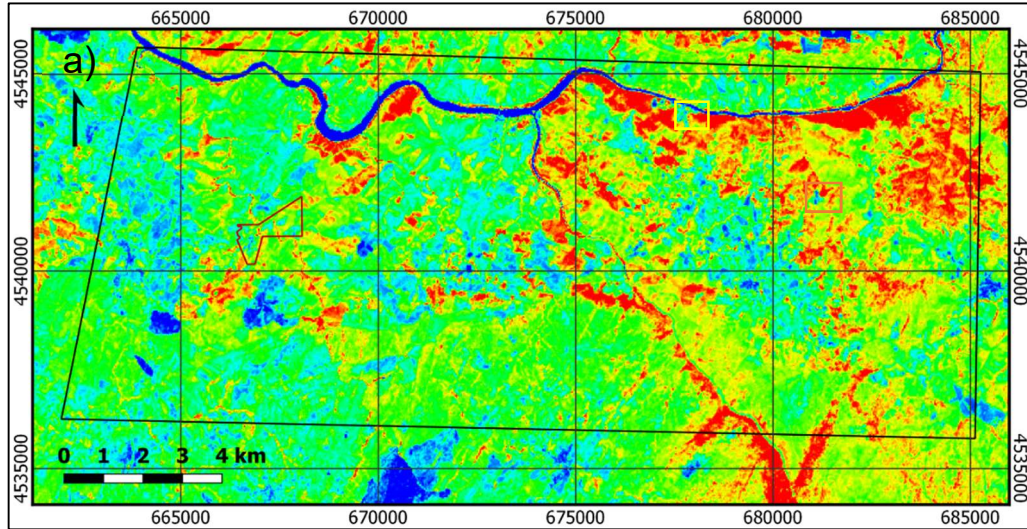
Figure 33-a is a color density slice version of ASTER 7/5 band ratio (Figure 33-c). The color intervals of the density slice image were attributed based on the histogram showed in Figure 33-b. Yellow and red areas correspond to the highest surface reflectance values (yellow ≈ 0.96; red ≥ 1.1).

The results obtained by ASTER's band ratio are very different from the results obtained for the other sensors: Figure 33 indicates that known mineralized areas present high- to very-high contents in kaolinite unlike the results presented in Figure 32. It should be taken into account that ASTER's 7/5 ratio is used to discriminate only kaolinite and not a wide range of clay minerals.

Figure 33 – Kaolinite mapping through band rationing: a) ASTER's ratio 7/5 image with density slice (high ratio values shown in red); b) histogram for ASTER's 7/5 image; c) ASTER's ratio 7/5 image.

Band ratio 7/6 for ASTER images is used for discriminating areas with high muscovite content. However, in this work, 7/6 ratio was proposed to highlight Li-mineralizations due to a similar behavior of lepidolite and spodumene in the referred bands (Figure 34).

A colored density slice version of band ratio 7/6 (Figure 34-c) is shown in Figure 34-a, with the respective color assignments shown in the histogram of Figure 34-b. Yellow and red areas correspond to the highest surface reflectance values (yellow ≈ 1; red ≥ 1.06) and should indicate Li-bearing rocks.

Known Li mineralized areas are correctly identified in yellow and red colors in Figure 34-a. Urbanized areas and agricultural fields also present high reflectance, as can be observed in Figure 34-c and therefore present equally yellow and red colors. Light and dark blue areas correspond to zones with high vegetation coverage.

Figure 34 – Li-mineralization mapping through band rationing (ASTER): a) ASTER's ratio 7/6 image with density slice (high ratio values shown in red); b) histogram for ASTER's 7/6 image; c) ASTER's ratio 7/6 image.

Another self-proposed ratio to discriminate Li-mineralizations based mainly in the spectral behavior of spodumene is 3/5 for Landsat 8 (Figure 35-a, -b, -c), 2/4 for Landsat 5 (Figure 35-d, -e, -f), 1/3 for ASTER images (Appendix C) and 3/8 for Sentinel-2 (Appendix C).

As it can be seen by the gray-scale images (Figure 35-c, -f), that the proposed ratios highlight in bright color the mineralized areas, but also several other areas. However, colored density slice images (Figure 35-a, -d) based on the gray scale images histograms (Figure 35-b, -e) allow to successfully differentiate Li-bearing rocks: these areas present the highest reflectance values and are mapped in red color (surface reflectance values ≥ 0.59 for Landsat 8; surface reflectance values ≥ 0.77 for Landsat 5).

A comparison between Landsat 5 images (before the opening of Bajoca and Alberto mines) and Landsat 8 images, shows that no signal is detected in these areas before exploitation.

Very low (dark blue) to low (light blue) reflectance values correspond to densely vegetated areas.
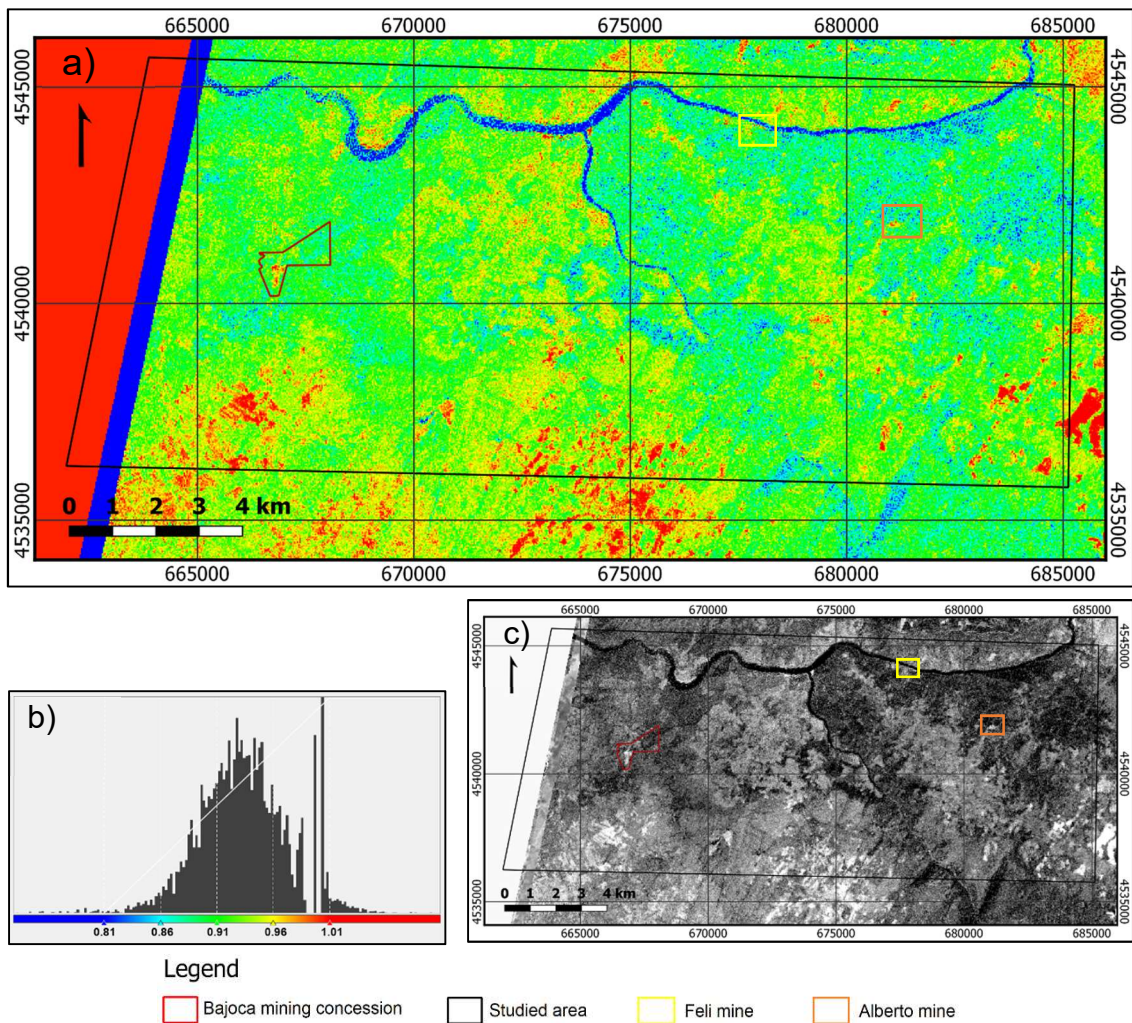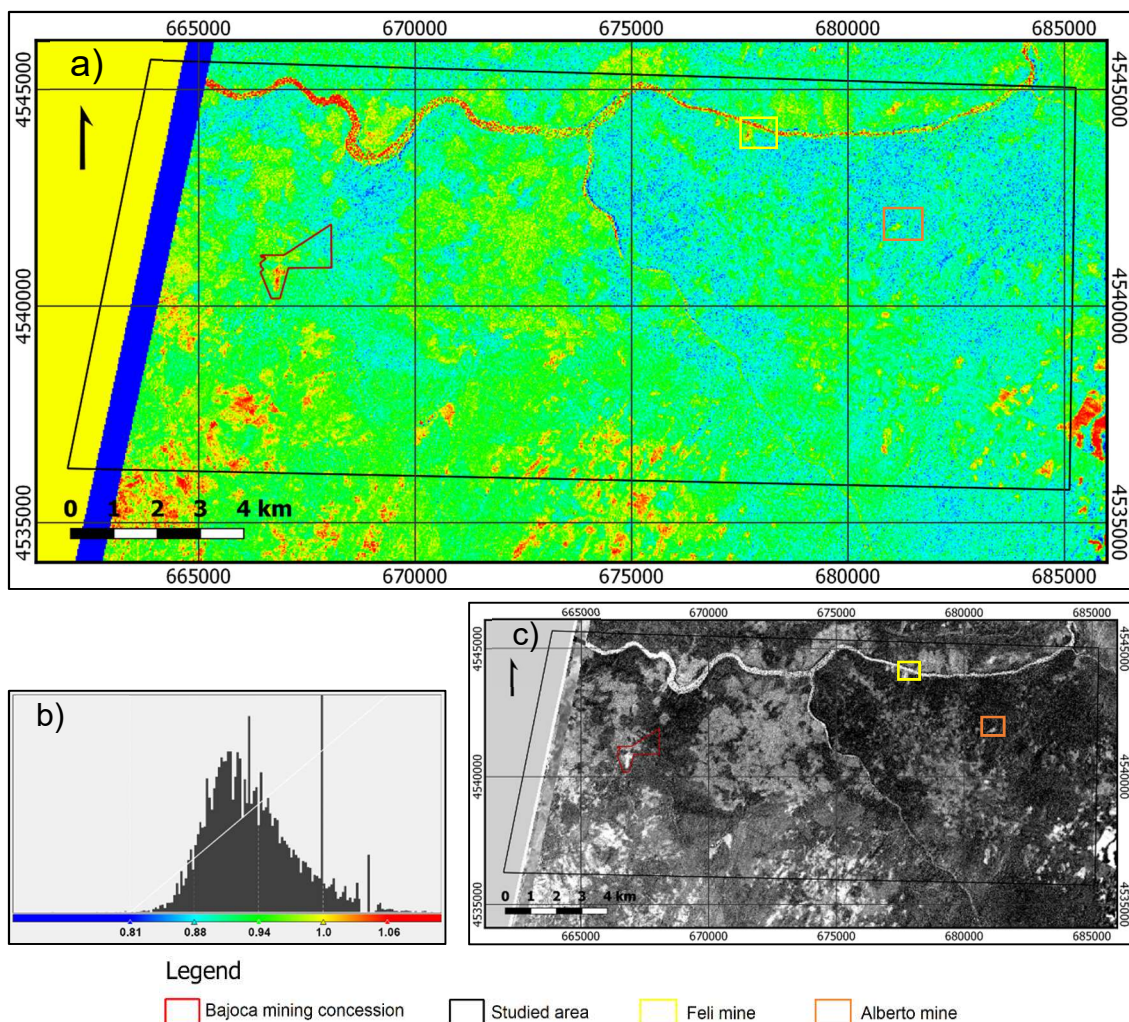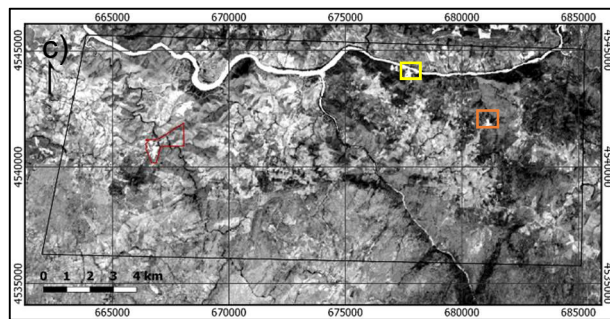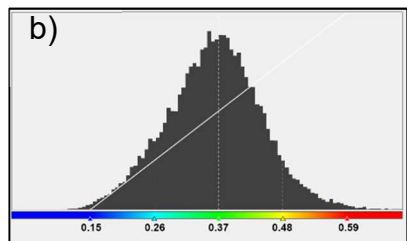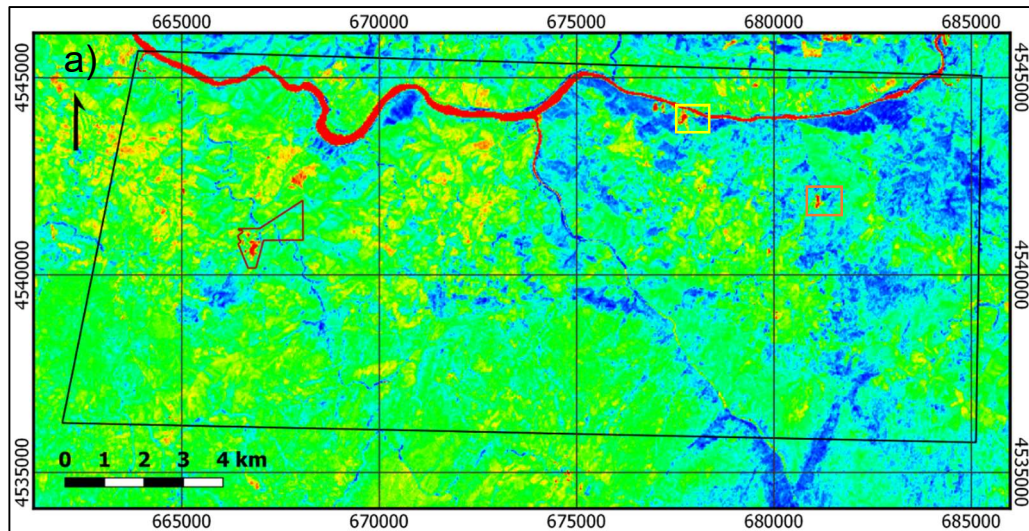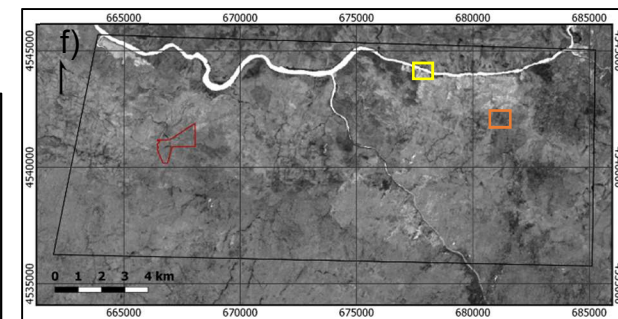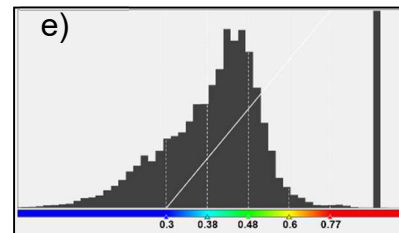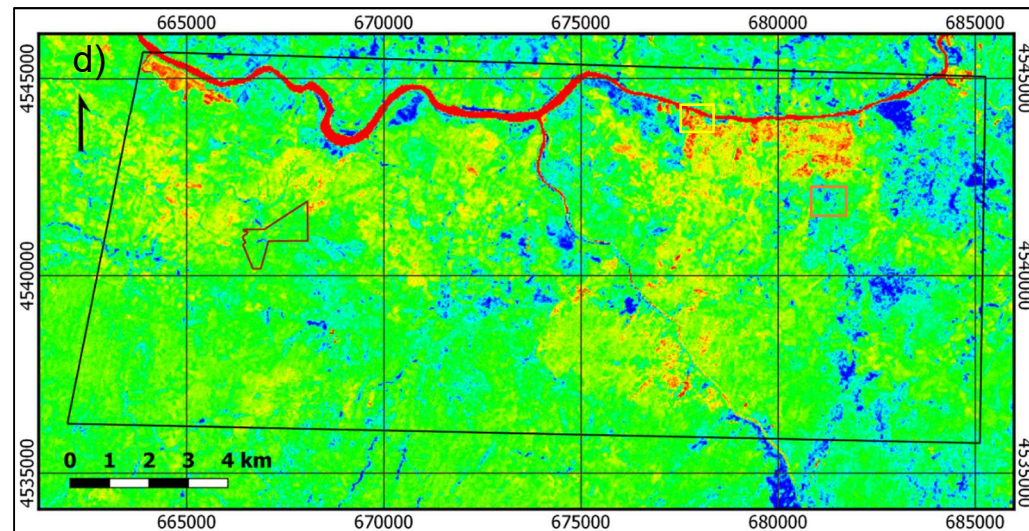
Figure 35 – Li-mineralization mapping through band rationing: a) Landsat 8's ratio 3/5 image with density slice (high ratio values shown in red); b) histogram for Landsat 8's 3/5 image; c) Landsat 8's ratio 3/5 image; d) Landsat 5's ratio 2/4 image with density slice (high ratio values shown in red); e) histogram for Landsat 5's 2/4 image; f) Landsat 5's ratio 2/4 image.

The last successful self-proposed ratio to discriminate Li-mineralizations, based mainly in the lepidolite spectral curve, is 4/7 for Landsat 8 (Figure 36-a, -b,-c), 3/7 for Landsat 5 (Figure 36-d, -e, -f) and 4/12 for Sentinel-2 (Appendix C).

A color density slice version of band ratio 4/7 for Landsat 8 (Figure 36-c) is shown in Figure 36-a, with the respective color assignments shown in the histogram of Figure 36-b. Yellow and red areas correspond to the highest surface reflectance values (yellow ≈ 0.81; red ≥ 0.99) and therefore should indicate altered rocks.

Figure 36-d is a color density slice version of Landsat 5's 3/7 band ratio (Figure 36-f). The color intervals of the density slice image were attributed based on the histogram of Figure 36-e. Yellow and red areas correspond to the highest surface reflectance values (yellow ≈ 0.78; red ≥ 0.91).

In the three sensors, there is a clear compositional difference between the granites and metasediments from the CXG: granitoid rocks present a lower reflectance. Burned areas present the reflectance even when compared with the granites.

In the Landsat 5 images there is no high reflectance in Bajoca or Alberto mines. However, in Landsat 8 and Sentinel-2, these areas as well as the Feli open-pit mine present very high reflectance as proven by the red color in the density slice images. These temporal differences are the prove that this band ratio is sensible to spectral signature of Li-bearing rocks.

Landsat 8
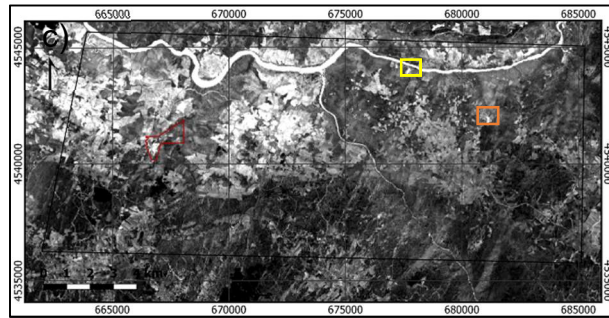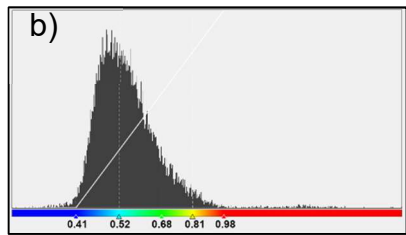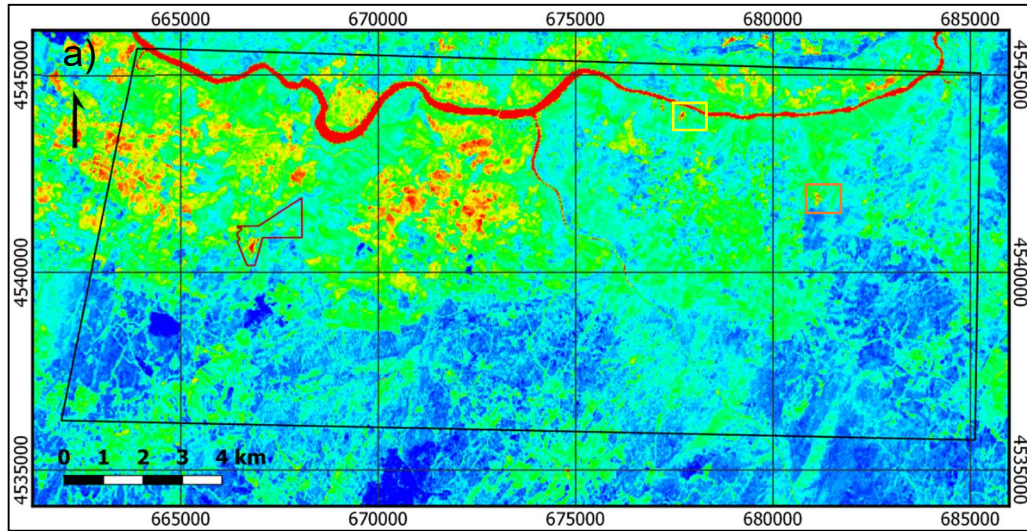
Landsat 5
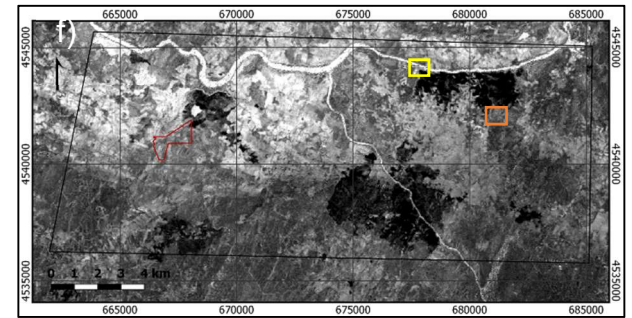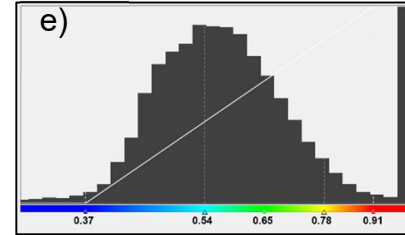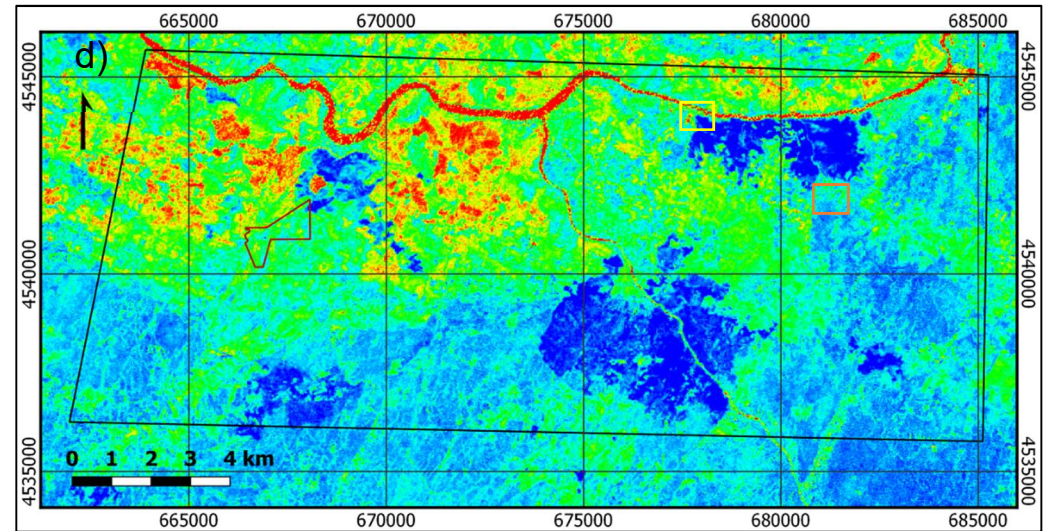
Figure 36 – Band ratios capable of detecting Li-mineralizations: a) Landsat 8's ratio 4/7 image with density slice (high ratio values shown in red); b) histogram for Landsat 8's 4/7 image; c) Landsat 8's ratio 4/7 image; d) Landsat 5's ratio 3/7 image with density slice (high ratio values shown in red); e) histogram for Landsat 5's 3/7 image; f) Landsat 5's ratio 3/7 image.

6.3 Principal Component analysis (PCA)

The principal component analysis (PCA) was firstly applied to all visible, NIR and SWIR bands of each sensor. This means it was applied to 9 bands in the ASTER's case (Table 11), and to 6 bands in the case of Landsat 8 (Table 12), Landsat 5 (Table 13) and Sentinel-2 images (Table 14). The result of this method was, respectively 9 and 6 uncorrelated PC bands (Appendix D1). The output is also a set of image statistics – eigenvalues and eigenvector loadings – in table format.

The magnitude and sign (positive or negative) of the eigenvectors depend on which spectral properties of vegetation, rocks, and soils are responsible for the statistical variance mapped into each principal component (PC) (Loughlin, 1991).

The eigenvalues give an indication of decreasing variance in successive PCs (Loughlin, 1991). To aid in the eigenvalue interpretation, they can be expressed in percentage (accounted variance).

For ASTER, the PC1 (Table 11) accounts for 95.401% of the total variance of the raw data and is composed by a positive weighting of all 9 bands. According to Loughlin (1991), the strong correlation between the different image channels is due the overall scene brightness or albedo and is therefore mapped in PC1.

The eigenvector loadings of PC2 (Table 11) indicate that this PC describes the difference between VNIR (bands 1 to 3) and SWIR (4 to 9). The materials with high reflectance in VNIR appear in bright pixels in PC2 due the positive eigenvector loadings. PC3 eigenvector loadings (Table 11) demonstrate that it is dominated by vegetation due to the high loading in band 3: the positive sign indicates that vegetation is mapped in bright pixels.

Because the eigenvector loadings for band 1 and band 2 in PC6 of Table 11 are opposite in sign and present high magnitude, we can predict that ferric iron is mapped in dark pixels in PC6 (negative eigenvector loadings of band 2).

PC can be arranged in RGB combinations as showed in Figure 37. In this combination PC6, PC2 and PC5 were inserted in the Red, Green and Blue channels (respectively).

Table 11 – PCA on 9 ASTER bands: Eigenvector and eigenvalues matrix.

	PC1	PC2	PC3	PC4	PC5	PC6	PC7	PC8	PC9
Band 1	0.40410	0.48038	-0.13540	0.02788	-0.16963	0.71364	0.13855	0.14196	0.09713
Band 2	0.37943	0.48402	-0.49374	-0.11106	0.27024	-0.51704	-0.09303	-0.09292	-0.08942
Band 3	0.35947	0.30941	0.79550	0.26570	-0.02174	-0.25176	-0.07251	-0.04980	-0.00512
Band 4	0.40101	-0.36282	0.16979	-0.36081	0.68435	0.15703	0.15641	0.09168	0.15058
Band 5	0.30266	-0.20939	0.00190	-0.29708	-0.31544	0.10337	-0.17599	-0.79635	-0.03103
Band 6	0.32238	-0.20325	0.01663	-0.42902	-0.56465	-0.29034	0.18961	0.48074	-0.01568
Band 7	0.28389	-0.29901	-0.17419	0.55260	-0.02667	-0.06848	0.61006	-0.14107	-0.31116
Band 8	0.26901	-0.28275	-0.20610	0.42999	-0.09314	-0.08322	-0.35402	0.09327	0.68606
Band 9	0.23286	-0.23040	-0.05600	0.15342	0.04087	0.16954	-0.61481	0.25778	-0.62543
Eigenvalues	13547.88	418.0773	122.4712	50.30109	24.89371	15.91865	9.334749	7.312073	4.819969
Accounted variance	**95.40083**	**2.943998**	**0.862412**	**0.354208**	**0.175295**	**0.112095**	**0.065733**	**0.05149**	**0.033941**
Cumulative variance	95.40083	98.34483	99.20724	99.56145	99.73674	99.84884	99.91457	99.96606	100

In Figure 37, red areas, mainly represented by burned areas, correspond to the highest content of ferric iron; the granites appear in a pinkish color (which indicates that ferric oxide is present but mixed with other elements) and are distinct from the metasediments which appear in yellow to yellowish green color. Urbanized areas and agricultural fields present mainly blue color. The aplite-pegmatite vein of Bajoca mine appears in white, while Feli and Alberto mines show a white to pinkish white color.

Legend

☐ (red) Bajoca mining concession ☐ (black) Studied area ☐ (yellow) Feli mine ☐ (orange) Alberto mine
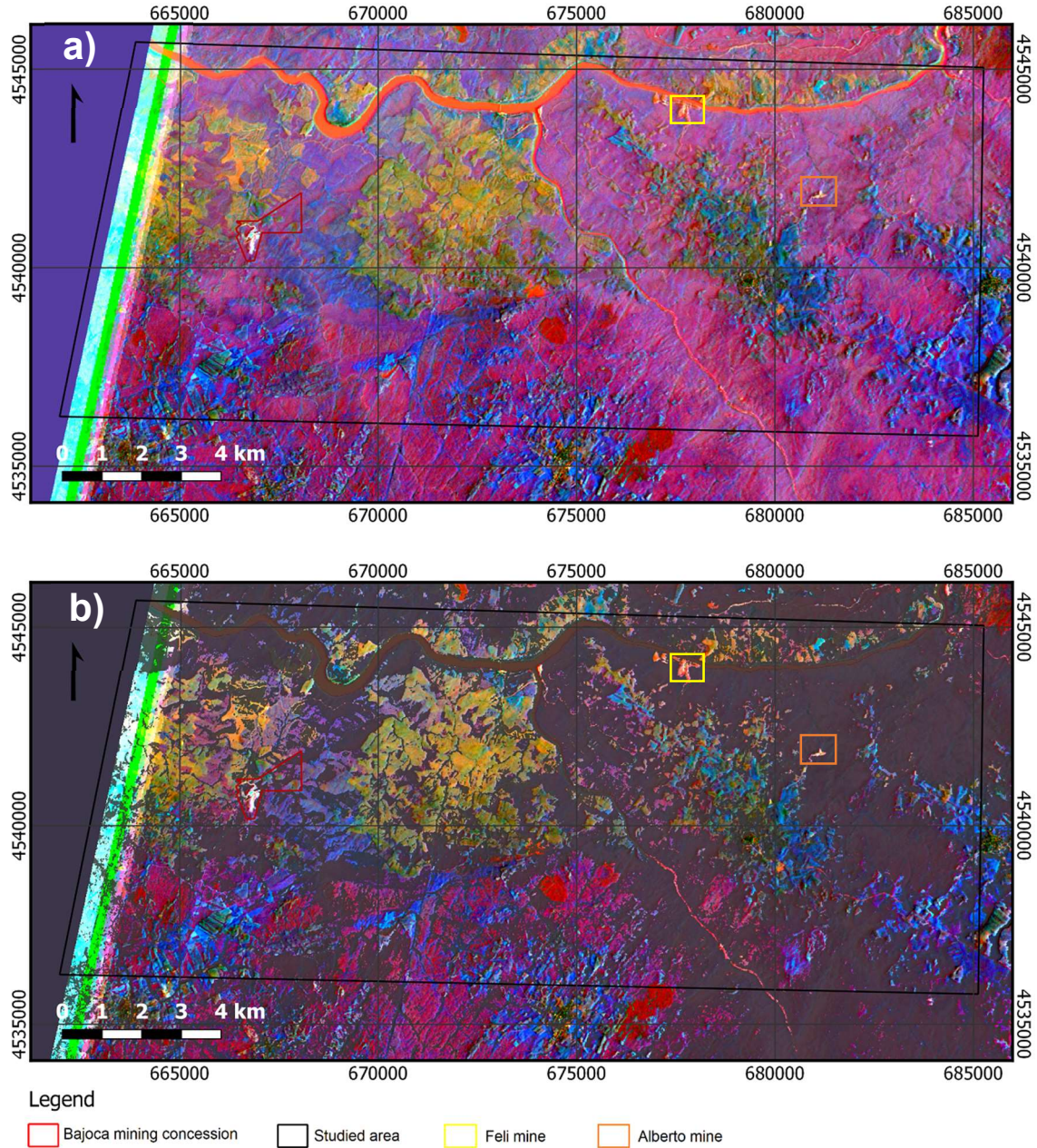
Figure 37 – RGB combination of ASTER's PC 6, 2 and 5: a) with no mask; b) with a water vegetation mask. Red areas, mainly represented by burned areas, correspond to the highest content of ferric iron. The granites (pinkish color) are differentiated from the metasediments (yellow to yellowish green color). Urbanized areas and agricultural fields present mainly blue color. The aplite-pegmatite vein of Bajoca mine appears in white, while Feli and Alberto mines show a white to pinkish white color

For Landsat 8, the PC1 (Table 12) accounts for 97.180% of the total variance of the raw data, is composed by a negative weighting of all 6 bands and mainly represents the albedo.

Table 12 – PCA on 6 Landsat 8 (OLI) bands: Eigenvector and eigenvalues matrix.

	PC1	PC2	PC3	PC4	PC5	PC6
Band 2	-0.31190	0.23866	0.52849	-0.59964	-0.11383	0.44039
Band 3	-0.31050	0.15151	0.43704	0.00879	-0.05447	-0.82860
Band 4	-0.33423	-0.05951	0.37349	0.76580	-0.21770	0.33379
Band 5	-0.49225	0.69425	-0.49966	0.09921	0.12057	0.04099
Band 6	-0.54152	-0.53284	-0.37100	-0.20914	-0.48766	-0.06035
Band 7	-0.39880	-0.38814	0.05390	-0.01814	0.82725	0.05233
Eigenvalues	194964001	4288560	1045337	216085.3	102449.3	5836.951
Accounted variance	**97.179641**	**2.137629**	**0.521048**	**0.107708**	**0.051066**	**0.002909**
Cumulative variance	97.179641	99.31727	99.83832	99.94602	99.99709	100

The eigenvector loadings of PC2 (Table 12) indicate that this PC maps vegetated areas in bright pixels due to the high loading in band 5 (which coincides with the NIR reflectance peak of vegetation). PC2 accounts for 2.138% of the total variability.

Because the eigenvector loadings for band 2 and band 4 in PC4 of Table 12 are opposite in sign and present high magnitude, we can predict that iron oxides are mapped in bright pixels in PC4 due positive eigenvector loadings of band 4.

Hydroxyl-bearing minerals are mapped as dark pixels in PC5 due to the fact that the negative contribution from band 6 and positive from band 7 (Table 12).

For Landsat 5, PC1 (Table 13) is composed by a negative weighting of all 6 bands, accounts for 92.591% of the total variance of the raw data and mainly represents the albedo.

Table 13 – PCA on 6 Landsat 5 (TM) bands: Eigenvector and eigenvalues matrix.

	PC1	PC2	PC3	PC4	PC5	PC6
Band 1	-0.44631	-0.63796	0.39391	-0.44958	0.03077	-0.18864
Band 2	-0.23296	-0.23503	0.14561	0.32022	-0.16466	0.86002
Band 3	-0.28724	-0.10087	0.15904	0.74314	-0.32752	-0.47170
Band 4	-0.34744	-0.32070	-0.85256	0.07851	0.20660	-0.02708
Band 5	-0.65652	0.59358	-0.06961	-0.29121	-0.35447	0.03673
Band 7	-0.33510	0.26910	0.25814	0.22831	0.83447	0.01383
Eigenvalues	6827.62	356.585	103.632	60.5107	20.0538	5.57522
Accounted variance	**92.5907**	**4.83572**	**1.40537**	**0.8206**	**0.27195**	**0.07561**
Cumulative variance	92.5907	97.4265	98.8318	99.6524	99.9244	100

The eigenvector loadings of PC2 (Table 13) indicate that this PC describes the difference between VNIR (bands 1 to 4) and SWIR (5 and 7). The materials with high reflectance in SWIR appear in bright pixels in PC2 due the positive eigenvector loadings. PC2 accounts for 4.836% of the total variability. PC3 eigenvector loadings (Table 13) indicate that the PC3 enhances vegetation in dark pixels because of the high negative loading in band 4.

Opposite sign and high magnitude of the eigenvector loadings of band 1 and band 3 in PC4 of Table 13 indicate that iron oxides are mapped in bright pixels in PC4 due to positive eigenvector loadings of band 3.

Hydroxyl-bearing minerals are mapped as dark pixels in PC5 because of the negative contribution from band 5 and positive from band 7 (Table 13).

For Sentinel-2, PC1 (Table 14) is composed by a negative weighting of all 6 bands, accounts for 97.948% of the total variance of the raw data and mainly represents the albedo.

Table 14 – PCA on 6 Sentinel-2 bands: Eigenvector and eigenvalues matrix.

	PC1	PC2	PC3	PC4	PC5	PC6
Band 2	-0.29133	-0.29522	0.50909	-0.58679	-0.19965	0.42966
Band 3	-0.26729	-0.19670	0.42034	-0.03638	0.04668	-0.84242
Band 4	-0.28775	0.01106	0.45491	0.59213	0.50814	0.31829
Band 8	-0.45686	-0.68651	-0.46335	0.26831	-0.17468	0.05279
Band 11	-0.61706	0.39385	-0.36241	-0.38013	0.43236	-0.03663
Band 12	-0.41400	0.49761	0.10568	0.29536	-0.69448	0.01666
Eigenvalues	14738871	220496.6	52282.12	24740.67	10711.67	516.6703
Accounted variance	**97.9482**	**1.4653**	**0.3474**	**0.1644**	**0.0712**	**0.0034**
Cumulative variance	97.9482	99.4135	99.761	99.9254	99.9966	100

The eigenvector loadings of PC2 (Table 14) indicate that the PC2 enhances vegetation in dark pixels because of the high negative loading in band 8.

Opposite sign and high magnitude of the eigenvector loadings of band 2 and band 4 in PC4 of Table 14 indicate that iron oxides are mapped in bright pixels in PC4 (Figure 38). Similarly, hydroxyl-bearing minerals are mapped in bright pixels on PC5 since the contribution from band 11 is positive and from band 12 is negative (Table 14).
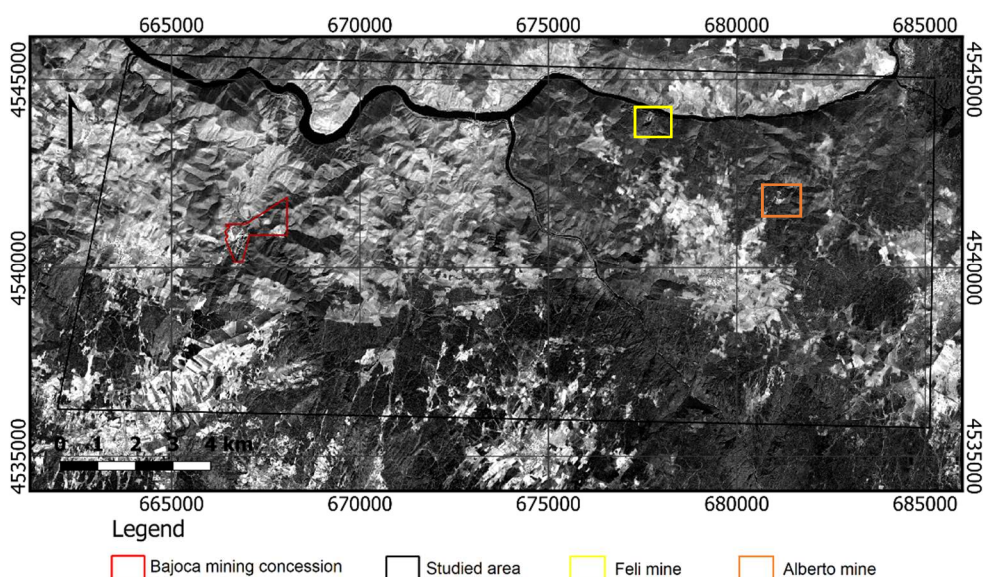
Figure 38 – PC4 of six-band PCA on Sentinel-2 highlighting iron oxides in bright pixels. Iron oxides are mapped in higher quantity in Bajoca and Alberto mines when compared with Feli mine.

In all cases, the first three PC explain most of the image variability and, when combined in a RGB combination, they can be useful for lithological mapping. RGB combination PC3-PC2-PC1 shows the best lithological contrast in Landsat 5 (Figure 39-a, -b) and Sentinel-2 (Figure 39-c, -d). The granites are mapped in green color while the metasediments appear in purple or pink color. Burned areas are characterized by a whitish tint. Although the known Li-mineralized areas are not clearly differentiated from the host rocks, they present a distinct signal (materialized in red, orange or pink color) that is not present in the Bajoca and Alberto mines in the Landsat 5 images (Figure 39-a, -b).

Other combinations were also tested. RGB combination containing PC4, PC5 and PC1 for Landsat 8 (Figure 40-a, -b) and Landsat 5 (Figure 40-c, -d) discriminates the metasediments in pink color and vegetated areas and water bodies in blue color. Burned areas appear in greenish bright spots. This combination is also very sensitive to the urbanized and agricultural areas which area mapped in several different colors. Iron oxides are discriminated in red and are present in all three open-pits in the Landsat 8 images. In the Landsat 5 images, only Feli mine shows the presence of iron oxides.
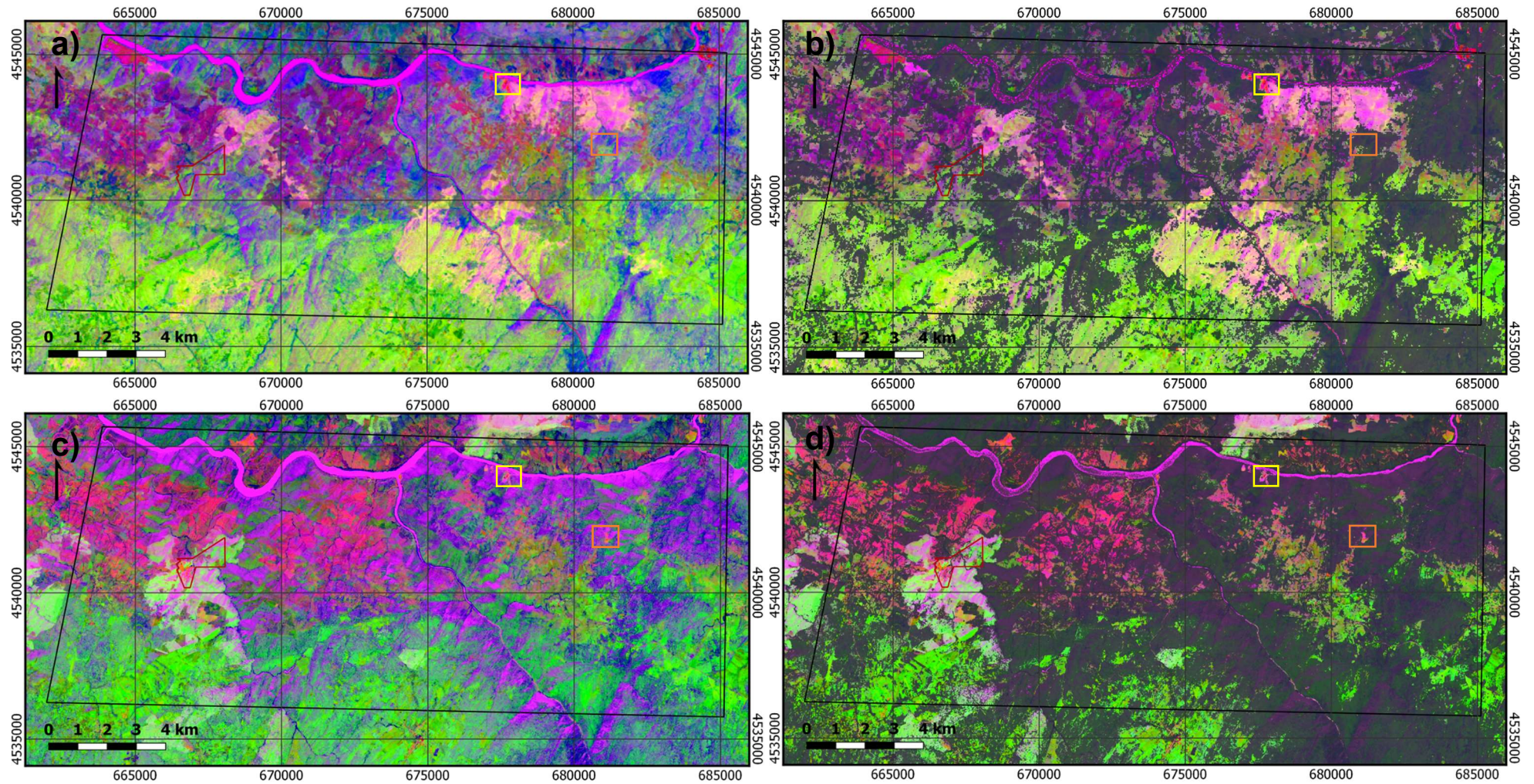
Figure 39 – RGB combination of PC 3, 2 and 1: a) for Landsat 5 with no mask; b) for Landsat 5 with a water vegetation mask; c) for Sentinel-2 with no mask; d) for Sentinel-2 with a water and vegetation mask. The granites (green color) are clearly differentiated from the metasediments (purple or pink color). Burned areas are characterized by a whitish tint. The known Li-mineralizations appear materialized in red, orange or pink color, except for the Bajoca and Alberto mines in Landsat 5 (a and b).
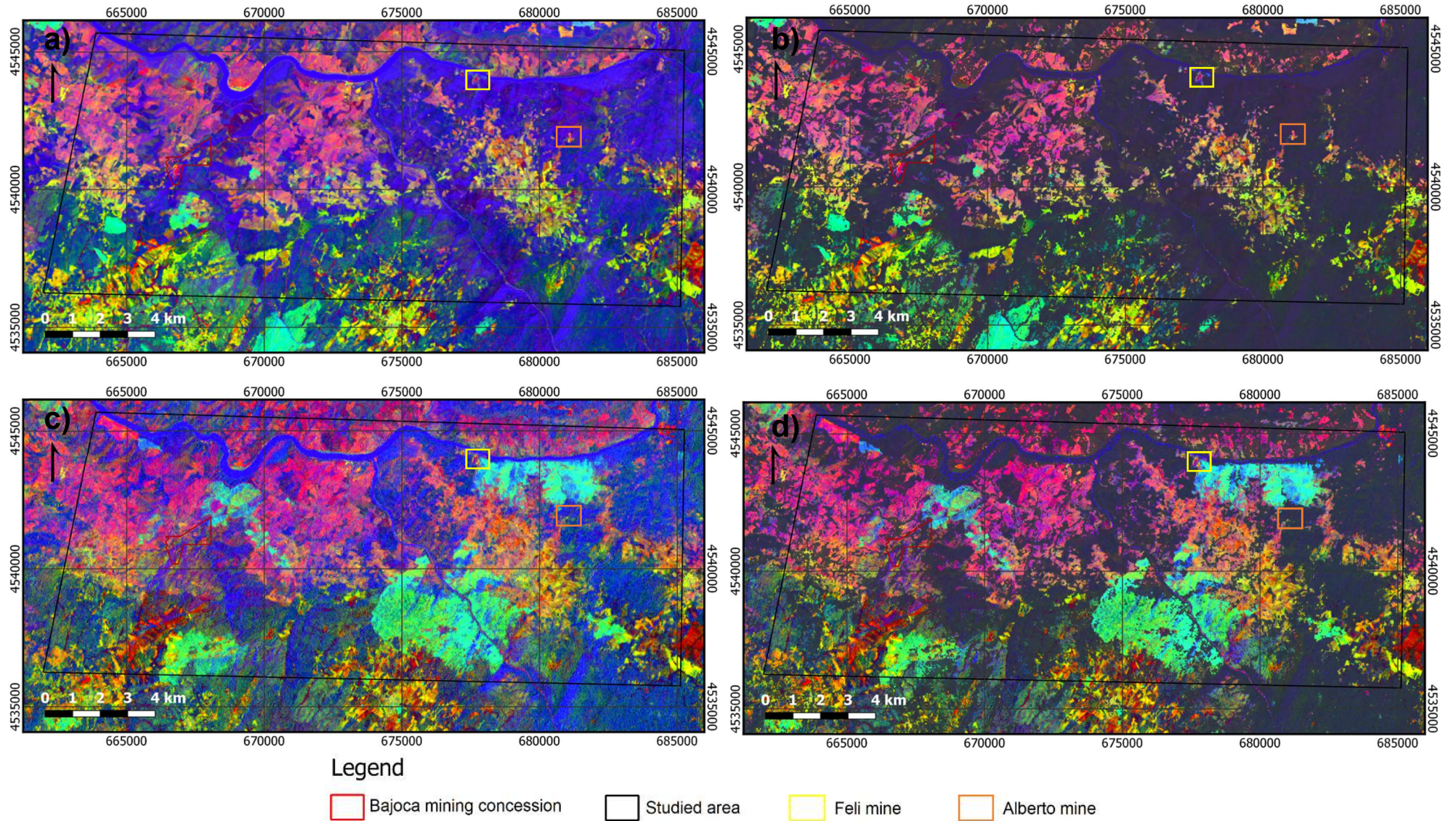
Figure 40 – RGB combination of PC 4, 5 and 1: a) for Landsat 8 with no mask; b) for Landsat 8 with a water vegetation mask; c) for Landsat 5 with no mask; d) for Landsat 5 with a water and vegetation mask. Red areas correspond to the highest content of iron oxides. The metasediments appear in pink color, vegetated areas and water bodies in blue color and burned areas appear in greenish bright spots. No sign of iron oxides is visible in the Bajoca and Alberto mines before their opening (c and d).

In order to try to isolate target spectral signatures, PCA was applied to selected subsets of the satellites' bands. This is the base of the "Crosta technique" (Loughlin, 1991).

In the ASTER's case, the four subsets proposed by Crosta *et al*. (2003) in an adaptation of the "Crosta technique", were used to map the following alteration minerals: alunite, illite and muscovite, kaolinite and smectite, and kaolinite, respectively.

Following the reasoning process described for the PCA of VNIR and SWIR bands, we can predict that PC1 (Table 15) maps mainly the albedo and that PC2 describes the contrast between the visible and the SWIR. To determine which PC maps alunite, we need to examine the eigenvector loadings for bands 5 and 7, in both of PC3 and PC4: the PC that has a moderate or strong loading from both bands, with opposite signs is the one that maps alunite. In this case, PC4 maps alunite in bright pixels (Figure 41-a). PC3 is brightest for vegetation.

Table 15 – PCA for alunite mapping (ASTER): Eigenvector and eigenvalues matrix.

	PC1	PC2	PC3	PC4
Band 1	-0.59661	-0.41752	-0.6835	0.050736
Band 3	-0.53339	-0.42121	0.728957	0.081806
Band 5	-0.43797	0.471264	0.037655	-0.76464
Band 7	-0.40956	0.652815	0.006021	**0.637224**
Eigenvalues	6335.479	186.9639	69.64581	24.79689
Accounted variance	95.74714	2.825558	1.052547	0.374752
Cumulative variance	95.74714	98.5727	99.62525	100

In the same way, PC1 presented in Table 16 maps mainly the albedo. PC2 describes the contrast between the visible and the SWIR. Moderate to strong loadings from both bands 5 and 6, with opposite signs indicate that PC4 maps illite and muscovite in dark pixels. Negating PC4 maps these minerals in bright colors (Figure 41-b).

Table 16 – PCA for illite and muscovite mapping (ASTER): Eigenvector and eigenvalues matrix.

	PC1	PC2	PC3	PC4
Band 1	-0.58161	-0.45337	-0.67534	0.010168
Band 3	-0.52029	-0.43093	0.737204	-0.01114
Band 5	-0.42764	0.533609	-0.00092	**-0.72965**
Band 6	-0.45624	0.569223	0.021079	**0.683657**
Eigenvalues	6661.963	169.7329	69.73961	8.849987
Accounted variance	96.40648	2.456235	1.009215	0.12807
Cumulative variance	96.40648	98.86272	99.87193	100

PC1 showed in Table 17 maps mainly the albedo and PC2 describes the contrast between the visible and the SWIR. Moderate to strong loadings from both bands 4 and 9, with opposite signs indicate that PC4 maps kaolinite and smectite in dark pixels. Negating PC4 maps these minerals in bright colors (Figure 41-c).

Table 17 – PCA for kaolinite and smectite mapping (ASTER): Eigenvector and eigenvalues matrix.

	PC1	PC2	PC3	PC4
Band 1	-0.57805	-0.80985	0.099964	-0.00297
Band 4	-0.57989	0.476963	0.497899	**-0.43397**
Band 6	-0.46551	0.227828	-0.84914	-0.1018
Band 9	-0.33598	0.254454	0.14515	**0.895153**
Eigenvalues	6548.282	201.167	22.57846	15.05072
Accounted variance	96.48161	2.963971	0.332668	0.221755
Cumulative variance	96.48161	99.44558	99.77824	100

Equally, PC1 presented in Table 18 maps mainly the albedo and PC2 describes the contrast between the visible and the SWIR. Kaolinite is mapped in PC4 due to moderate to strong loadings from both bands 4 and 6, with opposite signs (Figure 41-d).

Table 18 – PCA for kaolinite mapping (ASTER): Eigenvector and eigenvalues matrix.

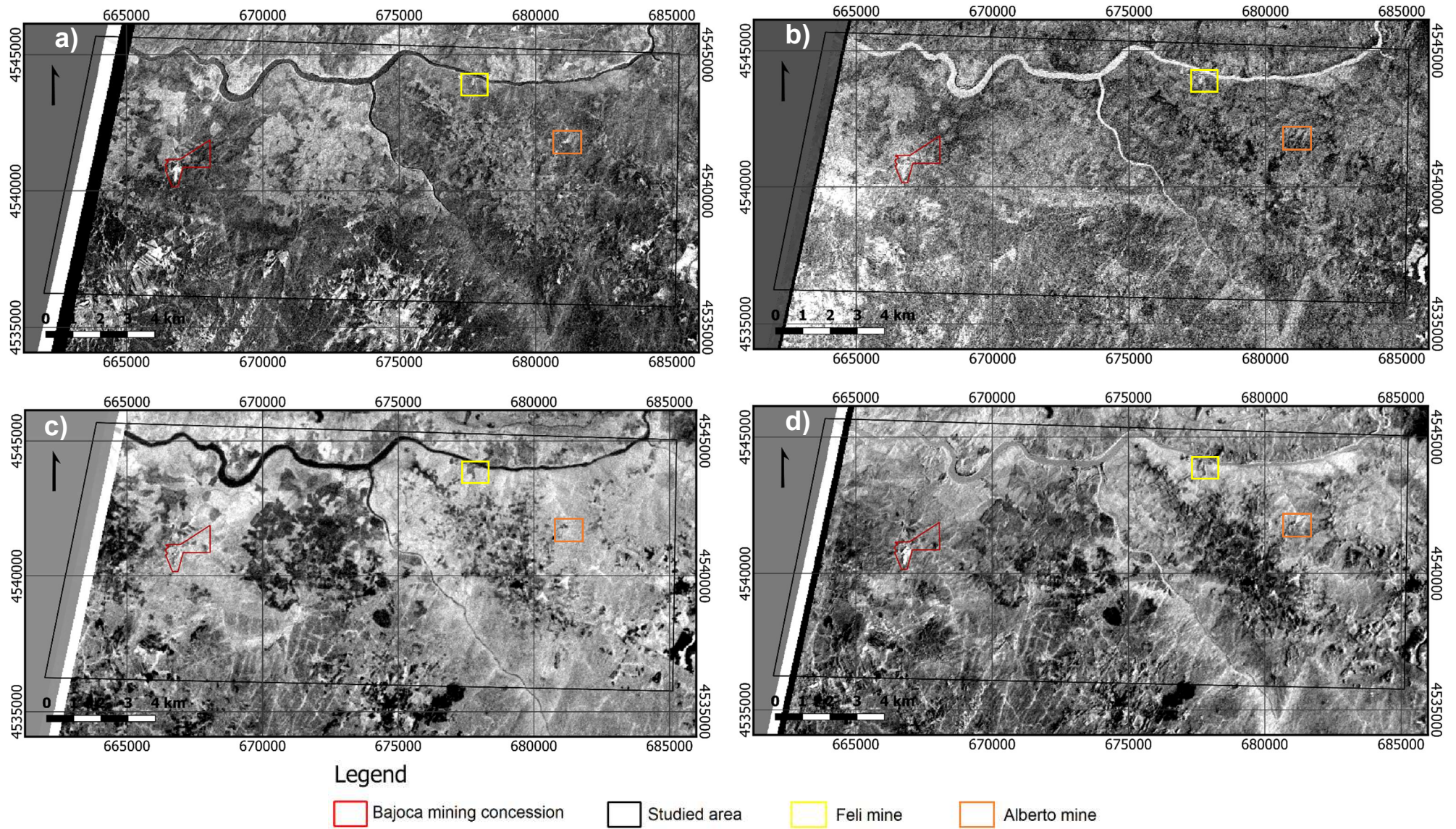|	PC1	PC2	PC3	PC4
Band 1	-0.56184	-0.82021	0.046885	0.096896
Band 4	-0.5649	0.4324	-0.39966	**0.578095**
Band 6	-0.45335	0.196791	-0.31713	**-0.80943**
Band 7	-0.39963	0.318681	0.858779	-0.03516
Eigenvalues	6905.74	208.1374	38.54643	22.35819
Accounted variance	96.25017	2.900957	0.537249	0.311622
Cumulative variance	96.25017	99.15113	99.68838	100

Figure 41 – Alunite (a), Illite and muscovite (b), kaolinite and smectite (c), kaolinite (d) images where the respective minerals appear in bright pixels. The Bajoca mine presents a strong signal for alunite and kaolinite. The three open-pits present a low response to the kaolinite and smectite subset.

For Landsat 8, Landsat 5 and Sentinel-2 two approaches were used: (i) the application or adaptation of the "Crosta technique" in which the PCA is applied to a subset of four bands; (ii) the application or adaption of the technique proposed by Chavez & Kwarteng (1989) where PCA is applied to a subset of two bands.

Each one of these methods was applied to the three sensors in order to map ferric iron, hydroxyl bearing minerals and lithium bearing minerals.

In the four-band subset, the process is similar to the described before: PC1 showed in Table 19 (Landsat 5) maps the albedo; PC2 describes the difference between VNIR and SWIR; examining the eigenvector loadings for bands 1 and 3, in both of PC3 and PC4, we can predict that ferric iron is mapped in PC4 due to moderate to strong loadings from both bands, with opposite signs. Because of the positive loading of band 3 in PC4, ferric iron appears in bright pixels.

The same principles were applied to Landsat 8 and Sentinel-2, and in both cases PC4 is the PC that maps ferric iron. The correspondent eigenvector and eigenvalues matrices are presented in Appendix D2.

Table 19 – PCA for ferric iron mapping (four Landsat 5 bands): Eigenvector and eigenvalues matrix.

	PC1	PC2	PC3	PC4
Band 1	-0.48986	-0.67048	-0.48455	**-0.27513**
Band 3	-0.31328	-0.09211	-0.09008	**0.940882**
Band 4	-0.38276	-0.31475	0.865298	-0.07542
Band 5	-0.7179	0.665511	-0.0914	-0.18263
Eigen values	5696.117	312.7069	95.71014	49.59516
Accounted variance	92.55764	5.081253	1.555218	0.805884
Cumulative variance	92.55764	97.6389	99.19412	100

In the case of the two-band subset, the process is even simpler: the target spectral information is usually mapped in PC2, and the examination of the eigenvector sign allows to find if the target information is mapped in bright or dark pixels. Table 20 presents the eigenvector and eigenvalues matrix for Landsat 8 and based on the analysis of the eigenvalues we can predict that ferric iron is mapped in bright pixels in PC2 (Figure 42-a).

Table 20 – PCA for ferric iron mapping (two Landsat 8 bands): Eigenvector and eigenvalues matrix.

	PC1	PC2
Band 2	0.685208	**-0.72835**
Band 4	0.728348	**0.685208**
Eigenvalues	41239207	415821
Accounted variance	99.00175	0.998249
Cumulative variance	99.00175	100

The correspondent matrices for Landsat 5 and Sentinel-2 are presented in Appendix D2. For Landsat 5 to present ferric iron in bright pixels, it was necessary to negate PC2. The resultant images are shown in Figure 42. The image results from the four-band subset are presented in Appendix D2.

The two-band method appears to be more selective since fewer areas were discriminated with bright pixels. Both methods indicate that ferric iron is present in the Bajoca and Alberto mines except in Landsat 5 images (before the opening of the mines). Only the four-band subset appears to discriminate ferric iron in the Feli mine.

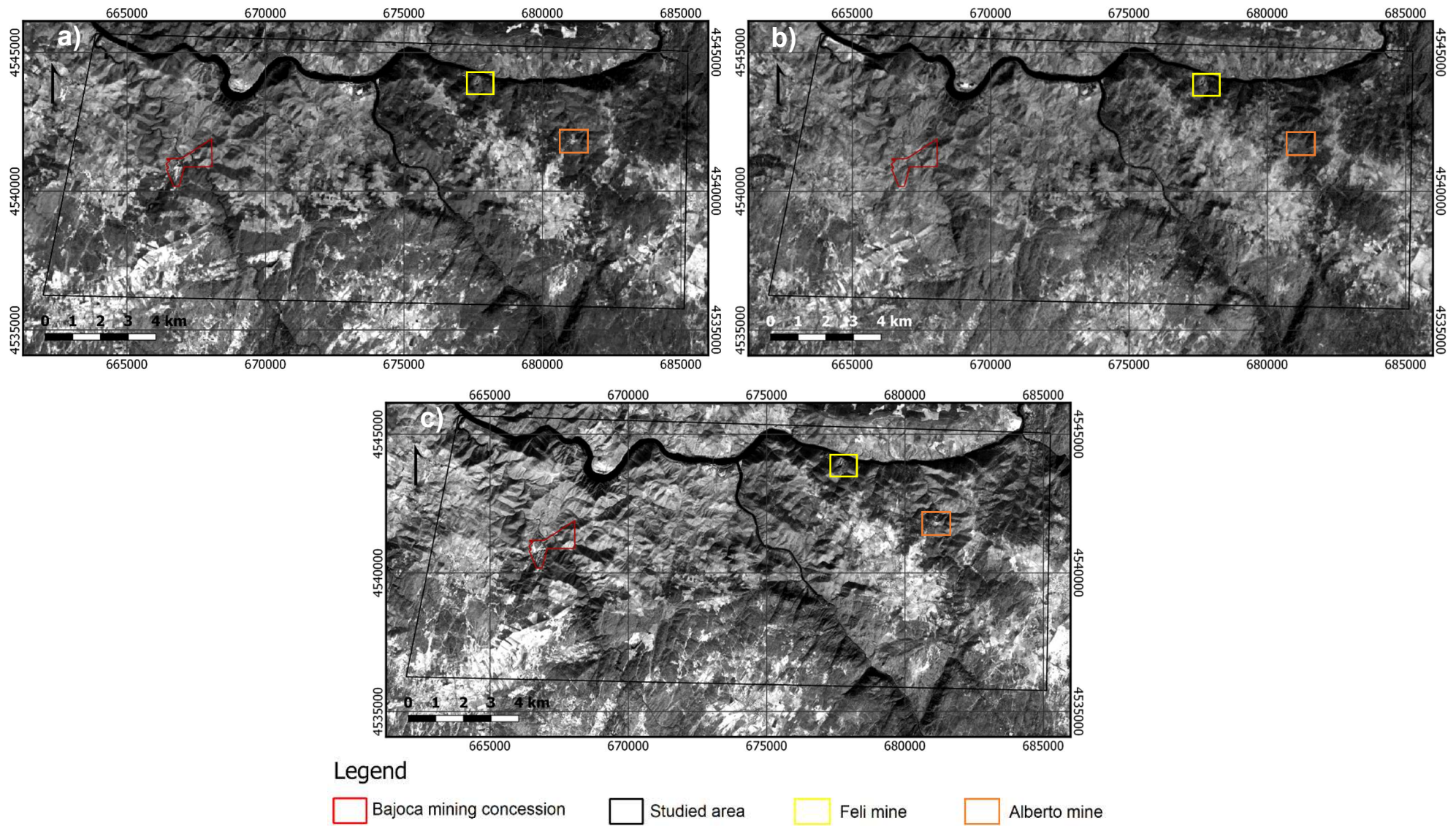# Ferric iron (selective PCA on 2 bands)

Figure 42 – Selective PCA on 2 bands to highlight ferric iron in bright pixels: a) PC2 from the Landsat 8 subset; b) negated PC2 from the Landsat 5 subset; c) PC2 from the Sentinel-2 subset. Feli mine presents a lower ferric iron content than Bajoca and Alberto mines. Before the opening of the Bajoca and Alberto mines (b), no sign of the presence ferric iron is visible.

In the four-band subset to discriminate hydroxyl bearing minerals, PC1 presented in Table 21 (Sentinel-2) maps the albedo; PC2 describes the difference between VNIR and SWIR; and PC4 maps hydroxyl minerals in bright pixels due to the positive loading from band 12 (Figure 43-c).

The same process was applied to Landsat 5 and 8, and in both cases PC4 is the one that maps hydroxyl minerals. The correspondent eigenvector and eigenvalues matrices are presented in Appendix D2.

Table 21 – PCA for hydroxyl mineral mapping (four Sentinel-2 bands): Eigenvector and eigenvalues matrix.

	PC1	PC2	PC3	PC4
Band 2	-0.31604	-0.3018	0.89371	-0.1016
Band 8	-0.49634	-0.73638	-0.39803	0.23011
Band 11	-0.67153	0.3596	-0.18657	**-0.62042**
Band 12	-0.45034	0.48718	0.08972	**0.74283**
Eigenvalues	713083.9	309200.6	66105.28	1739.112
Accounted variance	65.4128	28.36368	6.063988	0.159533
Cumulative variance	65.4128	93.77648	99.84047	100

In the case of the two-band subset, PC2 showed in Table 22 (Sentinel-2) maps hydroxyl minerals in dark pixels. The negation of PC2 shows these minerals in bright pixels. The correspondent matrices for Landsat 5 and 8 are presented in Appendix D2.

Table 22 – Principal component analysis for hydroxyl mineral mapping (two Sentinel-2 bands): Eigenvector and eigenvalues matrix.

	PC1	PC2
Band 11	0.82901	-0.55924
Band 12	0.55924	0.82901
Eigenvalues	8222452.878	24945.17472
Accounted variance	99.6975	0.3025
Cumulative variance	99.6975	100

The resultant images from the four-band subset are shown in Figure 43. The image results from the two-band subset are presented in Appendix D2. In Landsat 5, known mineralized areas do not show any distinct signal from the host rocks. For the other satellites, both methods indicate a very low to moderate in hydroxyl minerals in the open-pit areas.

Hydroxyl minerals (selective PCA on 4 bands)
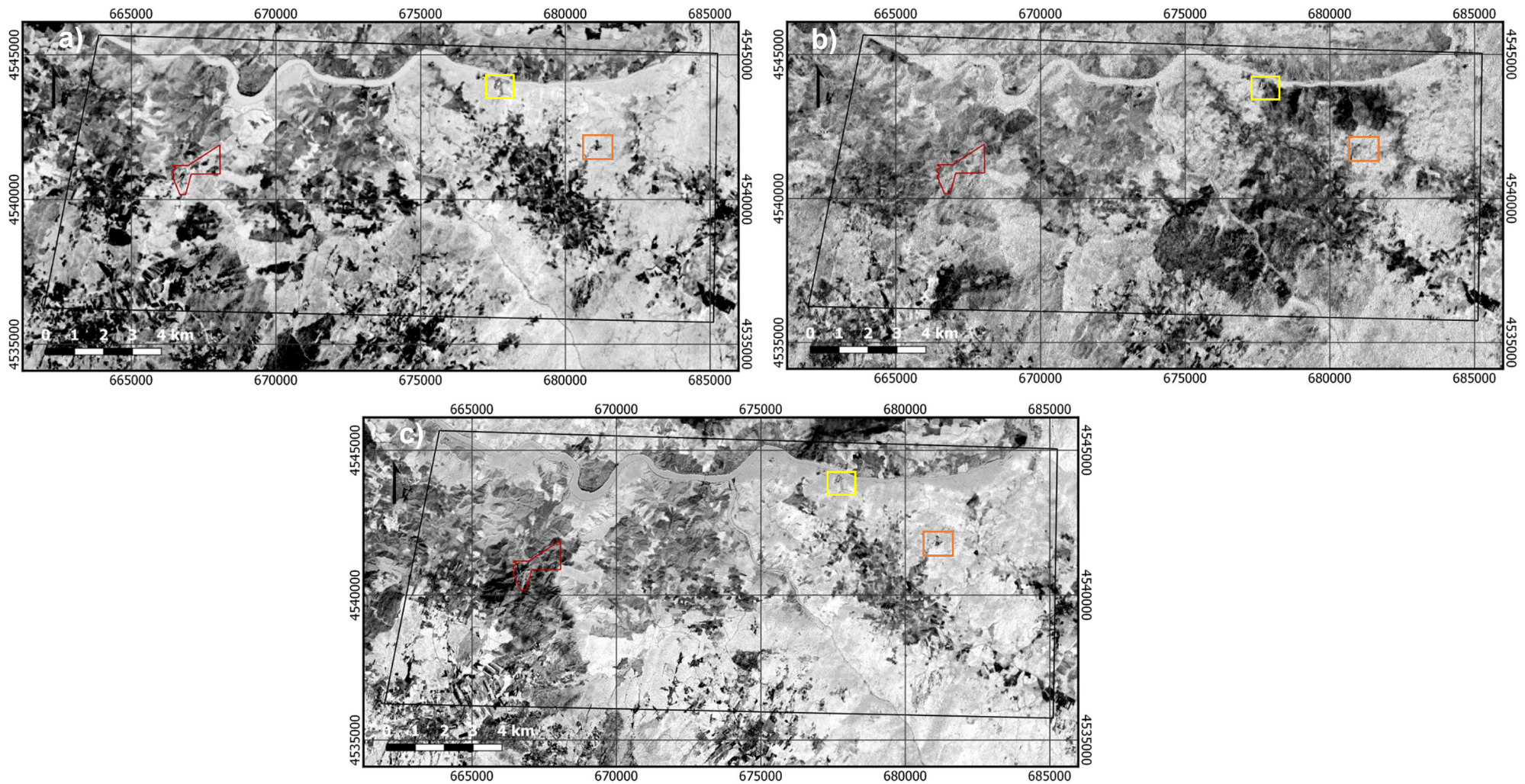
Figure 43 – Selective PCA on 4 bands to discriminate hydroxyl minerals in bright pixels: a) PC2 from the Landsat 8 subset; b) PC2 from the Landsat 5 subset; c) PC2 from the Sentinel-2 subset. Very to moderate content in hydroxyl minerals is visible in the known Li-bearing zones. Before the opening of the Bajoca and Alberto mines (b), no distinctive spectral response from the Li-bearing veins is observable.

To discriminate Li-bearing minerals an adaptation of the previously mentioned techniques was performed.

In the four-band subset, PC1 presented in Table 23 (ASTER) maps the albedo and PC4 maps Li-bearing in dark pixels due to the positive loading from band 3. The negation of PC4 shows the target minerals in bright pixels (Figure 44-d).

The correspondent eigenvector and eigenvalues matrices for Landsat 5/8 and Sentinel-2 are presented in Appendix D2. In all cases PC4 is the one that maps Li-bearing minerals. PC4 of Sentinel-2 was negated to show Li-minerals in bright pixels.

Table 23 – PCA for lithium mapping (four ASTER bands): Eigenvector and eigenvalues matrix.

	PC1	PC2	PC3	PC4
Band 1	-0.0328	0.193184	0.752713	-0.62851
Band 3	-0.02975	0.148778	0.609957	0.777774
Band 11	-0.62342	-0.76449	0.163905	-0.00615
Band 14	-0.78063	0.596744	-0.18577	0.001678
Eigenvalues	1833423	768.7164	515.5552	68.36881
Accounted variance	99.92628	0.041897	0.028099	0.003726
Cumulative variance	99.92628	99.96817	99.99627	100

In the case of the two-band subset, PC2 of Table 24 (ASTER) maps Li-bearing minerals in bright pixels. The correspondent matrices for Landsat 5/8 and Sentinel-2 are presented in Appendix D2. PC2 of Landsat 5 and 8 were negated to show Li-bearing minerals in bright pixels.

Table 24 – PCA for lithium mapping (two ASTER bands): Eigenvector and eigenvalues matrix.

	PC1	PC2
Band 1	-0.74511	**0.666944**
Band 3	-0.66694	**-0.74511**
Eigenvalues	4123.304	69.76079
Accounted variance	98.33628	1.663718
Cumulative variance	98.33628	100

The resultant images from the four-band subset are shown in Figure 44. The results from the two-band subset are presented in Appendix D2.

In the four-band subset, known mineralized areas in Landsat 5 (Figure 44-c) do not show any distinct signal from the host rocks. The two-band subset appears to be more sensitive the signature of Li-minerals because the Feli mine is highlighted in the correspondent Landsat 5 image.

For the other satellites, both methods discriminate correctly known Li -bearing areas in bright pixels.

Some urbanized/agricultural areas are also highlighted in bright pixels, which reinforces the need to exclude these areas from the image processing.

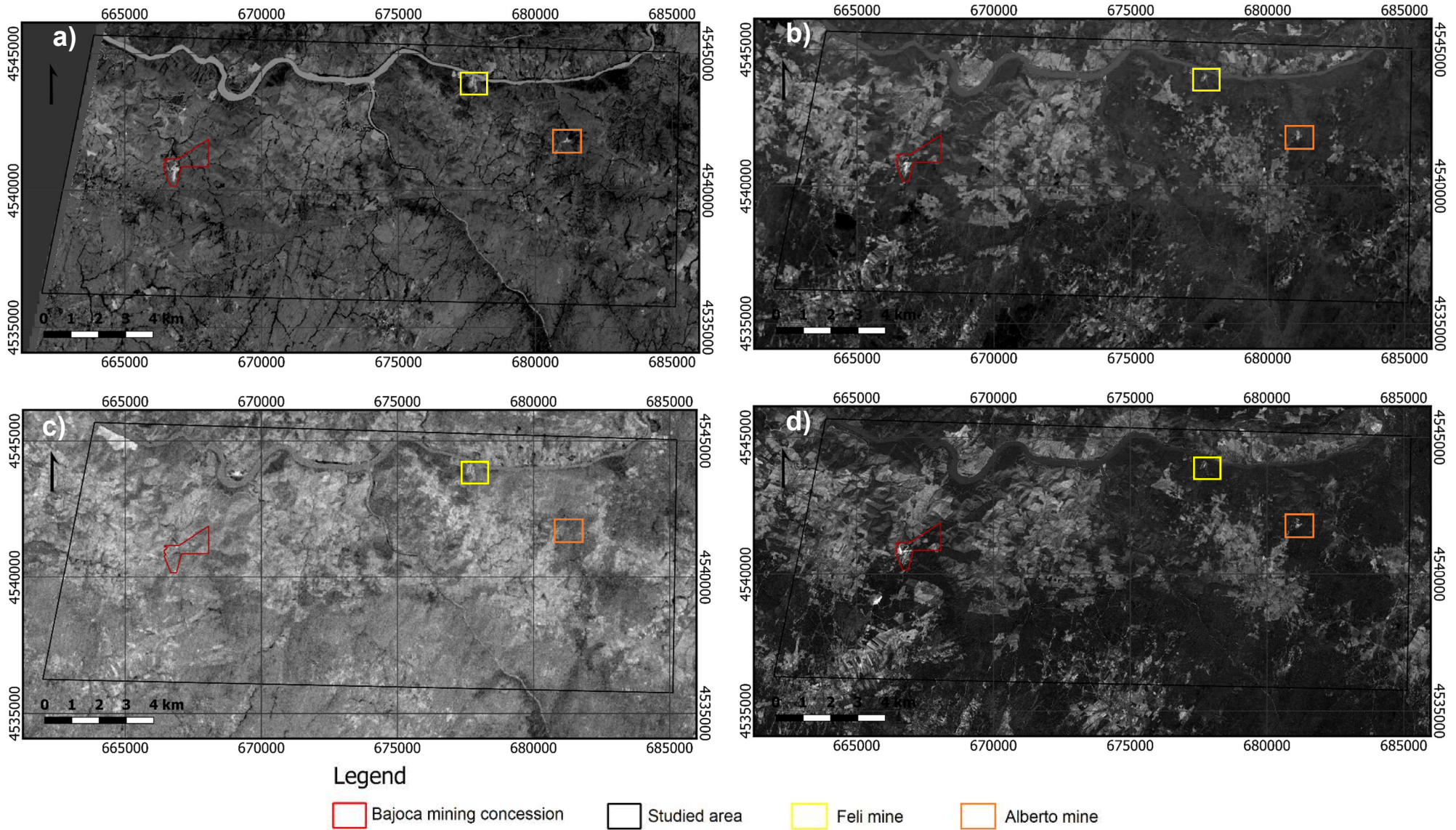# Li-bearing minerals (selective PCA on 4 bands)

Figure 44 – Selective PCA on 4 bands to Li-bearing minerals in bright pixels: a) negated PC4 from the ASTER subset; b) PC4 from the Landsat 8 subset; c) PC4 from the Landsat 5 subset; d) negated PC4 from the Sentinel-2 subset. Before the opening of the Bajoca and Alberto mines (b), there is no distinctive spectral response from the Li-bearing veins.

6.4 Lineament extraction

The application of four Prewitt filters on Sentinel-2 band 11 resulted in four edge enhanced grey-scale images. Although each filter was supposed to emphasize linear features in the respective directions, only the NE-SW filtered image allowed to identify geological faults, not only with an NE-SW trend, but also with other orientations.

The structural map was then constructed based on the manual extraction of approximately 150 lineaments from the NE-SW filtered band 11. The lineaments were then compared with the geological faults from the geological map at the scale 1:10,000 (Appendix A and E). The final results are presented in Figure 45 and Appendix E.
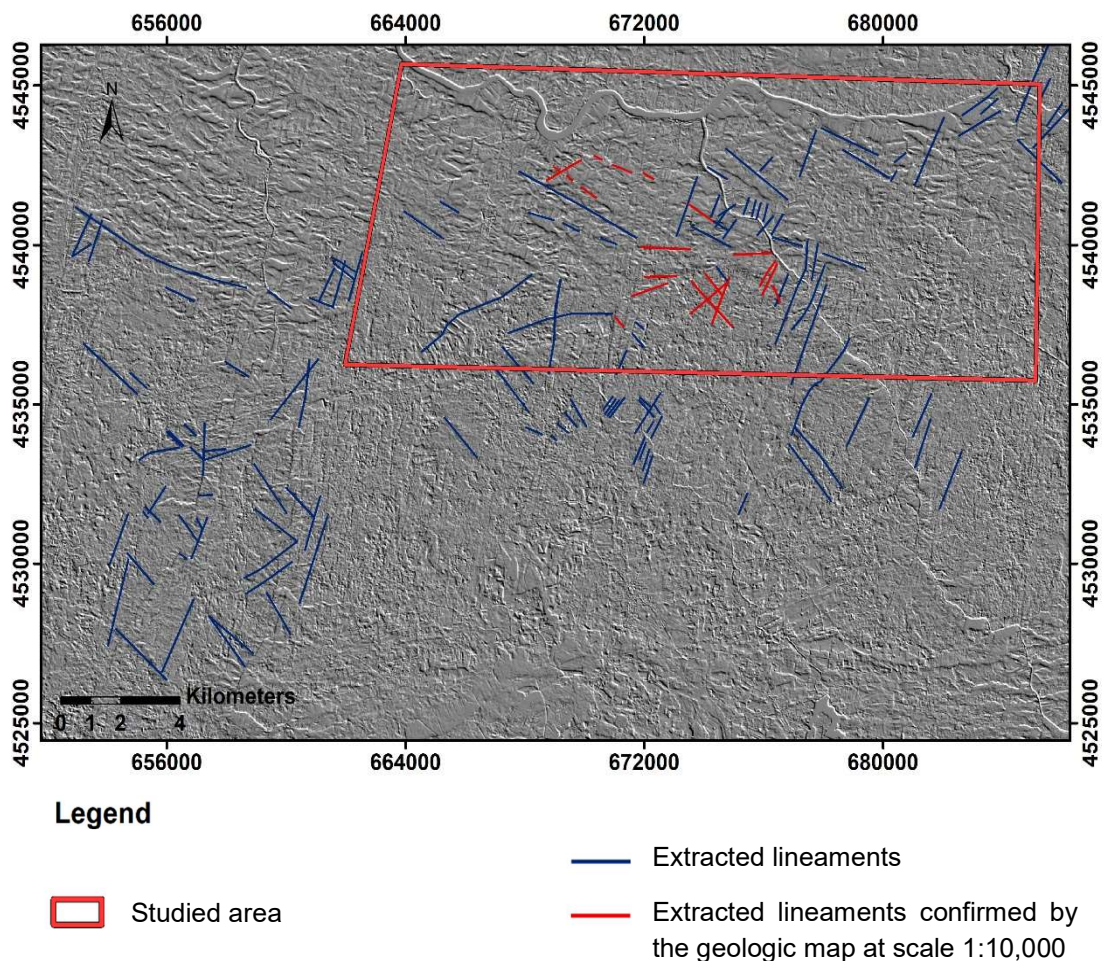

Figure 45 – Extracted lineaments over NE-SW filtered band 11 (Sentinel-2). Geological faults are mapped in red. Blue lines correspond to probable faults.

The mean direction of extracted lineaments was automatically computed in ArcMap, and then plotted in the rose diagram of Figure 46 to determine the predominant trends.
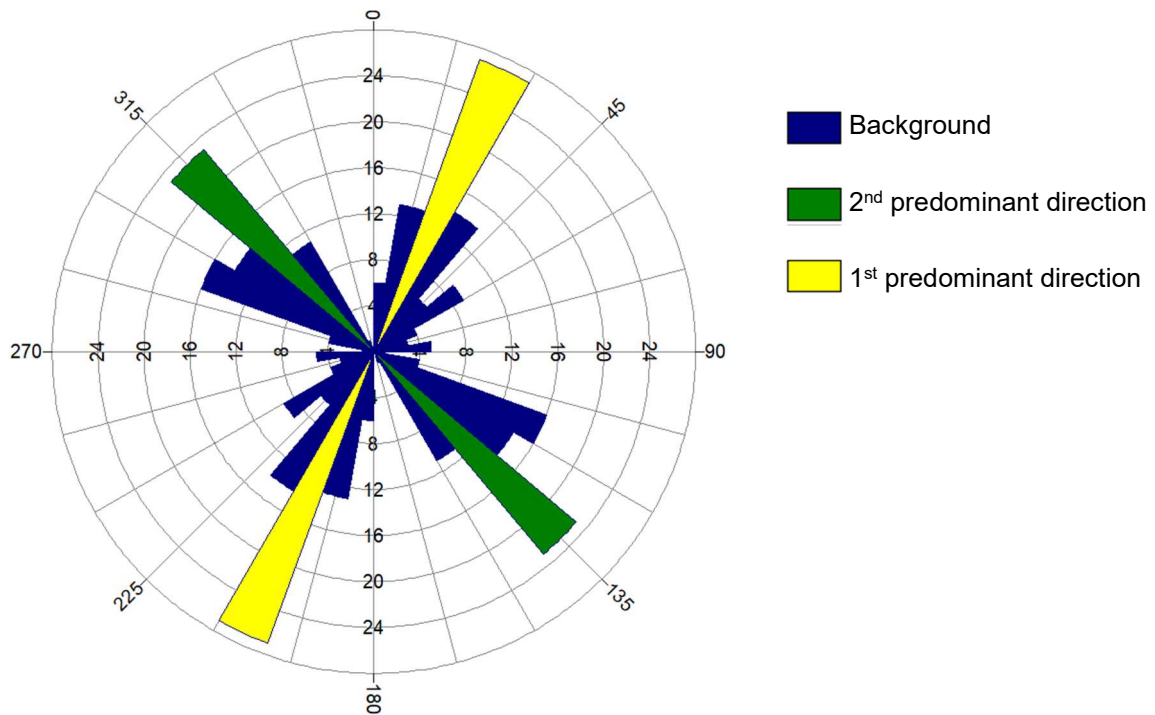
Figure 46 – Rose diagram where the trends of the extracted lineaments were plotted. Two main directions are visible: the first around N25°E, and the second, N135°E.

The lineaments can be grouped in two main classes: one NNE-SSW trending and the other NW-SE trending. A small group of lineaments with general orientation WSW-ENE is also visible. In addition, the comparison between the extracted lineaments and the geological map at the scale 1:10,000 also allowed to verify that the applied filter is not able to enhance all the existing faults.

To complete the structural map, the faults that were not identified in the filtered image were manually digitized. These faults along with the faults from the geological map at the scale 1:50,000 and the extracted lineaments were combined to create a structural map dropped over a simplified geological map (Figure 47).

Figure 47 – Structural map drapped over a simplified geological map. Geological base adapted from Silva *et al*. (1990a; b).

7 Discussion

As mentioned before, the recognition of mineralized areas is mainly performed through the identification of the associated alteration halos. The most common minerals associated wi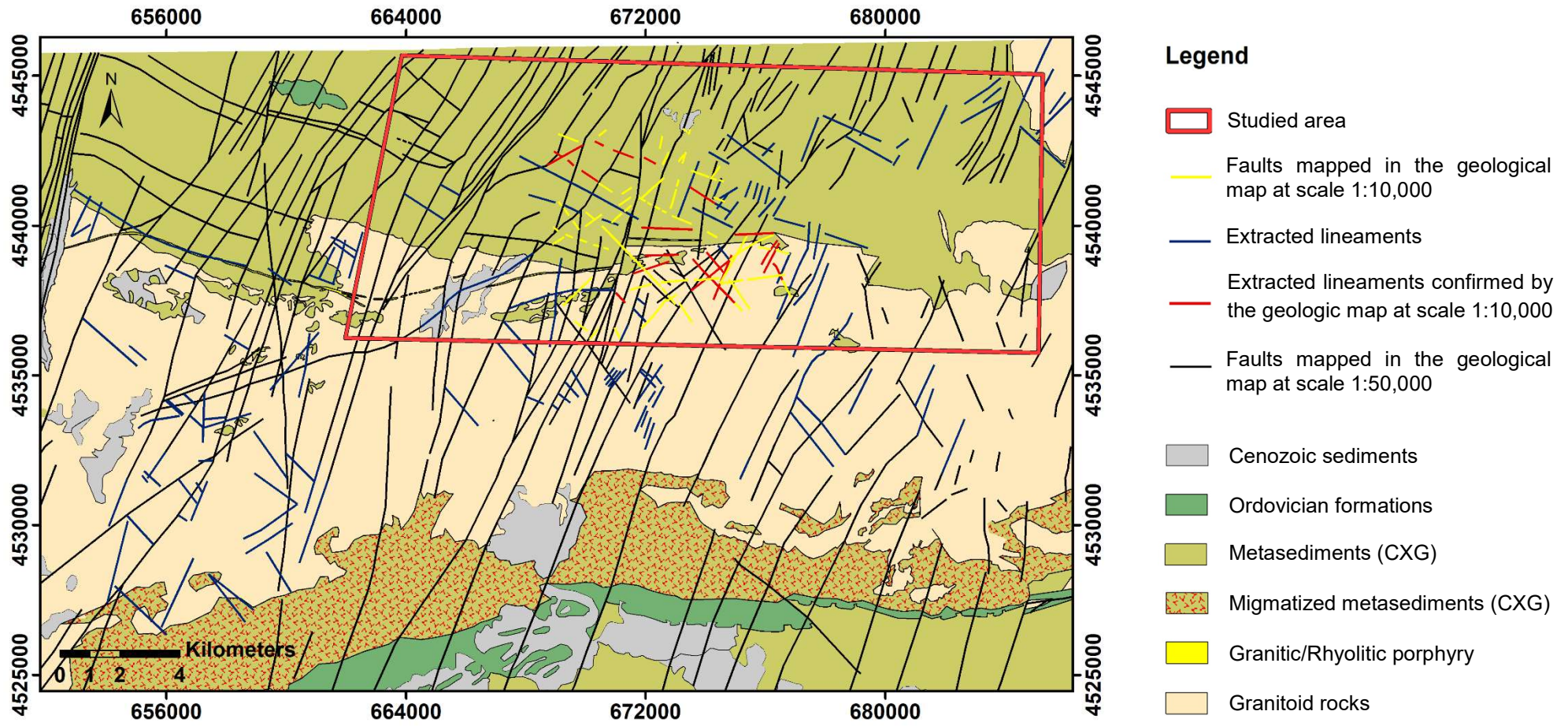th these alteration zones are iron oxides and clay minerals (Sabins, 1999). So, several known image processing methods were applied in order to identify hydrothermally altered zones in the studied area.

RGB 257 for Landsat 8 and RGB 2812 for Sentinel-2 (Figure 23) were applied to map iron oxides and clay minerals. In the red sea hills (Sudan), RGB 257 for Landsat 8 highlighted iron oxides in dark blue color (Ali & Pour, 2014). In the Fregeneda-Almendra area, only the Sentinel-2 combination presented blue colors. However, it was easy to establish a correspondence between the colors obtained for the two sensors: intense blue areas in Sentinel-2 correspond to burned areas which are mapped in intense purple colors in Landsat 8 images; blue areas in Sentinel-2 represent the granitoid rocks which are highlighted in purple color in Landsat 8. Taking this into account and since these combinations clearly discriminate the metasediments from the granitoid rocks, we can conclude that: (i) the burned areas are rich in iron minerals; (ii) the granites have a higher content in Fe than the metasediments. White areas are the most difficult to interpret. The color is the result of high reflectance in the three bands. This could mean a simultaneous presence of clay minerals and iron oxides near the open-pit mines, but it also could be due to a mixture of signals from other minerals. In the Bajoca mine, Almeida (2003) described the formation of iron oxides and clay minerals associated with fault zones.

The RGB 573 (Landsat 8), RGB 472 (Landsat 5) and RGB 8123 (Sentinel-2) were also able to identify hydrothermally altered rocks (Figure 24 and Figure 25). In the Kuju volcano surroundings (Japan), according to Mia & Fujimitsu (2012), the equivalent of RGB 573 combination for Landsat 7 ETM+, mapped hydrothermally altered zones in deep green and blue colors. In the Fregeneda-Almendra aplite-pegmatite field, Bajoca, Feli and Alberto open pit mines appear with a bluish tint indicating hydrothermal alteration. The burned areas present a green color that could also indicate hydrothermal alteration. This may indicate that fire exposure can lead to the formation of minerals that are also formed through hydrothermal alteration processes or that it can induce geological changes which present similar signatures to hydrothermally altered areas. Either way, detailed compositional and spectral studies are needed to understand these results.

RGB combinations are the most difficult technique to interpret, because a mixture of signals from distinct minerals generates a mixture of colors often quite different from the results reported in the literature.

Band ratio were also applied to discriminate iron oxides and ferric iron (Figure 30). However, the ratios employed (4/2 for Landsat 8 and Sentinel-2, 3/1 for Landsat 5, and 2/1 for ASTER) are not sensible to the compositional differences between the metasediments and the granites. In fact, they highlight urbanized areas and agricultural fields as the areas where iron oxides/ferric iron are present. This may occur because: (i) these areas can have a similar behavior to iron oxides even if no Fe is present; or (ii) these areas present in fact a high content in iron oxides/ferric iron probably due to agricultural fertilizers and/or the presence of rusted materials. Iron oxides/ferric iron is also discriminated in the Quaternary fluvial terraces. According to Silva & Ribeiro (1991; 1994), these sedimentary deposits present indeed iron oxides. Nonetheless, these ratios did not highlight iron oxides in Bajoca, Feli and Alberto mines, although iron oxides have been described in these areas especially associated with fault zones.

Band ratios 6/5 (Landsat 8), 5/4 (Landsat 5) and 11/8 (Sentinel-2) were applied to discriminate ferrous minerals (Figure 31). Ratio 4/3, that was employed to map ferric oxides in ASTER images, presented similar results. All the ratios reflect the compositional differences between the granitoid rocks and the metasediments. The high iron content in the granites can be explained by the presence of biotite which is a ferromagnesian mineral much less common in the metasedimentary rocks because it is easily weathered. These ratios also highlight the burned areas as the zones that contain the highest content in ferrous minerals. Several authors reported the physical, chemical and mineralogical changes in soils due to wild fires, and one the of the common changes is the formation of iron oxide maghemite (*e.g.* Clement *et al*., 2011; Jardanova, 2016). Residual ash from forest fires can also present significant amounts of iron oxides (Lu *et al*., 2000). In what concerns the open-pits of Bajoca, Feli and Alberto, no ferrous minerals were identified. This shows the incapacity of the used band ratios to correctly map all the Fe-bearing areas.

To map alunite and/or clays such as kaolinite, montmorillonite, band ratios 6/7 (Landsat 8), 5/7 (Landsat 5) and 11/12 (Sentinel-2) were considered (Figure 32). In all cases, these minerals appear to be distributed near to the water lines and associated with some geological faults. In general, no clay minerals are identified in the known Li-mineralized areas. However, the application of band ratio 7/5 to ASTER bands (Figure 33), in order to map kaolinite, produced very different results: according to this ratio, kaolinite is

present in the Bajoca and Alberto mines. These incongruent results can be explained by the fact that ASTER has several narrower bands in the SWIR while Landsat (5 and 8) and Sentinel-2 present only two broad bands (see Figure 8). The higher spectral resolution of ASTER results in a higher efficiency in mineral mapping and discrimination. Agricultural fields also are highlighted as kaolinite-bearing areas. This could mean that the soils used in agriculture present high clay content.

Overall, the applied band ratios failed to identify minerals associated with hydrothermal alteration near the open-pits of Bajoca, Feli and Alberto which emphasizes the need to study and characterize the alteration associated in the Li-bearing pegmatites in order to develop more adequate remote sensing algorithms.

PCA proved to be more efficient than band ratio in identifying iron oxides whether when applied to all VNIR and SWIR bands (Figure 38) or in specific subsets (Figure 42). Both methods discriminated iron oxides/ferric iron in the Bajoca and Alberto mines. It is also worth mentioning that no presence of iron oxides was detected in Landsat 5 images (before the opening of the mines).

To map hydroxyl-bearing minerals (such as clays), PCA considering all VNIR and SWIR was also more effective than band ratio by highlighting the presence of hydroxyl minerals in Bajoca and Feli mines. When applied in two- and four-band subsets, PCA was incapable of highlighting hydroxyl minerals in the open-pit mines (Figure 43), but it shows a clear signal difference before and after the opening of the Bajoca and Alberto mines. Selective PCA on ASTER highlights more alteration minerals (like alunite, illite and kaolinite) in the Bajoca mine than in the other two (Figure 41).

Relatively to the RGB combinations using the PCs resultant from the PCA, ASTER combinations (Figure 37) were the best to discriminate Li-bearing pegmatites from host rocks, which may be due to the better spectral resolution. RGB combination of the first three PCs for Landsat 5 and Sentinel-2 (Figure 39) are good at highlighting the compositional differences between the granites and the metasediments. PC4-PC5-PC1 combination for Landsat 8 (Figure 40) was able to identify iron oxides in all three open-pits. Burned areas present always a distinct signal in the mentioned RGB combinations.

Analyzing all the results obtained, they indicate that in fact some alteration process is related to the Li-bearing pegmatites. Nonetheless, other tested algorithms from the literature (which were defined to other mineral deposits types) did not work well in this study. This emphasizes the need to develop specific algorithms for Li-mineralizations even more because so far only image classification algorithms were applied to select target Li areas (Perrotta *et al.,* 2005; Mendes *et al.,* 2017).

With that goal in mind, and based on the known spectral curves of Li-bearing minerals (Kokaly *et al*., 2017), some new approaches were proposed.

Two of the self-proposed RGB combinations were able to successfully highlight Li-bearing areas and distinguish them from the host rocks: the first comprises a SWIR, a visible and a thermal band (Figures 26 and 27), and the second two bands in the visible and one thermal band (Figures 28 and 29). The SWIR band in the first case combination allows to discriminate the granites from the metasediments. In both cases, the presence of the thermal band is the key to effectively highlight Li-bearing areas: since Sentinel-2 does not have available a band in TIR region, the thermal band was swapped by a SWIR band and the resultant combination is not able to discriminate the Li-pegmatites from the host rocks. This raises some questions: to what is due the importance of the thermal band in the discrimination of Li-bearing pegmatites? why Li-bearing pegmatites present this signal in the thermal band? Only detailed studies on the pegmatites, the related mineral assemblage and their spectral properties can answer these questions. On the other side, the similar response between Li-areas and urbanized zones and agricultural fields observed in these RGB combinations is a clear obstacle.

Li-bearing pegmatites were also highlighted through band ratios. Density slice versions of band ratio 7/6 for ASTER (Figure 34) and of ratio 3/5 (Landsat 8; Figure 35), 2/4 (Landsat 5), 3/8 (Sentinel-2) and 1/3 (ASTER) successfully differentiated Li-bearing areas from the host rock. In the first case, urbanized areas and agricultural fields also present a similar response to Li-bearing areas. To overcome this obstacle in the future, these areas could be excluded from the image processing. Nevertheless, it is essential to understand why these different areas present similar spectral behaviors and how it is possible to separate the two signals. It is also clear the importance of the density slice method, without which the discrimination of Li-bearing areas from the background was impossible.

Other band ratios capable of recognizing and highlighting Li-bearing areas are 4/7 (Landsat 8), 3/7 (Landsat 5) and 4/12 (Sentinel-2) but, as it can be seen from Figure 36, it is necessary to enhance the thresholds defined for the density slice method in order to completely discriminate Li-bearing pegmatites from the host rocks. In fact, this reinforces the need the establish a threshold that indicates with better confidence the presence of Li-bearing minerals for all band ratios.

In what concerns to PCA, it is very difficult to try to identify and isolate Li-bearing minerals through the observation of the eigenvalues obtained in the eigenvector matrices for all VNIR and SWIR bands. Oppositely, selective PCA proved to be a powerful resource

capable of isolating the spectral inputs of Li-bearing pegmatites for both two- and four-band subsets (Figure 44). In addition to the Li-bearing areas, some urbanized/agricultural areas were also highlighted in bright pixels, which reinforces the need to exclude these areas from the image processing. Overall, the two-band subset appears to be more sensitive to the signature of Li-minerals and present fewer noise because only the target bands were used. It is essential, to define a threshold value from which only the Li-bearing minerals are being mapped. In the future, to aid visual interpretation, density slice could be applied. The selective PCA can also be applied to other bands containing the target spectral information of Li-bearing minerals.

In general, a comparison between Landsat 5 images (before the opening of Bajoca and Alberto mines) and the other images shows that no distinct signature is detected in these areas before exploitation. Considering that the exposition of the pegmatites (and thereafter of Li-bearing minerals) was very small before the opening of the mines, these temporal spectral differences indicate that the signals obtained in Landsat 8, Sentinel-2 and ASTER images are in fact due to the Li-bearing pegmatites.

The successful application of the proposed image processing algorithms in order to highlight Li-bearing pegmatites is proof of the remote sensing potential to delineate target areas in the near future.

In what concerns the extracted lineaments (Figure 45), they can be divided in two main classes according to their orientation: the first NNE-SSW trending and the other NW-SE trending. A third minor class presents a WSW-ENE general orientation.

The NNE-SSW and WSW-ENE lineaments are in line with the two types of faults mentioned by Silva & Ribeiro (1991; 1994): NNE-SSW sinistral strike-slip faults, and WSW-ENE sinistral shearings. Altough, NW-SE faults are not mentioned by the authors, there are some faults with that general orientation mapped wheter at the 1:50,000 scale (Silva *et al.*, 1990a, b) or at 1:10,000 scale (Viegas, 1983).

Although the applied filter is not able to enhance all the existing faults, probably because they can be concealed by urbanized areas, this method proved to be a powerful tool for structural mapping. The new extracted lineaments can help to better understand the structure of the region. Also, NNE-SSW lineaments can help to pin-point new target areas where Li-mineralized pegmatites could have been installed. If proven in the field as in fact geological faults, the extracted lineaments (specially the NW-SE trending) can be a major contribution on the geological knowledge of the area and on the actualization of the geological maps. In the future, lineament density studies can be made.

8 Conclusions

(i) The applied remote sensing methods are able to evidence some hydrothermal alteration associated with the Li-bearing pegmatites that needs to be characterized. RGB combinations and PCA are more effective than the band ratios.

(ii) Band rationing is a good strategy to identify and map the compositional differences between different lithologies.

(iii) The higher spectral resolution of ASTER allows for a better mineral discrimination. On the other hand, the lack of a thermal band from Sentinel-2 prevents the discrimination of Li-bearing pegmatites using only RGB combinations.

(iv) Remote sensing is a powerful tool to identify fracture patterns that may help explain pegmatite emplacement. The obtained structural lineaments can also be used to improve the existent geological maps.

(v) Although this study is just a first approach, the spectral signatures of Li-bearing pegmatites were already differentiated from the spectral signatures of the host rocks using RGB combinations, band ratios and PCA.

(vi) Band ratio also has great potential to study the geochemical changes in the soils induced by wild fires.

(vii) Despite the mentioned limitations, there is a great potential for the discrimination of Li-bearing pegmatites using remote sensing.

9 Future work

Considering the potential of the remote sensing methods used in this work in the identification of Li-bearing zones, they should be improved in order to establish a robust methodology. Other remote sensing techniques such as spectral unmixing and image classification algorithms can be tested. The validation of the obtained results in the field and the collection of mineral spectral signatures is also required.

To increase the efficiency of the tested algorithms sensors with a better spatial and spectral resolution could be used.

Detailed geological and geochemical studies on the alteration halos around Li-pegmatites are needed to fully understand the remote sensing results and to develop innovative and successful remote sensing algorithms.

Finally, the integration of the remote sensing results with structural and geologic data will allow to produce target exploration maps.

10 References

Ali, A., & Pour, A. (2014). Lithological mapping and hydrothermal alteration using Landsat 8 data: a case study in ariab mining district, red sea hills, Sudan. *International Journal of Basic and Applied Sciences*, 3(3), 199–208.

Almeida, C. (2003). Estudo do filão aplitopegmatítico da mina da Bajoca, Almendra. Contribuição científico-tecnológica. *Master Thesis. Universidade do Porto, Portugal*, p. 148.

Barberes, G. A. (2015, May). Remote sensing (Landsat-8) applied to shale gas potential evaluation. The case of South Portuguese Zone. *Proceedings of 'European Regional Conference and Exhibition'*, pp. 18-19.

Barberes, G. A., Barata, M. T., Pena dos Reis, R., Fonseca, P. E., & Pimentel, N. (2015). Integrated remote sensing data for hydrocarbon emanations detection applied in South Portuguese Zone, Portugal. *Proceedings of the 26th GRSG Annual Conference 'Challenges in Geological Remote Sensing'*.

Bea, F., Fershtater, G. & Corretgé, L. G. (1992). The geochemistry of phosphorus in granite rocks and effect of aluminium. *Lithos*, 29: 43–56. In: Vieira, R. (2010). Aplitopegmatitos com Elementos Raros da Região entre Almendra (V. N. de Foz-Côa) e Barca d'Alva (Figueira de Castelo Rodrigo). Campo Aplitopegmatítico da Fregeneda-Almendra. *phD Thesis*. Universidade do Porto, Portugal, p. 276.

Berger, B.R., King, T.V.V., Morath, L.C., & Phillips, J.D. (2003). Utility of high-altitude infrared spectral data in mineral exploration: application to northern Patagonia mountains, Arizona. *Economic Geology and the Bulletin of the Society of Economic Geologists* 98, 1003–1018. In: Van der Meer, F.D., van der Werff, H.M., van Ruitenbeek, F.J., Hecker, C.A., Bakker, W.H., Noomen, M.F., van der Meijde, M., Carranza, E.J.M., de Smeth, J.B., & Woldai, T. (2012). Multi- and hyperspectral geologic remote sensing: A review. *Int. J. Appl. Earth Obs. Geoinf. 14*, 112–128.

Brongniart, A. (1813). Essai d'une classification minéralogique des roches mélangées. (Essay of a mineralogical classification for mixed rocks). *Journal des Mines* 34, 32.

Brun, J.P. & Burg, J.P. (1982). Combined thrusting and wrenching in the Ibero-Armorican Arc: a corner effect during continental collision. *Earth Planet. Sci. Letters*, 61: 319-332. In: Pérez-Estaún, A., Bea, F., Bastida, F., Marcos, A., Martínez

Catalán, J.R., Martínez Poyatos, D., Arenas, R., Díaz García, F., Azor, A., Simancas, J.F. & González Lodeiro, F. (2004). La cordillera varisca europea: el Macizo Ibérico. In: Vera, J.A. (Eds.). *Geología de España.* Soc. Geol. España/Inst. Geol. Min. España (SGE/IGME), Madrid, pp. 21-25.

Buddington, A.F. (1959). Granite emplacement with special reference to North America. *Geological Society of America bulletin* 70, 671-747.

Cabral, J., Rebelo, J. A. & Ribeiro, A. (1983-1985). Neotectónica de Trás-os-Montes Oriental. *Bol. Soc. Geol. Portugal*, *24*: 193–197.

Cameron, E.N., Jahns, R.H., McNair, A.H., Page, L.R. (1949). Internal structure of granitic pegmatites. *Economic Geology*, Monograph 2, 115 p.

Canada Centre for Remote Sensing (CCRS) (2015a). Spatial Resolution, Pixel Size, and Scale. In *Fundamentals of Remote Sensing: A Canada Centre for Remote Sensing Remote Sensing Tutorial*. http://www.nrcan.gc.ca/earth-sciences/geomatics/satellite-imagery-air-photos/satellite-imagery-products/educational-resources/9407 . Accessed December 2017.

Canada Centre for Remote Sensing (CCRS) (2015b). Spectral Resolution. In *Fundamentals of Remote Sensing: A Canada Centre for Remote Sensing Remote Sensing Tutorial*. http://www.nrcan.gc.ca/earth-sciences/geomatics/satellite-imagery-air-photos/satellite-imagery-products/educational-resources/9393 . Accessed December 2017.

Canada Centre for Remote Sensing (CCRS) (2016). Radiometric Resolution. In *Fundamentals of Remote Sensing: A Canada Centre for Remote Sensing Remote Sensing Tutorial*. http://www.nrcan.gc.ca/earth-sciences/geomatics/satellite-imagery-air-photos/satellite-imagery-products/educational-resources/9379 . Accessed December 2017.

Capdevila, R. & Floor, P. (1970). Les différents types de granites hercyniens et leur distribution dans le nord ouest de l'Espagne. *Bol. Geol. Min. España*, T 81 (2-3): 215-225.

Capdevila, R., Corretgé, L. G. & Floor, P. (1973). Les granitoides varisques de la Meseta Ibérique. *Bull. Soc. Géol. France, XV* (3–4): 209–228.

Carnicero, M. A. (1982). Estudio del metamorfismo existente en torno al granito de Lumbrales (Salamanca). *Stvd. Geol*., 17: 7–20.

Carrington da Costa, J. (1950). Notícia sobre uma carta geológica do Buçaco, de Nery Delgado. Comun. Serv. Geol. Portugal, Lisboa. 28 p.

Černý, P. & Ercit, T. S. (2005). Classification of granitic pegmatites revisited.*Can. Mineral.*, 43: 2005–2026.

Černý, P. (1991a). Rare-element granitic pegmatites. Part I. Anatomy and internal evolution of pegmatite deposits. *Geosci. Can.*, 18: 49–67.

Černý, P. (1991b). Rare-element granitic pegmatites. Part II. Regional to global environments and petrogenesis. *Geosci. Can.*, 18: 68–81.

Charoy, B., & Noronha, F. (1999). Rare-element (Li-rich) granitic and pegmatitic plutons: a primary or superimposed signature. *Revista Brasileira de Geociências, 29*, pp. 3-8.

Chavez, P. S. & Kwarteng, A. Y. (1989). Extracting spectral contrast in   Landsat Thematic Mapper image data using selective principal component analysis. *Photogrammetric Engineering and Remote Sensing*, 55: 339-348.

Chavez, P. S. (1996). Image-Based Atmospheric Corrections - Revisited and Improved. *Photogrammetric Engineering and Remote Sensing*, American Society of Photogrammetry, 62, pp. 1025–1036.

Clark, J.O.E., Steigeler, S. (2000). The Facts on File Dictionary of Earth Science. *Checkmark Books*, New York, N.Y. 240p.

Clement, B.M., Javier, J., Sah, J.P., Ross, M.S. (2011). The effects of wildfires on the magnetic properties of soils in the Everglades. *Earth Surf. Process. Landforms* 36, 460-466.

Coke, C. (2000). Evolução geodinâmica do ramo sul da Serra do Marão um caso de deformação progressiva em orógenos transpressivos. *PhD thesis*, Univ. Trás-os-Montes e Alto Douro, 330 p. In: Dias, R., Ribeiro, A., Coke, C., Pereira, E., Rodrigues, J., Castro, P., Moreira, N., Rebelo, J. (2013). Evolução estrutural dos sectores setentrionais do Autóctone da Zona Centro-Ibérica. In: Dias, R., Araújo, A., terrinha, P., Kullberg, J.C. (Eds). *Geologia de Portugal. Volume I – Geologia Pré-mesozóica de Portugal*, Escolar Editora. pp. 73-147.

Coke, C., Pires, C. A. C., Sá, A. A., & Ribeiro, A. (2001). O Vulcanismo na transição Câmbrico/Ordovícico da Zona Centro-Ibérica na região de Trás-os-Montes (NE Portugal) como elemento de referência estratigráfica. *Cadernos Lab. Xeolóxico de Laxe*, Coruña, 26, 121-136.

Congedo, L. (2016). Semi-Automatic Classification Plugin Documentation. doi: http://dx.doi.org/10.13140/RG.2.2.29474.02242/1 .

Costa, M., Perrotta, M. M., Melo, T. G., & Turra, B. (2016). Estudos Espectrais: Análises Espectrais. In: V. Paes, L. D. Santos, M. F. Tedeschi, & L. M. Betiollo (Eds.), *Avaliação do potencial do litio no Brasil: área do Médio Rio Jequitinhonha, nordeste de Minas Gerais.* CPRM, pp. 99-105.

Couto, M.H. (1993). As mineralizações de Sb-Au da região Dúrico-Beirã. *Ph. D. thesis, Univ. Porto,* 606 pp.

Crósta, A. P., Souza Filho, C. R., Azevedo, F. & Brodie, C. (2010). Targeting key alteration minerals in epithermal deposits in Patagonia, Argentina, using ASTER imagery and principal component analysis. *International Journal of Remote Sensing*, 24:21, 4233-4240, DOI: <u>10.1080/0143116031000152291</u>.

Crósta, A. P., Souza Filho, C. R., Azevedo, F., & Brodie, C. (2003). Targeting key alteration minerals in epithermal deposits in Patagonia, Argentina, using ASTER imagery and principal component analysis. *International Journal of Remote Sensing, 24*(21), pp. 233-4240.

Dias, G. (2001). Fontes de Granitóides Hercínicos da Zona Centro-Ibérica (Norte de Portugal): evidências isotópicas (Sr, Nd). *Mem. Acad. Ciências Lisboa*, XXXIX: 121–143. In: Dias, G., Noronha, F., Almeida, A., Simões, P. P., Martins, H. C. B. & Ferreira, N. (2010). Geocronologia e petrogénese do plutonismo tardi-Varisco (NW de Portugal): síntese e inferências sobre os processos de acreção e reciclagem crustal na Zona Centro-Ibérica. In: J. M. Cotelo Neiva, A. Ribeiro, L. Mendes Victor, F. Noronha & M. Magalhães Ramalho (Eds.), *Ciências geológicas: Ensino, investigação e a sua história*, Assoc. Port. Geólogos, vol. I (Geologia clássica), p. 143–160.

Dias, G., Leterrier, J., Mendes, A., Simões, P. P. & Bertrand, J. M. (1998). U–Pb zircon and monazite geochronology of post-collisional Hercynian granitoids from the Central Iberian Zone (Northern Portugal). *Lithos, 45*: 349–369.

Dias, G., Noronha, F., & Ferreira, N. (2000). Variscan Plutonism in the Central Iberian Zone, Northern Portugal. *Eurogranites 2000 Field Meeting Guide*, September 2000, Portugal. p. 1–15.

Dias, G., Noronha, F., Almeida, A., Simões, P. P., Martins, H. C. B. & Ferreira, N. (2010). Geocronologia e petrogénese do plutonismo tardi-Varisco (NW de Portugal): síntese e inferências sobre os processos de acreção e reciclagem crustal na Zona Centro-Ibérica. In: J. M. Cotelo Neiva, A. Ribeiro, L. Mendes Victor, F. Noronha & M. Magalhães Ramalho (Eds.), *Ciências geológicas: Ensino,*

investigação e a sua história, Assoc. Port. Geólogos, vol. I (Geologia clássica), p. 143–160.

Dias, R. & Ribeiro, A. (1994). Constriction in a transpressive regime: the case of Ibero-Armoricain Arc. *J. Struct. Geol.*, 16(11): 1545-1554.

Dias, R. & Ribeiro, A. (1995). The Ibero Armorican Arc: a collision effect against an irregular continent?. *Tectonophysics*, 246: 113–128.

Dias, R., Ribeiro, A., Coke, C., Rodrigues, J., Pereira, E., Rebelo, J., & Moreira, N. (2013). Evolução estrutural dos sectores setentrionais do Autóctone da Zona Centro-Ibérica. In: Dias, R., Araújo, A., terrinha, P., Kullberg, J.C. (Eds). *Geologia de Portugal. Volume I – Geologia Pré-mesozóica de Portugal*, Escolar Editora. p. 69-144.

Díez Balda, M. A., Vegas, R. & González Lodeiro (1990). Central Iberian Zone: structure. In: R. D. Dallmeyer & E. Martinez Garcia (Eds.). *Pre-Mesozoic geology of the Iberian Peninsula,* Springer Verlag. Berlim. p. 172–188.

European Space Agency (ESA) (2018a). User Guides: Sentinel-2. Overview. https://sentinel.esa.int/web/sentinel/user-guides/sentinel-2-msi/overview. Accessed January 2018.

European Space Agency (ESA) (2018b). Missions: Sentinel-2. Overview. https://sentinel.esa.int/web/sentinel/missions/sentinel-2/overview. Accessed January 2018.

European Space Agency (ESA) (2018c). Technical Guides: Sentinel-2. MSI instrument. https://sentinel.esa.int/web/sentinel/technical-guides/sentinel-2-msi/msi-instrument. Accessed January 2018.

Farias, P., Gallastegui, G., González Lodeiro, F., Marquínez, J., Martín-Parra, L.M., Martínez Catalán, J.R., Pablo Maciá, J.G. & Rodríguez-Fernández, L.R. (1987). Aportaciones al conocimiento de la litoestratigrafía y estructura de Galicia Central. *Mem. Museu Mineral. Geol*. Fac. Ciências Univ. Porto, 1: 411-431.

Ferreira, A. B. (1971). O Rebordo ocidental da Meseta e a Depressão Tectónica de Longroiva. *Finisterra*, Lisboa, 6 (12), pp. 196-217.

Ferreira, A. B. (1978). Planaltos e montanhas do norte da Beira. *Mem. Cent. Est. Geogr*., Lisboa, 4, 374 p.

Ferreira, N., Iglésias, M., Noronha, F., Pereira, E., Ribeiro, A. & Ribeiro, M. L. (1987). Granitóides da zona Centro Ibérica e seu enquadramento geodinâmico. In: F. Bea, A. Carnicero, J. C. Gonzalo, M. López-Plaza & M. D. Rodríguez Alonso

(Eds.), *Geología de los Granitóides y Rocas Asociadas del Macizo Hesperico*. Libro de Homenaje a L. C. García de Figuerola, Editorial Rueda. Madrid. p. 37–51.

Frutuoso, R. (2015). Mapping hydrothermal gold mineralization using Landsat 8 data. A case of study in Chaves license, Portugal. *Master Thesis. Universidade do Porto, Portugal.* p. 83.

Gabr, S., Ghulam, A., & Kusky, T. (2010). Detecting areas of high-potential gold mineralization using ASTER data. *Ore Geol. Rev.*, 38. pp. 59–69.

Gaspar, L. (1997). Contribuição para o estudo das mineralizações de volfrâmio (W), estanho (Sn) e lítio (Li) do sector Barca de Alva – Escalhão. *Master thesis*. Fac. Ciências, Univ. de Lisboa, Portugal. 267 p.

Gaspar, L. M., & Inverno, C. M. (2000). Mineralogy and metasomatic evolution of distal stratiform scheelite skarns in the Riba de Alva Mine, Northeastern Portugal. *Econ. Geol., 95*, pp. 1259-1275.

Ginsburg, A. I., Timofeyev, L. N. & Feldman, L. G. (1979). Principles of geology of the granitic pegmatites. Nedra, Moscovo. 296 p. In: Černý, P. & Ercit, T. S. (2005). Classification of granitic pegmatites revisited.*Can. Mineral.*, 43: 2005–2026.

Goinhas, J. A. C., & Viegas, L. F. (1982). Província metalogenética estanífera e tungsténica ibérica. Considerações sobre as ocorrências de tungsténio em Portugal, sua prospecção e potencialidade. *Simp. Tungsténio CEE.*, Lisboa. In: Silva, A. F., & Ribeiro, M. L. (1991). Notícia explicativa da folha 15-A – Vila Nova de Foz Côa – da carta Geológica de Portugal na escala 1/50.000. *Serv. Geol. Portugal.*, p. 52.

Han, T. & Nelson, J. (2015). Mapping hydrothermally altered rocks with Landsat 8 imagery: A case study in the KSM and Snow field zones, northwestern British Columbia. In: Geological Fieldwork 2014, British Columbia Ministry of Energy and Mines, British Columbia Geological Survey Paper, 2015-1, pp.103-112.

Heinrich, E. W. (1948). Pegmatites of Eight Mile Park, Fremont County, Colorado. *The American Mineralogist*, V. 33, p. 420-448, 550-588.

Hung, L. Q., Batelaan, O., & De Smedt, F. (2005). Lineament extraction and analysis, comparison of LANDSAT ETM and ASTER imagery. Case study: Suoimuoi tropical karst catchment, Vietnam. *Proc. SPIE 5983, Remote Sensing for Environmental Monitoring, GIS Applications, and Geology*, V.

Iglesias, M. & Ribeiro, A. (1981a). Zones de cisaillement ductile dans l'arc Ibéro-Armoricain. *Comun. Serv. Geol. Portugal*, 67 (1): 85–88.

Iglésias, M., & Ribeiro, A., (1981b). Position stratigraphique de la formation Ollo de Sapo dans la region de Zamora (Espagne) – Miranda do Douro (Portugal). *Comun. Serv. Geol. Portugal*, 67 (1): 141–146.

Inzana, J., Kusky, T., Higgs, G., & Tucker, R. (2003). Supervised classifications of Landsat TM band ratio images and Landsat TM band ratio image with radar for geological interpretations of central Madagascar. *J. Afr. Earth Sci*., 37. pp. 59–72.

Jackson, J.A., 1997. Glossary of Geology. 4th Ed. American Geological Institute, Alexandria, Virginia. 472p.

Japan Association on Remote Sensing (JARS) (1993). Remote Sensing Note. Available at http://www.jars1974.net/pdf/rsnote_e.html. Accessed December 2017.

Jet Propulsion Laboratory (JPL) (2004a). ASTER: Advanced Spaceborne Thermal Emission and Reflection Radiometer. https://asterweb.jpl.nasa.gov/index.asp. Accessed December 2017.

Jet Propulsion Laboratory (JPL) (2004b). ASTER: Mission. https://asterweb.jpl.nasa.gov/mission.asp. Accessed December 2017.

Jet Propulsion Laboratory (JPL) (2004c). ASTER: Instrument Characteristics. https://asterweb.jpl.nasa.gov/characteristics.asp. Accessed December 2017.

Johnson, B. A., Tateishi, R. & Hoan, N. T. (2012). Satellite Image Pansharpening Using a Hybrid Approach for Object-Based Image Analysis. *ISPRS International Journal of Geo-Information*, 1, 228.

Jordanova, N. (2016). Effects of wildfires on the magnetism of soils: possible application in soil science and paleoenvironmental studies. In: N. Jardanova (Ed), *Soil Magnetism: Applications in Pedology, Environmental Science and Agriculture*, 419-420.

Julivert, M., Fontboté, J., Ribeiro, A., & Conde, L. (1972). Mapa Tectónico de la Península Ibérica Y Baleares a escala 1:1 000 000. *Instituto Geológico Y Minero de España*. 113 p.

Julivert, M., Fontboté, J., Ribeiro, A., & Conde, L. (1974). Memória explicativa del Mapa Tectónico de la Península Ibérica y Baleares. Esc.: 1/ 1000000. In*st. Geol. Min. España,* Madrid. 133 pp.

Kalinowski, A., & Oliver, S. (2004) Aster mineral index processing manual. Remote Sensing Applications. Geoscience Australia. Available at: http://www.ga.gov.au/webtemp/image_cache/GA7833.pdf . Accessed October 2017.

Key, C.H., & Benson, N.C (2005). Landscape Assessment: Ground Measure of Severity, the Composite Burn Index, and Remote Sensing of Severity, the Normalized Burn Index. In: Lutes, D., Keane, R., Caratti, J., Key, C.H., Benson, N.C., Sutherland, S., Gangi, L. (Eds.), *FIREMON: Fire Effects Monitoring and Inventory System*, Rocky Mountains Research Station, USDA Forest Service: Fort Collins, CO, USA.

Kokaly, R.F., Clark, R.N., Swayze, G.A., Livo, K.E., Hoefen, T.M., Pearson, N.C., Wise, R.A., Benzel, W.M., Lowers, H.A., Driscoll, R.L., & Klein, A.J., 2017, USGS Spectral Library Version 7: U.S. Geological Survey Data Series 1035, 61 p., https://doi.org/10.3133/ds1035.

Lagarde, J. L., Capdevila, R., & Fourcade, S. (1992). Granites et collision continentale: l'exemple des granitoïdes carbonifères dans la chaîne hercynienne ouest-européenne. *Bull. Soc. géol.,* 163 (5), pp. 597-610.

Lillesand, T., Kiefer, R., & Chipman, J. (2015). Remote Sensing and Image Interpretation. 7th Edition, Wiley, New York, 784.

Lima A.M.C., Almeida, C., & Noronha, F. (2003b). A zonação mineralógica do filão principal da Mina da Bajoca no campo aplitopegmatítico de Almendra (Nordeste de Portugal). *VI Congresso Nacional de Geologia*, Lisboa.

Lima A.M.C., Vieira, R.C., & Almeida, C. (2003c). Caracterização científica e tecnológica dos aplitopegmatitos com elementos raros da região de Almendra – Barca de Alva (Nordeste de Portugal): possíveis implicações no domínio sócio-económico, *III Seminário de Recursos Geológicos, Ambiente e Ordenamento do Território*, Universidade de Trás-os-Montes e Alto Douro, Departamento de Geociências.

Lima, A., Almeida, C., Noronha, F. & Vide, R. (2003a). Geoquímica dos filões litiníferos no campo aplitopegmatítico de Almendra – Barca de Alva (Nordeste de Portugal). *Resumos do 7°Congresso de Geoquímica dos Países de Língua Portuguesa*, p. 43.

Lima, A., Vieira, R., Martins, T., & Noronha, F. (2010). Minerais de lítio. Exemplo dos campos aplitopegmatíticos de Barroso-Alvão e Almendra-Barca D'Alva. In: J. M. Cotelo Neiva, A. Ribeiro, L. Mendes Victor, F. Noronha, & M. Magalhães

Ramalho (Eds.), *Ciências geológicas: Ensino, investigação e a sua história* (Vols. I – Geologia clássica, pp. 89–98). Assoc. Port. Geólogos.

London, D. (2008). Pegmatites. The Canadian Mineralogist, Special Publication 10. R. F. Martin (Ed.), Mineral. Assoc. Can. Québec, Canadá. 347 p

López-Plaza, M., Carnicero, A. & Gonzalo, J. C. (1982). Estudio geológico del campo filoniano de La Fregeneda (Salamanca). *Stvd. Geol. Salman*., XVII: 89–98.

Lotze, F. (1945). Zur Gliederung der Varisziden der Iberischen Meseta. Geotekt. Forsch., 6: 78-92. In: Pérez-Estaún, A., Bea, F., Bastida, F., Marcos, A., Martínez Catalán, J.R., Martínez Poyatos, D., Arenas, R., Díaz García, F., Azor, A., Simancas, J.F. & González Lodeiro, F. (2004). La cordillera varisca europea: el Macizo Ibérico. In: Vera, J.A. (Eds.). *Geología de España.* Soc. Geol. España/Inst. Geol. Min. España (SGE/IGME), Madrid, pp. 21-25.

Lotze, F. (1956). Über sardische Bewegun in Spanien und ihre Beziehungen zur assyntischen Faltung. Geotect. Symp. Hans Stille, 129–139. In: Díez Balda, M. A., Vegas, R. & González Lodeiro (1990). Central Iberian Zone: structure. In: R.D. Dallmeyer & E. Martinez Garcia (Eds.). *Pre-Mesozoic geology of the Iberian Peninsula*, Springer Verlag. Berlim. p. 172–188.

Loughlin, W. P. (1991). Principal Component Analysis for Alteration Mapping. *Photogram. Eng. Rem. Sens*., 57, 1163-1169.

Lu, H., Liu, T., Gu, Z., Liu, B., Zhou, L., Han, J., Wu, N. (2000). Effect of burning C3 and C4 plants on the magnetic susceptibility signal in soils. *Geophys. Res. Lett*. 27 (13), 2013-2016.

Mangas, J. (1987). Estudio de las inclusiones fluidas en los yacimientos españoles de estaño asociados a granitos hercínicos. *PhD thesis*. Universidad de Salamanca. In: Martín-Izard, A., Reguilón, R. & Palero, F. (1992). Las mineralizaciones litiníferas del oeste de Salamanca y Zamora. *Estud. Geol*., 48: 19–30.

Manuel, R., Brito, M. G., Chichorro, M., & Rosa, C. (2017). Remote Sensing for Mineral Exploration in Central Portugal. *Minerals, 7* (184), p. 30. doi:10.3390/min7100184

Manuel, R., Brito, M. G., Rosa, C., & Chichorro, M. (2015) Remote sensing for mineral exploration in the Góis region, central Portugal. *V Congresso de Jovens Investigadores em Geociências (Estremoz), Livro de Atas.* p. 4.

Martín, M.P. (1998). Cartografía e inventario de incendios forestales en la Península Ibérica a partir de imágenes NOAA-AVHRR. *PhD thesis*. Departamento de Geografía, Universidad de Alcalá.

Martínez Catalán, J.R., Martínez Poyatos, D. & Bea, F. (Coords.) (2004): Zona Centroibérica: Introducción. In: Vera, J.A. (Ed.), *Geología de España*. Soc. Geol. España/Inst. Geol. Min. España (SGE-IGME), Madrid: pp.68-69.

Martínez, F. J., Corretgé, L. G. & Suárez, O. (1990). The Central Iberian Zone (autochthonous sequences): distribution, characteristics and evolution of metamorphism. In: R. D. Dallmeyer & E. Martínez García (Eds), Pre-Mesozoic Geology of Iberia. Springer-Verlag. Berlim. p. 207–211.

Martinez, F.J., Julivert, M., Sebastian, A, Arboleya, M.L. & Ibarguchi, J.I. (1988). Structural and thermal evolution of high-grade areas in the north western parts of the Iberan Massif. *Amer. J. Sci*., 288, pp. 969-996.

Martín-Izard, A., Reguilón, R. & Palero, F. (1992). Las mineralizaciones litiníferas del oeste de Salamanca y Zamora. *Estud. Geol*., 48: 19–30.

Mateus, A. (1995a). Evolução tectono-térmica e potencial metalogenético do troço transmontano da Zona de Falha Manteigas-Vilariça-Bragança. Tese de Doutoramento. Fac. de Ciências da Univ. Lisboa. Tomo 1: 195 p., Tomo 2: 994 p. In: Vieira, R. (2010). Aplitopegmatitos com Elementos Raros da Região entre Almendra (V. N. de Foz-Côa) e Barca d'Alva (Figueira de Castelo Rodrigo). Campo Aplitopegmatítico da Fregeneda-Almendra. *phD Thesis*. Universidade do Porto, Portugal, p. 276.

Mateus, A. (1995b). Tectono-Thermal evolving path and metallogenetic potencial of the Manteigas-Vilariça-Bragança Northern domain, NE Portugal. Gaia: Rev. Geoc., 11: 84–85.

Matte, P. (1986). Tectonics and plate tectonics model for the Variscan belt of Europe. *Tectonophysics* 126, 329 – 374.

Matte, P. (2001). The Variscan collage and orogeny (480-290 Ma) and the tectonic definition of the Armorican microplate: a review. *Terra Nova*. 13, pp.122–128.

Matte, P., & Ribeiro, A. (1975). Forme et orientation de l´ellipsoïde de déformation dans la virgation hercynienne de Galice. Relations avec le plissement et hypothèses sur la genèse de l´arc ibéro-armoricain. *C. R. Acad. Sc. Paris*, Série D, 280: 2825-2828. In: Pérez-Estaún, A., Bea, F., Bastida, F., Marcos, A., Martínez Catalán, J.R., Martínez Poyatos, D., Arenas, R., Díaz García, F., Azor, A.,

Simancas, J.F. & González Lodeiro, F. (2004). La cordillera varisca europea: el Macizo Ibérico. In: Vera, J.A. (Eds.). *Geología de España*. Soc. Geol. España/Inst. Geol. Min. España (SGE/IGME), Madrid, pp. 21-25.

Medeiros, A. C., & Faria, F. L. (1953). Estudos de algumas formações calcárias dos distritos de Vila Real, Viseu e Guarda. *Est. Not. Trab. Serv. Fom. Min.*, Porto, 8 (3-4), pp. 297-312.

Mendes, D., Perrotta, M. M., Costa, M. A. C., & Paes, V. J. C. (2017). Mapeamento espectral para identificação de assinaturas espectrais de minerais de lítio em imagens ASTER (NE/MG). *Anais do XVIII Simpósio Brasileiro de Sensoriamento Remoto*, p. 5273-5280. Santos -SP, Brasil, May 2017.

Mia, M.B. & Fujimitsu, Y. (2012). Mapping hydrothermal altered mineral deposits using Landsat 7 ETM+ image in and around Kuju volcano, Kyushu, Japan. *Journal of Earth System Science*, 121(4), pp. 1049 – 1057.

Moradi, M., Basiri, S., Kananian, A., & Kabiri, K. (2015). Fuzzy logic modeling for hydrothermal gold mineralization mapping using geochemical, geological, ASTER imageries and other geo-data, a case study in Central Alborz, Iran. *Earth Sci Inform,* 8 (1), pp. 197-205.

Moreira, N., Búrcio, M., Dias, R., & Coke, C., 2010. Partição da deformação Varisca nos sectores de Peso da Régua e Vila Nova de Foz Côa (Autóctone da Zona Centro Ibérica). *Comunicações Geológicas,* 97, 147-162.

Mwaniki, M. W., Moeller, M. S., & Schellmann, G. (2015). A comparison of Landsat 8 (OLI) and Landsat 7 (ETM+) in mapping geology and visualising lineaments: A case study of central region Kenya. *ISPRS - International Archives of the Photogrammetry, Remote Sensing and Spatial Information Sciences*, XL-7/W3, 897–903.

National Aeronautics and Space Administration (NASA) (2018a). Landsat 1. https://landsat.gsfc.nasa.gov/landsat-1/. Accessed January 2018.

National Aeronautics and Space Administration (NASA) (2018b). Landsat 2. https://landsat.gsfc.nasa.gov/landsat-2/. Accessed January 2018.

National Aeronautics and Space Administration (NASA) (2018c). Landsat 3. https://landsat.gsfc.nasa.gov/landsat-3/. Accessed January 2018.

National Aeronautics and Space Administration (NASA) (2018d). Landsat 4. https://landsat.gsfc.nasa.gov/landsat-4/. Accessed January 2018.

National Aeronautics and Space Administration (NASA) (2018e). Landsat 5. https://landsat.gsfc.nasa.gov/landsat-5/ . Accessed January 2018.

National Aeronautics and Space Administration (NASA) (2018f). The Multispectral Scanner System. https://landsat.gsfc.nasa.gov/the-multispectral-scanner-system/ . Accessed January 2018.

National Aeronautics and Space Administration (NASA) (2018g). The Thematic Mapper. https://landsat.gsfc.nasa.gov/the-thematic-mapper/ . Accessed January 2018.

National Aeronautics and Space Administration (NASA) 2013. Landsat 7 Science Data User's Handbook. Available at https://landsat.gsfc.nasa.gov/wp-content/uploads/2016/08/Landsat7_Handbook.pdf. Accessed December 2017.

Noronha, F. (2007). The Hercynian orogeny in the NW of Iberian Peninsula. In: A. Lima & E. Roda-Robles (Eds.), *Granitic Pegmatites: the state of the art, Field trip guidebook*, Dep. Geologia FCUP, Porto, Portugal, May 2007, Memórias n.° 9, p. 9–13.

Noronha, F., Ferreira, N., & Marques Sá, C. (2006). Rochas Granitóides: Caracterização petrológica e geoquímica. In: Pereira, E. (Coord.), Carta Geológica de Portugal na escala 1:200000 – Notícia explicativa da Folha 2, Lisboa, *Serv. Geol. Portugal,* 49-68.

Noronha, F., Ramos, J. M. F., Rebelo, J. A., Ribeiro, A. & Ribeiro, M. L. (1979). Essai de corrélation des phases de déformation hercynienne dans le Nord-Ouest Péninsulaire. *Bol. Soc. Geol. Portugal*, 21 (2–3): 227–237.

Noronha, F., Ramos, J. M. F., Rebelo, J. A., Ribeiro, A. & Ribeiro, M. L. (1981). Essai de corrélation des phases de déformation hercynienne dans le Nord-Ouest Péninsulaire. *Leid. Geol. Meded*, 52 (1): 87–91.

Noronha, F., Ribeiro, M.A., Almeida, A., Dória, A., Guedes, A., Lima, A., Martins, H.C., Sant'Ovaia, H., Nogueira, P., Martins, T., Ramos, R., Vieira, R., 2013. Jazigos Filonianos Hidrotermais e Aplitopegmatíticos Espacialmente Associados a Granitos (Norte de Portugal). In: Dias, R., Araújo, A., Terrinha, P., Kullberg, J.C. (Eds.), *Geologia de Portugal, Volume I - Geologia Pré-mesozóica de Portugal*. Escolar Editora, Lisboa, pp. 403–438.

Oen, I.S. (1958). The geology, petrology and ore deposits in the Viseu region, northern Portugal. *Comun. Serv. Geol. de Portugal*, 41: 199 pp.

Oen, I.S. (1970). Granite intrusion, folding and metamorphism in central northern Portugal. *Boletín Geológico y Minero*, LXXXI-II-III: 271-298.

Oliveira, J. M. S. (1982). Orientação geoquímica com vista à escolha da metodologia a seguir na prospecção de mineralizações de estanho e volfrâmio. *Comun. Serv. Geol. Portugal*, 68 (2): 171–178.

Oliveira, J. M. S., & Cramez, P. (1982). Geoquímica do Sn e do W em granitóides hercínicos portugueses na perspectiva da sua especialização metalogenática. *Bol. Soc. Geol. Portugal*, Lisboa, 23, pp. 101-107.

Oliveira, J. M. S., Pereira, E. & Simões, M. (1982). A litogeoquímica na definição das relações entre granitóides e mineralizações de Sn-W. *Comun. Serv. Geol. Portugal*, Lisboa, 68 (1), pp. 55–66.

Ortega, E. & González Lodeiro, F. (1986). La discordância intra-Alcudiense en el domínio meridional de la Zona Centroibérica. *Breviora Geol. Astúrica*, 27: 27–32.

Paixão, H. M., Martins, F. M., Zavala, L. M., & Jordán, A. (2013). Application of remote sensing techniques in the lithological characterization of Rocha da Pena (southern Portugal). *European Geosciences Union General Assembly, 7*.

Patrício, A. (1944). Notas sobre a morfologia da Beira transmontana. *Bol. Soc. Geol. Portugal*, Porto, 4 (1-2), pp. 61-68.

Pereira, B., Azevedo, J., Oliveira, J., Dias, P. S. A., Leal Gomes, C., Carvalho, J., & Marques, A. (2012). Contribution of remote sensing to the evidence and location of granite hosted pegmatites – Ponte da Barca (Minho). In: Ferreira, M. Q., Barata, M. T., Lopes, F. C., Andrade, A. I., Henriques, M. H., Pena dos Reis, R., Alves, E. I. (Eds.) *Para Desenvolver a Terra: Memórias e Notícias de Geociências no Espaço Lusófono.* Imprensa da Universidade de Coimbra. pp. 235-244.

Pereira, E. (1987). Estudo geológico estrutural da região de Celorico de Bastos e sua interpretação geodinâmica. *PhD thesis.* Fac. Ciências Univ. de Lisboa. 274 p. In: Dias, R., Ribeiro, A., Coke, C., Pereira, E., Rodrigues, J., Castro, P., Moreira, N., Rebelo, J. (2013). Evolução estrutural dos sectores setentrionais do Autóctone da Zona Centro-Ibérica. In: Dias, R., Araújo, A., terrinha, P., Kullberg, J.C. (Eds). *Geologia de Portugal. Volume I – Geologia Pré-mesozóica de Portugal*, Escolar Editora. pp. 73-147.

Pereira, E., Ribeiro, A. & Meireles, C. (1993). Cisalhamentos Hercínicos e controlo das mineralizações de Sn-W, Au e U na Zona Centro Ibérica, em Portugal. *Cuaderno Lab. Xeolóxico de Laxe*. Coruña. Vol. 18, pp.89-119.

Pereira, I. (2014). Capítulo III – Zona de Cisalhamento de Juzbado Penalva do Castelo e Tectónica Regional. In: Petrologia e geoquímica dos migmatitos e granitóides do sector Figueira de Castelo Rodrigo - rio Águeda: evolução litológica e estrutural no contexto da zona de Cisalhamento Juzbado - Penalva do Castelo. Master thesis, Universidade de Évora. pp. 57-68.

Pérez-Estaún, A., Bea, F., Bastida, F., Marcos, A., Martínez Catalán, J.R., Martínez Poyatos, D., Arenas, R., Díaz García, F., Azor, A., Simancas, J.F. & González Lodeiro, F. (2004). La cordillera varisca europea: el Macizo Ibérico. In: Vera, J.A. (Eds.). *Geología de España*. Soc. Geol. España/Inst. Geol. Min. España (SGE/IGME), Madrid, pp. 21-25

Perrotta, M.M., Souza Filho, C.R., & Leite, C.A.S. (2005). Mapeamento espectral de intrusões pegmatíticas relacionadas a mineralizações de lítio, gemas e minerais industriais na região do vale do Jequitinhonha (MG) a partir de imagens ASTER. In: *Anais do XII Simpósio Brasileiro de Sensoriamento Remoto*, p. 1855-1862. Goiânia, Brasil, December 2005.

Pinto, A. F. F. (1984a). Rochas calcossilicatadas do Complexo Xisto-Grauváquico: mineralogia, geoquímica, evolução genética. *Comum. Serv. Geol. Portugal*, Lisboa, 70 (1), pp. 55-62.

Pinto, A. F. F. (1984b). Rochas epidosíticas de Almendra: mineralogia, geoquímica, evolução genética. *Comum. Serv. Geol. Portugal*, Lisboa, 70 (1), pp. 63-71.

Pour, A., & Hashim, M. (2015). Hydrothermal alteration mapping from Landsat-8 data, Sar Chesmeh copper mining district, south-eastern Islamic Republic of Iran. *Journal of Taibah University for Science, 9*, pp. 155-166.

Prasad, A. D., Jain, K., & Gairola, A. (2013). Mapping of Lineaments and Knowledge Base Preparation using Geomatics Techniques for part of the Godavari and Tapi Basins, India: A Case Study. *International Journal of Computer Applications* 70(9):39-47.

Quesada, C. (1990). Precambrian successions in SW Iberia: their relationship to 'Cadomian' orogenic events. In: R. S. D'Lemos, M. a. Strachan and C. G. Topley (Eds.). *The Cadomian Orogeny*. Geol. Soc. Spec. Public., 51: 353-362. In: Oliveira, J.T., Pereira, E., Piçarra, J.M., Young, T. & Romano, M. (1992). O Paleozóico Inferior de Portugal: síntese da estratigrafia e da evolução paleogeográfica. In: Gutiérrez Marco, J.G., Saavedra, J. & Rábano, I. (Eds.) *Paleozoico Inferior de Ibero-América*, Univ. Extremadura, pp. 359-375.

Rabaça, T. L., Conde, L. N., Pinto, A. F., & Pereira, A. J. (2004). Avaliação das potencialidades de técnicas de detecção remota como suporte à cartografia geológica na região central de Portugal. *Revista Electrónica de Ciências da Terra, 2*(1), pp. 1-14.

Rajesh, H. M. (2004). Application of remote sensing and GIS in mineral resource mapping—An overview. *Mineralogical Journal*, 99(3), p. 83–103.

Ramos, J. M. F., Oliveira, J. M., Viegas, L. F. S. & Simões, M. (1978). Prospecção Geológico-Mineira na Região de Almendra–Castelo Melhor. Congresso, Ordem dos *Engenheiros*. In: Silva, A. F., & Ribeiro, M. L. (1991). Notícia explicativa da folha 15-A – Vila Nova de Foz Côa – da carta Geológica de Portugal na escala 1/50.000. *Serv. Geol. Portugal.*, p. 52.

Ramsay, J., & Htiber, M. (1987). The techniques of modern structural geology. Volume 2: folds and fractures. Academic Press Limited, London.

Rebelo, J. A. & Romano, M. (1986). A contribution to the lithostratigraphy and paleontology of the Lower Paleozoic rocks of the Moncorvo region, northeast Portugal. *Comun. Serv. Geol. Portugal*, 72 (1-2): 45–57

Ribeiro, A. (1974). Contribution à l'étude tectonique de Trás-os-Montes oriental. *Mem. Serv. Geol. Portugal, Lisboa*, 24 (Nova Série). 168 p.

Ribeiro, A. (1990). Part IV – Central-Iberian Zone. Introduction. In: Dallmeyer, R. D. & Martinez Garcia, E. (Eds.) *Pre-Mesozoic Geology of Iberia*, Springer-Verlag, Berlin, Heidelberg, pp. 143-144.

Ribeiro, A., Antunes, M., Ferreira, M., Rocha, R., Soares, A., Zbyszewski, G., Almeida, F., Carvalho, D. & Monteiro, J. (1979). Introduction à la Géologie Générale du Portugal. *Serv. Geol. Portugal*, Lisboa.114 p.

Ribeiro, A., Munhá, J., Dias, R., Mateus, A., Pereira, E., Ribeiro, L., Fonseca, P., Araújo, A., Oliveira, T., Romão, J., Chaminé, H., Coke, C., & Pedro, J. (2007). Geodynamic evolution of SW Europe Variscides. *Tectonics,* 26, 1-24.

Ribeiro, A., Pereira, E. & Dias, R. (1990). Structure in the Northwest of the Iberian Peninsula. In: Dallmeyer, R.D. & Martinez Garcia, E. (Eds.): *Pre-Mesozoic Geology of Iberia*, Springer-Verlag, Berlin, Heidelberg, pp. 220-236.

Ribeiro, A., Pereira, E., & Rodrigues, J. (2006). Tectónica. In: Pereira, E. (Coord.), Carta Geológica de Portugal na escala 1:200000 – Notícia explicativa da Folha 2, Lisboa, *Serv. Geol. Portugal*, 69-76.

Ribeiro, M. L. (2001). Notícia explicativa da carta geológica simplificada do Parque Arqueológico do Vale do Côa. Parque Arqueológico do Vale do Côa. Vila Nova de Foz Côa. 71 p.

Ribeiro, M.A., Sousa, M.B., & Noronha, F. (1993). A Formação de Envendos e as rochas ácidas associadas. *Publ. Museu e Lab. Miner. e Geológico da Fac. Ciências do Porto*, Nova Série, 7, 1-20. ISSN 0370-0631

Richards, J. A. & Jia, X. (2006). Remote Sensing Digital Image Analysis: An Introduction. 4th edition. Berlin, Germany: *Springer*. p. 454.

Rockwell, B.W., & Hofstra, A.H. (2008). Identification of quartz and carbonate minerals across northern Nevada using ASTER thermal infrared emissivity data— implications for geologic mapping and mineral resource investigations in well-studied and frontier areas. *Geosphere* 4, 218–246.

Roda, E. (1993). Distribución, Caracteristicas y Petrogenesis de las Pegmatitas de La Fregeneda (Salamanca). *phD thesis*. Dep. Min. y Petrol. – UPV, Bilbau, Espanha. 199 p.

Roda, E., Pesquera, A., Velasco, F. & Fontan, F. (1999). The granitic pegmatites of the Fregeneda area (Salamanca, Spain): characteristics and petrogenesis. *Mineral. Mag.*, 63 (4): 535–558.

Roda, E., Vieira, R., Lima, A., Pesquera, A., Noronha, F., & Fontan, F. (2007). The Fregeneda-Almendra pegmatitic field (Spain & Portugal): mineral assemblages and regional zonation. In: T. Martins, & R. Vieira (Eds.), *Granitic Pegmatites: the state of the art, Book of Abstracts. Memórias n.° 8*, pp. 81–82. Porto, Portugal: Dep. Geologia FCUP.

Roda, E., Vieira, R., Pesquera, A., & Lima, A. (2010). Chemical variations and significance of the phosphates from the Fregeneda-Almendra pegmatite field, Central Iberian Zone (Spain and Portugal). *Mineral. Petrol., 100*(1-2), 23–34.

Rodrigues, J., Pereira, E., & Ribeiro, A. (2011). Complexo de Mantos Parautóctones do NE de Portugal: Estrutura interna e Tectonoestratigrafia. In: Dias, R., Araújo, A., terrinha, P., Kullberg, J.C. (Eds). *Geologia de Portugal. Volume I – Geologia Pré-mesozóica de Portugal*, Escolar Editora. pp. 269-325.

Rodríguez Alonso, M.D., Díez Balda, M.A., Perejón, A., Pieren, A., Liñán, E., López Díaz, F., Moreno, F., Gámez Vintaned, J.A., Gónzalez Lodeiro, F., Martínez Poyatos, D. & Vegas, R. (2004). Domínio del Complejo Esquisto-Grauváquico:

Estratigrafía. La secuencia litoestratigráfica del Neoproterozóico-Câmbrico Inferior. In: Vera, J.A. (Eds.). *Geología de España*. SGE-IGME, Madrid, 78-81.

Romão, J., & Ribeiro, A. (1992). Thrust tectonics of sardic age the Rosmanihal área (Beira Baixa, Central Portugal). *Comum. Serv. Geol. Portugal*. Tomo 78, fasc. 2. 87-95p.

Romão, J., Coke, C., Dias, R., & Ribeiro, R. (2005). Transient inversion during the opening stage of the wilson cycle «sardic phase» in the iberian variscides – stratigraphic and tectonic record. *Geodinamica Acta* 18/2. In: Dias, R., Ribeiro, A., Coke, C., Pereira, E., Rodrigues, J., Castro, P., Moreira, N., Rebelo, J. (2013). Evolução estrutural dos sectores setentrionais do Autóctone da Zona Centro-Ibérica. In: Dias, R., Araújo, A., terrinha, P., Kullberg, J.C. (Eds). *Geologia de Portugal. Volume I – Geologia Pré-mesozóica de Portugal*, Escolar Editora. pp. 73-147.

Rowan, L. C., & Mars, J. C. (2003). Lithologic mapping in the Mountain Pass, California area using Advanced Spaceborne Thermal Emission and Reflection Radiometer (ASTER) data. *Remote Sensing of Environment, 84*(3), pp. 350-366.

Sabins, F. F. (1997). Remote Sensing—Principles and Interpretation. 3rd Edition, W.H. Freeman, New York, NY.

Sabins, F. F. (1999). Remote sensing for mineral exploration. *Ore Geology Reviews, 14*, pp. 157–183.

Sabins, F. F., & Miller, R. M. (1994). Resource assessment — Salar de Uyuni and vicinity. *Proceedings of Tenth Thematic Conference on Geologic Remote Sensing*. Environmental Research Institute of Michigan, Ann Arbor, MI, pp. 192–1103. In: Sabins, F. F. (1999). Remote sensing for mineral exploration. *Ore Geology Reviews, 14*, pp. 157–183.

San José, M.A., Pieren, A.P., Garcia-Hidalgo, J.F., Vilas, L., Herranz, P., Pelaez, J.R., Perejon, A. (1990). Central Iberian Zone. Autochthonous sequences: Ante-Ordovician stratigraphy. In: Dallmeyer, R.D. & Martinez Garcia, E. (Eds.). *Pre-Mesozoic Geology of Iberia*, Springer-Verlag, Berlin, Heidelberg, pp. 147- 159.

Schermerhorn, L.J.G. (1956). Igneous, metamorphic and ore geology of the Castro Daire – São Pedro do Sul – Sátão region (northern Portugal). *Comun. Serv. Geol. de Portugal*, 37, 617 pp.

Sides, E., Vairinho, M., & Woldai, T. (2000). Application of image enhancement of remote sensed data for geological mapping in the Moura-Ficalho area, Portugal. *Comunicações do IGM, Tomo 87*, pp. 113-126

Silva, A. F. & Ribeiro, A. (1985). Thrust Tectonics of Sardic Age in the Alto Douro Region (Northeastern Portugal). *Comun. Serv. Geol. Portugal*, 71 (2): 151–157.

Silva, A. F., & Ribeiro, M. L. (1991). Notícia explicativa da folha 15-A – Vila Nova de Foz Côa – da carta Geológica de Portugal na escala 1/50.000. *Serv. Geol. Portugal.*, p. 52.

Silva, A. F., & Ribeiro, M. L. (1994). Notícia explicativa da folha 15-B – Freixo de Espada à Cinta – da carta Geológica de Portugal na escala 1/50.000. *Inst. Geol. e Mineiro*, p. 48.

Silva, A. F., Rebelo, J. A ., & Ribeiro, M. L. (1988a). Carta Geológica de Portugal na escala 1/50.000 – folha 11-C – Torre de Moncorvo. *Serv. Geol. Portugal*.

Silva, A. F., Rebelo, J. A., & Ribeiro, M. L. (1989). Notícia Explicativa da folha 11-C – Torre de Moncorvo – da Carta Geológica de Portugal na escala 1/50.000. *Serv. Geol. Portugal,* Lisboa, 65 pp.

Silva, A. F., Santos, A. J., Ribeiro, A., & Ribeiro, M. L. (1990a). Carta Geológica de Portugal na escala 1/50.000 – folha 15-A – Vila Nova de Foz Côa. *Serv. Geol. Portugal.*

Silva, A. F., Santos, A. J., Ribeiro, A., Cabral, J., & Ribeiro , M. L. (1990b). Carta Geológica de Portugal na escala 1/50.000 – folha 15-B – Freixo de Espada à Cinta. *Serv. Geol. Portugal*.

Silva, A., Romão, J., Sequeira, A., & Ribeiro, M. L. (1988b). Geotransversal do Grupo das Beiras (Complexo Xisto-Grauváquico) entre os sinclinórios de Mação e Penha Garcia (Centro-Leste de Portugal). *XI Reunião Geol. Oeste Peninsular*, Bragança. In: Romão, J., Ribeiro, A. (1992). Thrust tectonics of sardic age the Rosmanihal área (Beira Baixa, Central Portugal). *Comum. Serv. Geol. Portugal*. Tomo 78, fasc. 2. 87-95p.

Silva, I. (2013). Geología de las zonas Centro Ibérica y Galicia – Trás-Os-Montes en la parte oriental del Complejo de Morais, Portugal/España. *phD Thesis*. Universidad de Salamanca, Spain, p. 445.

Simmons, W. B. & Webber, K. L. (2008). Pegmatite genesis: state of the art. *Eur. J. Mineral.*, 20: 421–438.

Simmons, W.B., Webber, K.L., Falster A.U. & Nizamoff, J.W. (2003). Pegmatology, Pegmatite Mineralogy, Petrology and Petrogenesis. Rubelite Press, New Orleans, Lousiana.

Sinergeo, Lda. & Universidade do Minho (2013). PROSPEG – Projecto de prospecção, análise distanciada e detecção remota de pegmatitos. *Sinergeo - Soluções Aplicadas em Geologia, Hidrogeologia e Ambiente, Lda*. 146 p.

Singh, A., & Harrison, A. (1985). Standardized principal components. *Int. J. Rem. Sens*, 6(6), pp. 883–896. In: Mia, M.B. & Fujimitsu, Y. (2012). Mapping hydrothermal altered mineral deposits using Landsat 7 ETM+ image in and around Kuju volcano, Kyushu, Japan. *Journal of Earth System Science*, 121(4), pp. 1049 – 1057.

Sousa, M. B. (1981). Complexo Xisto-Grauváquico do Douro: os xistos cloríticos com magnetite e o seu valor estratigráfico. *Comun. Serv. Geol. Portugal*, 67 (1): 53–55.

Sousa, M. B. (1982). Litostratigrafia e estrutura do "Complexo Xisto-Grauváquico Ante-Ordovícico" – Grupo do Douro (Nordeste de Portugal). *Unpublished Ph-D thesis*. Centro de Geociências da Univ. Coimbra, 222 pp.

Sousa, M. B. (1983a). Considerações paleogeográficas e ensaio de correlação das formações do Grupo do Douro (CXG) com as formações ante-Ordovícicas da Zona Centro-Ibérica. *Memórias e Notícias*, *Publ. Mus. Lab. Min. Geol. Univ. Coimbra,* 95: 65-98

Sousa, M. B. (1983b). Litostratigrafia do CXG – Grupo do Douro (NE de Portugal). *Memórias e Notícias, Publ. Mus. Lab. Min. Geol. Univ. Coimbra*, 95: 3-63.

Sousa, M. B. (1984). Considerações sobre a estratigrafia do Complexo Xisto-Grauváquico (CXG) e sua relação com o Paleozóico Inferior. *Cuad. Geol. Ibérica*, 9: 9-36.

Sousa, M. B., & Sequeira, A. D. (1989) Notícia Explicativa da folha 10-D – Alijó – da Carta Geológica de Portugal na escala 1/50.000. *Serv. Geol. Portugal.*

Sousa, M. B., Sequeira, A. D., Neiva, J. C., Neiva, A., & Azevedo, M. (1987). Carta Geológica de Portugal na escala 1/50.000 – folha 10-D – Alijó. *Serv. Geol. Portugal.*

Stussi, J. M. (1989). Granitoid chemistry and associated mineralization in the French Variscan. *Economic Geology,* 84 (5): 1363–1381. In: Dias, G., Noronha, F. & Ferreira, N. (2000). Variscan Plutonism in the Central Iberian Zone, Northern

Portugal. *Eurogranites 2000 Field Meeting Guide*, September 2000, Portugal. p. 1–15.

Teixeira, C. (1955). *Notas sobre geologia de Portugal. O Complexo Xisto Grauváquico Ante-Ordovícico*. Emp. Lit. Fluminense. Lisboa. 50 p.

Trueman, D.L., Černý, P. (1982). Exploration for rare-element granitic pegmatites. In: Černý, P. (Ed.) *Granitic Pegmatites in Science and Industry*. Mineralogical Association of Canada, Short Course Handbook 8, 463-494.

Tucker, C. J. (1979). Red and photographic infrared linear combinations for monitoring vegetation. *Remote Sens. Environ.*, 8, 127–150.

United States Geological Survey (USGS) (2017a). Original Spectra: Base Spectra. https://crustal.usgs.gov/speclab/QueryAll07a.php. Accessed January 2018.

United States Geological Survey (USGS) (2017b). Landsat Project Description. https://landsat.usgs.gov/landsat-project-description. Accessed December 2017.

United States Geological Survey (USGS) (2017c). Landsat Missions: Imaging the Earth Since 1972. https://landsat.usgs.gov/landsat-missions-timeline. Accessed December 2017.

United States Geological Survey (USGS) (2017d). Landsat Missions: Landsat 7. https://landsat.usgs.gov/landsat-7. Accessed January 2018.

United States Geological Survey (USGS) (2017e). https://landsat.usgs.gov/what-are-band-designations-landsat-satellites. Accessed December 2017.

United States Geological Survey (USGS) (2018). https://earthexplorer.usgs.gov/ . Accessed January 2018.

USGS Landsat Program (2017). "Comparison of #Landsat 7, 8, #Sentinel 2, #ASTER & #MODIS bands. View band designations for all #Landsat sensors at https://on.doi.gov/2mOjwjR". 3 March 2017, 8:30 am. Tweet. Available at https://twitter.com/usgslandsat/status/837696716417687553. Accessed December 2017.

Viegas, L. (1983). Recursos minerais de volfrâmio e estanho na região de Freixo-Escalhão. Relatório interno do Serv. Fom. Min., Porto. 45 p. (Unpublished).

Viegas, L., Lima, L.P., Soares, J. & Fonseca, E. C. (1983-85). Aplicação da análise estatística multi-variada ao estudo de amostras de sedimentos na região de Escalhão- Barca D'Alva (NE de Portugal). *Bol. Soc. Geol. Portugal*, XXIV: 161–169.

Vieira, R. (2010). Aplitopegmatitos com Elementos Raros da Região entre Almendra (V. N. de Foz-Côa) e Barca d'Alva (Figueira de Castelo Rodrigo). Campo Aplitopegmatítico da Fregeneda-Almendra. *phD Thesis*. Universidade do Porto, Portugal, p. 276.

Vieira, R., & Lima, A. (2005a). The rare element (Li-rich) pegmatite-aplite veins of the Almendra – Souto region. (Vila Nova de Foz-Côa and Penedono - NE Portugal). *Abstracts of the international meeting, crystallization processes in granitic pegmatites: petrologic, mineralogic and geochemical aspects*, Elba, Itália, p. 48–49.

Vieira, R., & Lima, A. (2005b). Relação geoquímica entre os aplitopegmatitos da região de Almendra – Souto e os granitos envolventes (NE de Portugal). *Livro de actas da XIV Semana de Geoquímica & VIII Congresso de Geoquímica dos Países de Língua Portuguesa, I*, 189–193.

Vieira, R., & Lima, A. (2007). Locality No. 3, Bajoca Mine, Almendra, Portugal. In: A. Lima, & E. Roda-Robles (Eds.), *Granitic Pegmatites: the state of the art, Field trip guidebook. Memórias n.° 9*, pp. 39-43. Porto, Portugal, May 2007: Dep. Geologia FCUP.

Vieira, R., Lima, A., & Roda, E. (2008). Aplitopegmatitos litiníferos do sector Almendra–Barca D'Alva (NE Portugal): Controlo estrutural e metamórfico. *Resumos da 8ª Conferência Anual do GGET, Dep. Geol. FCUP* (Memórias n.º 13), pp. 52–56.

Vieira, R., Lima, A., Roda, E., & Martins, T. (2007a). Lithium-bearing pegmatite resources at Fregeneda-Almendra pegmatitic field (Spain & Portugal). *Goldschmidt Conference Abstracts, Geochim. Cosmochim. Acta, 71* (15-1).

Vieira, R., Lima, A., Roda, E., & Pesquera, A. (2007b). Mica-geochemistry from Fregeneda (Spain) – Almendra (Portugal) Pegmatitic Field Veins: preliminary data. *Resumos da XV Semana de Geoquímica e VI Congresso Ibérico de Geoquímica*, 57-60.

Vieira, R., Silva, F., & Roda, E. (2007c). Lithium Pegmatites Exploration in eastern Portugal using Statistical and Geoestatistical Analysis. *Resumos do 23º International Applied Geochemistry Symposium (IAGS 2007)*, 63.

Weier, J. & Herring, D. (2000). Measuring vegetation (NDVI&EVI). Available at: https://earthobservatory.nasa.gov/Features/MeasuringVegetation/ . Accessed October 2017.

Appendices

Appendix A – Geological map at the scale 1:10,000 (Viegas, 1983)
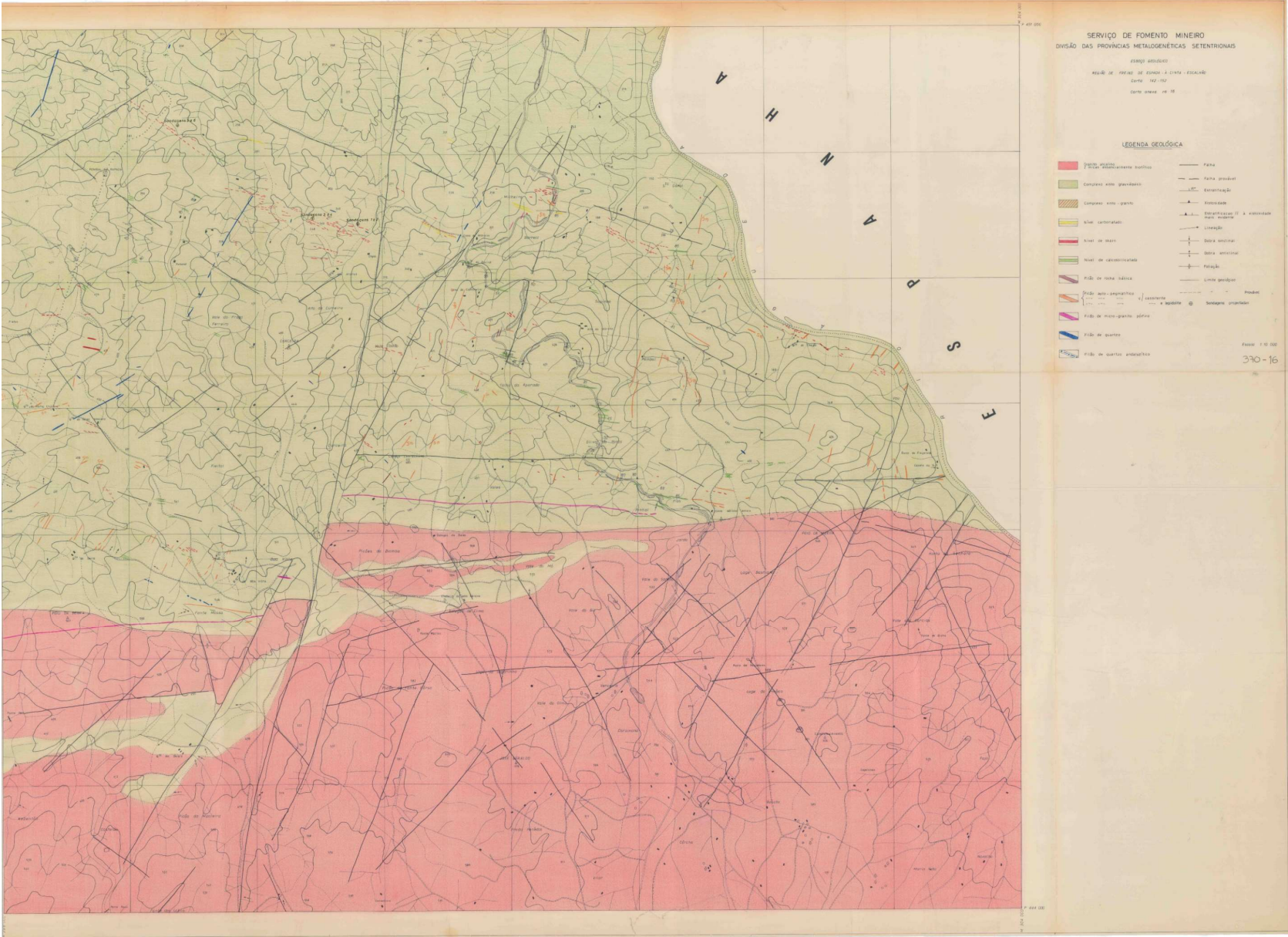
Appendix B – Burned areas

In order to discriminate burned areas two spectral indices were applied: (i) the Burned Area Index (BAI), and (ii) the Normalized Burn Ratio (NBR).

The Burned Area Index (Martín,1998) highlights burned land in the Red (R) to Near-Infrared (NIR) spectrum and emphasizes the charcoal signal is post-fire images. The BAI is calculated through the following expression:

$$BAI = \frac{1}{(0.1 + R)^2 + (0.06 + NIR)}$$

Brighter pixels in the BAI resulting image indicate burned areas.

The Normalized Burn Ratio (NBR) was designed to highlight burned areas and estimate fire severity (Key & Benson, 2005). The formula is similar to NDVI, except shortwave-infrared (SWIR) wavelengths are used instead of the Red band:

$$NBR = \frac{NIR - SWIR}{NIR + SWIR}$$

Healthy vegetation has very high reflectance in the NIR and low reflectance in the SWIR region, while recently burned areas present the opposite behavior. Taking this into account, high NBR values generally indicate healthy vegetation and low values indicate bare ground and recently burned areas.

The two indexes were applied to all satellite products. Sentinel-2 and Landsat 5 images are the ones which present a higher burned area. In the case of ASTER and Landsat 8, the burned areas are relatively small and more difficult to identify.

In this study, NBR is better at highlighting the burned areas because the normalization of the index removes within-scene topographic effects (Key & Benson, 2005).

Landsat 5 Burned Area Index and Normalized Burn Ratio

Legend

| | Bajoca mining concession | | Studied area | | Feli mine | | Alberto mine |
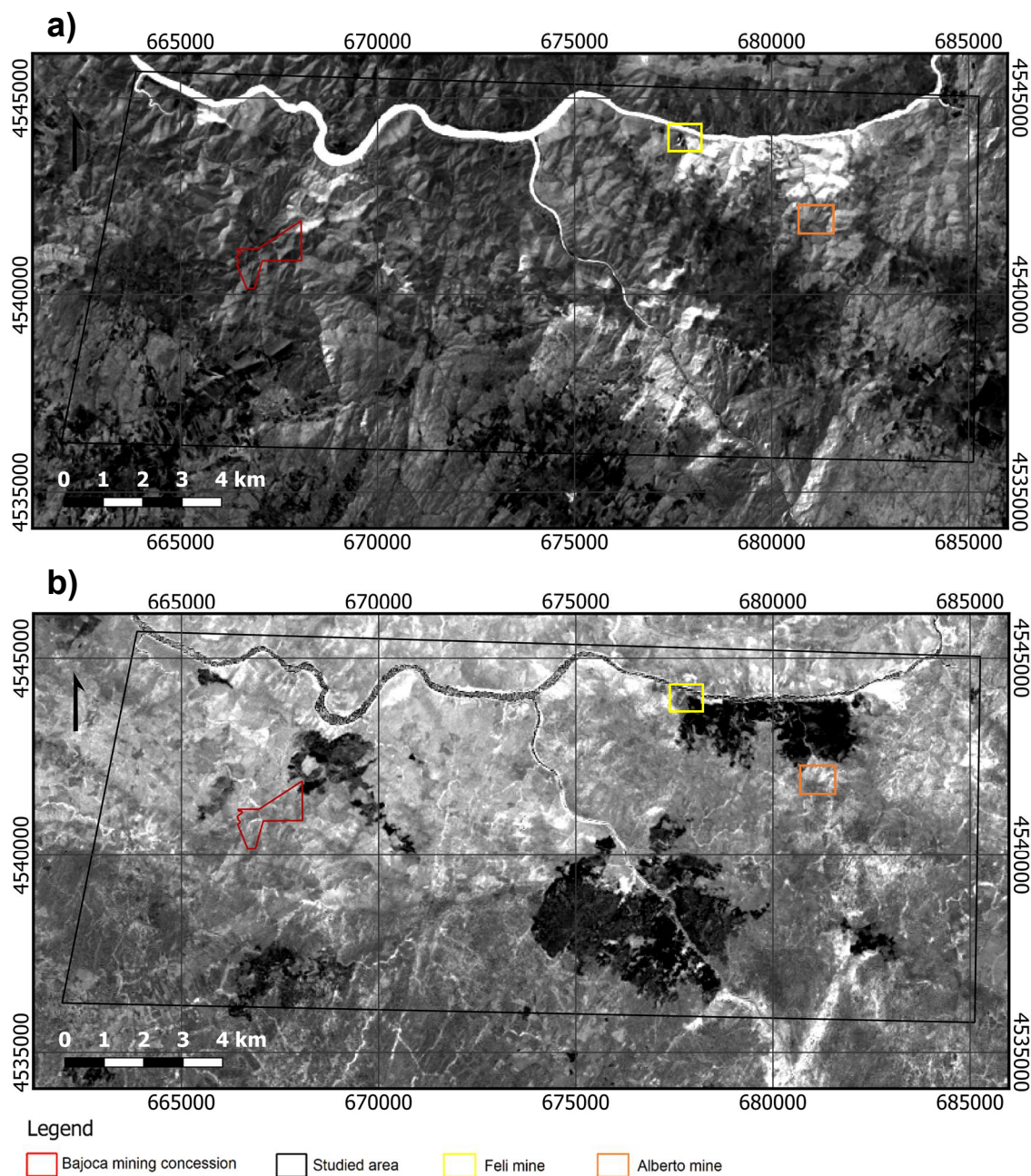
Sentinel-2 Burned Area Index and Normalized Burn Ratio

a)

b)

Legend

☐ Bajoca mining concession   ☐ Studied area   ☐ Feli mine   ☐ Alberto mine

ASTER Burned Area Index and Normalized Burn Ratio
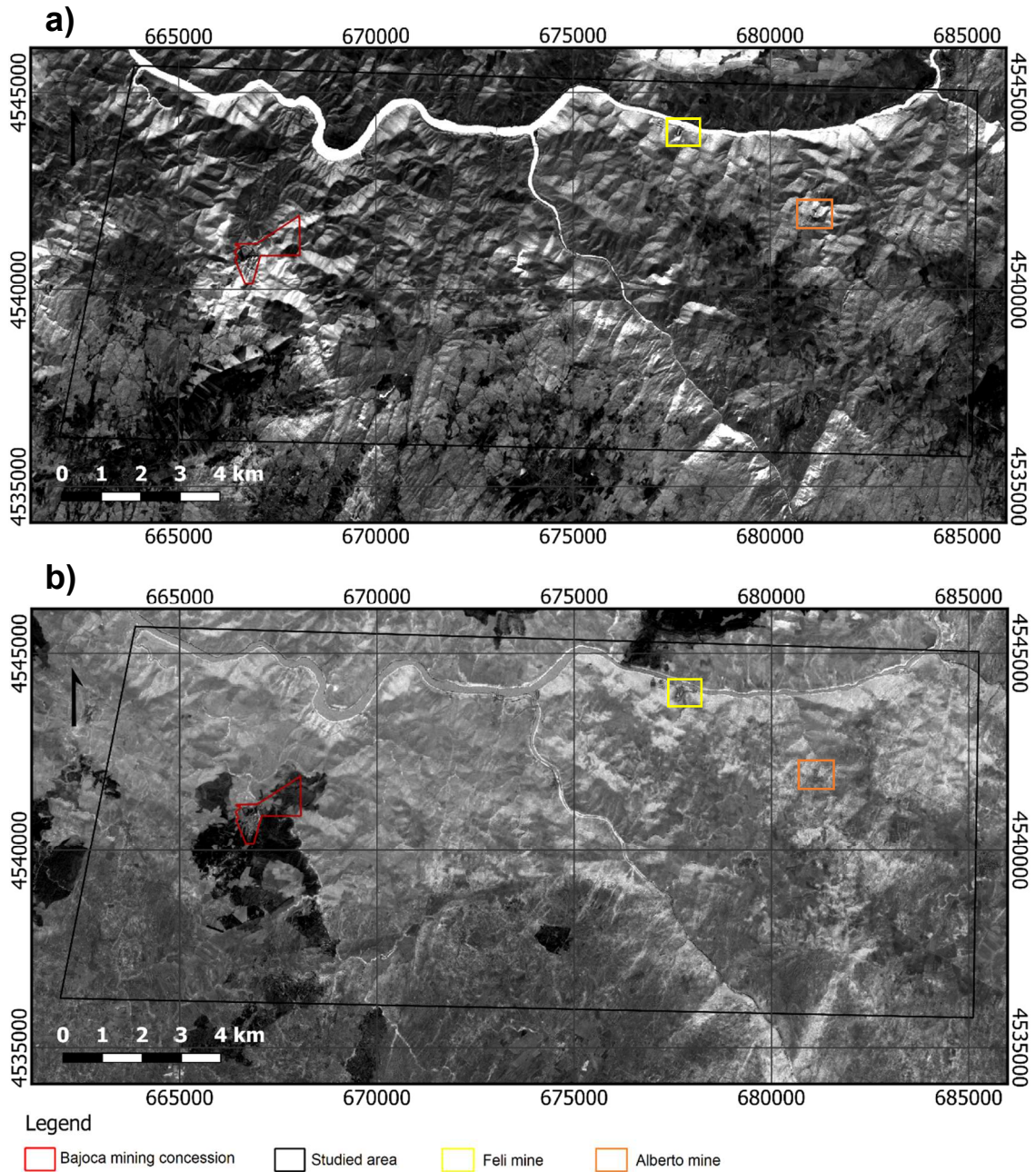
Legend

Bajoca mining concession	Studied area	Feli mine	Alberto mine
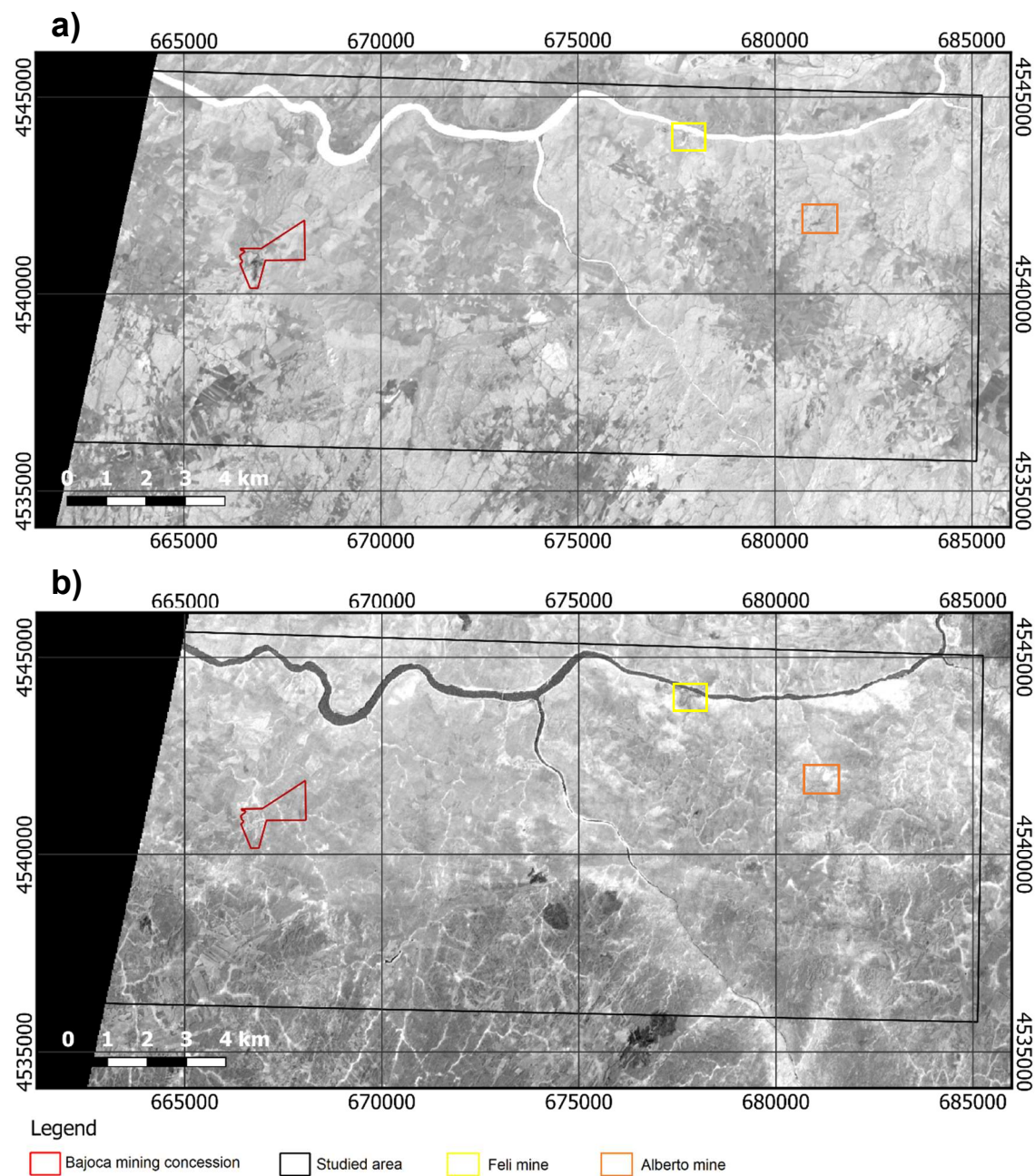
Landsat 8 Burned Area Index and Normalized Burn Ratio

a)

b)

Legend

☐ Bajoca mining concession　☐ Studied area　☐ Feli mine　☐ Alberto mine
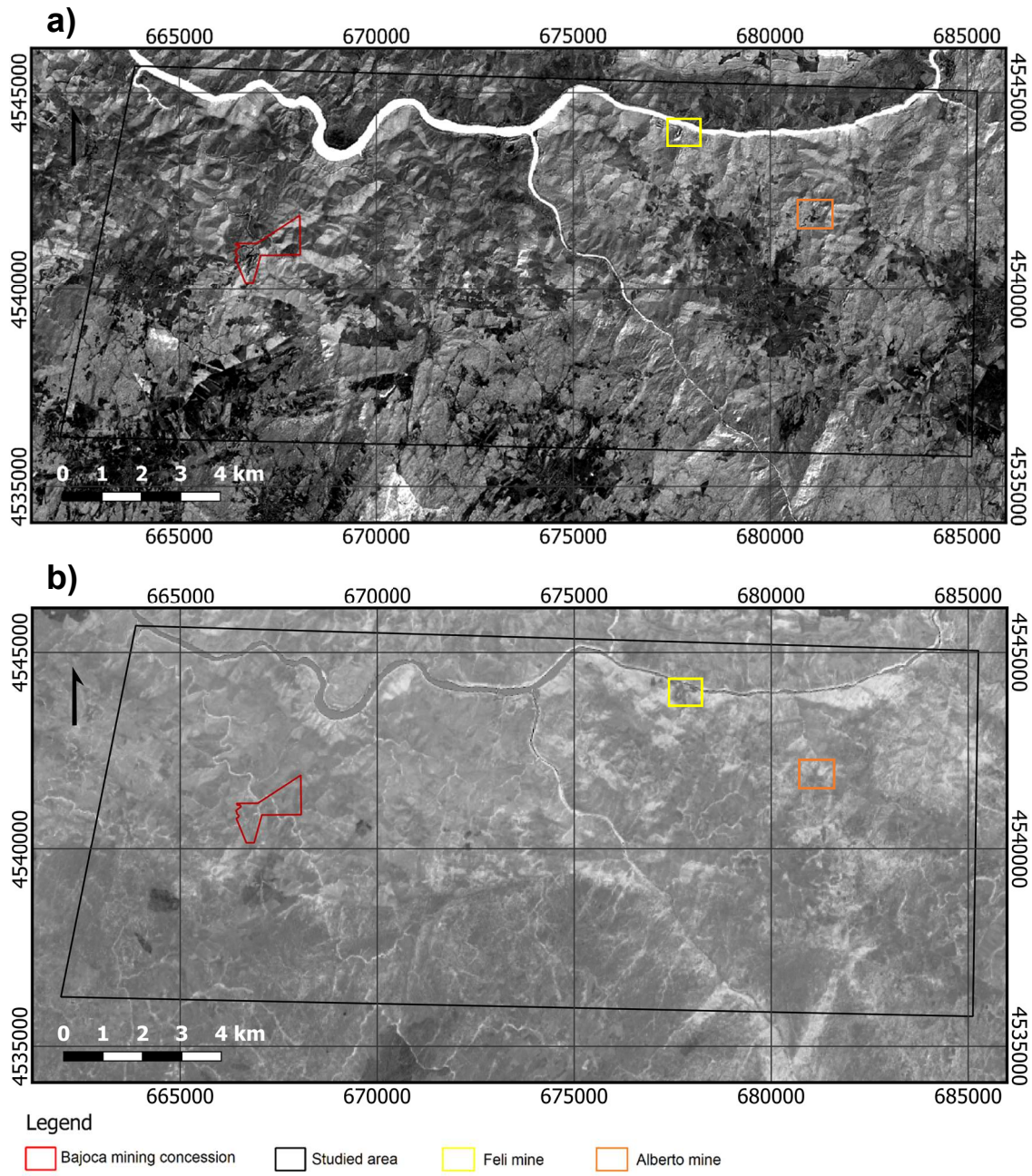
Appendix C – Band ratio

Iron oxides

Landsat 8

Landsat 5

Landsat 8: a) ratio 4/2 image with density slice (high ratio values shown in red); b) histogram of 4/2 image; c) Ratio 4/2 image.

Landsat 5: d) ratio 3/1 image with density slice (high ratio values shown in red); e) histogram of 3/1 image; f) Ratio 3/1 image.

Ferric oxides (ASTER) and ferrous minerals (Sentinel-2)
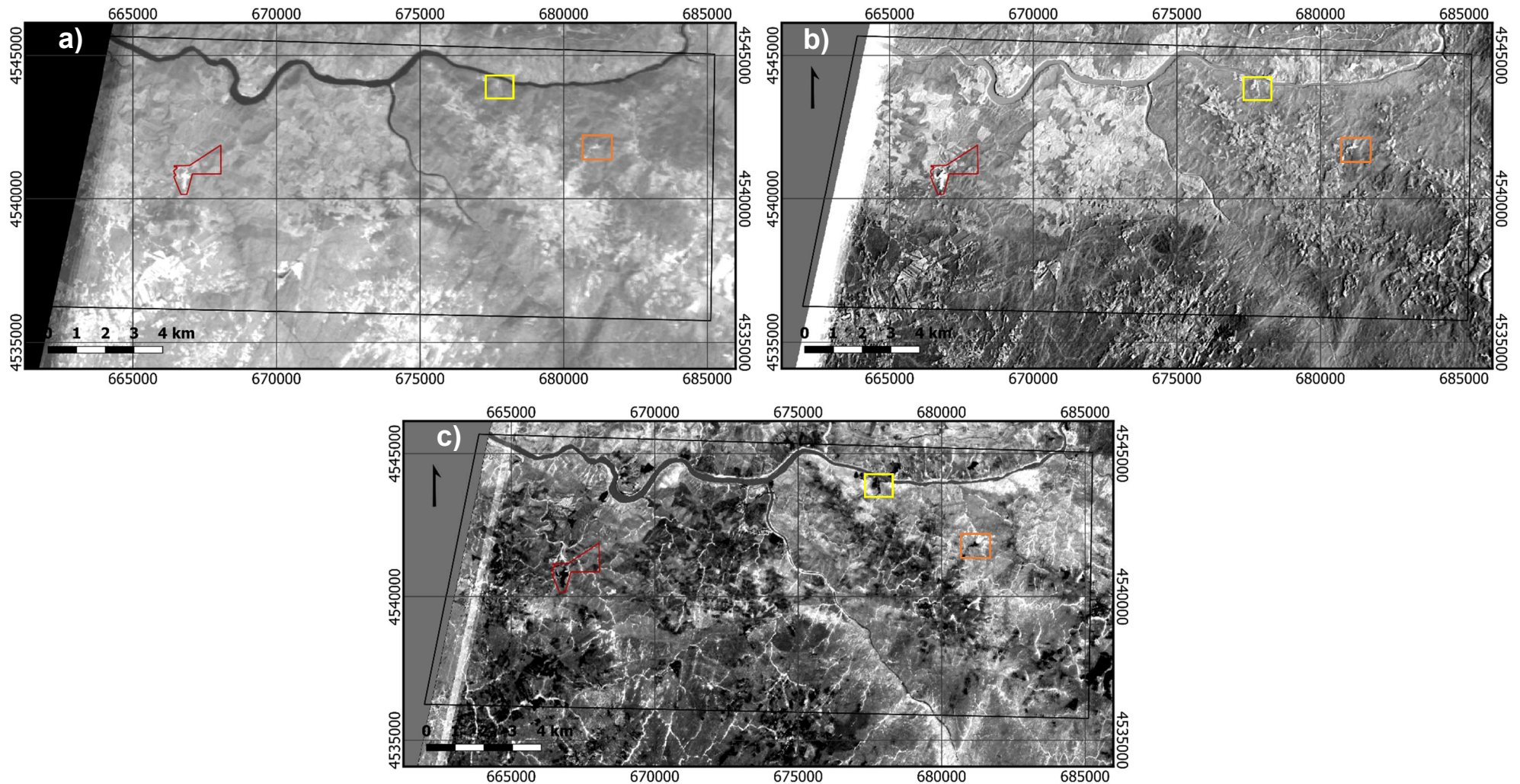
ASTER

Sentinel-2
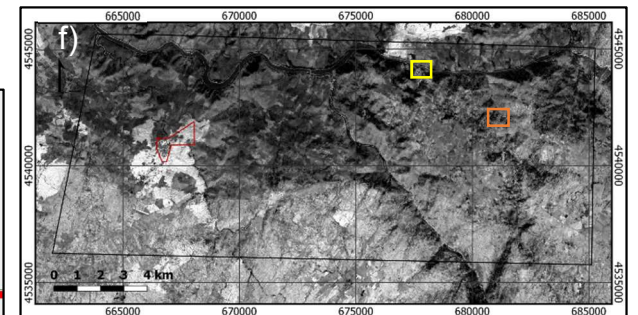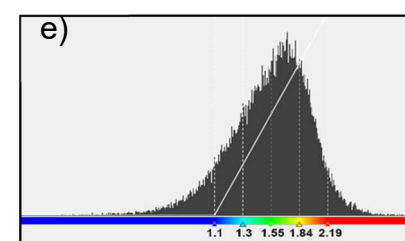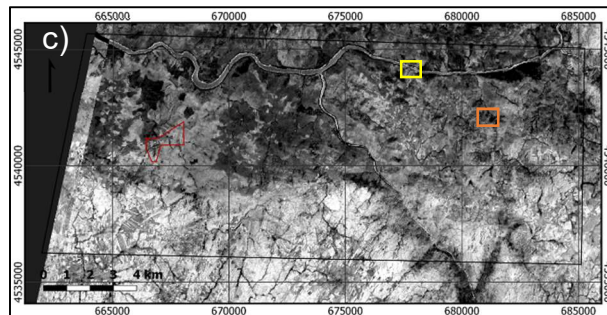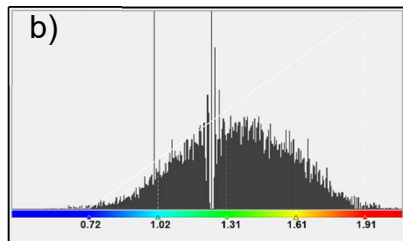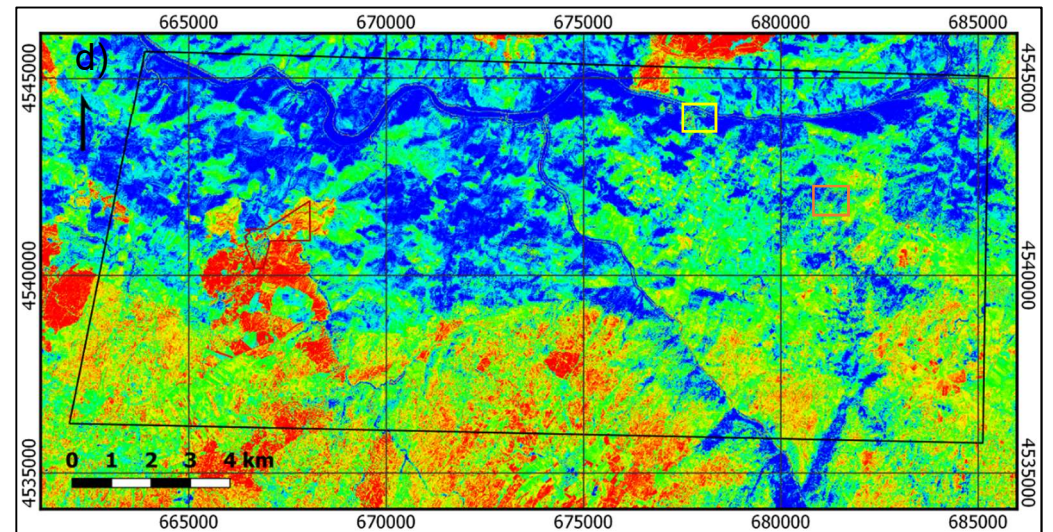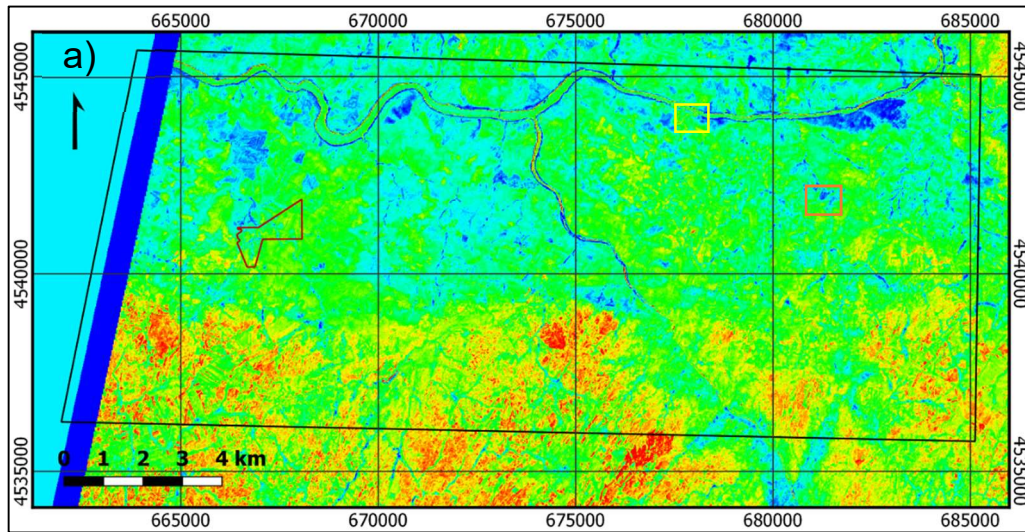
Legend

Bajoca mining concession   Studied area   Feli mine   Alberto mine

ASTER: a) ratio 4/3 image with density slice (high ratio values shown in red); b) histogram of 4/3 image; c) Ratio 4/3 image.

Sentinel-2: d) ratio 11/8 image with density slice (high ratio values shown in red); e) histogram of 11/8 image; f) Ratio 11/8 image.

Alunite and clay minerals

Sentinel-2

Legend

☐ (red) Bajoca mining concession ☐ (black) Studied area ☐ (yellow) Feli mine ☐ (orange) Alberto mine
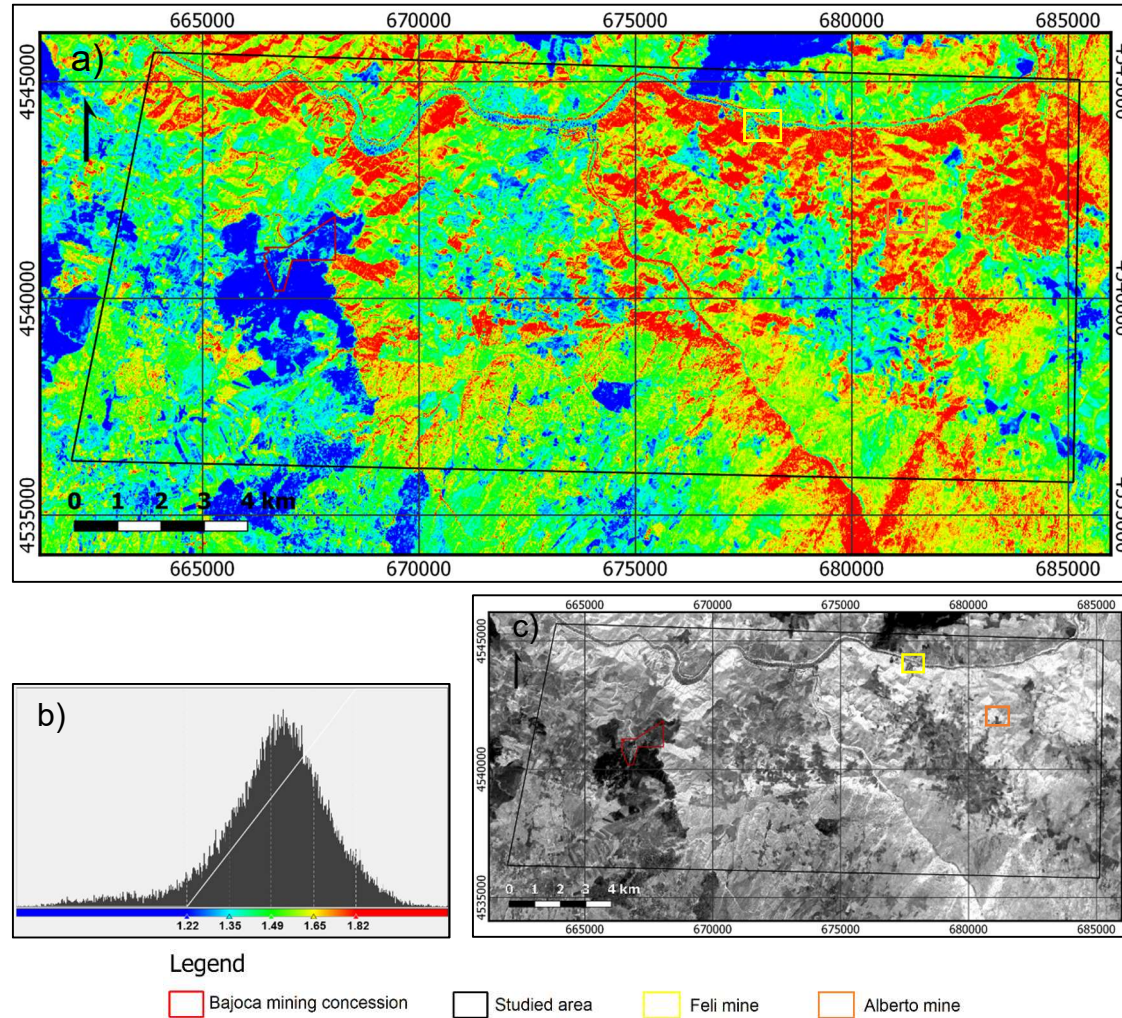
a) ratio 11/12 image with density slice (high ratio values shown in red); b) histogram of 11/12 image; c) Ratio 11/12 image.

Li-bearing minerals (based on the spodumene spectrum)

ASTER

Sentinel-2
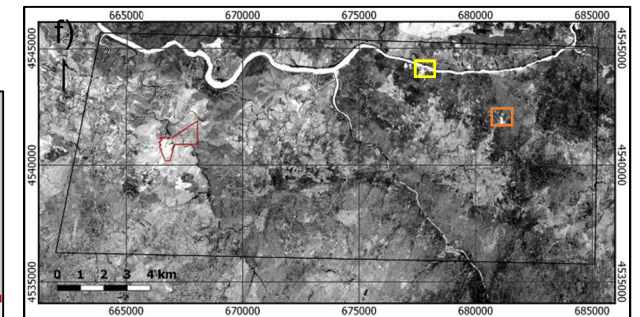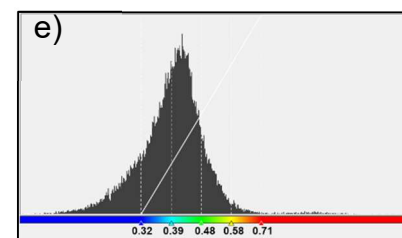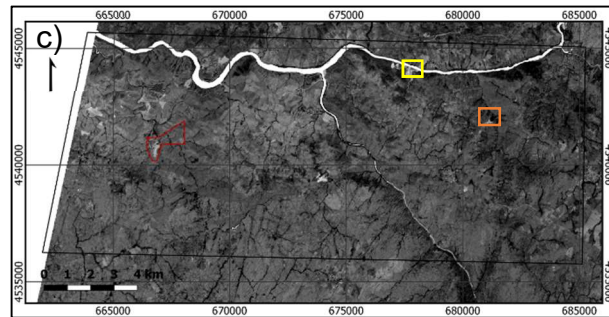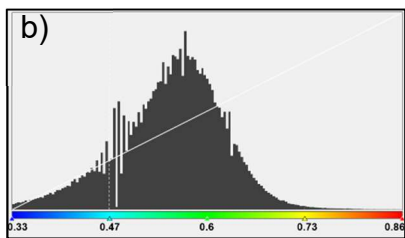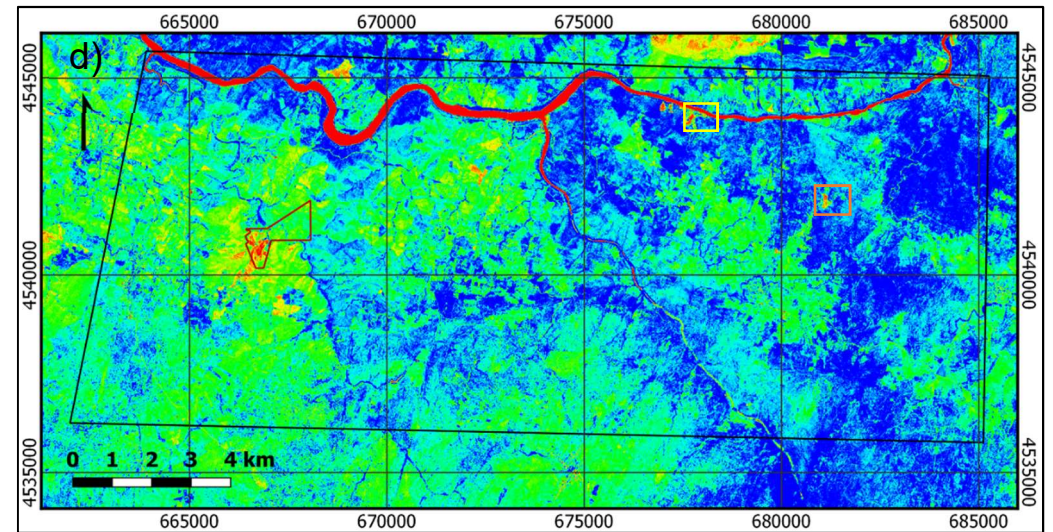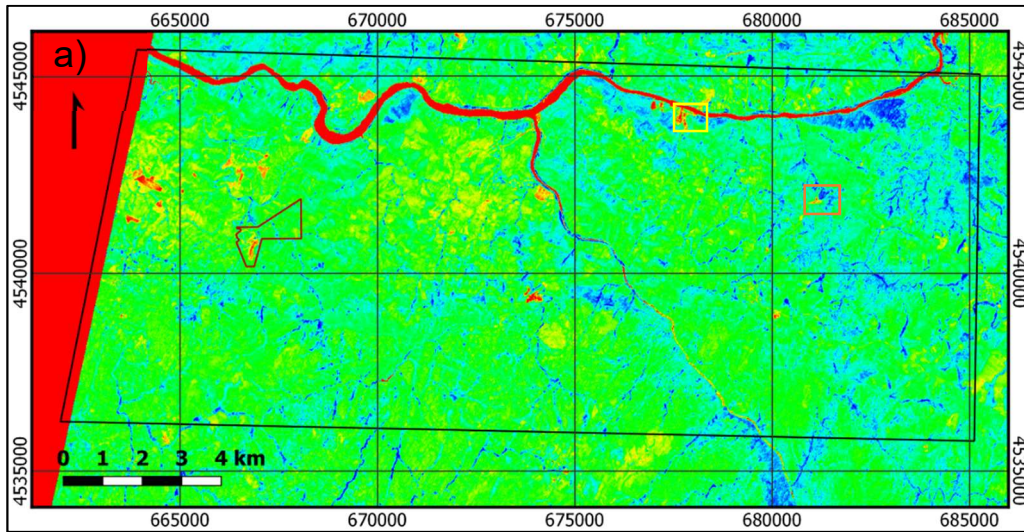
Legend

Bajoca mining concession   Studied area   Feli mine   Alberto mine

ASTER: a) ratio 1/3 image with density slice (high ratio values shown in red); b) histogram of 1/3 image; c) Ratio 1/3 image.

Sentinel-2: d) ratio 3/8 image with density slice (high ratio values shown in red); e) histogram of 3/8 image; f) Ratio 3/8 image.

Li-bearing minerals (based on the lepidolite spectrum)

Sentinel-2
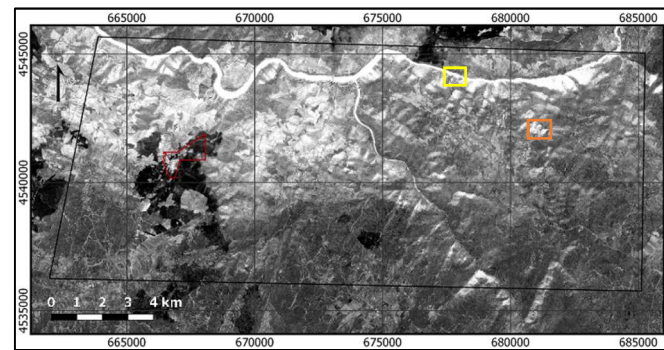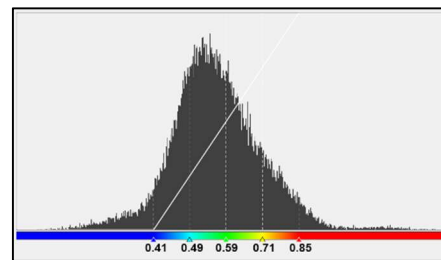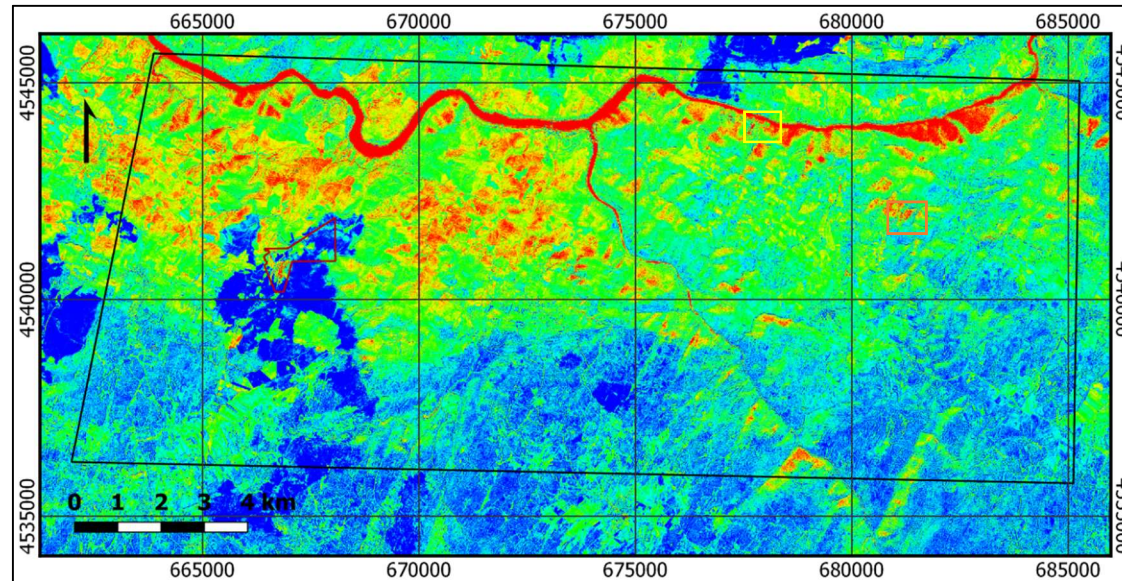
Legend

| | Bajoca mining concession | | Studied area | | Feli mine | | Alberto mine |

a) ratio 4/12 image with density slice (high ratio values shown in red); b) histogram of 4/12 image; c) Ratio 4/13 image.

Appendix D – Principal components analysis

D1: PCA on all VNIR and SWIR bands

ASTER (PCA on 9 bands)

Legend

☐ (red) Bajoca mining concession ☐ (black) Studied area ☐ (yellow) Feli mine ☐ (orange) Alberto mine

a) PC1; b) PC2; c) PC3

ASTER (PCA on 9 bands)
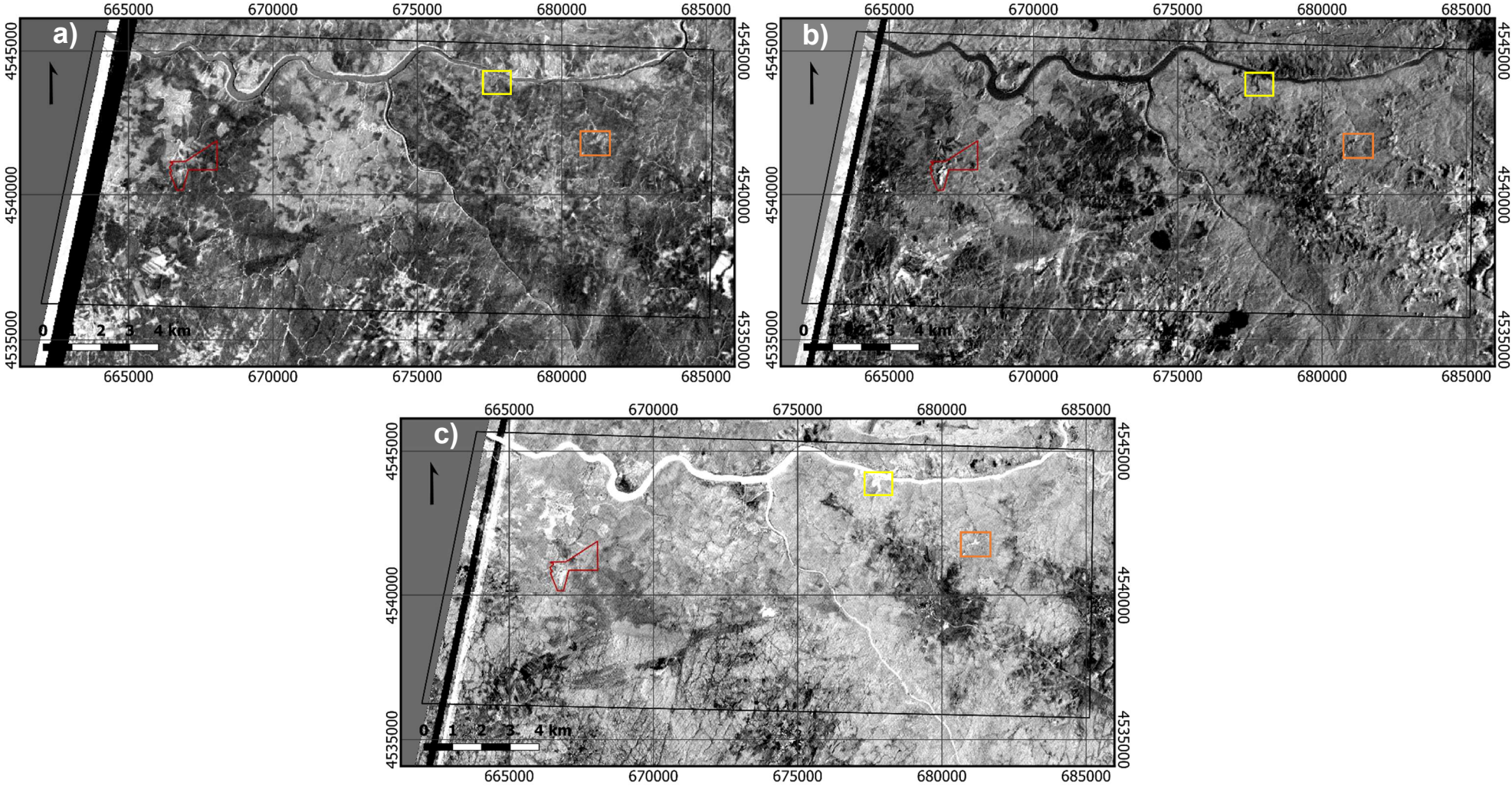
Legend

Bajoca mining concession Studied area Feli mine Alberto mine

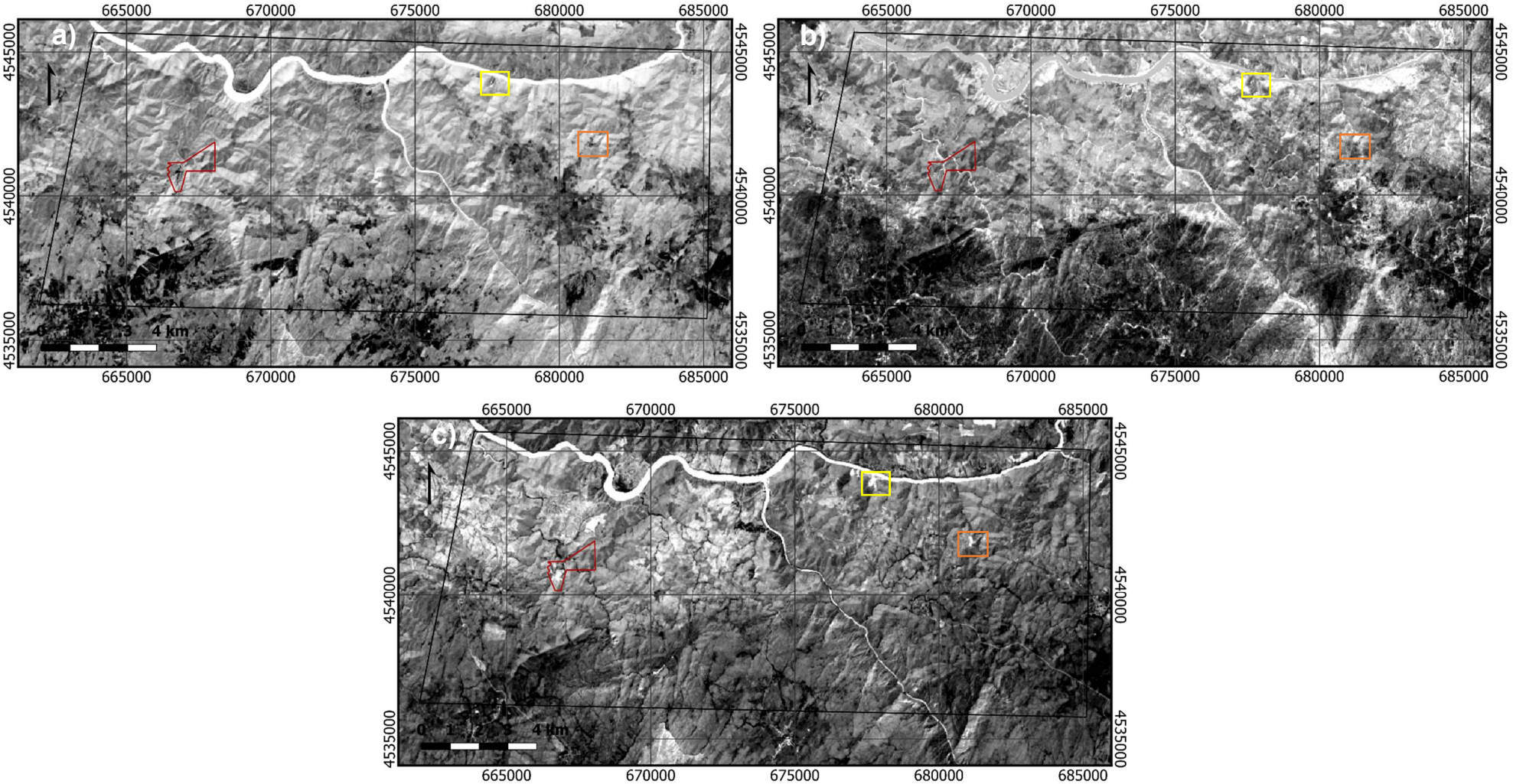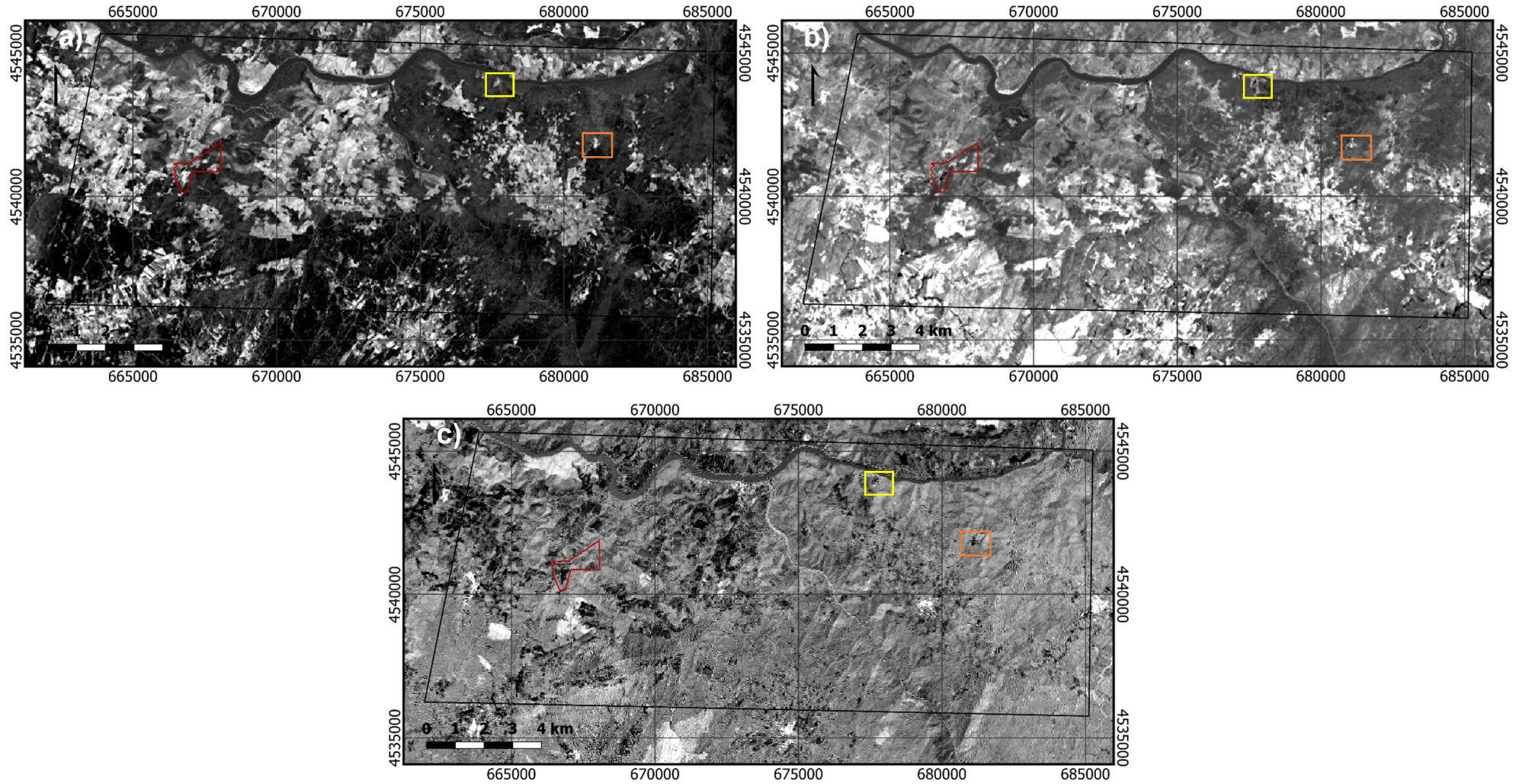a) PC4; b) PC5; c) PC6

ASTER (PCA on 9 bands)
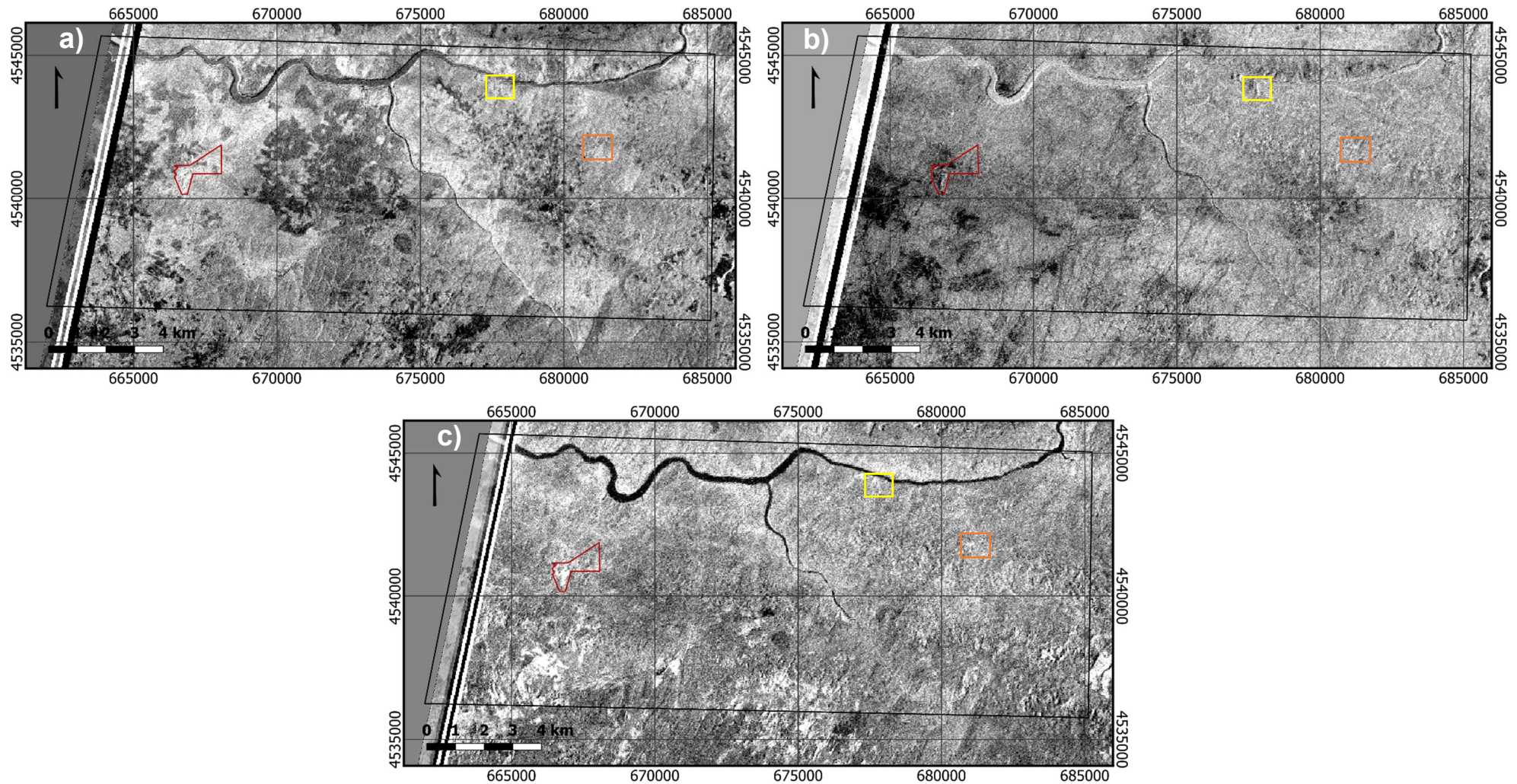
Legend

Bajoca mining concession	Studied area	Feli mine	Alberto mine

a) PC7; b) PC8; c) PC9

Landsat 8 (PCA on 6 bands)

Legend

☐ Bajoca mining concession   ☐ Studied area   ☐ Feli mine   ☐ Alberto mine
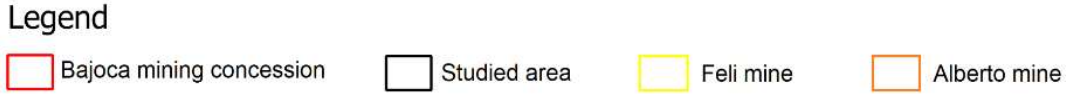
a) PC1; b) PC2; c) PC3

Landsat 8 (PCA on 6 bands)
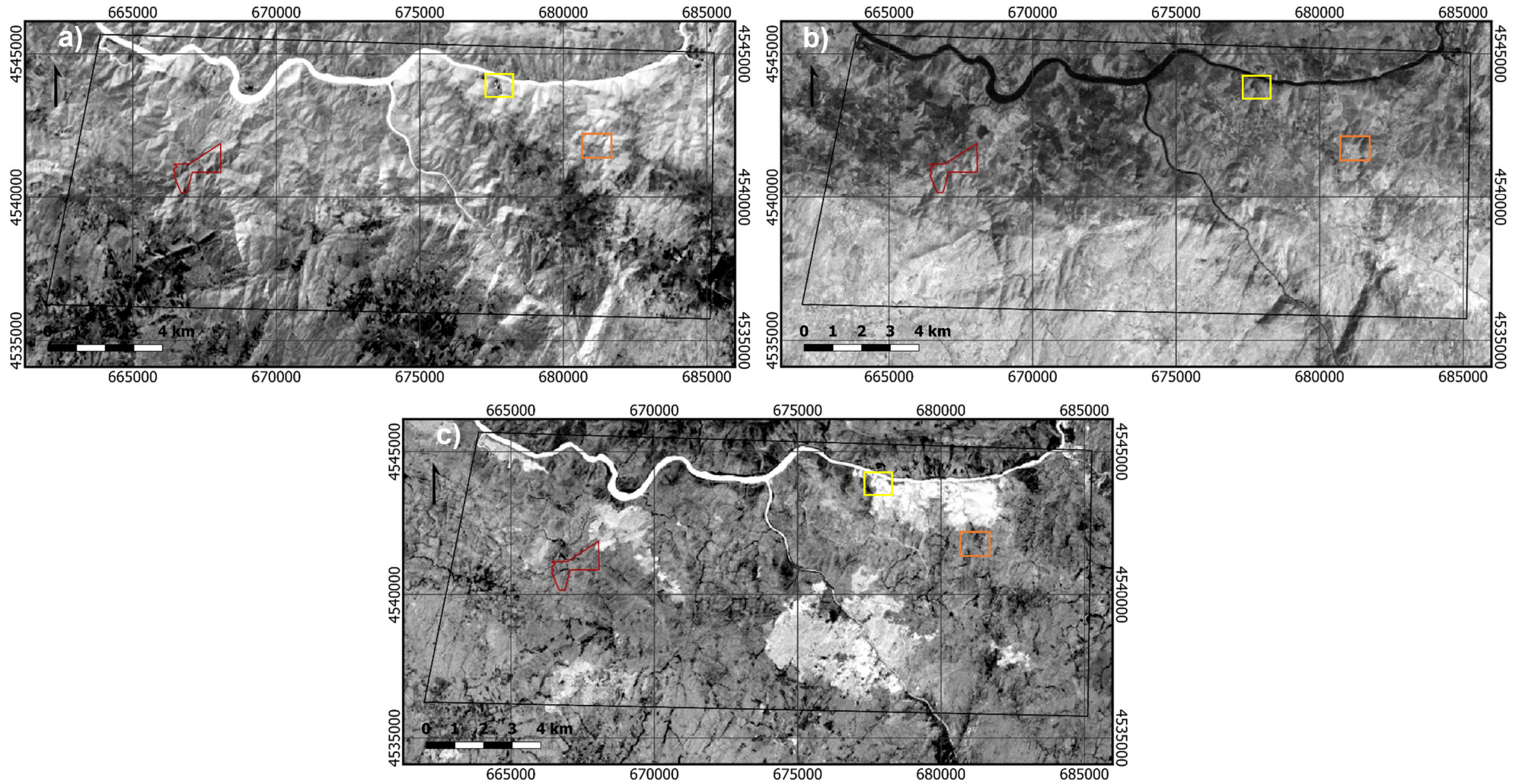

a) PC4; b) PC5; c) PC6

Landsat 5 (PCA on 6 bands)

Legend

Bajoca mining concession   Studied area   Feli mine   Alberto mine

a) PC1; b) PC2; c) PC3

Landsat 5 (PCA on 6 bands)
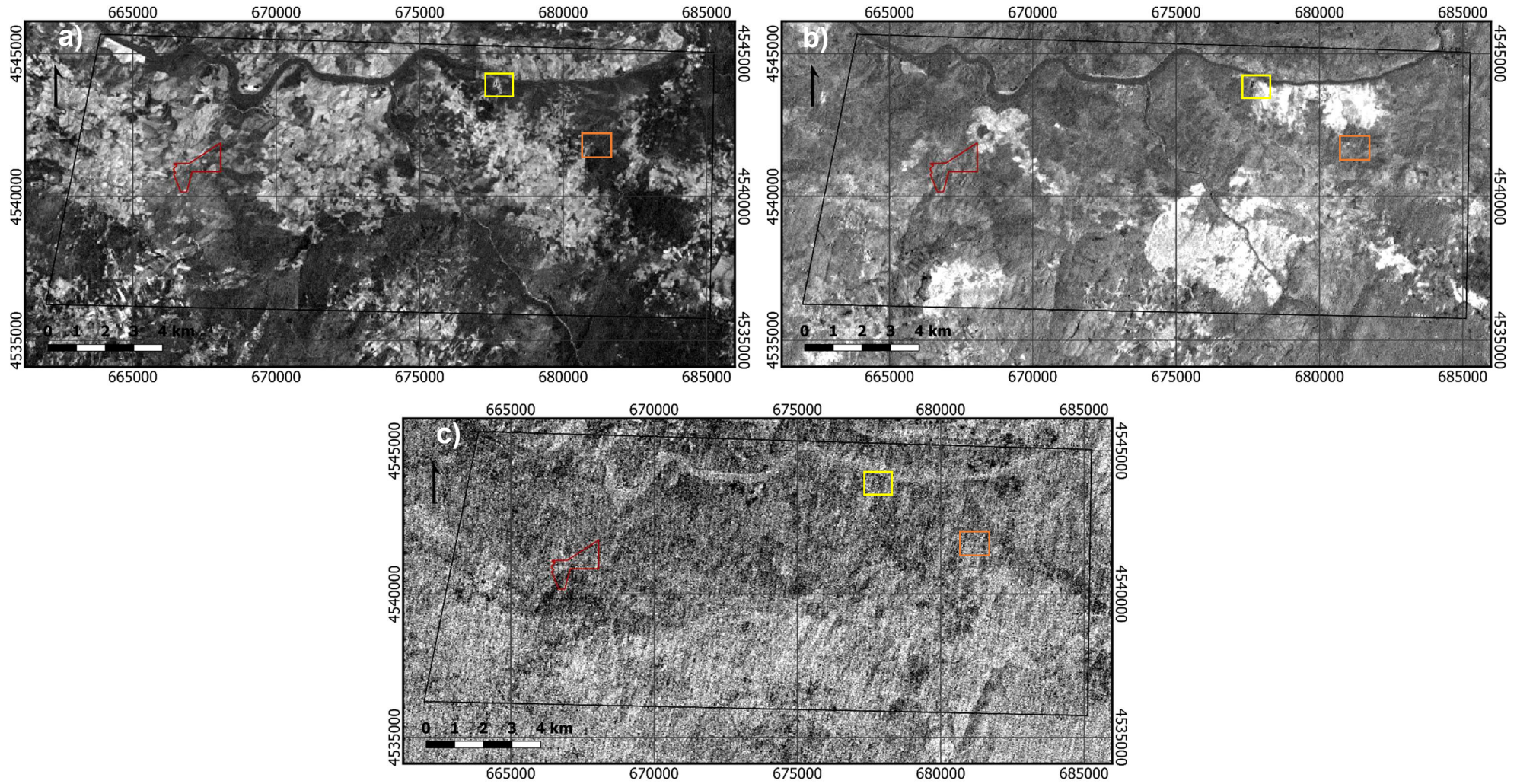
Legend

Bajoca mining concession | Studied area | Feli mine | Alberto mine

a) PC4; b) PC5; c) PC6

Sentinel-2 (PCA on 6 bands)

Legend

☐ Bajoca mining concession ☐ Studied area ☐ Feli mine ☐ Alberto mine

a) PC1; b) PC2; c) PC3
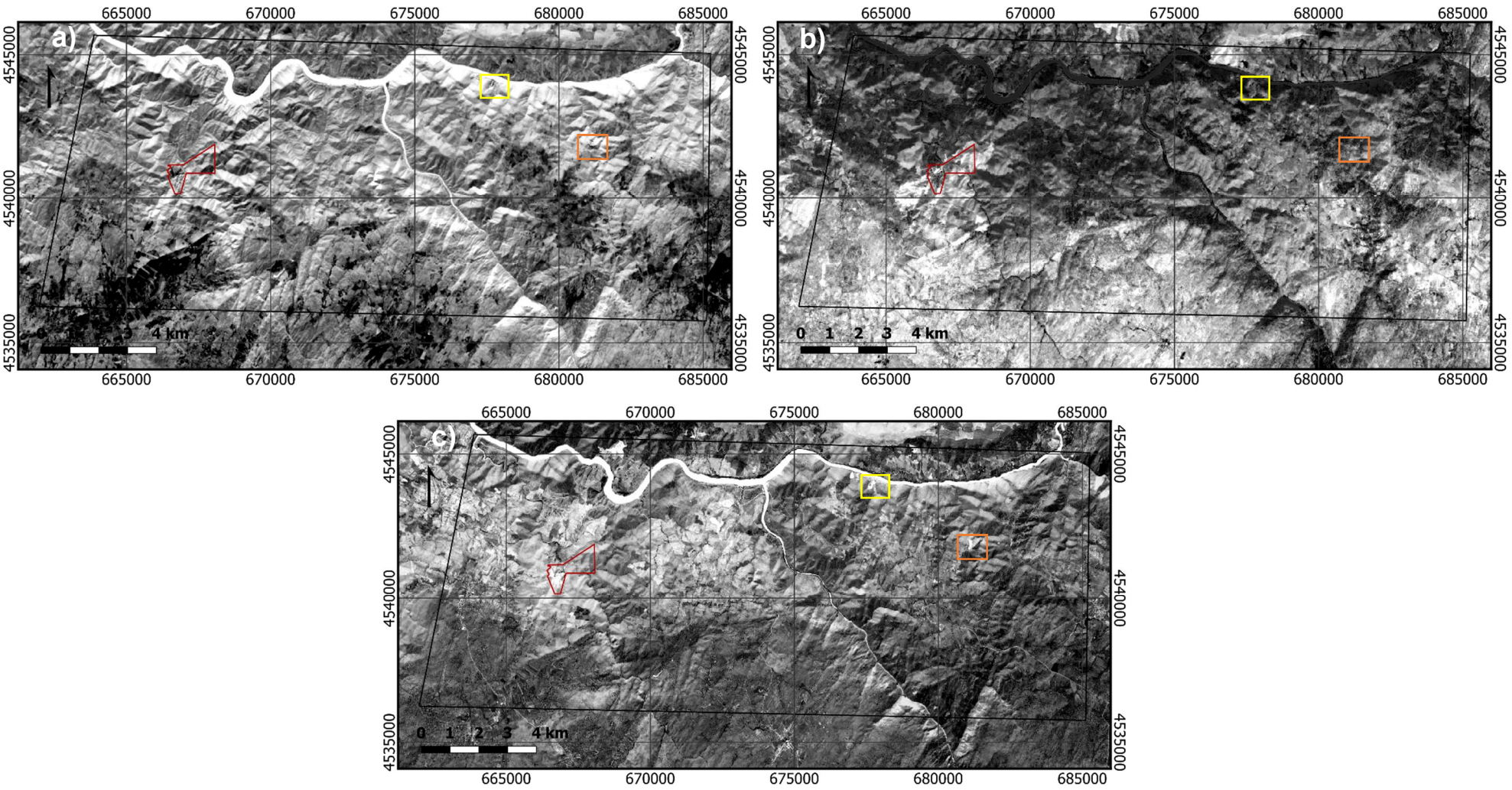
Sentinel-2 (PCA on 6 bands)

Legend

- Bajoca mining concession
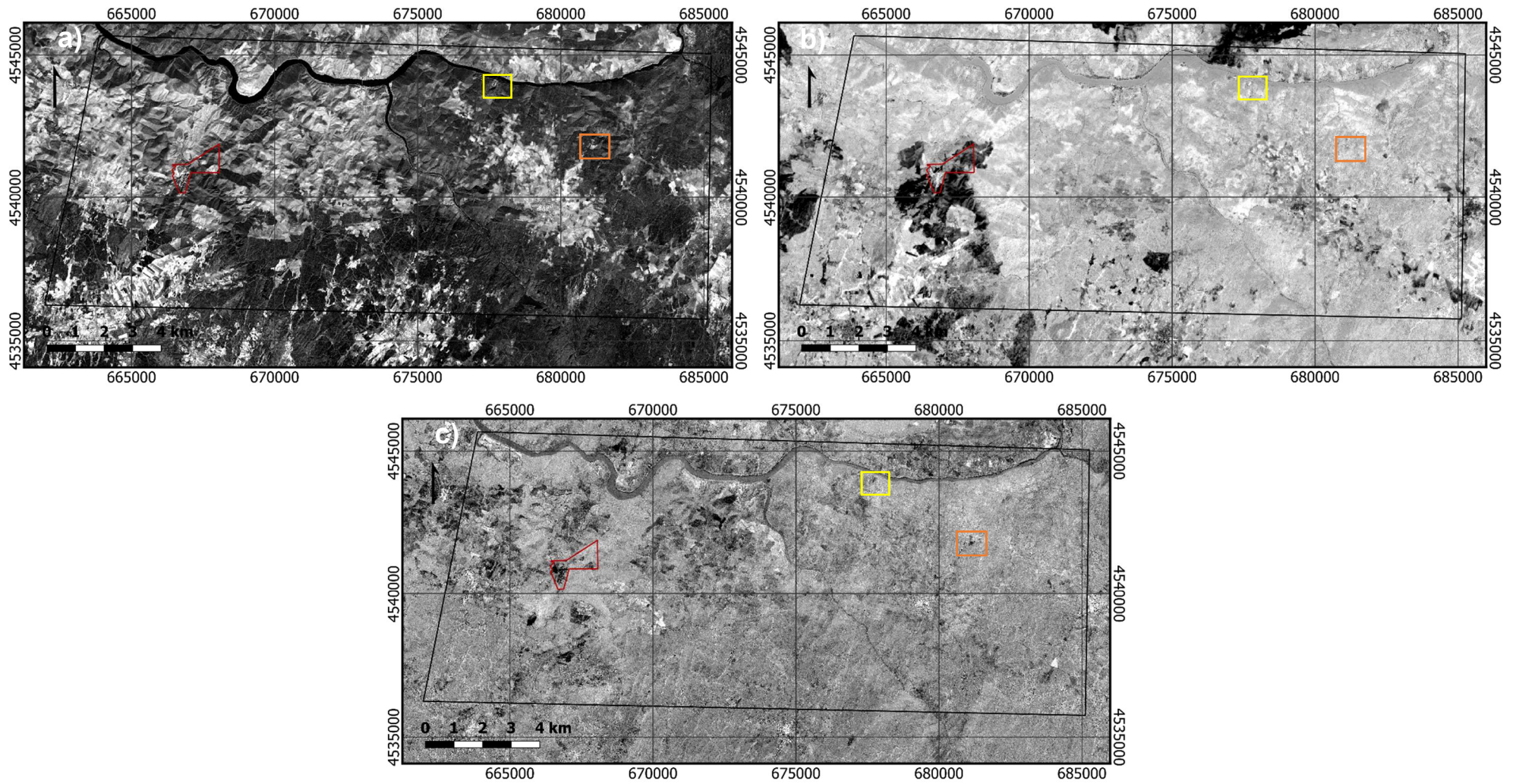- Studied area
- Feli mine
- Alberto mine

a) PC4; b) PC5; c) PC6

D2: Selective PCA

Ferric iron (4 bands)

Principal component analysis for ferric iron mapping (four Landsat 8 bands): Eigenvector and eigenvalues matrix

	PC1	PC2	PC3	PC4
Band 2	-0.36141	0.207367	0.685589	**-0.59695**
Band 4	-0.38638	-0.12621	0.500217	**0.76457**
Band 5	-0.57326	0.694055	-0.42341	0.101884
Band 6	-0.62567	-0.67776	-0.31698	-0.22068
Eigenvalues	1.45E+08	1.45E+08	1.45E+08	1.45E+08
Accounted variance	96.98306	96.98306	96.98306	96.98306
Cumulative variance	96.98306	96.98306	96.98306	96.98306

Principal component analysis for ferric iron mapping (four Sentinel-2 bands): Eigenvector and eigenvalues matrix

	PC1	PC2	PC3	PC4
Band 2	0.33523	-0.26717	0.66202	**-0.61479**
Band 4	0.32995	0.07314	0.5629	**0.75427**
Band 8	0.52724	-0.72393	-0.41826	0.1517
Band 11	0.70766	0.63182	-0.26444	-0.17347
Eigenvalues	713083.9	309200.6	66105.28	1739.112
Accounted variance	65.4128	28.36368	6.063988	0.159533
Cumulative variance	65.4128	93.77648	99.84047	100

Ferric iron (2 bands)

Principal component analysis for ferric iron mapping (two Landsat 5 bands): Eigenvector and eigenvalues matrix

	PC1	PC2
Band 1	-0.85561	**0.517613**
Band 3	-0.51761	**-0.85561**
Eigenvalues	41239207	415821
Accounted variance	99.00175	0.998249
Cumulative variance	99.00175	100

Principal component analysis for ferric iron mapping (two Sentinel-2 bands): Eigenvector and eigenvalues matrix

	PC1	PC2
Band 2	0.71423	**-0.69991**
Band 4	0.69991	**0.71423**
Eigenvalues	2505325.753	30139.90684
Accounted variance	98.8113	98.8113
Cumulative variance	98.8113	98.8113

Ferric iron (selective PCA on 4 bands)
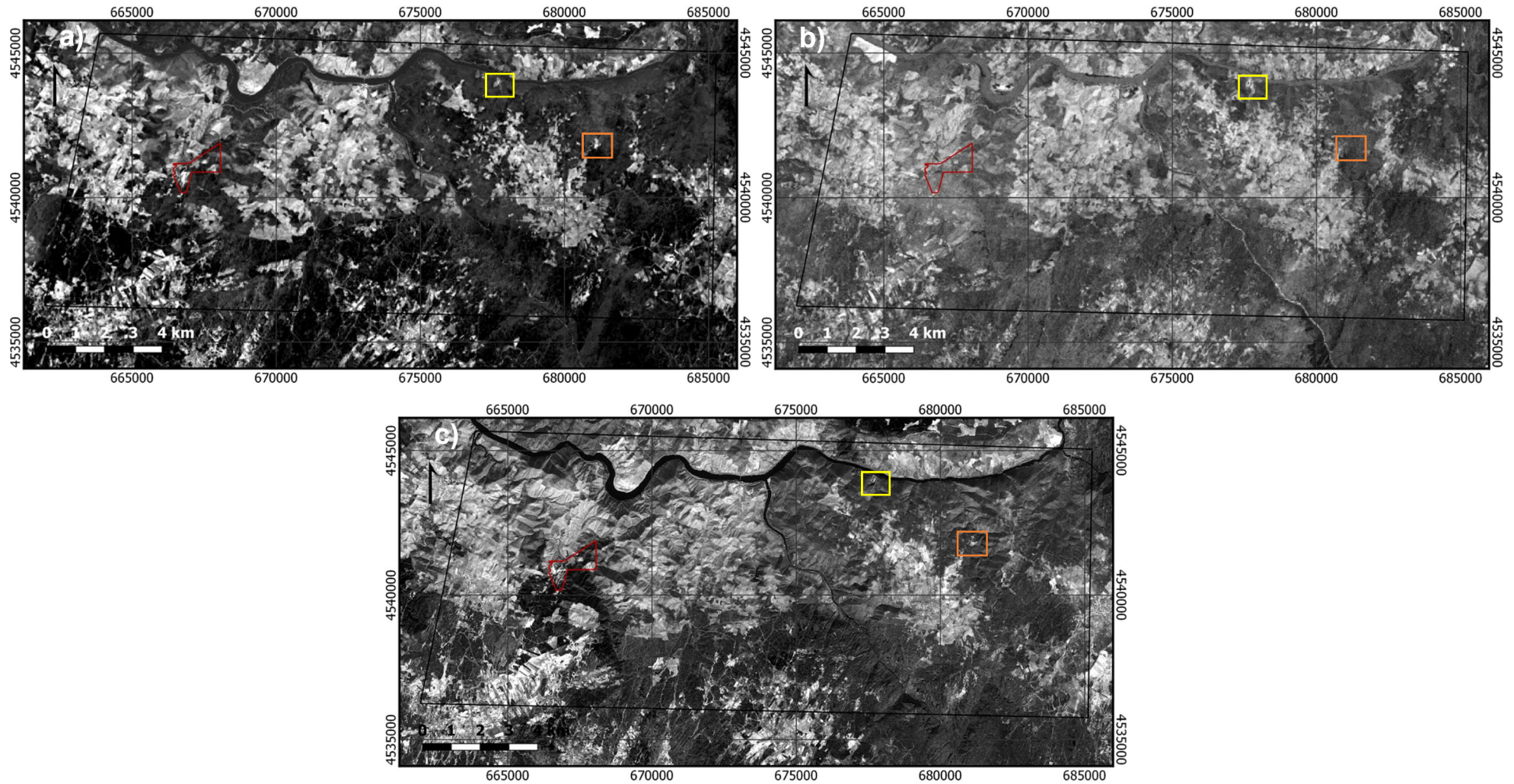
Legend

Bajoca mining concession	Studied area
Feli mine	Alberto mine

a) PC4 from the Landsat 8 subset; b) PC4 from the Landsat 8 subset; c) PC4 from the Sentinel-2 subset

Hydroxyl minerals (4 bands)

Principal component analysis for hydroxyl mineral mapping (four Landsat 8 bands): Eigenvector and eigenvalues matrix

	PC1	PC2	PC3	PC4
Band 2	-0.34922	0.241737	0.857386	-0.29068
Band 5	-0.55312	0.726695	-0.38556	0.131594
Band 6	-0.60934	-0.51744	-0.28214	**-0.53043**
Band 7	-0.44812	-0.38176	0.191384	**0.785382**
Eigenvalues	1.55E+08	1.55E+08	1.55E+08	1.55E+08
Accounted variance	96.89612	96.89612	96.89612	96.89612
Cumulative variance	96.89612	96.89612	96.89612	96.89612

Principal component analysis for hydroxyl mineral mapping (four Landsat-5 bands): Eigenvector and eigenvalues matrix

	PC1	PC2	PC3	PC4
Band 1	-0.47676	-0.70417	-0.50978	-0.13032
Band 4	-0.37262	-0.38003	0.826178	0.184833
Band 5	-0.70966	0.542057	0.029735	**-0.44907**
Band 7	-0.36088	0.256711	-0.23806	**0.8644**
Eigenvalues	5903.826	5903.826	5903.826	5903.826
Accounted variance	92.76451	92.76451	92.76451	92.76451
Cumulative variance	92.76451	92.76451	92.76451	92.76451

Hydroxyl minerals (2 bands)

Principal component analysis for hydroxyl mineral mapping (two Landsat 8 bands):
Eigenvector and eigenvalues matrix

|	PC1	PC2
Band 6	-0.80572	**0.592293**
Band 7	-0.59229	**-0.80572**
Eigenvalues	90126127	168615.1
Accounted variance	99.81326	0.186739
Cumulative variance	99.81326	100

Principal component analysis for hydroxyl mineral mapping (two Landsat 5 bands):
Eigenvector and eigenvalues matrix

	PC1	PC2
Band 5	-0.89157	**0.452879**
Band 7	-0.45288	**-0.89157**
Eigenvalues	3862.588	30.62377
Accounted variance	99.21341	0.786594
Cumulative variance	99.21341	100

Hydroxyl minerals (selective PCA on 2 bands)
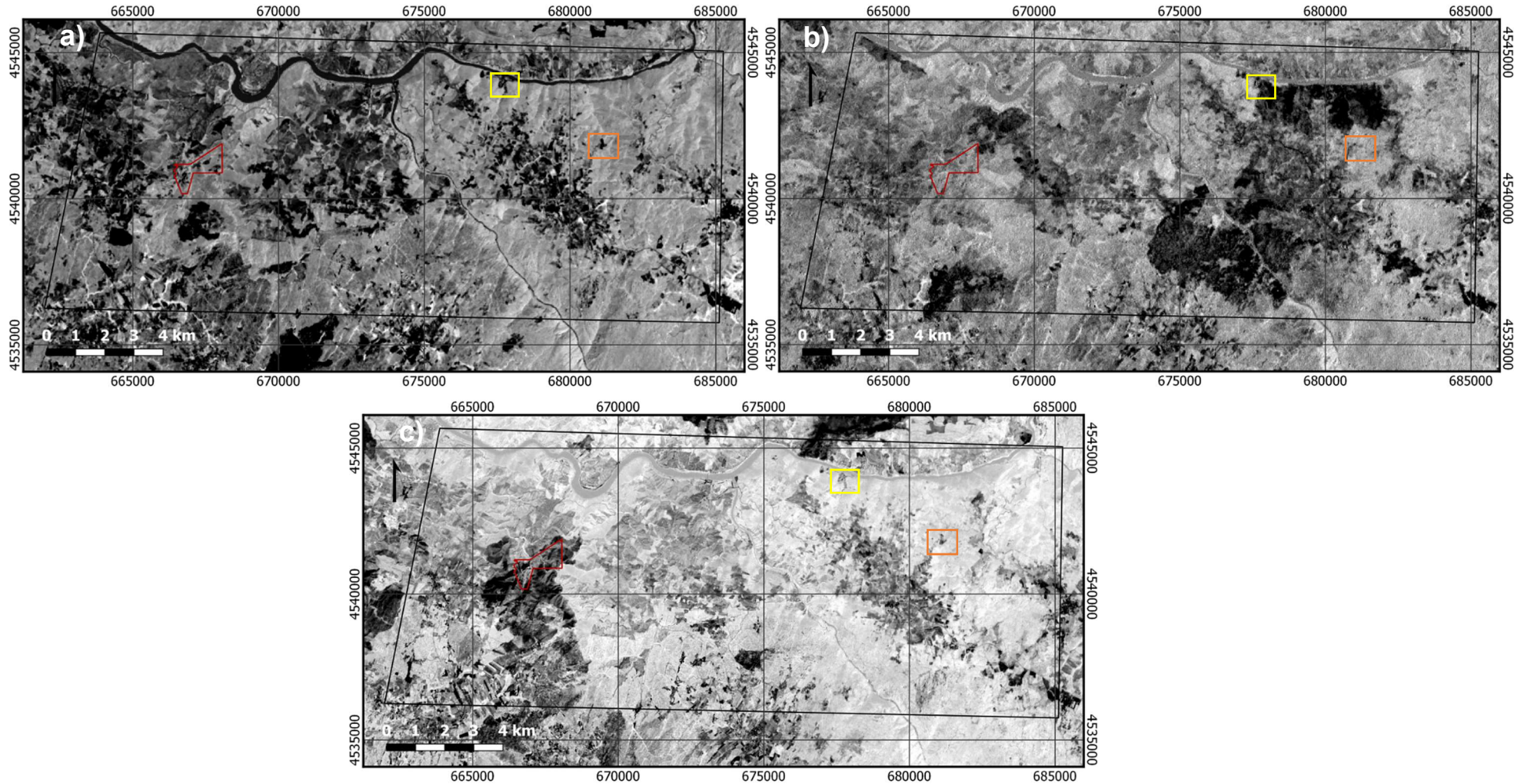
Legend

Bajoca mining concession	Studied area	Feli mine	Alberto mine

a) PC2 from the Landsat 8 subset; b) PC2 from the Landsat 8 subset; c) negated PC2 from the Sentinel-2 subset

Li-bearing minerals (4 bands)

Principal component analysis for lithium mapping (four Landsat 8 bands): Eigenvector and eigenvalues matrix

	PC1	PC2	PC3	PC4
Band 2	-0.2866	0.280253	-0.56807	-0.71877
Band 3	-0.28132	0.324294	-0.57711	**0.694724**
Band 5	-0.44949	0.678137	0.581239	**-0.01573**
Band 11	-0.79792	-0.59701	0.080075	0.022091
Eigenvalues	2.28E+08	7145705	948391.5	55640.59
Accounted variance	96.5417	3.032244	0.402445	0.023611
Cumulative variance	96.5417	99.57394	99.97639	100

Principal component analysis for lithium mapping (four Landsat 8 bands): Eigenvector and eigenvalues matrix

	PC1	PC2	PC3	PC4
Band 1	-0.42629	0.608007	0.544938	-0.38942
Band 2	-0.21021	0.36581	0.073188	**0.903681**
Band 4	-0.32949	0.405966	-0.83461	**-0.17338**
Band 6	-0.8158	-0.57594	0.033472	0.040663
Eigenvalues	7172.809	534.7539	100.5855	17.44264
Accounted variance	91.65837	6.833399	1.285341	0.222892
Cumulative variance	91.65837	98.49177	99.77711	100

Principal component analysis for lithium mapping (four Sentinel-2 bands): Eigenvector and eigenvalues matrix

|	PC1	PC2	PC3	PC4
Band 2	0.33816	-0.26251	-0.7015	0.56977
Band 3	0.3096	-0.167	-0.45342	-0.81894
Band 8	0.53171	-0.65632	0.53383	0.03929
Band 11	0.7121	0.68734	0.13165	0.05614
Eigenvalues	11010702	157937.3	44014.22	3588.291
Accounted variance	98.1675	1.4081	0.3924	0.032
Cumulative variance	98.1675	99.5756	99.968	100

Li-bearing minerals (2 bands)

Principal component analysis for lithium mapping (two Landsat 8 bands): Eigenvector and eigenvalues matrix

	PC1	PC2
Band 3	0.523175	-0.85223
Band 5	0.852226	0.523175
Eigenvalues	68002892	669544.1
Accounted variance	99.02502	0.974982
Cumulative variance	99.02502	100

Principal component analysis for lithium mapping (two Landsat 8 bands): Eigenvector and eigenvalues matrix

	PC1	PC2
Band 2	0.535765	-0.84437
Band 4	0.844367	0.535765
Eigenvalues	1297.41	43.30514
Accounted variance	96.77	3.230002
Cumulative variance	96.77	100

Principal component analysis for lithium mapping (two Sentinel-2 bands): Eigenvector and eigenvalues matrix

	PC1	PC2
Band 3	0.49806	**0.86714**
Band 8	0.86714	**-0.49806**
Eigenvalues	4238345	26410.16
Accounted variance	99.3807	0.6193
Cumulative variance	99.3807	100

Li-bearing minerals (selective PCA on 2 bands)
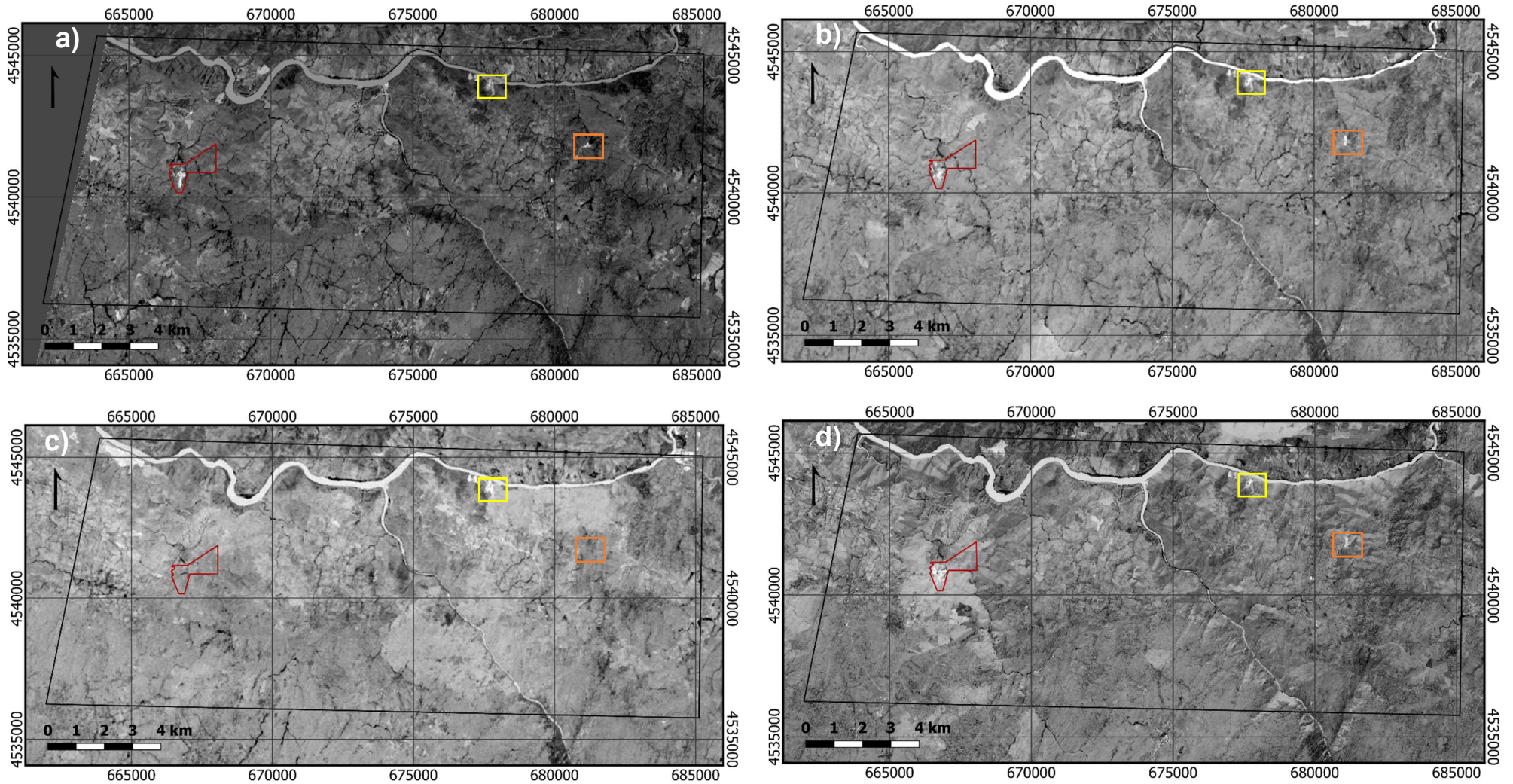
Legend

Bajoca mining concession   Studied area   Feli mine   Alberto mine

a) PC2 from the ASTER subset; b) negated PC2 from Landsat 8 subset; c) negated PC2 from the Landsat 8 subset; d) PC2 from the Sentinel-2 subset
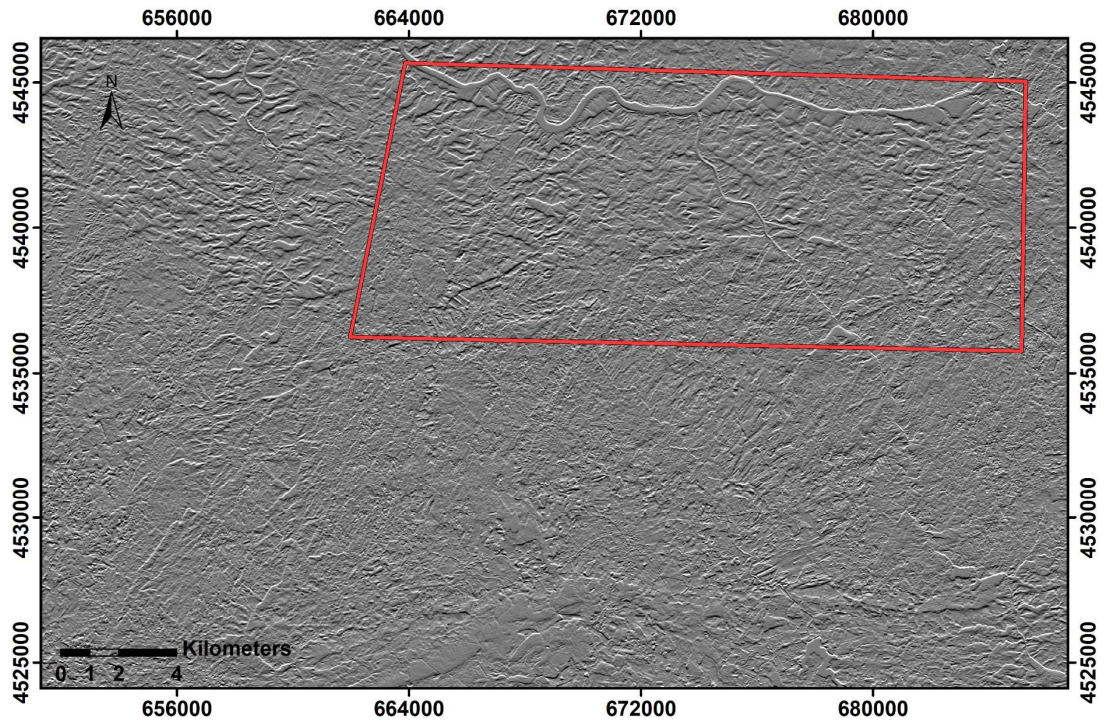
Appendix E – Lineament extraction

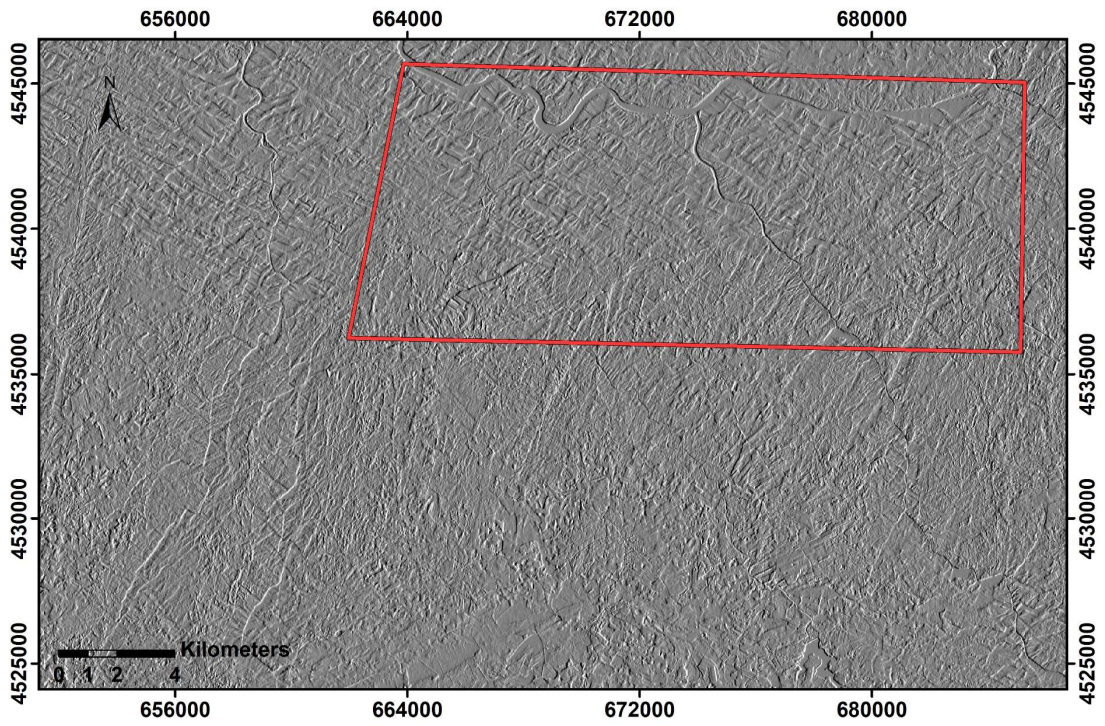E1: Filtered images

E2: Lineament extraction process
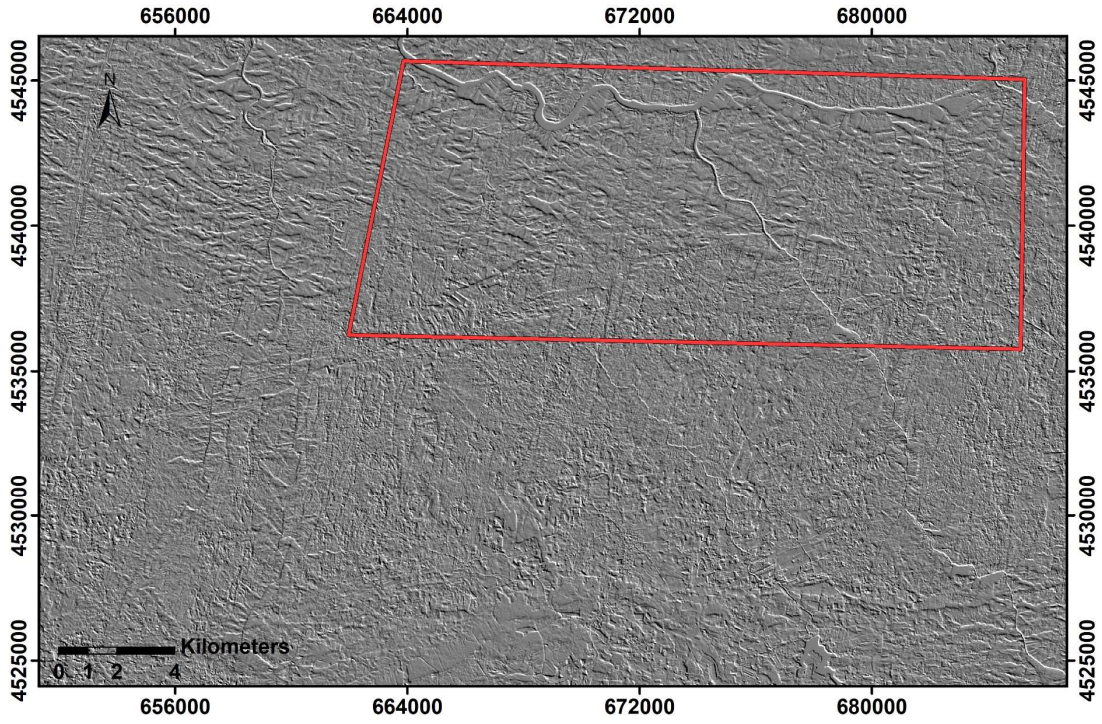
E3: Extracted lineaments

E1: Filtered images

N-S

E-W

NE-SW

NW-SE

E2: Lineament extraction process

Legend

⎯⎯⎯ (red) Extracted lineaments

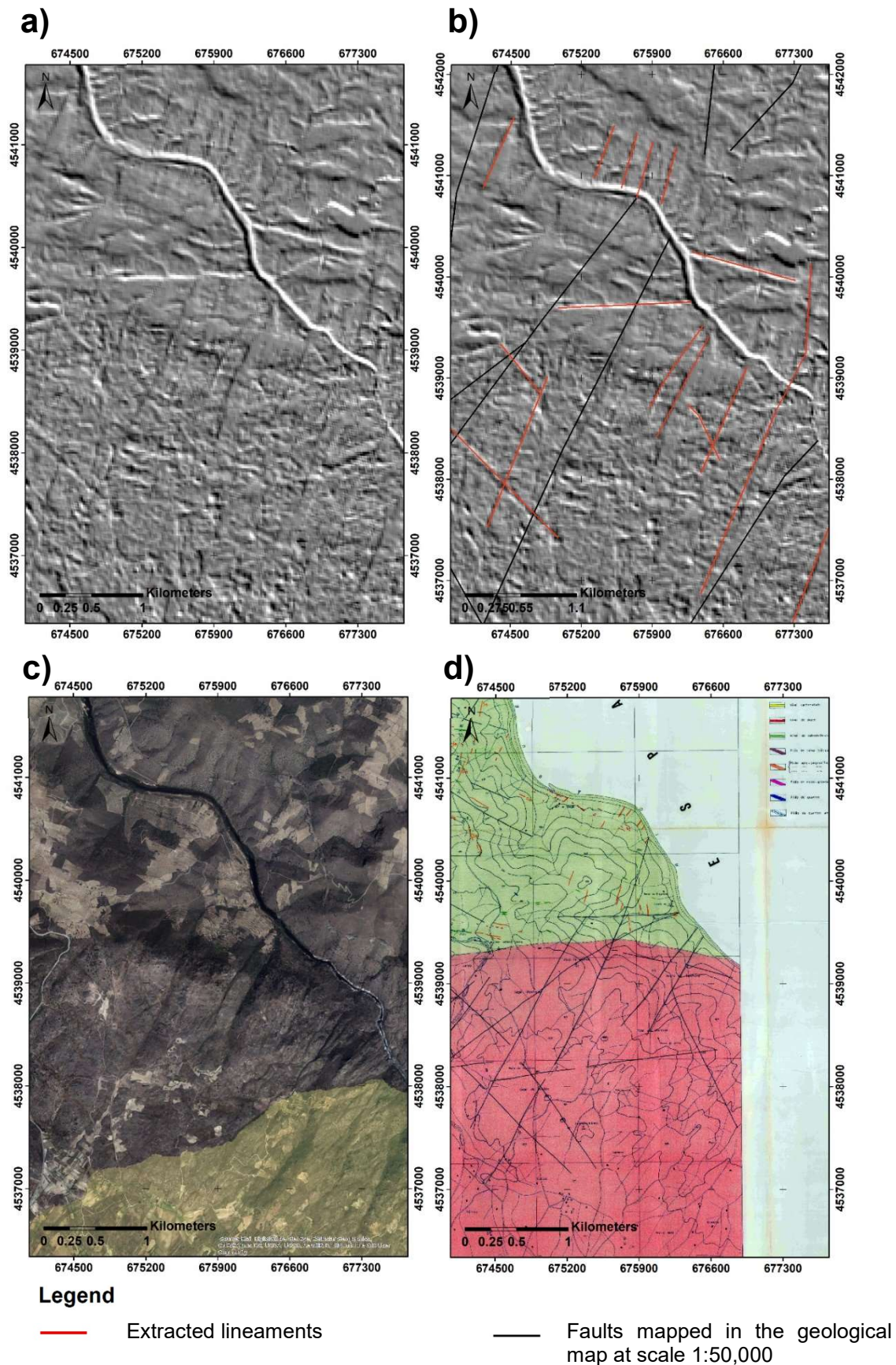⎯⎯⎯ (black) Faults mapped in the geological map at scale 1:50,000
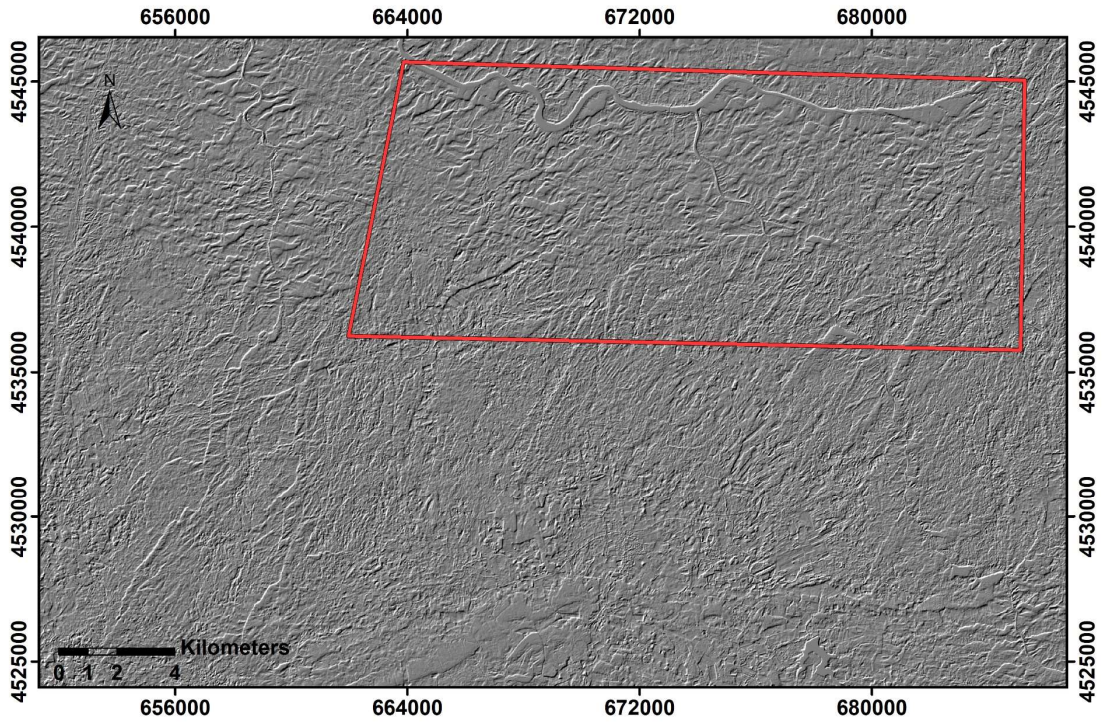
a) NE-SW filtered band 11; b) lineaments extracted based on the filtered image (a); c) ArcMap's "World Imagery" basemap used to separate possible geological structures from other linear features; d) geological map at the scale 1:10,000 used to compare with the extracted lineaments.

E3: Lineaments extracted

Legend

▢	Bajoca mining concession	—	Extracted lineaments
▭	Studied area	—	Extracted lineaments confirmed by the geologic map at scale 1:10,000